Mapping of the electric field using transmission electron microscopy

Lucas Bruas

THÈSE

Pour obtenir le grade de

DOCTEUR DE L'UNIVERSITÉ GRENOBLE ALPES

École doctorale : PHYS - Physique
Spécialité : Physique de la Matière Condensée et du Rayonnement
Unité de recherche : Laboratoire d'Electronique et de Technologie de l'Information (LETI)

Cartographie de champs électriques en microscopie électronique en transmission à balayage

Mapping of the electric field using transmission electron microscopy

Présentée par :

Lucas BRUAS

Direction de thèse :

Jean-Luc ROUVIERE DIRECTEUR DE RECHERCHE, CEA CENTRE DE GRENOBLE	Directeur de thèse
David COOPER INGENIEUR HDR, CEA CENTRE DE GRENOBLE	Co-directeur de thèse

Rapporteurs :

RAFAL E. DUNIN-BORKOWSKI
PROFESSEUR, RHEINISCH-WESTFALISCHE TECH. HOCH. AA
ANA M. SANCHEZ
FULL PROFESSOR, UNIVERSITY OF WARWICK

Thèse soutenue publiquement le **17 octobre 2023**, devant le jury composé de :

RAFAL E. DUNIN-BORKOWSKI PROFESSEUR, RHEINISCH-WESTFALISCHE TECH. HOCH. AA	Rapporteur
ANA M. SANCHEZ FULL PROFESSOR, UNIVERSITY OF WARWICK	Rapporteure
TREVOR P. ALMEIDA DOCTEUR EN SCIENCES, UNIVERSITY OF GLASGOW	Examinateur
MOIRA HOCEVAR CHARGEE DE RECHERCHE HDR, CNRS DELEGATION ALPES	Examinatrice
WILLIAMS LEFEBVRE PROFESSEUR DES UNIVERSITES, UNIVERSITE DE ROUEN NORMANDIE	Président
EIRINI SARIGIANNIDOU MAITRE DE CONFERENCES HDR, GRENOBLE INP	Examinatrice

Introduction

Semiconductor devices consist of a structure containing charged regions at equilibrium. By applying a voltage to a region of the device, the charge can then flow from a region of high potential to a region of lower potential due to the presence of an electric field. The presence of charge flow, or current, means that the device is on as opposed to off. The first example of a modern electronic device is the transistor, which was created at Bell Labs in 1947. The transistor is the key component of modern electronic design, and it was the first electrical component that could control the current flow by creating an electric field at an electrical contact.

Since this discovery, the electronic industry has continuously made improvements in terms of quality, speed and especially the size of the components. Moore's law, formalized in 1965, described this reduction in size. It predicted a doubling every 18 months of the number of components per area in an integrated circuit. As a consequence, the semiconductor industry also has to improve the characterization techniques used to assess the quality of the components. Inside today's common consumer electronic devices, such as laptops or smartphones, the processor is built using 7 to 10 nm transistors. Because of this reduction in size, we now talk about nano-electronics. To assess the quality of such tiny components, state-of-the-art microscopy is required. The transmission electron microscope (TEM) has been a tool that has been widely used since the beginning of the development of transistor technology. This is due to its high spatial resolution, which has been used to accurately measure the structure of the individual components. Improvements in the detection capability, stability and automation of modern TEM tools now allow measurements to be made of composition, strain fields and the electromagnetic fields, all with nanometer scale resolution.

The measurement of the electric field is of huge interest as its position, orientation and strength will control the properties of an electronic device. However, this measurement with the required resolution and accuracy is difficult. TEM is well-adapted for field measurements as the incident electrons are sensitive to both the electromagnetic fields and electromagnetic potentials. In this Phd thesis, the pixelated-STEM technique was developed and compared to two other techniques that are better known. These techniques are the TEM-based off-axis electron holography (which will now be referred as electron holography) and segmented differential phase contrast (DPC). By electron holography, maps of the electrostatic potential can be obtained using electron interference. The negatively charged electron beam is

deflected either side of a positively charged wire or birpsim to interfere with itself. The interference fringes contain information about the phase of the electrons from which the local potential can be obtained. If measurements of the electric field are required, then it can be derived from the potential map. This technique is well-developed in several labs around the world and has been the focus of many years of development at CEA LETI. Therefore, it will be used as the benchmark for this work in terms of potential and field mapping. The second technique, DPC is based on the detection of the deflection of a convergent beam as it passed through a region containing an electric field. This is done by measuring the changes in beam current measured on a segmented detector. The pixelated differential phase contrast approach uses the same principle as DPC, but uses a pixelated detector to collect the full distribution of the scattered electron beam from which we hope to be able to quantify the measurements of the electric field.

To study and compare the three techniques, different specimens were examined to develop the quantification procedure and highlight the experimental difficulties. The first sample consists of a silicon pn junction. This choice was motivated by the fact that silicon is widely used in microelectronics devices and its growth and doping are well developed, thus it is the one of the least complex components to study. Then samples made of silicon/silicon oxide (Si/SiO_2) and silicon / silicon germanium superlattices (Si/SiGe) were studied. They were chosen because such materials are typically used in transistor architecture and these were used to study the effect of interfaces on the measured electric fields. The last samples shown in this thesis comprised a LED structure made of gallium nitride (GaN) containing indium gallium nitride (InGaN) quantum wells (QW)s. These samples were extracted from blue micro-LEDs. These samples were found to be complex for characterization due to the small size of the QWs, the hexagonal lattice of GaN, the fact that the InGaN layers are easily damaged by the electron beam and finally, the presence of piezo electric polarization in the QWs. Thus, within this manuscript we show different architectures and compositions that presents incrementally more complex challenges.

Benchmarking the three techniques on these different sample and comparing the results will gives the key to understand what improvements are brought by pixelated-STEM and what are respectively the limits of each technique. This manuscript includes four chapters presenting the results obtained during the thesis:

Chapter 1: firstly, the basics of semiconductor, electric field and TEM imaging are described. Then the basics of holography, DPC and 4D-STEM are presented. For each technique, the acquisition and the data processing are detailed and the main experimental

consideration are given. Important concepts such as the weak phase object approximation and the rigid shift model for the STEM-based techniques are presented. A section is then dedicated to strain mapping using 4D-STEM. This chapter ends by describing TEM sample preparation by focused ion beam milling.

Chapter 2: this chapter is dedicated to a thorough study of a Si pn junction. It begins with a theoretical approach coupled with simulation in order to obtain quantitative values of the expected field. Next holography is performed to benchmark the electric field measurement in the junction using a well-known technique. Then different modes of 4D-STEM are explored: low magnification (LM) and nano-beam (NB). For both modes the limits are highlighted. Then a section focuses on how to overcome the diffraction artefacts encountered in STEM mode when trying to measure field. Finally, the effect of the electron dose on the junction are investigated and improvements brought by new generation of fast camera are shown.

Chapter 3: in this chapter, the influence of chemical interfaces is highlighted. The first section details experimental work and simulation on Si/SiO_2 interface. This first study shows that the tail of the electron probe influences the results when scanning several nanometers away from the interfaces. Then SiGe 10nm wide layers in Si are studied, it is shown that quantitative germanium concentration can be obtained from holography and 4D-STEM. To finish the study on SiGe, the artefact and limits brought by the interface i.e. the step in mean inner potential (MIP) between Si and SiGe are experienced in 4D-STEM.

Chapter 4: to begin this chapter, preliminary work on the InGaN sample is presented. It encompasses different experiences and simulation performed to estimate the electric field in the QWs. Then holography and DPC are used to benchmark the field measurement in such sample. Then using simulation, the combine effect of piezo field and MIP on the diffraction pattern is shown. After that the limits of 4D-STEM in such sample is highlighted. Then a section is dedicated to the influence of the beam damage on the sample and new generation of fast camera is tested. Finally, in the last section, energy filtering precession and data treatment are tested to see if the artefacts previously shown can be overcome.

Conclusion and outlook: a summary of the main results obtained during this thesis are presented. Especially, the improvements brought by 4D-STEM compare to holography

and DPC. The new limits that 4D-STEM reaches are remind and finally, outlook of work for deeper understanding of the 4D-STEM field measurement technique are suggested.

Appendix: at the end of this manuscript, three appendixes are gathered and describe the following topics:

A. Conversion of .xyz files into µTSEM input file (python script)

B. Generation of SiGe sample superlattice for µSTEM simulation (python script)

C. Generation of InGaN sample superlattice for µSTEM simulation (python script)

1 Electric field and strain mapping in semiconductors by means of transmission electron microscopy

The decrease in size of microelectronics components leads to a need of characterization techniques with the appropriate spatial resolution. As these components are reduced in size, smaller volumes are probed leading to a need for high sensitivity or precision. At the same time, the material properties need to be measured accurately [1]. A transmission electron microscope (TEM) is the instrument of choice to measure material properties at the nanoscale as the wavelength of an electron is 2.5 pm at 200 keV. Although the aberrations in a TEM lead to a spatial resolution that is much below the theoretical limit, the development of routine and stable aberration correction makes sub angstrom imaging straightforward.

In a modern electron microscope, the stability combined with the development of faster and more accurate detectors allows multiple techniques such as structural imaging by HAADF STEM, compositional imaging by Electron Energy Loss Spectroscopy (EELS) and Energy Dispersive X-Ray Spectroscopy (EDX) and strain mapping by Nanobeam Diffraction to be performed quickly and easily. All these characterization techniques help to improve the process flow for the realization of nanoscale electronic components. However, as electrons are charged particles sensible to changes in potential, it allows us to measure these potentials with a nanoscale resolution.

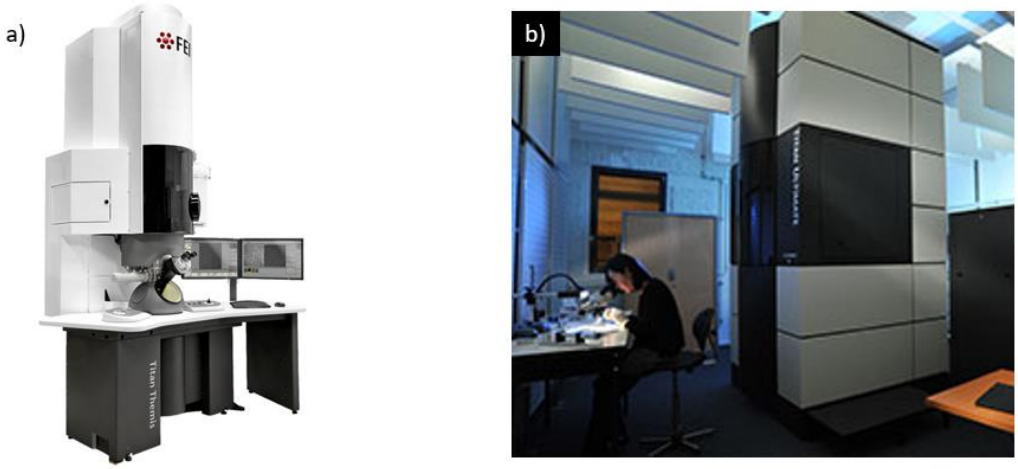

Figure 1-1 : Pictures of the two microscopes used for the work presented in this manuscript. a) FEI Titan Themis b) FEI Titan Ultimate

The two microscopes we used in this work are a FEI Titan Themis and FEI Titan Ultimate (see Figure 1-1). Both of these microscopes are equipped with a high brightness field emission gun (X-FEG). The Titan Themis has a probe spherical aberration corrector and is equipped with a high sensitivity Super-EDX system, a segmented DPC detector, a fast 4k CETA camera situated above the Gatan Tridium energy filter. The Titan Ultimate is a

spherical aberration double corrected (probe and image) microscope. It also has a segmented DPC detector, a Gatan Quantum Energy Filter, a 4k Oneview camera below the energy filter It also has an electron biprism for electron holography experiments. Both microscopes are equipped with a field emission gun (FEG) exclusively operating at 200kV in the frame of this work.

This chapter begins by giving some relevant information about semiconductor theory and the basics of TEM. Then off-axis electron holography (holography) is explained. The experimental acquisition and the data processing are detailed, added to that some considerations and artefacts are discussed. Then the STEM field mapping techniques are explained, that encompass segmented differential phase contrast (DPC) and pixelated-STEM (from now on we refer to this technique as 4D-STEM). As for holography, the experimental acquisition, the data processing and some considerations are presented. Then the strain mapping by 4D-STEM is explained. The last section is dedicated to the sample preparation by FIB. Different FIB protocols are presented and artefacts due to FIB preparation are discussed.

1.1 Measuring the electrical properties of semiconductor devices.

1.1.1 Semiconductor properties and samples choice

Semiconductor materials are the key elementary bricks that are used to build nano-electronic devices. Their properties allow the current flow to be controlled. semiconductors have resistivity between conductors (generally metal) and no-conductors (such as plastic or ceramic). In its pure state a semiconductor is referred to as intrinsic and at 0K it is an insulator. The resistivity of a material depends on the band gap, which is the energy that an electron needs to move from valence to conduction energy band and thus take part in the current flow. So, the wider the band gap, the more resistive the material is. Semiconductors have band gap from 0.6 to 1.5 eV. Insulators have wider band gap and conductors have no band gap. In a semiconductor, if electrons received external energy (such as thermal energy), they can access the conduction band. The range of energy gaps in semiconductors are in the same range as visible photons energy, which makes semiconductors ideal for opto-electronic devices such as LEDs or photovoltaic cells. The most widely used material in semiconductor devices is silicon. What makes a semiconductor useful is the introduction of impurities, which is called doping. Doping introduces new accessible energy level in the band gap, so

the electrons have smaller energy steps to climb to reach the conduction band, thus changing the resistivity of the materials.

The choices of samples were motivated by the materials used today to build a wide range of semiconductor devices. The first sample is a silicon pn junction. The silicon is the most common semiconductor in devices and its properties are well documented. Also studied, a sample containing silicon oxide (SiO2), which is a material typically used in MOS transistor. The sample present an interface between the SiO2 that is amorphous and the Si that is crystalline. Then a sample of silicon-germanium (SiGe) was studied, this material is used for state-of-the-art transistor devices as it can induce deformation and increase the mobility of the carries. The interest to study this sample in the context of this thesis comes from the difference of mean inner potential (MIP) between Si and Ge in a perfect crystalline sample. And finally, a sample with quantum wells (QWs) of gallium-indium-nitride (InGaN) on a gallium nitride (GaN) substrate was studied. Such nitride architecture is used in optoelectronic devices. This sample comes from a blue-LED and is the last that was studied as is present the most challenging characteristics in terms of size. In the end, all these materials cover a wide range of semiconductors properties and applications.

1.1.2 The Electric Field

The optoelectronic properties in semiconductor devices are determined on how the electrons and holes can flow within the device as it is operated. In terms of physics, what makes the electrons flow is the electric field i.e. a difference of potential. The equation 1.1 makes the link between the electric field $\vec{E}$ and the electrostatic potential V.

$$\overrightarrow{E} = -\overrightarrow{grad}(V) \tag{1.1}$$

Therefore, an electric field is present where the potential is not constant. In other words, a difference of potential creates an electric field. The electric field is linked to the charge density by the Maxwell-Gauss equation:

$$div\,\vec{E} = \frac{\rho}{\epsilon_0} \tag{1.2}$$

So, the electric field derivation is dependent on the position of the charges in the matter. This is why doping a semiconductor i.e. adding charges changes its electrical properties. This will be more detailed in the chapter 2. Then, by combining the two previous equation it appears

that the potential second derivation depends on the charges position, this is known as the Poisson's equation:

$$\Delta V = -\frac{\rho}{\epsilon_0} \quad 1.3$$

In the frame of this work, electric fields coming from three different sources will be studied: that arising from doping, differences in MIP and the piezoelectric effect.

Doping: it is the introduction of well-chosen impurities in the materials in order to change the potential i.e. the resistivity. Some of the material atoms are substitute to another chemical entity which have a different number of electrons. This leads to negative of positive free charges depending on the impurities atomic number. The doping allows to tune the properties of a large variety of devices. That is why, the semiconductor industry needs dopant mapping at nanoscale to assess the quality of devices building process [1]. As an example, a pn junction is a components based on that doping processed, it is composed of two regions with different doping between which a difference of potential is present [2].

Mean inner potential: the MIP can be defined as the local volume average of the coulomb electrostatic-potential of a material with respect to a distant vacuum reference at zero volts [3]–[5]. The MIP can be compute using density functional theory [6], [7]. It depends on both composition and structure [8]. Therefore, each material has a different MIP and when two different materials are in contact a difference of potential is present at the interfaces. The difference of MIP creates intense field in very thin region. These intense field can generate measurement artefacts as it will be shown later in this manuscript. MIP values are usually an order of magnitude higher than the small change of potential in a device such as a change of potential due to different doping.

Piezoelectric effect: the piezoelectric effect is the interaction between the mechanical and the electrical state of a crystal. It means that for such material a change in the electrical state of the material induce a change in the mechanical state and vice versa [9]. In our case, the piezoelectricity we studied is the accumulation of charges in materials due to a mechanical stress. This charges accumulation is present in polar materials. It means that their electric charges are separated i.e. a polar structure is made of electric dipole. It is close to an ionic structure and it has a slight positive charge on one end and a positive one the other end. When strain is applied to the structure (epitaxy or mechanical stress) it leads to a displacement of the positive charge relative to the negative one thus leading into an electric field called: piezoelectric field. It has been shown that such piezoelectric field deteriorate the properties

of some devices [10], [11]. In the case of a QWs LED, the presence of a piezo-electric field will change the maximum emission wavelength inducing a color shift of the LED. It also separates the holes from the electrons reducing the recombination rate and thus the efficiency of the device.

1.2 Why use a Transmission Electron Microscope?

The main interest in using electrons is the short wavelength in the range of 4 to 2 pm for 80 to 300 keV electrons respectively. Even though the aberrations in the electromagnetic lenses that are used to focus the electrons are extremely high, even in an uncorrected TEM, images can be obtained with atomic resolution. Aberration correction is almost standard now in modern TEMs and sub angstrom resolution imaging can be performed easily, even using lower electron acceleration voltages such as at 80 kV. There are two main modes of performing imaging in a TEM, classic TEM uses the interference of an electron wave that is incident on a thin specimen in order to provide an image. This was the original method of imaging by high resolution transmission electron microscopy (HR-TEM). The positions of the atoms can then be determined by comparing the exit wave function with simulations that take into account parameters such as the thickness of the specimen and the aberrations of the imaging system. Due to the complexity of HR-TEM, it is typically only used for very niche applications, such as the imaging of carbon nanotubes, nanoparticles and 2D materials. Lorenz mode off-axis electron holography is a medium resolution version of TEM.

Scanning transmission electron microscopy (STEM) is the second main mode of TEM. In this mode the sample is scanned with a convergent beam of electrons and different segmented

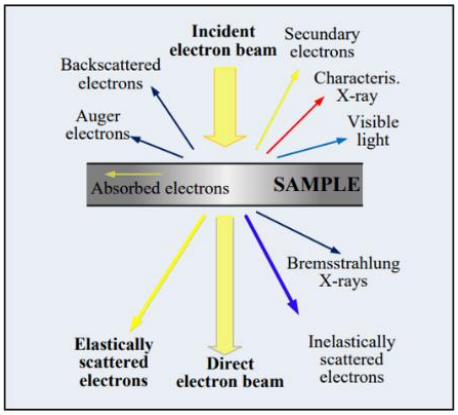

Figure 1-2 : Signals generated in a TEM when the electron beam probes a sample.

detectors measure the intensity of the signal that is scattered across an angular range for each position of the scan. For example, high-angle annular dark field (HAADF) STEM is known as Z-contrast STEM as heavier elements scatter the electrons over higher angles compared to lighter materials. Annular Dark Field (ADF) STEM is more sensitive to lighter elements and diffraction contrast as it measures a range of scattering angles closer to the transmitted beam compare to HAADF. More recently the whole distribution of the scattered electrons has been recorded due to the development of fast pixelated detectors. The use of such pixelated detectors has been leading the work withing the manuscript.

The use of an electron beam for characterization of semiconductor devices has more advantages than just overcoming the resolution limits. Figure 1-2 shows that a wide range of secondary signals are generated from the specimen. By using an appropriate detector this gives access to structural, chemical or even electrical properties in the same microscope.

1.2.1 Off axis electron holography

As the development of 4D-STEM will be compared to off-axis electron holography (holography), we begin with a discussion of this technique. Holography is performed in TEM mode and uses an electron biprism to interfere a plane object wave with a reference wave to create an interference pattern. From the position of the interference fringes, local measurements of the phase can be made from a simple Fourier reconstruction from which the electrostatic potential can be calculated.

1.2.1.1 Weak phase object approximation

For electron holography when an electron wave passes through a region containing an electrostatic potential there will be a change in phase relative to an electron wave travelling the same distance in vacuum [12]. The electron wave at the exit of the sample can be expressed as:

$$\begin{aligned}\psi_{exit}(x,y) &= \psi_{in}(x,y).T(x,y) \\ &= \psi_{in}(x,y).\exp[i\phi(x,y) - \mu(x,y)]\end{aligned} \tag{1.4}$$

Where $\psi_{in}(x,y)$ is the incident electron wave, μ account for the absorption and ϕ account for the phase shift of the electron wave. For the exit wave which leaves the sample, the phase shift of the electron wave is dependent on the electrostatic potential $V(r)$ and the magnetic vector potential $A(r)$ of the sample.

$$\phi(r) = \frac{e}{\hbar v}\int_{-\infty}^{+\infty} V(r)\,dz\; - \frac{e}{\hbar}\int_{-\infty}^{+\infty} A(r)dz \tag{1.5}$$

Where e is the elementary charge, $\hbar$ is the Plank's reduced constant, v is the relativistic velocity of the electron. For non-magnetic samples that are tilted to a low diffracting condition, the phase will be changed by the potential and the phase shift can be expressed as:

$$\phi(x,y) = \sigma V_t \tag{1.6}$$

Where σ is the interaction constant and V_t is the projected potential along the thickness [13]. The interaction constant depends on the wavelength and the energy of the electrons. Assuming a thin sample the absorption influence on the exit wave can be neglected:

$$\psi_{exit}(x,y) = \psi_{in}(x,y).\exp[i\sigma V_t(x,y)] \tag{1.7}$$

And finally, if projected potential is assumed to be small ($\sigma V_t \ll 1$) then the equation become:

$$\psi_{exit}(x,y) = \psi_{in}(x,y).(1 - \sigma V_t) \tag{1.8}$$

This is the weak phase object approximation (WPOA) and it only holds for thin specimen [14], [15]. With thicker samples the electron beam intensity will be reduced and the electron plane will lose its coherency but thick samples are required as the signal we measure is proportional to the thickness [16] . In this work, as we do not measure absolute values of potential relative to vacuum, but changes in potential between two adjacent regions, we believe that when the sample is tilted to a low diffracting condition then the WPOA is valid for thick samples if difference in phase is measured. In a case where the WPOA does not holds in the acquisition orientation, the electrons undergo multiple scattering which leads to the loss of the phase information and makes the holograms uninterpretable.

1.2.1.2 Experimental holography

The set up for electron holography in a TEM is similar to Young's slits experiment [17]. A schematic of the experimental setup for holography is shown in Figure 1-3. A FEG emits a coherent electron wave. One part of the wave goes through the vacuum and the second one goes through the sample. A voltage is applied to Möllenstedt biprism inserted bellow the sample [18]. The biprism overlaps the two parts of the plane wave, which can be described as two virtual sources (S_1, S_2), which interfere with each other to form the electron hologram.

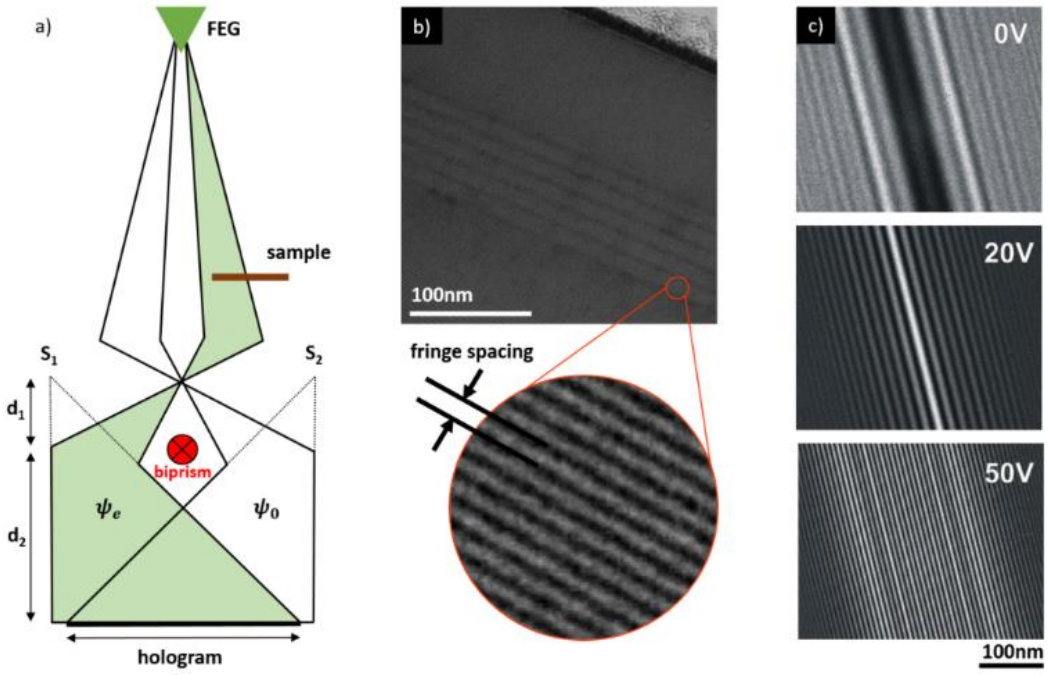

Figure 1-3 : Hologram acquisition and fringe spacing. a) Hologram recording schematic. b) Example of a hologram and zoom on the fringes. c) Influence of the biprism voltage on the fringe spacing from 0V to 50V.

The hologram contains information about the amplitude and the phase shift of the wave transmitted through the sample. The intensity of the hologram is described by the following equation:

$$I_{hol}(r) = |\Psi_0(\vec{r}) + \Psi_e(\vec{r})|^2 = A_0^2(\vec{r}) + A_e^2(\vec{r}) + 2\mu(\vec{r})A_0(\vec{r})A_e(\vec{r})\cos\left(2\pi\overrightarrow{q_e}.\vec{r} + \phi(\vec{r})\right) \quad (1.9)$$

Where A_0 is the amplitude of the incident wave, A_e is the amplitude of the wave after traveling through the sample, q_e is the carrier wave frequency of the hologram, $\vec{r}$ is the in-plane position vector, and ϕ is the phase change induce by the sample. The spatial resolution of the phase image is limited by the fringe spacing s of the hologram (Figure 1-3-b). The fringe spacing can be calculated using this equation:

$$s = \lambda\left(\frac{d_1 + d_2}{2\alpha d_1}\right) \quad (1.10)$$

where λ is the electron wavelength, d_1 is the distance between the virtual sources plane and

the biprism plane, d_2 is the distance between the biprism plane and the detector plane, α is the deflection angle of the wave due to the biprism. The angle α is controlled by the biprism voltage, so a higher biprism voltage will increase the resolution as it makes the virtual sources move further away from the biprism i.e it increases the distance d_1. *Figure 1-3-c* shows the influence of the biprism voltage on the fringe spacing.

1.2.1.3 Hologram reconstruction

Typically, an electron hologram is recorded by a pixelated detector. Next, a reconstruction process is required to obtain the amplitude A and the phase ϕ. The whole processing is shown in Figure 1-4. The first step is a complex Fourier transform (FFT) of the hologram. For a hologram with a carrier wave frequency q_e the Fourier transform is:

$$FT[I_{hol}(r)] = \delta(q) + FT[A^2(r)]$$

$$+ \delta(q + q_c) \otimes FT[A(r)\exp[i\phi(r)]]$$

$$+ \delta(q - q_c) \otimes FT[A(r)\exp[-i\phi(r)]] \quad (1.11)$$

The three line of equation 1.11 can be seen as the three bands in the FFT of the hologram. The center band ($q = 0$) contains information about the conventional intensity image. The side band around ($q = + q_c$) contains the information about the phase and amplitude of the electrons that is carried by the interference fringes. The third band ($q = - q_c$) contains the same information as the previous one but with a difference in the phase sign [19]–[21]. To extract only the information about the phase and amplitude carried by the hologram, a circular mask is used to select one of the sidebands. A typical size of mask is between ½ and 1/3 of the distance between the side band and the center band such that information from the center band is not used in the reconstruction. Increasing the size of the mask improve the resolution of the reconstructed image but also increase the noise, 1/3 is usually a good compromise. The last step of the reconstruction is an inverse FFT in order to obtain a complex image which can be separated in a phase image and an amplitude image with the two equations 1.12 and 1.13 where $\mathcal{R}$ and $\mathcal{I}$ respectively represent the real and complex part of the image.

$$A(r) = \sqrt{\mathcal{R}^2 + \mathcal{I}^2} \quad (1.12)$$

$$\phi(r) = \tan^{-1}\left(\frac{\mathcal{I}}{\mathcal{R}}\right) \tag{1.13}$$

Equation 1.6 shows that the potential is proportional to the phase. The phase has to be divided by the interaction constant σ and the thickness t in order to obtained the potential. Finally, the electric field can be derived from the potential using equation 1.1.

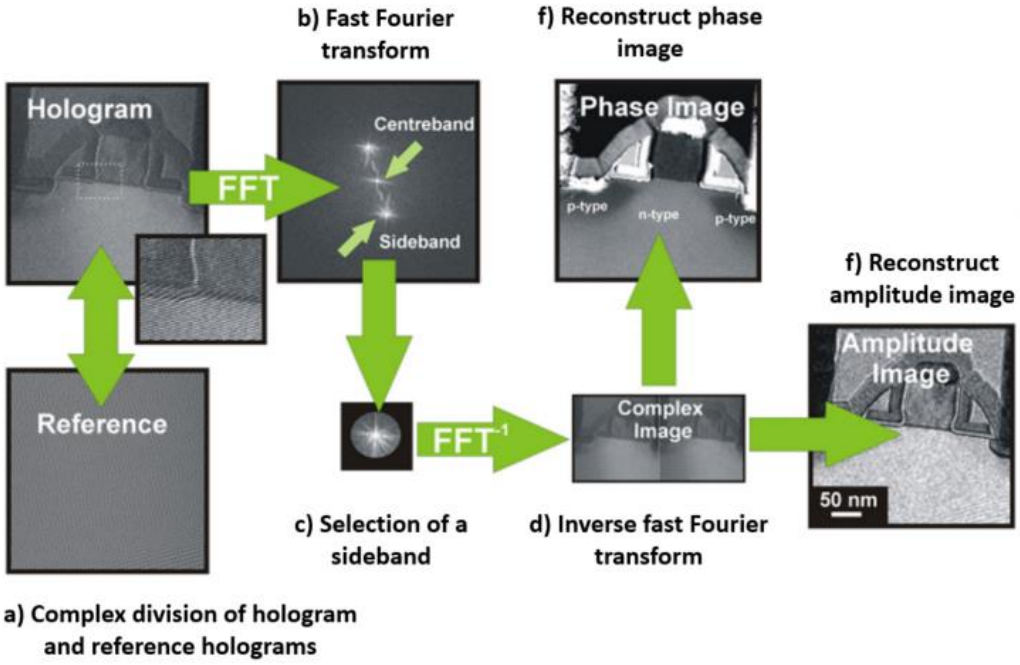

Figure 1-4 : Hologram reconstruction process.

1.2.1.4 Experimental considerations and artefacts

The holography experiments are based on the theory previously described, but in order to avoid artefacts many things have to be considered.

Phase sensitivity: The electrons emitted from the FEG need to be sufficiently coherent to provide interference fringes with high contrast. In addition, the drift of the sample can lead to a deterioration in spatial resolution and instabilities in the biprism can lead to poor contrast. A sufficiently high current is needed so that holograms can be recorded in short time periods of the range 2-10 seconds. In the Titan Ultimate equipped with a X-FEG, high performance power sources, and within an electromagnetically shielded environment, the

performance of holography has been significantly improved. The sensitivity in a reconstructed phase image is described by the following equation [22], [23], where μ is the hologram contrast and N_{el} is the electron counts per pixel :

$$\Delta\phi = \frac{\sqrt{2}}{\mu\sqrt{N_{el}}} \tag{1.14}$$

A phase resolution of around $2\pi/100$ can be achieved for a single hologram acquisition [24]. To increase the sensitivity the fringe contrast μ can be improved by introducing a smaller condenser aperture, a smaller spot size and a low gun extraction voltage, leading to a compromise between intensity and coherence. The biprism voltage can also be decreased to provide a narrower hologram so the fringes contrast is improved at the expense of a loss in resolution. A solution is to increase the electron counts N_{el} it can be done by simply increase the dwell time. Modern microscope stability allows typical dwell time to be in the range of 10 to 100s. Longer dwell time led to deterioration of the contrast due to the drift of either the sample, the electron source or the detector. The solution found to increase the electron counts without introducing drift is the acquisition of series of hologram with an acquisition time of about 8s and then the different holograms are aligned and summed [25]. This technique is used for all the hologram presented in this manuscript and the alignment is done with the Holoview software wrote by V. Boureau et al. in the DigitalMicrograph scripting language[24], [26].

Information loss: In order to prevent from information loss from sampling, each fringe must be recorded on several pixel of a detector. A good number is 6 pixel per fringes and as the camera has a finite number of pixels, a compromise has to be found between resolution and field of view [18]. Also, for quantitative measurement of the phase shift, a vacuum reference has to be in the field of view. With a camera of 2048 pixel² and a fringes width of 2nm, the maximum field of view will be of 500nm² [20]. This can lead to difficulties if in a real device characterization where the vacuum reference is far away. During this thesis the holography acquisition was done using the Gatan OneView camera. The camera has 4096pix² and is quite physically large being 6cm². This combination of number of pixels and size allows nanometer resolution to be more easily achieved with a large field of view such that a vacuum reference is present.

Fresnel diffraction: Fresnel fringes can be present in the hologram, they come from the electron beam diffracted by the edges of the biprism out of the image plane. Those fringes introduce interference contrast, which decrease the accuracy of the reconstructed image.

Their influence can be attenuated during the acquisition by increasing the biprism voltage at the expense of contrast such that the Fresnel fringes are not recorded by the camera. Another solution is post-acquisition filtering of the Fresnel fringes in the Fourier space.

Thickness variation: The TEM sample are prepared by focus ion beam (FIB, detailed in section 1.5), this state-of-the-art instrument allows precise milling of thin sample. Nevertheless, some artefacts must be considered. The combination of change in thickness and the value of MIP (between ten and twenty in the frame of this work) generates a signal that is often an order of magnitude higher than the signal that arises from dopants. so perfect parallel sided samples are required [13], [20] (also see equation 1.5).

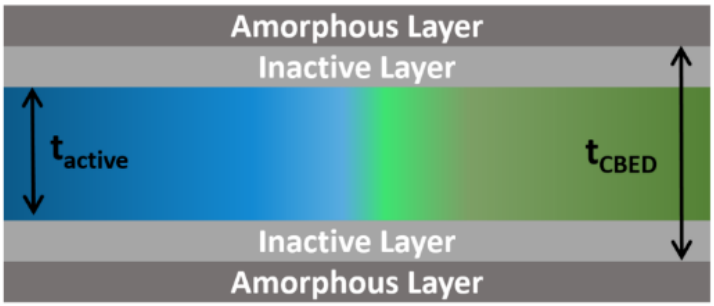

Figure 1-5 : Sample preparation artefacts, inactive and amorphous layers schematic. t_{CBED} *is the thickness measured by convergent beam electron diffraction, it encompasses the active and the inactive layers.*

Inactive thickness : During the sample preparation, a part of the Ga^+ ion use for the milling is implanting in the sample creating an amorphous layer. The FIB preparation also creates defects deep in the sample. Such defects trap dopants and form an electrically inactive layer under the amorphous one. When measuring the thickness by convergent beam electron diffraction (CBED) the measured thickness encompasses the inactive layer. The schematic in Figure 1-5 shows the different layers. To minimize the inactive thickness care must be taken during the FIB preparation such as using a low accelerating voltage during ion milling [27]–[30]. Annealing the sample also decreases the influence of the defect [31]. Inactive thickness can also be measured [16], [32] and subtract to the total thickness in the processing. Finally the use of thick sample permit to reduce the influence of the surface effect and the result are closer to what could be expected for bulk specimen [33].

Dynamical diffraction and resolution in projection : This is absolutely the key step for electron holography as dynamical diffraction will strongly affect the phase of an electron

[19], [34], [35]. Relatively thick specimens are required for electron holography (to reduce the effects of surface charging influence and increase the total phase shift which is proportional to the integration of the potential along the thickness) [16]. The solution found is to tilt the specimen away from zone axis, tilting the sample permits to minimize the diffraction influence. The tilt induces a loss of resolution in projection along the thickness[36], [37]. The loss in resolution δ can be calculated using equation 1.15 where t is the thickness and θ is the sample tilt from zone axis.

$$\delta = t.\theta \tag{1.15}$$

To conclude on the introduction of the off- axis electron holography, this technique has been developed and improved for years. Many artefacts have been understood and overcome. Holography now allows to measure phase shift with very high sensitivity at nanoscale resolution on hundreds of nanometers field of view. Apart from the alignment of the microscope, the hologram acquisition takes only a few minutes. The processing has also been developed making the holography convenient to measure dopant concentration, potential and electric field.

1.2.2 Scanning Transmission Electron Microscopy

In STEM mode the sample is scanned using a convergent beam and the scattered electrons or emitted X-Rays are measured point by point to build up the required image. This can be for Z-contrast imaging when a HAADF detector is used, for compositional mapping when an EDX detector is used, for the mapping of composition, bonding or plasmons when a post-specimen energy loss spectrometer is used, or as we will see for the mapping of electromagnetic fields. In the FEI Titan microscopes, there are three condenser lenses C1, C2 and C3 that allow the probe to be formed with a chosen convergence angle and camera length which is necessary when performing pixelated and DPC STEM measurements. De-scan coils that are situated below the sample allow the beam to be scanned on the sample while the beam stays on the optical axis. The Figure 1-6 depicts the microscope setup in STEM mode [38].

Ideally for high resolution STEM mapping, the electron probe must be as small as possible to have maximum spatial resolution. The real probe shape is complex, when a circular aperture (our C2 aperture) is illuminated with a planar wave, it creates a focused probe in the far field that has an Airy shape [39]–[41]. Such probe is depicted in Figure 1-7. At the entrance of the specimen, the electron probe intensity may be described as:

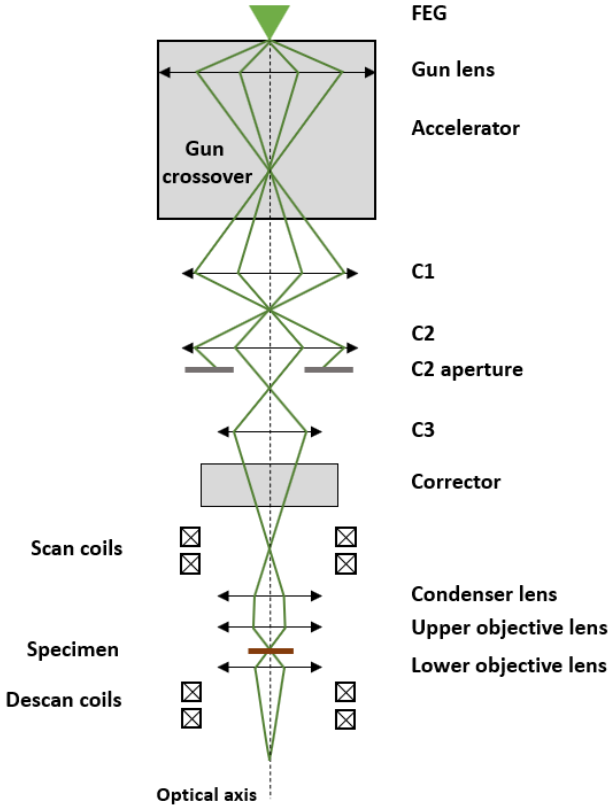

Figure 1-6 : Schematic of a microscope setup in STEM mode. Only the main components and a few electron trajectories are depicted.

$$|\psi_{in}(x,y)|^2 = I_0 \left[\frac{J_1(2\pi k_0 \alpha r)}{2\pi k_0 \alpha r}\right]^2 \tag{1.16}$$

Where I_0 is an intensity normalization, r is the polar coordinate, J_1 is the first order Bessel function of the first kind. The wave vector k_0 is equal to $1/\lambda$ and α is the convergence semi angle [42]. If aberrations are neglected, the size of the probe can be described by the diameter of the central Airy disk:

$$d_d = \lambda \frac{1.22}{\sin(\alpha)} \tag{1.17}$$

Where d_d is the diameter of the central Airy disk, λ is the electron wavelength, n is the refraction indice. For a constant wavelength i.e. a constant acceleration voltage, increasing the convergence angle improves the resolution. The Rayleigh criteria gives the smallest resolvable distance. In the case of a system only limited by diffraction, resolution is the radius ($d_d/2$) of the central Airy disk. To take into account some of the aberrations encountered in a microscope, the probe diameter equation becomes:

$$d^2 = d_g^2 + d_d^2 + d_s^2 + d_c^2 \tag{1.18}$$

Where d_g is the geometrical diameter of the probe, d_s and d_c are respectively the spherical and chromatic aberration. Equation 1.18 can be expressed as:

$$d^2 = \frac{4I_p}{\pi^2 \beta \alpha^2} + \frac{1.22^2}{\alpha^2}\lambda^2 + \frac{C_s^2 \alpha^2}{4} + \left(\frac{C_c \Delta E}{E}\alpha\right)^2 \tag{1.19}$$

In this equation E is the beam energy, ΔE is the energy spread, α is the convergence semi angle, C_s and C_c are the spherical and chromatic aberration respectively, I_p is the beam current and β is the gun brightness. In our case, both the Titan Themis and Ultimate are equipped with a probe aberration corrector which reduces the spherical aberration. Both are also equipped with a high-performance field emission gun (X-FEG) of high brightness which gives an electron distribution of high coherence. The Titan Ultimate has a monochromator which can be used to filter the electrons depending on their energy, however, this was not used in these experiments. The chromatic aberration will only have a small effect and the use of a monochromator significantly adds to the complexity of the experiments. To this end, the spatial resolution for the different electron microscope setups is diffraction limited, thus it can be reasonably considered that, as the convergence angle increases in the range of 1-25 mrad, the probe size decreases. This range encompass all the values of convergence angle used for this work.

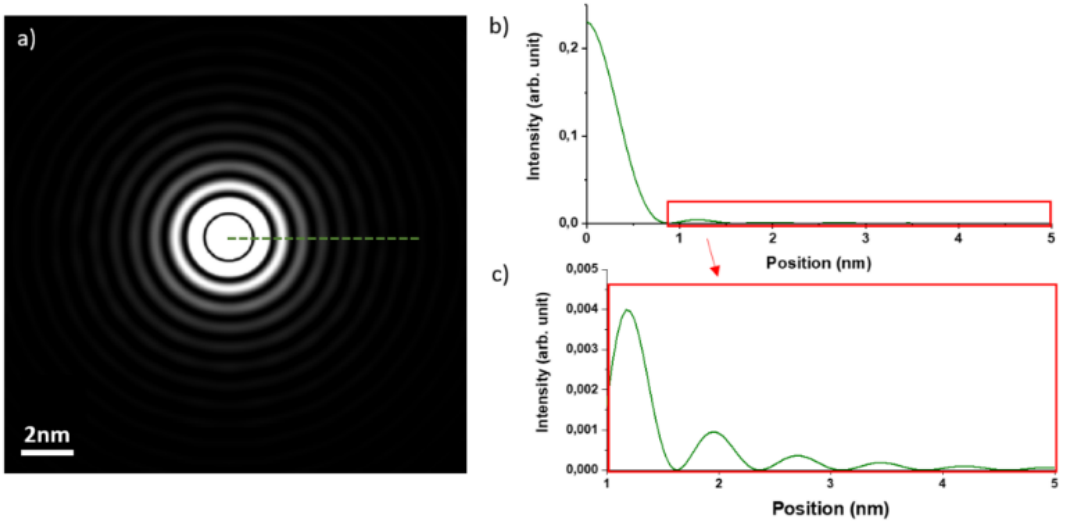

Figure 1-7 : Airy disk probe simulated using µSTEM software. The convergence angle used for this simulation is 1.7mrad. a) Image of the simulated probe. b) Profile of the probe intensity taken from the center of the probe. c) Zoom of the profile on the intensity rebound present in (b).

Setting	**High-resolution (HR)**		**Nano-beam (NB)**		**Low-magnification (LM)**	
Convergence angle	20mrad		2mrad		0.2mrad	
Probe size	0.1nm		1nm		10nm	
Camera length	0.2m		2m		20m	
Detector	Segmented	Camera	Segmented	Camera	Segmented	Camera
Mode	HR-DPC	HR-4D-STEM	NB-DPC	NB-4D-STEM	LM-DPC	LM-4D-STEM
Application	Atomic electric field		Piezo-electric field		pn junction electric field	

Table 1-1 : Listing of the modes used and grouped depending on the convergence angle i.e. the resolution used. All the values are typical values to gives the reader an idea of the order of magnitude. The probe size is the size of the central disk.

Figure 1-7- (a) shows a simulated probe, where the contrast has been set to saturate the center so the "weak rings" are visible. Figure 1-7- (b) and (c) show profiles of the probe intensity. The central disk of the probe is brighter than all the rebound of the probe. Usually, the probe size is assumed to be given by equation 1.17, which is the size of the first Airy disk. But the bright central disk of such probe only encompass 84% of the total intensity [42]. This probe size would be relevant for a Gaussian probe with the same FWHM. To encompass 95% of the intensity the probe size has to be estimated with:

$$d_{0.95} = \frac{3.92\,\lambda}{\alpha} \tag{1.20}$$

This equation shows that the probe size is underestimated by a factor 3 if we consider only the central disk. Nevertheless, for many TEM measurement considering only the central beam is reasonable. Later in this manuscript, it will be shown that the probe tail has influence on electromagnetic field measurement [43].

For the STEM measurements that were performed in this thesis the convergence angle was set to different values from 100 µrad up to 25 mrad. This range of convergence angle can be divided in three STEM mode that are detailed in Table 1-1. The high-resolution (HR) mode is used especially for HAADF STEM imaging or short range electric field mapping [44]–[46]. Then there is the Nanobeam (NB) mode used for example in strain measurement and long range electric field mapping [47], [48]. Finally, the low-magnification (LM) mode used in DPC experiment [49], [50].

1.2.3 Electron beam deflection model

In STEM mode when the beam scans a sample where an electric field is present, the Lorentz force $\overrightarrow{F_{elec}}$ deflect the electron beam. This force is described by equation 1.21 where e is the elementary charge of an electron, $\vec{E}$ is the electric field, $\vec{v}$ is the electron velocity and $\vec{B}$ is the magnetic field. In the case of this thesis the studied samples have no magnetic properties so the magnetic part of this equation can reasonnably be neglected.

$$\overrightarrow{F_{elec}} = -e.\vec{E} + e\vec{v} \times \vec{B} \tag{1.21}$$

Figure 1-8 shows an electron deflected by an electric field and sample parameters that influence the deflection angle, γ. The deflection angle can be calculated using a semi-classical model where neither energy loss or scattering is considered. The calculation of the deflection angle is shown here and the approximations are justified. To calculate the deflection angle, only the force perpendicular to the beam direction have an influence and this perpendicular component can be expressed using Newton 2nd law where $a_\perp$ is the acceleration of the electron perpendicular to the beam direction and m_e^* is the relativistic mass of an electron:

$$F_\perp = a_\perp . m_e^* \tag{1.22}$$

The electron beam needs a certain amount of time τ to travel all the way through the sample. It can be expressed using v_0 the initial electron velocity and t the sample thickness:

$$\tau = \frac{t}{v_0} \tag{1.23}$$

Considering the perpendicular acceleration constant, the perpendicular velocity at the exit of the sample can be expressed as:

$$v_\perp = -\frac{E_\perp \, e \, t}{v_0 \, m_e^*} \tag{1.24}$$

The angle of deflection γ depends on the two velocity components, perpendicular and parallel. Its expression is :

$$\gamma = \tan^{-1}\left(\frac{v_\perp}{v_0}\right) \approx \frac{v_\perp}{v_0} \tag{1.25}$$

This equation stands only for a small angle [51]. Finally the electric field can be expressed with the different parametres:

$$E_\perp = -\frac{\gamma \, m_e^* \, v_0^2}{e \, t} \tag{1.26}$$

Measuring the deflection angle of the electrons and using equation 1.26 allows to obtain quantitative values of electric field [34], [50].

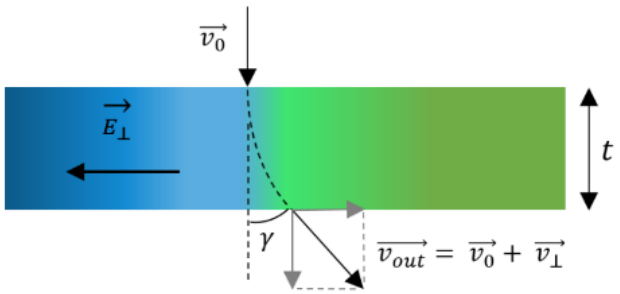

Figure 1-8 : Parameters that influence the beam deflection in semi classical model. The deflection angle is described by equation 1.26.

1.3 Experimental field measurement by STEM

As described previously, the electromagnetic fields can also be measured point by point from the deflection of the transmitted beam as it is scanned across the specimen [34], [52]. The electron deflection induced by the electric field is measured using either a segmented or pixelated detector and the electric field can be calculated at each point. DPC is a technique that has been used since the 1970s [53]–[55]. The availability of fast pixelated detectors has brought this scanning approach to field mapping back into fashion [56].

1.3.1 Differential phase contrast

The technique of segmented differential phase contrast uses a four quadrant ADF detector that is inserted below the sample to measure the deflection of the electron beam. For simplicity this will now be referred as DPC in this manuscript. In a field free region, the electron beam is centered on the detector (Figure 1-9-a). Then as the beam travels through an area with an electric field, beam deflection occurs as shown in Figure 1-9-(b). Along the scan, four intensity images are recorded simultaneously by the four quadrants of the detector as show in Figure 1-9-(c),(d),(e) and (f). Then opposite quadrant images are subtracted. Figure 1-9-(g) and Figure 1-9-(h), represent respectively the difference between the orange and blue quadrant, and the difference between the green and yellow quadrant. If the sample is well oriented relatively to the detector, then Figure 1-9-(g) and (h) can be assumed as x and y coordinate of the DPC signal $\overrightarrow{I_{DPC}}$. With such acquisition, an intensity vector proportional to the electric field is obtained [34]. From this vector, with a detector calibration, quantitative field values can be extracted [57].

Depending on the specimen that need to be characterized, two parameters must be chosen carefully: the convergence angle α and the camera length L. Table 1-1 summarize the different mode of DPC and gives typical application of such mode [20]. The convergence angle controls the resolution so it has to be as wide as possible (equation 1.20). The camera length controls the sensitivity of our measurement. Indeed, the horizontal shift S_{DPC} record on the detector plane can be expressed as a function of the camera length L and the deflection angle γ:

$$S_{DPC} = \tan(\gamma) \, . \, L \tag{1.27}$$

And as γ is small (tens of mrad) the equation can be simplified as:

$$S_{DPC} = \gamma . L \tag{1.28}$$

The camera length and convergence angle must be adapted to the physical size of the detector. Thus, a compromise between resolution and sensitivity is needed. As Figure 1-10-(a) and (b) show, if a large convergence angle is used, then a rather short camera length is required, and vice versa. The combination of α and L determines the covering ratio i.e. the area ratio of the direct beam and the DPC detector, which determines the sensitivity in terms of signal over noise ratio (SNR). This covering ratio has to be small to obtain a good SNR [58]–[60]. Figure 1-10-(c) shows a combination of parameters which create a beam wider than the detector, it is not a valid combination for a DPC experiment because no intensity difference can appear as all the quadrants are fully illuminated even when the beam is deflected.

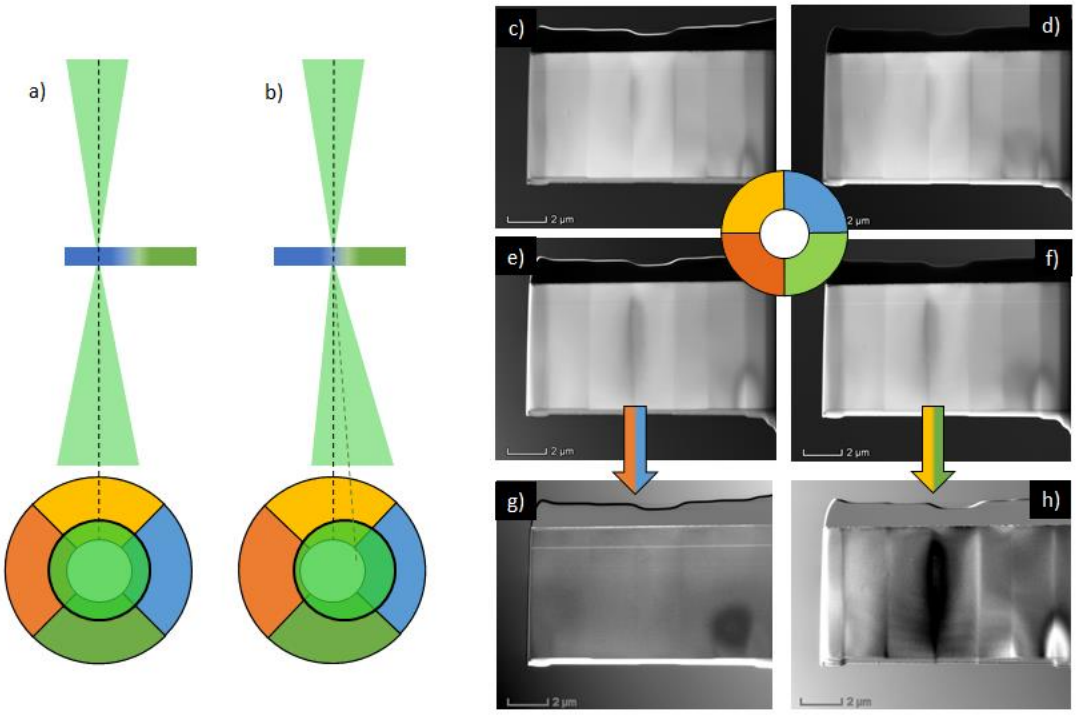

Figure 1-9: Differential phase contrast schematic. a) Beam centered on the detector; no field is present. b) The beam is deflected; a field is present. c)-f) are intensity recorded by each of the four quadrants during the scan. g)-h) are the intensity subtraction of opposite quadrants.

1.3.2 Calibration for quantitative DPC

Although DPC is not directly quantitative, there are several ways to access the quantitative field value. For example, the deflection angle can be expressed as a function of the DPC signal:

$$\gamma = \frac{\left\|\overrightarrow{I_{DPC}}\right\|}{K_\gamma} \tag{1.29}$$

With $\overrightarrow{I_{DPC}}$ the total DPC signal vector and K_γ a coefficient that can be express as:

$$K_\gamma = \pi . R . j . \delta . L \tag{1.30}$$

Where R is the beam diameter, j is the beam current density, δ is a constant that account for digital conversion of the detector and L is the camera length [61]. The link between the deflection angle and the DPC signal depends on the factor K_γ, yet a calibration as to be performed in order to get a value of K_γ with some well-known deflection angle. This calibration is most of the time done using a parallel plate capacitor whose characteristics (thickness and electric field) are already determined or by manually move the beam on the detector [42], [54], [55].

Another way to quantify the DPC signal is to use a center of mass (CoM) approach. Usually to do so, people use a segmented detector with more than four segments but the basis is the same whatever the number of segments. CoM of the beam intensity in the diffraction plane (same as detector plane) can be calculated using:

$$k_{CoM}(R) = \frac{\int k . I(k,R) dk}{\int I(k,R) dk} \tag{1.31}$$

Where R is the probe scan position i.e. a pixel of the DPC map, k is a vector in the diffraction plane and $I(k,R)$ is the intensity of the transmitted beam. With a segmented detector this equation can be approximated by:

$$k_{CoM}(R) = \frac{\sum_j k_j I_j(R)}{\sum_j I_j(R)} \tag{1.32}$$

Where k_j is the center of mass of the j^{th} segment of the detector (physical center of mass) and I_j is the intensity recorded by this segment [63]–[66]. Once the CoM position is calculated, subtracting the value to a reference pixel in which no field is present gives a CoM

shift. Assuming the transmitted beam to be homogeneous, this CoM shift is theoretically equal to the DPC shift of equation 1.27 so it can then be converted in a deflection angle and latter in a quantitative field value [57].

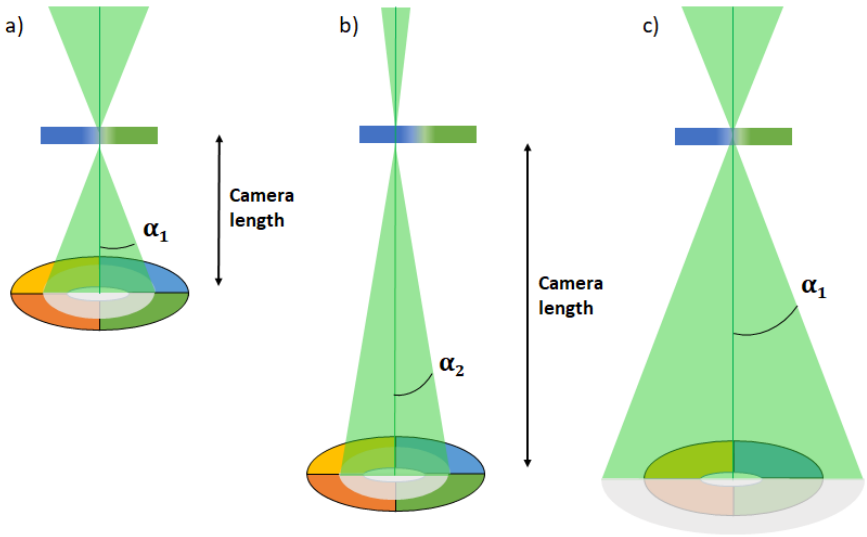

Figure 1-10 : DPC schematic. a) DPC set so the beam fit on the detector. b) DPC set with a longer camera length, but a smaller convergence angle than in (a). The covering ratio is the same as in (a). c) Wrong combination of convergence angle and camera length. The transmitted beam is wider than the detector.

1.3.3 4D- STEM acquisition

The availability of fast pixelated cameras and powerful computers have opened the path to the explosion of interest in 4D-STEM [67]–[69]. It is an improved way of doing DPC experiments where all the scattered and deflected electrons are recorded at each point of the scan and the data can be carefully post processed. The CCD camera used for recording in 4D-STEM is often larger than the ADF detector used for DPC thereby for the same camera length a bigger convergence angle can be set and the transmitted beam still fit on the camera. Such acquisitions were not widespread in the past because of the speed of CCD cameras and certainly due to the power of desktop computers. However, some early 4D STEM imaging was performed in order to provide strain maps in 2D using locally measured diffraction patterns. The size of data sets obtained by 4D-STEM can be huge. For example, if a 2k by 2k camera is used, a 100 pixel² map will lead to a 40 Gb data set.

Many different signals can be obtained for a 4D-STEM data set [11], [45], [65]. By using a mask to measure the intensity of the electrons that have been scattered over a desired angle, virtual bright-field or dark-field detector can be created. For field mapping, the deflection of the transmitted beam can be measured. Figure 1-11 shows a schematic of the 4D-STEM acquisition and processing. Regarding the 4D-STEM processing, on top the raw data set is schematize with a transmitted beam record for each pixel of the scan. Then the data are processed to obtained a shift vector map. The shift is calculated compare to a reference (pixel surrounded in red). Finally, the shift is converted in units of electric field. A map with contrast proportional to the field intensity is then accessible.

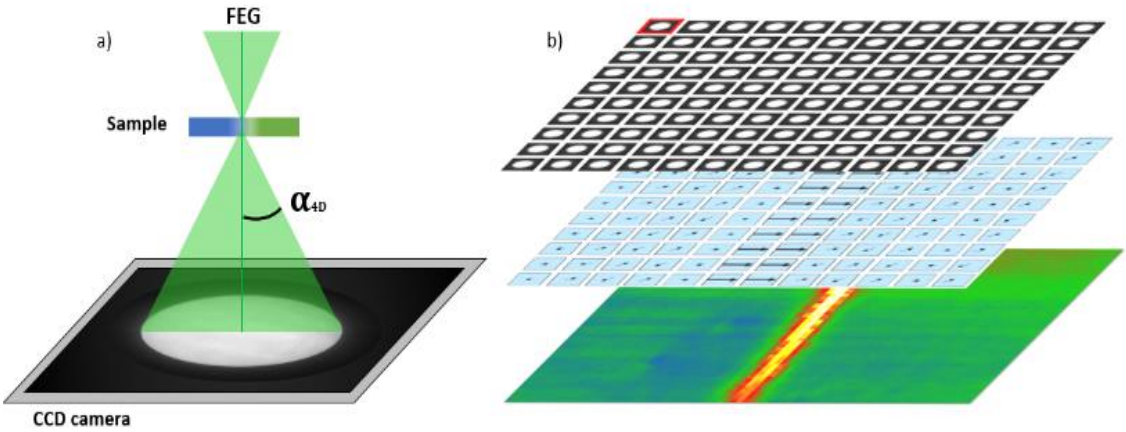

Figure 1-11 : 4D-STEM schematic. a) Acquisition schematic. b) Processing schematic with on top a raw data set, which gather the diffraction pattern on each point of the scan. Then the matrix of the beam shift vector. At the bottom a map with contrast proportional to the field intensity.

1.3.4 4D-STEM processing

The objective of the data processing for field mapping is to detect the shift of the beam compared to a reference that has been acquired from a field free region. Here, three different algorithms were tested: one based on the center of mass (CoM) and two other based on template matching. The two template matching algorithms have only one difference; one uses a template that comes from the data set and the other uses an artificial template that fits a disk on the data. These two processing techniques will be referred as template matching (TM) and disk template matching (DTM). The CoM algorithm is widely used by the 4D-STEM community and is present in many studies [56], [70], [71]. The TM and DTM are much less frequently used [72]. For both types of algorithms, the first step is to choose a

reference. The ideal case is to choose a reference in an area where there is no electric field, but if the reference includes field or any artefact the shift map will have an offset value that can be removed afterwards. The position of the reference is denoted as R_{ref} in the following equations. For the DTM this step is replaced by the creation of a disk template.

For the CoM processing, the position of the CoM is calculated using the same formula as equation 1.32 but instead of summing on the detector segment the sum is made over the pixels of the camera and can be expressed as:

$$k_{CoM}(R) = \frac{\sum_{pix} k_{pix} I_{pix}(R)}{\sum_{pix} I_{pix}(R)} \tag{1.33}$$

Where R is the position of the probe on the sample, k_{pix} is the pixel position in the diffraction pattern and $I_{pix}$is the pixel intensity. From the position of the intensity centre of mass the shift S_{CoM} compare to the reference is calculated as follow:

$$S_{CoM}(R) = k_{CoM}(R) - k_{CoM}(R_{ref}) \tag{1.34}$$

Regarding the TM and DTM processing, once the reference is chosen or created, a 2D cross correlation is done between the reference diffraction pattern and the processed pattern (position R). The TM processing is depicted in Figure 1-12. The formula of the cross correlation is:

$$(I_{ref} * I_R)(k) = \iint I_{ref}(r) \times I_R(r+k)dr \tag{1.35}$$

Where I_{ref} and I_R are respectively the intensity of the reference and the intensity of the diffraction pattern in the processed pixel. The cross-correlation output is a 2D image in which the position of the maximum can be seen as the position where the two diffraction patterns overlapped the best. For sub-pixel precision, an interpolation function fits the cross-correlation around the maximum. The maximum of this interpolated function is return as the new maximum of cross-correlation. The shift vector goes from the center of the image to the maximum of the cross-correlation.

The shift obtained with both algorithms is expressed in units of pixels. The shift has to be calibrated to obtain a quantitative field value. The calibration is done using the half convergence angle α. The calibration coefficient η is calculated as follow:

$$\eta = \frac{2\alpha}{D_{pix}} \tag{1.36}$$

Where D_{pix} is the beam diameter in pixel. Therefore, the calibration of the deflection per pixel is included in the dataset.

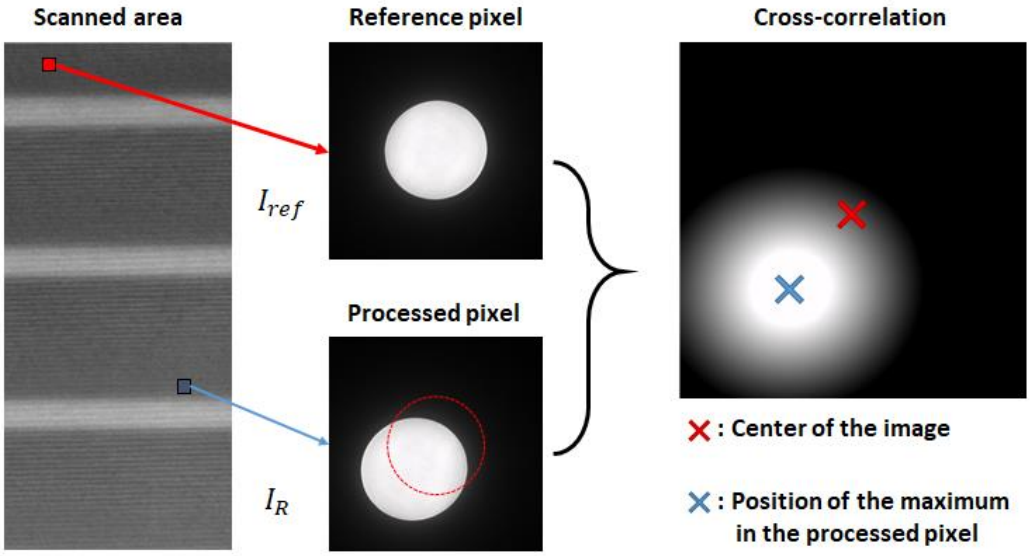

Figure 1-12 : Template matching schematic. The red dotted circle in the processed pixels represent the position of the beam in the reference. The shift vector is between the center of the image and the maximum of the cross-correlation.

1.3.5 Experimental and processing consideration

This section gathers the main artefacts present in STEM field measurement and some solutions are presented.

The effect of spatial resolution on rigid shift: The rigid shift model assumed that all the electrons in the beam are deviated by the same amount. The conic shape of the beam will lead to difference of deflection, an electron traveling parallel to the optic axis will not be deflected exactly by the same amount as an electron on the edge of the cone. But the convergence angles used are small and in the case of a 20 mrad convergent beam (which is the widest angle used in the frame of this thesis) the difference of deflection is about 0.02%. This difference can be neglected so the convergence angle does not create deflection difference between electrons. In contrast, the probe size affects the homogeneity of the deflection of the transmitted beam. Indeed, the assumption of a beam rigidly shifted is only

valid if the probe size is small compared to the one of the measured electric field. In other words, the field must be constant in the probe [27], [60]. This is where the probe shape is important as the aberrations in the probe, such as the Airy rings might break the assumption of the field being constant. Figure 1-13 shows schematics the different beam behaviors in presence of electric field. When the beam scans an area where the electric field is constant, the beam is shifted (Figure 1-13-b). In the case of a field that varies in the probe, there is no shift of the beam but the intensity inside the beam is redistributed (Figure 1-13-c). In both case the field has an influence on the beam so the field can be detected. In the rigid shift case, the beam deflection can be converted into field values using equation 1.26. In the case of a redistribution of intensity, the shift of the intensity CoM will be measured [32], [61]. The complexity of the redistribution of intensity leads to difficulties when trying to obtain quantitative field values.

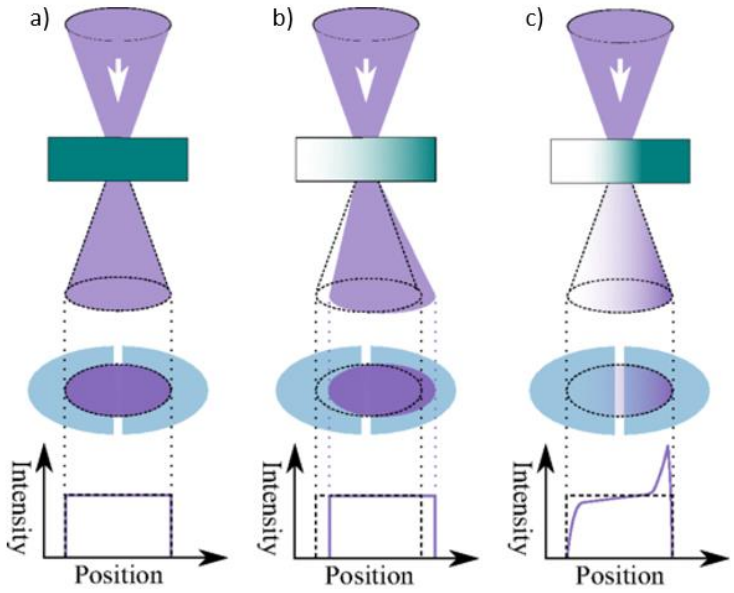

Figure 1-13 : Rigid shift schematic. a) The probe is in an area without field, the beam is not deflected. b) The probe is in an area with field. The probe is small enough to consider the field constant. The beam is rigidly shifted. c) The probe is in an area with field but this time the field varies in the probe. A redistribution of intensity occurs.

Dynamical diffraction and resolution in projection: As for holography, limiting the dynamical diffraction is absolutely key. Therefore, the sample has to be tilted off-axis in order to minimize diffraction influence. The problem is that in STEM mode the convergence of the beam means that it is even more difficult to find a low diffracting condition as the

electrons are incident on the specimens from a range of angles. The off-axis tilt imposed by the dynamical diffraction decreases the resolution. This tilt has to be minimized, during this thesis the sample were tilted mainly around the growth direction axis, to limit blurring of the interfaces that were studied [11], [34], [75].

Inactive thickness: Again, as for holography, the inactive thickness will be present due to the FIB milling (see Figure 1-5). How to minimize the sample preparation artefacts are details in section 1.5.

Thickness variation of the TEM specimen: it is also an issue in STEM mode. Firstly, equation 1.26 shows that for a constant electric field, the deflection angle depends on the thickness. So, changes in thickness introduce signal variation where it should be constant. Here the sample used can be several hundred of nanometer thick, therefore the small variation of thickness (tens of nm) has a negligible influence. It is the same artefacts as in holography but there is more in STEM mode. A thickness variation along the x axis induce a change in the projected phase $\phi(x)$ that the electrons see. This results in deflection (or refraction in terms of optics) [64], [76]. The gradient of the projected phase is linked to the deflection angle γ:

$$\gamma(x) = \frac{\lambda}{2\pi} \nabla_x \phi(x) \tag{1.37}$$

In this equation λ is the electron wavelength. Using equation 1.6 that makes the link between phase and potential equation 1.37 becomes:

$$\gamma(x) = \frac{\lambda\sigma}{2\pi} \left[\nabla_x V(x).t + V(x).\nabla_x t\right] \tag{1.38}$$

Considering that the sample has no electrostatic potential, then only mean inner potential V_0 is present i.e. the potential is constant along x. Equation 1.38 becomes:

$$\gamma(x) = \frac{\lambda\sigma}{2\pi} V_0.\nabla_x t \tag{1.39}$$

This equation shows that even without electric field (constant potential) a deflection can occur if the thickness is variating. This property is used to measure the mean inner potential of wedge crystal [77].

De-scan misalignment: In STEM mode the scan coils depicted in Figure 1-6 allows shifting the beam from the optic axis while keeping it perpendicular to the optic axis. This way the

sample is scan with a beam perpendicular to its surface. At the exit of the sample, the beam has to be tilted back to the optic axis. In DPC or 4D-STEM, the displacement of the beam on the detector plane has to be detected. That is why the de-scan alignment must be as precise as possible otherwise the beam will move when the sample is scanned. In practice a de-scan misalignment will results in a shift ramp or parabola across the acquired map. Such effect can be removed during the data processing by fitting and then subtracting a ramp or a parabola to the shift map.

Sample damage: the focused electron beam used to scan the sample will interact with the sample. In this work, the probe size and the current are typically 1 nm and 100pA. Such current focus in $1nm^2$ can literally drill holes in the sample. During microscopy session, the beam was blanked while making the alignment to prevent the sample damage. But depending on the sample, the current and the dwell time that are used, the sample can be damage during STEM acquisition.

Dynamical charging: the sample undergoes charging when STEM measurements are performed. The focus probe introduces a large quantity of electron in each scan position. Therefore, we are not sure that the sample reaches a steady charged state. Such sample charging can induce imaging instabilities [78], [79]

Limits of DPC: DPC has the advantage of being a very fast technique and gives a map with non-quantitative field contrast in a fraction of a second. However, the calibration can be very time consuming. In addition, the size of the detector leads to a compromise between resolution and sensitivity. The sensitivity and the accuracy will also depend on the geometry and size of the detector [80] [64]. However, the main limit of DPC is its “blindness”. The DPC acquisition is done on the four quadrants of the detector leading in a data sets of four images (see Figure 1-9-c-f) but there is no information about the diffraction pattern recorded and therefore DPC is not able to capture the fine details of the intensity distribution in the diffraction plane [50], [64]. Figure 1-14 shows two examples of transmitted beam with intensity variation. Figure 1-14-(a) is an electron beam which travelled through a 110nm thick GaN sample. Figure 1-14-(b) shows a 100µrad beam after traveling a 350nm thick silicon pn junction. In this last one, the edges of the beam are either darker or brighter than the center of the beam. In such case, DPC gives a contrast in the phase image but the information regarding the redistribution of intensity is not accessible and therefore the quantification becomes irrelevant.

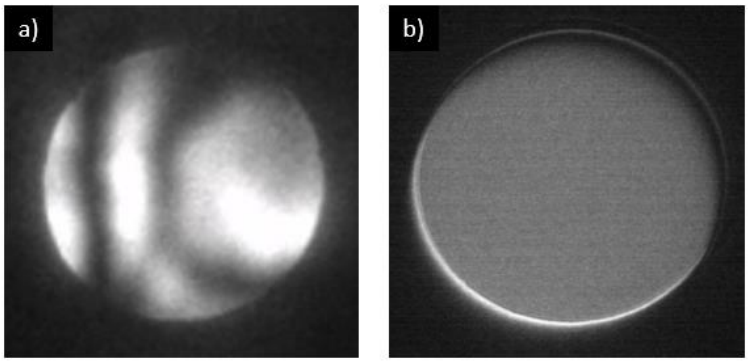

Figure 1-14 : Example of non-homogeneous beam intensity. a) Beam after travelling through a 110nm thick GaN sample close to a zone axis. b) Redistribution of intensity in a beam after travelling through a 350nm thick silicon pn junction far from a zone axis.

CoM considerations: In terms of accuracy, many things can make the CoM move: a shift of the beam, a redistribution of intensity inside the beam, the movement of a higher-order Laue zone (HOLZ) line due to strain. All these examples could be interpreted as shift of the beam in the resulting shift maps whereas some of them are artefacts of the acquisition [16], [50], [74].

TM and DTM considerations: the TM and DTM processing are based on the 2D-cross-correlation (equation 1.35) between the processed pattern and the reference. The output of the 2D-cross-correlation is a 2D-image and in this image the position of the maximum is assumed to be the shift of the pattern compare to the reference (see Figure 1-12). Such numerical approach has a sensitivity of 1 pixel but to increase the sensitivity it was coupled with an interpolation function. The interpolation function takes several pixels around the maximum and interpolates a continuous function. The maximum of this function is then considered to be the shift of the pattern compare to the reference. With this improvement the sensitivity of the TM and DTM is now sub-pixel.

The validity of the TM or DTM processing is based on the assumption that the electric field rigidly shifts the beam. If a redistribution of intensity occurs, the interpretation of the shift value given by TM is not useful. The cross-correlation is sensitive to noise, sharpness of the edges HOLZ lines, redistribution of intensity and size of the template (in the case of the DTM) [75]. All these influences a schematize in Figure 1-15. All these artefacts make the detection of the maximum challenging especially in the case where several of them are present in the data set.

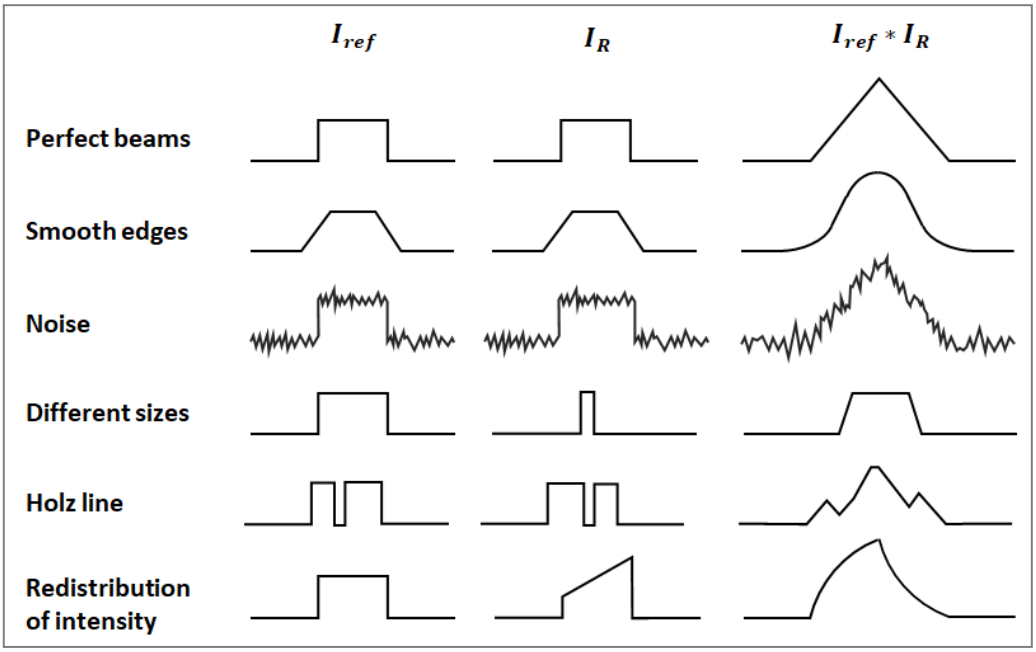

Figure 1-15 : 2D schematic of the influence of different artefacts on the cross-correlation.

1.4 Strain measurement with precession

The measurement of deformation is important in microelectronics as the band structure of the material changes under mechanical strain. When a transistor is subjected to either compressive strain for p-type or tensile strain for n-type, strong gains in electron mobility are observed. The optoelectrical properties can also change in strained materials. As we will see in chapter 5, a strong piezoelectric field can appear in epitaxially grown nitride materials which strongly affects the wavelength of the light emission [81]–[84].

1.4.1 Strain influence in real and reciprocal space

When a semiconductor is grown by epitaxy, it is usually the objective for the atomic planes (perpendicular to the interface) of the layers to be aligned with the atomic planes of the substrate. As such the lattice parameter differences should not be too high otherwise defects and dislocations will occur which will lead to a degradation in the quality of the material [85]. Figure 1-16-(a) shows how the lattice parameters of the grown material are modified in the case of a substrate having smaller lattice parameters. In the plane $(\vec{x}, \vec{z})$ the lattice

parameter is the same for both substrate and epitaxied material. The Poisson ratio gives the relation between the compressive strain induce by epitaxy in the $\vec{x}$ direction and the resulting expansion in the $\vec{y}$ growth direction.

$$\nu = -\frac{\Delta c}{\Delta a} \tag{1.40}$$

Such equation will be used in simulation in order to get expected values of strain. The change in lattice parameter from the substrate to grown material modifies the diffraction pattern. Indeed, the distances in reciprocal space are inversely proportional to distances in real space. Figure 1-16-(b) shows how the diffraction pattern is modified by the strain. It can be seen that the material expands in the growth direction i.e. the distances between atoms increase in this direction, so the distances in this same direction decrease in the diffraction pattern and vice versa in the perpendicular direction. In the $\vec{y}$ direction, the strain of the material ϵ_c^{mat} can be expressed as:

$$\epsilon_c^{mat} = \frac{c + \Delta c}{c} - 1 \tag{1.41}$$

Where $c + \Delta c$ is the lattice parameter of the strained material and c is the lattice parameter of the same material without strain. Therefore, the strain is commonly measured compare to the substrate:

$$\epsilon_c = \frac{c + \Delta c}{c_{sub}} - 1 \tag{1.42}$$

Where c_{sub} is the substrate lattice parameter in the considered direction. For strain measurements, diffraction patterns are acquired in the substrate and in the region of interest. Then the distances g between the central beam and a diffracted beam are measured. Then the strain in reciprocal space can be calculated using this equation:

$$\epsilon_c = \frac{g_{sub}}{g} - 1 \tag{1.43}$$

With g and g_{sub} respectively the distance between beams in reciprocal space, in the region of interest and in the substrate. This calculation of the strain assumes that the specimen behaves as a bulk sample meaning that the surface relaxation is neglected.

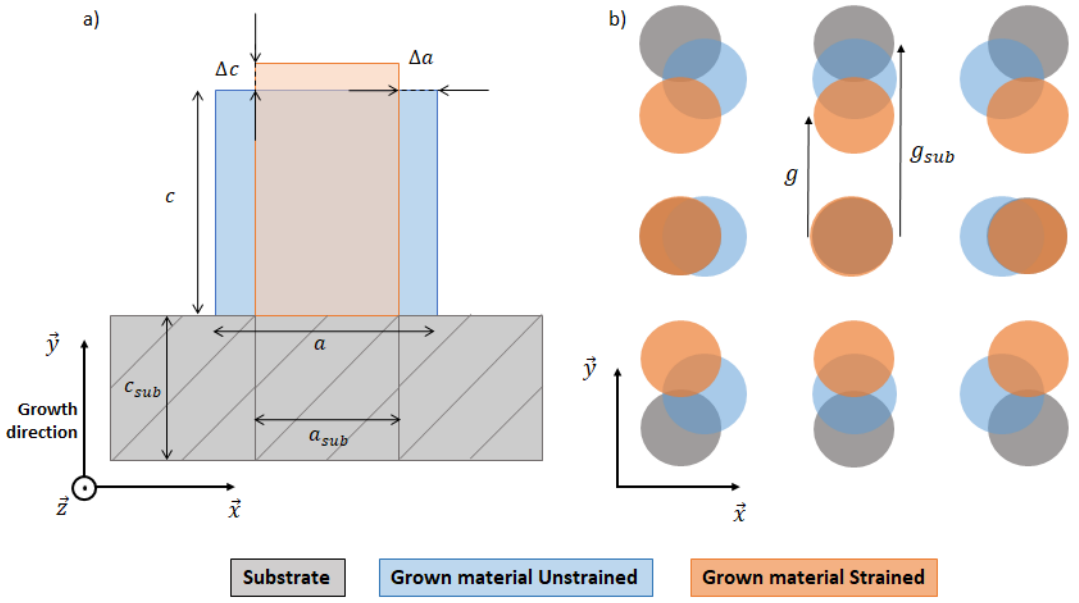

Figure 1-16 : Influence of epitaxy on the materials lattice parameters. a) Lattice parameters matching in the plane of epitaxy ($\vec{x}, \vec{z}$) and deformation of the material in the $\vec{y}$ direction. b) Influence of strain i.e. modification of the lattice parameter on the diffraction pattern in reciprocal space.

1.4.2 Improvement brought by precession for diffraction measurements

The simplest way to measure strain is to compare locally measured diffraction patterns with a reference. At CEA a home written Digital Micrograph script is used to determine strain maps using this method. It detects the position of the diffracted beams and calculates the distances between them using a TM algorithm [47]. Figure 1-17-(b) shows a diffraction pattern from Si looking down the [110] zone axis. The first order of diffraction spots can be seen, but they are full of unwanted contrast arising from dynamical diffraction. This would make an automated method of measuring the positions of the diffracted beams complicated and could introduce inaccuracies in the measurement of strain for non-perfect specimens and at interfaces [86].

Precession has been used at CEA for ten years now to improve strain measurement. Instead of scanning the sample with a beam parallel to the optic axis, the beam is tilted around the optical axis as depicted in Figure 1-17-(a). Usual values for precession tilt are in the range of 0° to 0.5° which leads to an averaging of the intensity in the diffracted beams and allows a better accuracy in the measurement of their position [66]. Another great improvement brought by precession for strain measurement is the illumination of more diffracted beams

[87], [88]. The improvements in the quality of the diffraction patterns can be seen in Figure 1-17-(b) without precession and (c) which uses a precession angle of 0.25°. In addition, the improvements in the diffraction patterns looking down a 110 nm thick GaN sample observed down the [010] zone axis are shown in Figure 1-17-(d) and (e) where a precession angle of 0.25° is again used.

In the next chapters precession will be used to decrease the influence of dynamical diffraction while measuring electric field.

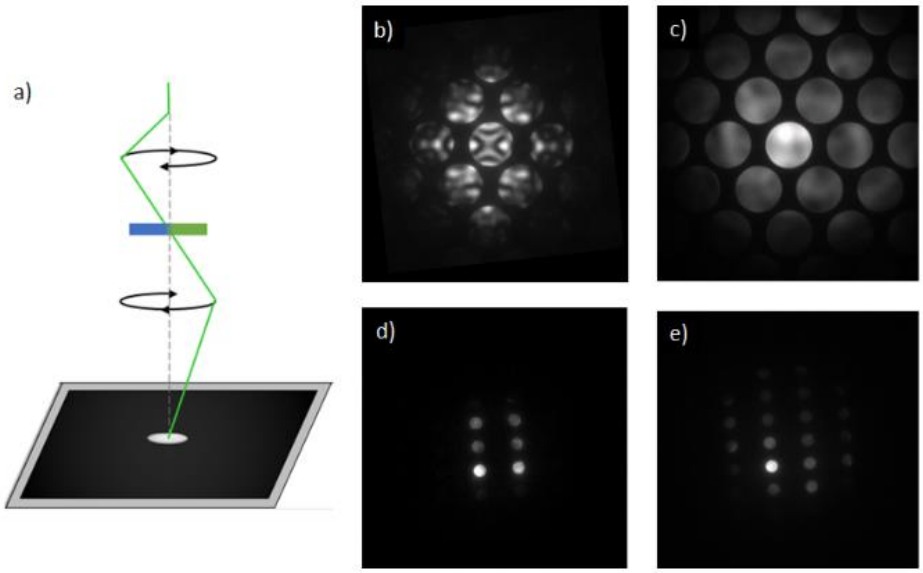

Figure 1-17 : Effect of precession on diffraction pattern. a) Precession schematic, b) and c) are respectively the diffraction pattern in Si down [110] zone axis without and with precession. d) and e) are respectively the diffraction pattern in GaN down the [010] zone axis without and with precession.

1.5 Sample preparation

Semiconductors are grown on wafers that can be as large as 300 mm diameter in the case of silicon, or a few inches in the case of diodes grown on GaN and sapphire. To be able to make observations by TEM, the region of interest needs to be extracted and attached to a TEM grid which allows the sample to be manipulated. In the past this was done by mechanical

polishing, however the invention of the FIB allows high quality specimens to be prepared from regions with µm scale site specificity.

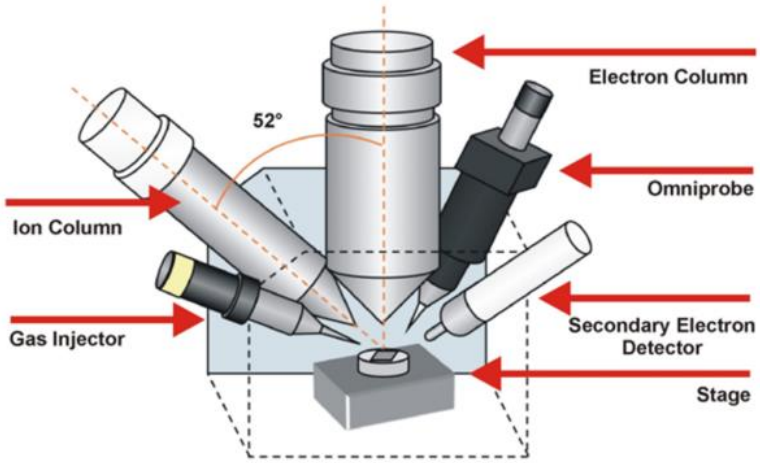

Figure 1-18 : Schematic of the arrangement inside a modern dual-beam FIB

1.5.1 Focused ion beam

A FEI Strata 400S dual beam has been used to prepare all of the samples studied in this manuscript. It is equipped with a FIB column with a Ga^+ ion source for the etching and an SEM column with an electron source for the electronic imaging. A schematic of an FIB is presented in Figure 1-18. The use of the Ga ion beam allows the specimen to be etched for removing the thin TEM lamella and the sample can be imaged using the secondary electrons that are ejected during the milling process. Most modern FIBs are so called Dual-Beam tools as they have a conventional SEM which can be used to provide high quality images of the specimen while not damaging regions of interest due to Ga ion implantation.

The different steps of the FIB preparation are the following one. Firstly, protective layer of about 1µm is deposited on top of the region of interest. This thick protective layer of Pt or W will prevent Ga implantation during the milling, it will also protect the sample during the thinning. The technique used for the sample extraction is commonly named lift out. The material is milled around the region of interest. This milling is done by step deeper and deeper as we get closer to the region of interest. Once the surrounding of the region of interest is milled, the specimen is tilted so the base and the edges of the sample can be cut. A small amount of material is left at one end of the sample to hold it in place. The TEM lamella is then extracted from the bulk specimen using the Omniprobe micromanipulator system. It is made of a tungsten needle, which has to be carefully put in contact of the sample and welded to it. Then the last contact between the bulk and the lamella is milled. At this point the lamella

is only attached to the needle. The sample can be removed from the bulk and brought to the TEM grid, where it is welded. Then the Omniprobe is detach from the sample and removed from the chamber. Finally, the sample is thinned and cut to prevent from bending [89].

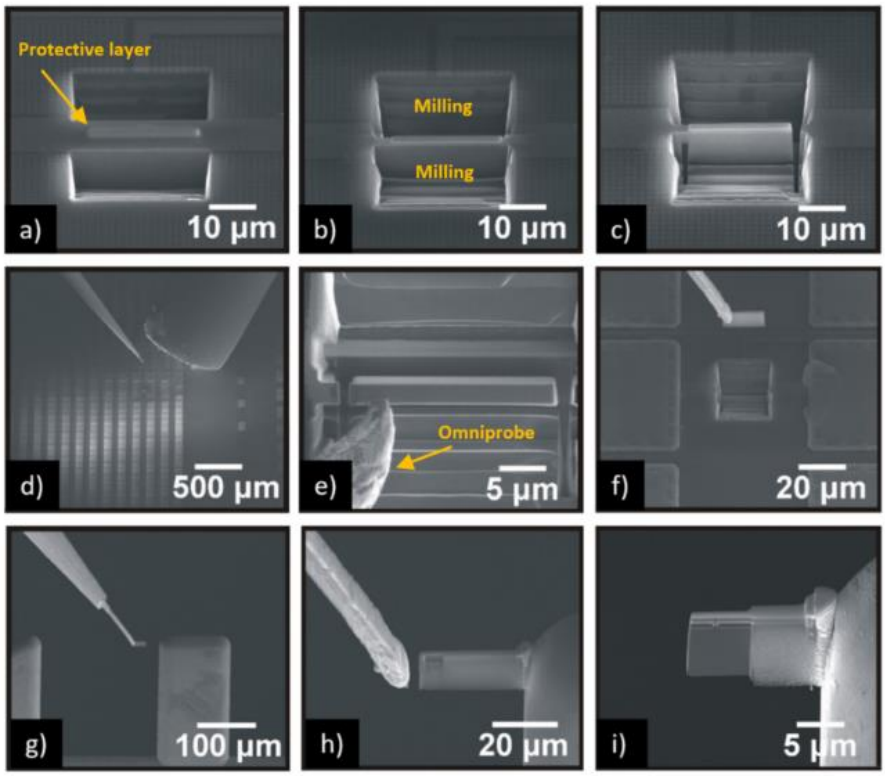

Figure 1-19 : TEM sample preparation steps. a) Protective layer has been deposit on the region of interest and the milling has began. b) The milling on on top and botttom is done. c) The view is tilted and the dark contrast around the lamella show that the cut were done around the sample. At this point the only connection between the bulk and the lamella is on the top left of the lamella. d) On a larger scale we see the Omniprobe reaching the lamella and the gas deposition system. e) The Omniprobe has been welded to the lamella and the lash cut was made to free the sample. f) The sample is removed from the lamella. g) The sample is brougth to the welding spot on the TEM grid. h) The sample is welded to the grid and the detatched from the needle. i) The sample after the final thinning.

1.5.2 TEM lamella for In-Situ biasing experiment

The sample preparation for in-situ biasing is slightly different from the one for classical TEM. The sample preparation can also be done in a FEI Strata dual beam FIB tool. The step to extract the lamella are the same as previously. Then the lamella is welded to both side with tungsten on a special biasing chip visible in Figure 1-20. Metal deposition is then operated on the top and bottom edges of the sample to create the electrical contact. Isolation cuts are done so the current flows through the region of interest, i.e. the metallic contacts do not touch both right and left side of the grid, so the current as to flow through the junction when a bias is apply. The isolation cut and the metal contact are visible in Figure 1-20-(b).

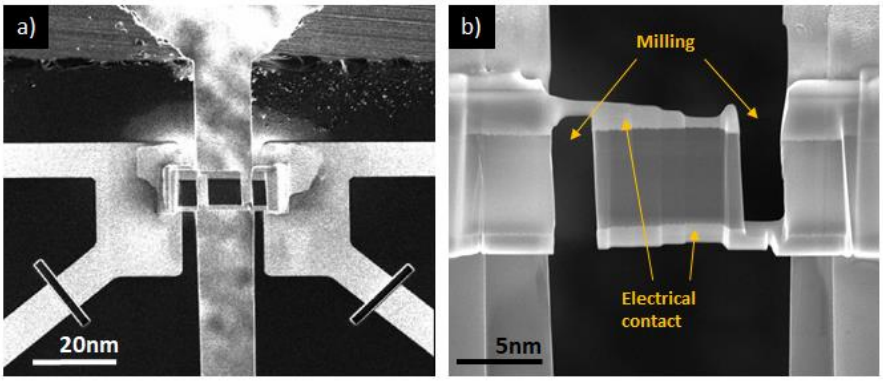

Figure 1-20 : Sample welding on the biasing chip. a) Sample deposed and welded between the two side of the chip. b) Zoom on the same sample, the milled area on both right and left edges plus the electrical contact on top and bottom are visible.

1.5.3 FIB considerations

In the experimental consideration for field measurements, it has been said that the quality of the TEM sample has a strong influence on the measurement. It is easier to make a good sample, than to perform the complicated analysis that is required for bad TEM lamella. The two main artefacts coming from FIB preparation are:

Non parallel side: modern FIB allows parallel sides specimens to be prepared with relative ease. However, small changes in specimen thickness will lead to phase gradients for electron holography measurements. In general, in a well-prepared specimen with a field of view of less than a micron, this can be subtracted as a gradient across the region of interest.

Inactive thickness: The ion etching done by FIB leads to ion implantation. Above a certain concentration of ion, the material is amorphized. This layer of amorph material is the inactive thickness. In order to remove this layer on all the sample a low voltage cleaning at 2kV was performed [28], [32].

Surface current: The amorphous surface layers can received sufficient Ga ion implantation to provide metallic short circuits on the faces of the sample. In order to avoid the current to flow around the surface while biasing the sample were all prepared using an operating voltage of the FIB of 16kV instead of 30 kV. The surfaces of the samples are then cleaned at 2 kV.

1.6 Multi-slices simulation using µSTEM

Multi-slice simulations of the diffraction patterns through the samples have been performed to check the validity of the 4D-STEM experimental data. As the samples are thick, they are considered as a stack of very thin slices in which the WPOA holds. Then, the electron wave propagation through the slices is performed one after the other [9], [42], [43]. Figure 1-21 depicts the basis of the multi-slice simulation. Details of the µSTEM electron scattering model have been detailed by Allen & al [90]. The Debye Waller factors which characterize the attenuation of the electron wave due to thermal motion of atoms, comes from the work of Schowalter & al [91], [92]. The transfer function of a Δz-thick slice is derived from equation 1.7 and 1.8. This transfer function can be expressed as:

$$\Delta T(x,y) = exp\left[i\sigma \int_{z}^{z+\Delta z} V(x,y,z)dz \right] = 1 - i\sigma \int_{z}^{z+\Delta z} V(x,y,z)dz \qquad (1.44)$$

Multi-slice simulations were performed using µSTEM to generate diffraction patterns. The software uses a crystal input file which gather the coordinates of atoms in a unit cell. Then the software repeats the unit cell to create a wider and thicker crystal that represent a real sample. In the frame of this thesis, the simulations were useful for diffraction patterns at the vicinity of an interface. therefore, it was necessary to create tailored input files with crystal interfaces. The important parameters for such tailored input files are the real space sampling Δx, the scattering angle sampling $\Delta\beta$ and the maximum scattering angle β_{max}.

The real space sampling is the distance on the atomic structure between two simulated diffraction patterns. The maximum scattering angle gives maximum range of angle present

in the simulated diffraction pattern. The real space sampling can be calculated using this equation:

$$\Delta x = \frac{L_x}{N_x} \tag{1.45}$$

Where L_x is the size of the crystal structure and N_x is the number of pixels of the simulated patterns. The two parameters L_x and N_x are accessible. The scattering angle can be calculated using:

$$\Delta\beta = \frac{1}{L_x \,.\, k} \tag{1.46}$$

Where k is the wavevector, equal to 39.875Å^{-1} at 200kV acceleration voltage. And finally, the maximum scattering angle is calculated using:

$$\beta_{max} = \frac{\Delta\beta . N_x}{3} \tag{1.47}$$

Multi-slice simulations were performed on three different structures. The first one is an Si/SiO_2 interface. The second one is a SiGe layer embedded in Si. The last structure in an InGaN quantum well in GaN lattice.

Si/SiO_2: the input file comes from a previous study done by P. Ganster & al. In this previous study, the strain was the matter of interest. The structure was numerically created and for more details on the SiO2 structure the reader can refer to [93]. The file they used for their simulation was already a list of atoms position representing a 100×150×100Å^3 structure. We converted it into a µSTEM input file using the script in appendix A. The thickness was limited to 2Å to limit the number of atoms in the input file. Finally, the structure was repeated so the simulated pattern has a resolution of 0,029mrad and a maximum scattering angle of 30mrad.

SiGe: the structure was created using the script in appendix B. The SiGe sample was grown along the [110] axis and the FIB preparation led to a direction of observation along the [001] axis. In this input file, the dimension of the atomic lattice is 7x400x7Å^3. The structure contains one 100Å wide layer of SiGe in a Si crystal. Such structure has to be tiled 57 times in the x direction in order to create a scared structure of 400x400x7 Å^3. Then this structure is sliced into four thinner slices of less than 2Å. The parameters of the simulation are such the resolution and maximum scattering angle are the same as the one of the SiO2.

InGaN: the sample was grown along the [001] axis and the FIB preparation leads to a direction of observation down the [1-10] axis. The structure was created layer by layer and the final structure is 3.2 x 805 x 5.5Å^3 (appendix C). The structure contains a 70Å wide layer of $In_{0.14}Ga_{0.86}N$. The structure was tiled 251 times in order to obtain a slice of 805 x 805 x 5.5Å^3. Again, the simulation parameters were chosen so the resolution is the same as the one in the SiO2.

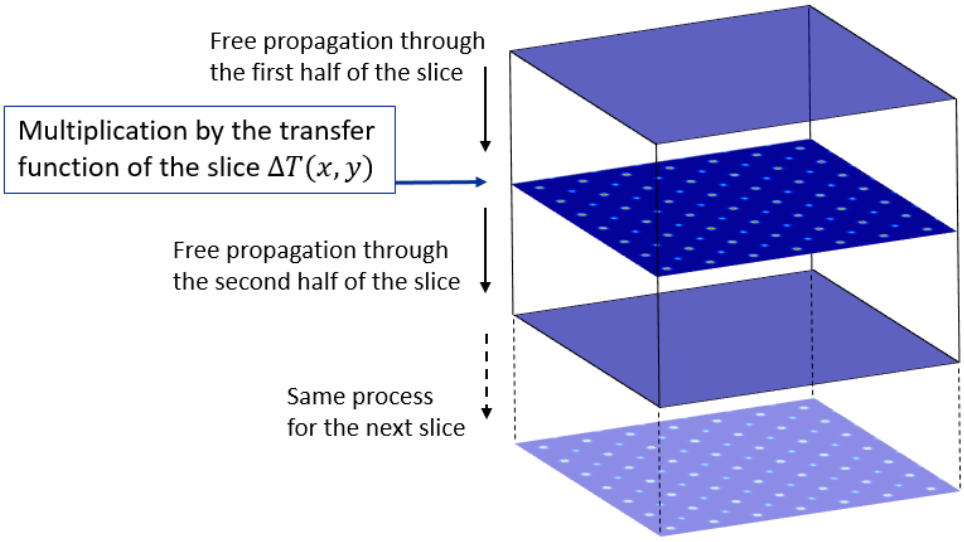

Figure 1-21: Multi-slices simulation schematic. Propagation of the electron beam through one slice. The transfer function ΔT is described by equation 1.44

Some simulations performed in µSTEM were compared to experimental data acquired using precession (see section 1.4.2). Therefore, a precession procedure was created to reproduce the influence of precession diffraction patterns. To do so, the sample is tilted 0.25° off axis (4 mrad) and 12 simulations are performed with 12 different azimuth tilts around the optical axis (every 30°), then the 12 different orientations are average. With this protocol of simulation, the dynamical diffraction has a low influence on the diffraction patterns.

2 Electric field mapping in a Silicon pn junction

Silicon is the dominant material used for the manufacture of semiconductor devices. One reason is because it is present in huge quantity on earth in the silicon dioxide, another is that it is well known how to grow perfect silicon wafers. To begin these studies, we first worked on silicon pn junction with a high dopant concentration of $10^{19}\,cm^{-3}$. This creates a depletion region of several tens of nanometers in which an electric field is present. A pn junction architecture is very convenient because the dopant concentration of both side is such that the mechanical properties of the silicon lattice does not change. This means that there is no strain or change in the lattice parameters from one side to another. In other words, with this sample there is only the electric field that varies in the depletion region. Another advantage using silicon is that due to the cubic lattice and perfect crystallinity, it is possible to tilt the sample to an orientation where the dynamical diffraction is not too strong and therefore limit the artefacts in the transmitted beam. The theoretical model of a pn junction is well known and so the pn junction behavior can be simulated. This way the experimental data can be compared to theoretical values.

Firstly, in this chapter the basic properties of the silicon pn junction are described and expected field values will be numerically estimated. Then field measurement will be done in low magnification STEM and the limits of this mode will be detailed. Then an in-situ experiment in nanobeam STEM mode on a biased silicon pn junction will be presented. This will show how the nanobeam mode allows quantitative measurement of the electric field in a pn junction. The effect of diffraction when processing the data will be detailed. Then the improvement brought by energy filtering and precession on the data acquisition that allows to keep simple algorithm to process the data. Finally, the influence of the electron beam on the sample will be discussed with data acquired using different electron dose. This last point will show that the probe uses in STEM interacts with the sample. The results are presented in a logical order and not a chronological order. That is why some experimental parameters will not be optimum.

2.1 Silicon pn junction

2.1.1 The pn junction

A pn junction occurs when a doped semiconductor with an excess of holes is put in contact with one which has an excess of electrons. For these studies, a phosphorus doped n-type layer was grown on top of a boron doped p-type silicon layer onto a lightly doped silicon

substrate by reduced pressure chemical vapor deposition (RPCVD). The contact between the two sides of the junction creates a depletion region with an electric field within it. To simplify the theory, the junction will be considered as abrupt meaning that no dopant diffusion occurred between the two sides. The dopant concentration will be considered uniform and equal to N_a and N_d respectively for the p and n region. With these assumptions, potential difference and electric field values can be obtained analytically.

The dopants change the position of the Fermi level; in the n-doped layer, the Fermi level increases compared to the p-doped layer where it decreases. Once these layers are in contact, the Fermi levels align themselves to reach an equilibrium leading in the energy band bending in the depletion region [94]. This is represented by the schematic in Figure 2-1-(b). This energy band bending multiplied by the elementary charge of the electron gives the difference of potential in the depletion region. The potential difference is called the built-in potential V_{bi} shown in Figure 2-1-(c). This difference of potential creates an electric field, which can be detected by 4D-STEM. The difference of potential depends on the dopant concentration in each side and can be calculated with this equation:

$$V_{bi} = \frac{kT}{q} ln\left(\frac{N_d N_a}{n_i^2}\right) \tag{2.1}$$

Where kT is the Boltzmann constant multiply by the temperature, q is the elementary charge of an electron and n_i^2 is the intrinsic charge concentration. With the Poisson's equation we can access the potential distribution and the electric field distribution. The Poisson's equation is:

$$\frac{d^2V}{dx^2} = -\frac{dE}{dx} = -\frac{\rho}{\epsilon_s} \tag{2.2}$$

Where V is the potential, E is the field, ρ is the charge density and ϵ_s is the permittivity of silicon. Now from this equation, in the depletion region between $-x_p$ and x_n the field can be calculated. In the P side of the depletion layer ($0 \geq x \geq -x_p$), from the uniform dopant concentration the charge density is assumed to be:

$$\rho = -qN_a \tag{2.3}$$

So equation (2.2) becomes:

$$\frac{dE}{dx} = -\frac{qN_a}{\epsilon_s} \tag{2.4}$$

By integrating equation (2.4) the electric field distribution in the P side is obtained:

$$E(x) = -\frac{qN_a}{\epsilon_s}x + C_1 = \frac{qN_a}{\epsilon_s}(x - x_p) \tag{2.5}$$

With a similar calculus on the N side ($0 \leq x \leq x_n$) the field in the N side is obtained:

$$E(x) = -\frac{qN_d}{\epsilon_s}(x - x_n) \tag{2.6}$$

The property of continuity of the electric field yields in $x = 0$:

$$|x_n|N_d = |x_p|N_a \tag{2.7}$$

These two equations 2.5 and 2.6 give the triangle shape of the field in the abrupt junction assumption. By integrating the field, the potential is deduced:

$$V(x) = \frac{qN_a}{2\epsilon_s}(x - x_p)^2 \qquad 0 \geq x \geq x_p \tag{2.8}$$

$$V(x) = -\frac{qN_a}{2\epsilon_s}(x - x_n)^2 \qquad 0 \leq x \leq x_n \tag{2.9}$$

Then the last important parameter of the pn junction that can be estimated is the depletion width. From equations 2.7, 2.8 and 2.9 the depletion width is calculated to be:

$$x_n - x_p = W_{dep} = \sqrt{\frac{2\epsilon_s V_{bi}}{q}\left(\frac{1}{N_a} + \frac{1}{N_d}\right)} \tag{2.10}$$

By assuming a dopant concentration of 10^{19}cm^{-3} on both sides, the built-in potential can be estimated using a simple approximation. The value found is about 1.09V thus the depletion region can be estimated to 16.7nm using equation 2.10. Then using equation 2.6 at x = 0, the maximum electric field is estimated to 1.32MV/cm. This was a first rough approximation that gives a range of value for the field. In a perfect case, the theory behind the pn junction can be easily understood. Even so, in our real sample the situation is more complex as the dopant concentration is not perfectly abrupt. To have a more accurate value of the field simulation needs to be run.

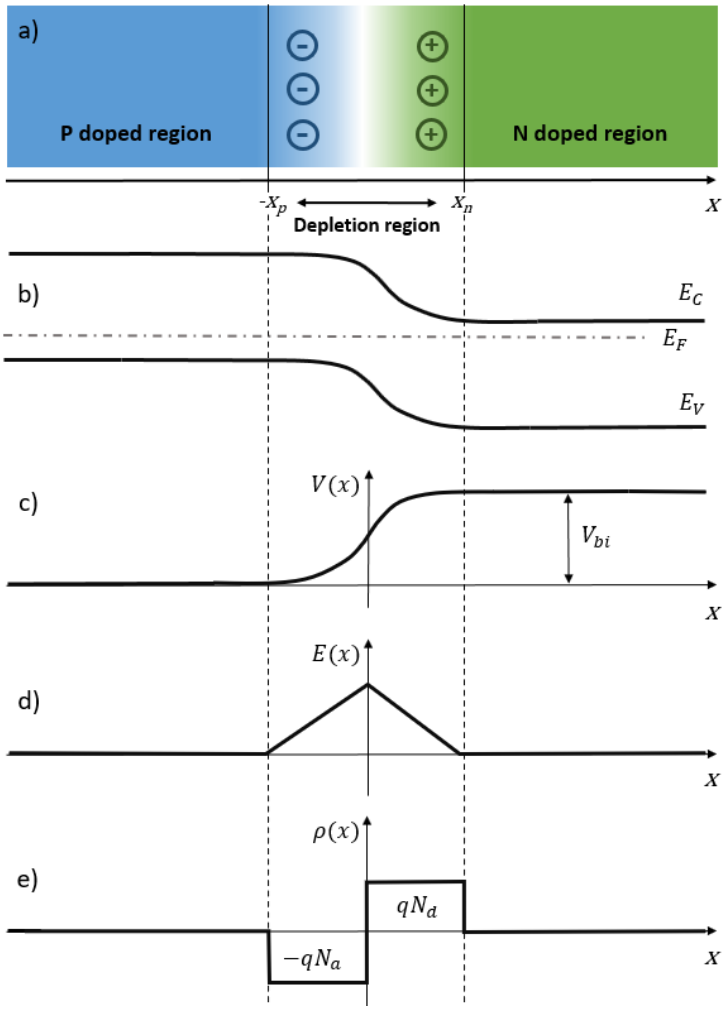

Figure 2-1 : Schematic of pn junction basic properties. a) pn junction schematic with the positive doping region in blue, the negative doping region in green and the sign of the charge accumulation in the depletion region. b) Band diagram with alignment of the fermi level and the bending of the conduction and valence energy band. c) Electrostatic potential $V(x)$ distribution with the built-in potential V_{bi}. d) Electric field $E(x)$ distribution. e) The charge distribution $\rho(x)$ with N_a and N_d the dopant concentration of acceptor and donor respectively.

2.1.2 Dopant measurement and electric field simulation

To accurate perform simulations of the expected potential and electric field, the exact profile of dopants in the pn junction was measured by second ion mass spectroscopy (SIMS) [27]. This technique uses an ion beam which energy is typically between 250eV and 30keV depending on the in-depth resolution needed which sputters ions from the surface of the

sample. The sputtered ions are then separated using a magnetic field and detected as a function of their mass [95], [96].

The concentration of boron and phosphorus, are shown in Figure 2-2-(a) confirming that the dopant distributions are as expected. On both sides the measured concentration is $10^{19}\mathrm{cm}^{-3}$. Then regarding the decrease of the dopant concentration, from the p-doped to the n-doped region and vice-versa the concentration of Boron or Phosphorus respectively drops quickly around $10^{16}cm^{-3}$. Finally, the concentration has an exponential decrease and not an ideal abrupt profile. An abrupt profile would be the perfect case of a junction described in the previous section, however when specimens are grown by epitaxy, there are often residual dopants in the growth chamber that float on the surface of the sample leading to non-abrupt junctions. The exponential profile measured here provide an input for numerical simulation of this PN junction. Now that the dopants profile is known, the field value and the depletion width will be simulated with more accuracy than in the analytical estimation.

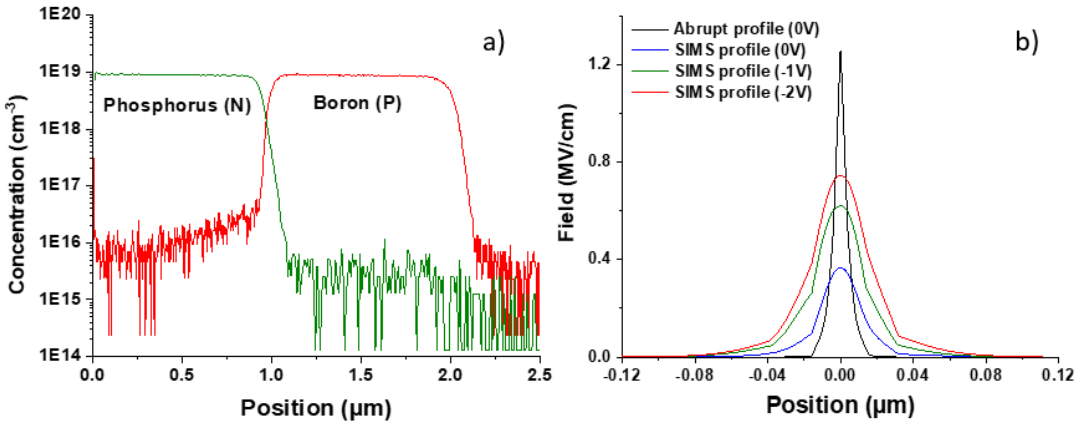

Figure 2-2 : a) Profiles of the dopant concentration acquired by SIMS. Boron concentration in red and Phosphorus in green. b) Simulated field profiles with different dopant profiles and with different bias voltage.

The junction was then simulated using Silvaco TCAD software such that the expected built-in potential, electric field and depletion width could be assessed. Several profiles of electric field across the junction are shown in Figure 2-2-(b). The first one is the case of an ideal abrupt profile, meaning that the concentration of dopant inputted in the software drops instantaneously from one side to another. This led to a value of field close to 1.3MV/cm and a depletion region 35nm wide. We will see later in this chapter that these values are far from what was experimentally measured. The other profiles shown are field profiles obtained by

inputting the SIMS profile. Without bias (blue curve), the field value is three time less than in the case of an abrupt junction. The depletion region is two times wider than with an abrupt profile. The two last profiles were obtained with the SIMS profile as input and a reverse bias of 1 V and 2 V respectively. This reverse bias increased the electric field and the width of the depletion region.

The values of electric field and depletion region width obtained here will be our theoretical reference for the rest of this chapter (see Table 2-1). The experimental results will be systematically compared to these simulated values.

Reverse Bias	Maximum Electric field	Depletion width	Depletion width FWHM
2 V	0.74 MV/cm	160 nm	30 nm
1 V	0.62 MV/cm	130 nm	28 nm
0 V	0.37 MV/cm	60 nm	25 nm

Table 2-1 : Simulated electric field and depletion with in a $10^{19}cm^{-3}$ *doped Si junction with different bias applied. For the depletion width we discuss both total and full width half maximum (FWHM) due to the large tails of the depletion width in Figure 2.2.*

2.1.3 Off axis holography on a biased pn junction

The bulk sample from which the junction comes from is the same as the one used in 2019 by Haas & al [49]. Some raw data from this previous study were reprocessed and results are presented here. Whereas today it is possible to obtain high spatial resolution and high sensitivity similtaniously by adding stacks of holograms together, here we used the most simple case. An FEI Themis microscope was used at an accelerating voltage of 200 kV and the biprism bias is such that the fringe spacing is 2.5 nm. Here a single hologram was acquired for 8 s using a Gatan Ultrascan 2k camera. The thickness of the sample was measured to be 225 nm by CBED and a reverse bias of 2 V was applied to the junction.

Figure 2-3 presents the results of this holography experiment. Phase and potential map are shown in (a) and (b). In (c) the field map zoomed on a smaller field of view is shown. The electric field considered here is the field perpendicular to the junction. From the profile in

(d), we can see that from one side to the other the phase difference is 5rad which is equivalent for that thickness to a potential difference of about 3 V. This is in total agreement with the expectation. Indeed, the built-in potential is about 1 V and a bias of 2 V is applied to the junction during the acquisition. Regarding the electric field derived from the potential, the maximum value is 0.62 ± 0.07 MV/cm which is in the same range as the 0.74 MV/cm expected with the 2 V bias. Also, regarding the width of the depletion region, here we measure a total width of 95 nm and a FWHM of 35 nm which is also in agreement with the FWHM simulation at 2 V reverse bias presented in Figure 2-2-(b).

This holography experiment is our benchmark in terms of field measurement by means of TEM. With this experiment, quantitative values of potential and electric field have been measured and are in agreement with the simulation.

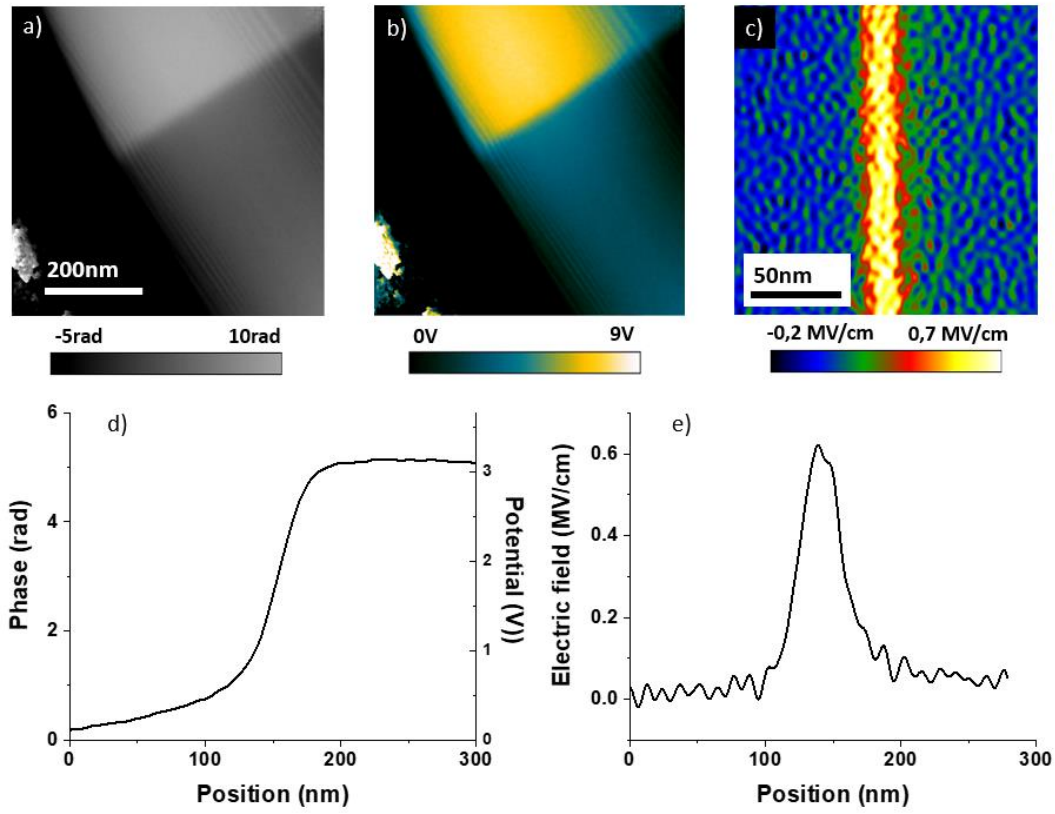

Figure 2-3 : Off axis holography on a biased pn junction. a) Phase map reconstructed from the raw hologram. b) Potential map calculated from the phase map using the equation 1.6. c) Electric field map obtained by derivation of the potential. d) Phase and equivalent potential profile taken across the junction. e) Field profile average over 20 nm taken across the junction from map (c).

2.2 Low magnification 4D-STEM for field mapping of a silicon pn junction

LM-STEM was the first mode explored in the frame of this work. This mode has advantages, one of them is the increased sensitivity provided by a much longer camera length. In LM-STEM convergence angle from 100 µrad up to 1 mrad are used in combination with a camera length of several meters or even tens of meters. Using such low convergence angles allows the transmitted beam to fit on the detector using these long camera lengths that leads to high sensitivity (see equation 1.27). But this is at the expense of the resolution as such convergence angle are not in the range of HR-STEM parameters. The purpose of this section is to show how the diffraction pattern is affected after traveling through a silicon junction TEM sample in LM-STEM mode and some limits of this mode will be detail.

2.2.1 Non-rigid shift in LM-STEM

Several TEM specimens of the pn junction sample were prepared by focus ion beam (FIB) in a FEI Strata dual beam FIB tool. Each sample was milled to contains several areas with different thickness from 100 up to 400 nanometers thick. The thickness was each time measured by convergent beam electron microscopy (CBED) in two-beam condition. For our LM-STEM acquisitions we used a range of convergence angle from 80µrad up to 800µrad. Using equation 1.17 the size of the central Airy disk is 38 nm and 3.8 nm for 80µrad and 800µrad respectively.

The Figure 2-4 shows how the intensity of the beam is affected after travelling through a 200nm thick specimen containing a pn junction. In this figure the transmitted beam inside the depletion region is shown for different convergence angles. The pattern was recorded at 18m camera length on a Oneview camera. The profiles of the different beam are comparable and in total agreement with the work done by L. Clark & al in [42]. For all convergence angle represented here there is no rigid shift. The field cannot be considered as constant in the probe; therefore, a redistribution of intensity occurs. This redistribution of intensity has a visible effect on the left edge of the beam where a peak appears while the probe scans the depletion region. As the convergence angle increase the effect of the redistribution of intensity become less important but still there is no rigid-shift of the beam. According to the simulation the depletion

region is 70nm wide. Even at 800 µrad, the size of the probe is not small enough for considering the field constant in it.

However, even without a rigid-shift of the beam, the field can be detected. To do so, the shift of the CoM of intensity is extracted from the raw data. In the case of a redistribution of intensity, the TM will give shift values that have no physical meaning as it was explained in section 1.3.5. So, the CoM algorithm is used to process the data acquired in LM-STEM mode.

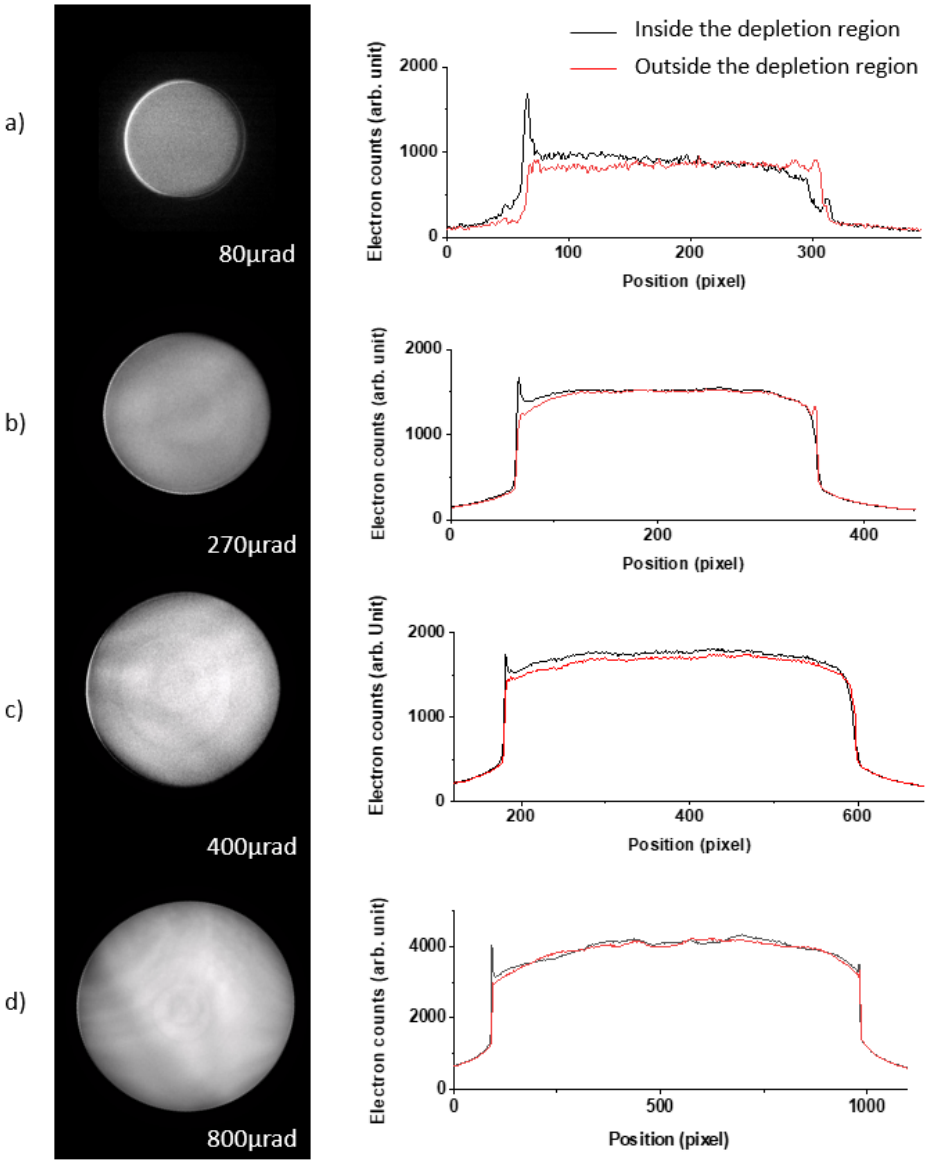

Figure 2-4 : Redistribution of intensity of the transmitted beam in LM-4D-STEM. The beam travels through a 200nm thick sample containing a pn junction. The camera length was set to 18m and different convergence angle were tested. Respectively the value of the half convergence angle is : a) 60µrad, b) 270µrad, c) 400µrad, d) 800µrad. For each convergence angle a profile of the beam has been taken in an area with no field (red curve) and is compare to the profile of the beam in presence of electric field (black curve)

To test the accuracy of CoM processing, a LM 4D-STEM dataset was acquired on a 330±10nm thick pn junction sample. The convergence angle was set to 610 µrad and the camera length to 18 m. The transmitted beam was recorded on a Oneview camera binned so the image is 512 pix². The results are shown in Figure 2-5. With these setting and equation 1.26 we expect the electron beam to be deflected by an angle of 38 µrad which on the camera must represent a shift of the transmitted beam of 7.5 pixels. The field map depicted in (a) show a clear contrast between the depletion region and the rest of the sample. The recorded transmitted beam presented in Figure 2-5-(b) and (c) respectively far from and in the depletion, region clearly show that the redistribution of intensity occurs. For a better reading of the field values, an average profile taken across the junction in the field map is depicted in Figure 2-5-(d). The maximum field value is about 0.04 MV/cm. It is ten times less than what the simulation predicted. The width of the depletion region is 130nm which is wider than expected. This might be cause by the sample tilt and by the fact that the junction signal is convolved with the probe shape. Also, the map in (a) shows a variation of the depletion width as we go from top to bottom. The difference between the experimental results and what the simulation predicts can originate from several artefacts. Some of them will be assessed in this chapter, among these we can site the dynamical diffraction, the drift or the sample charging.

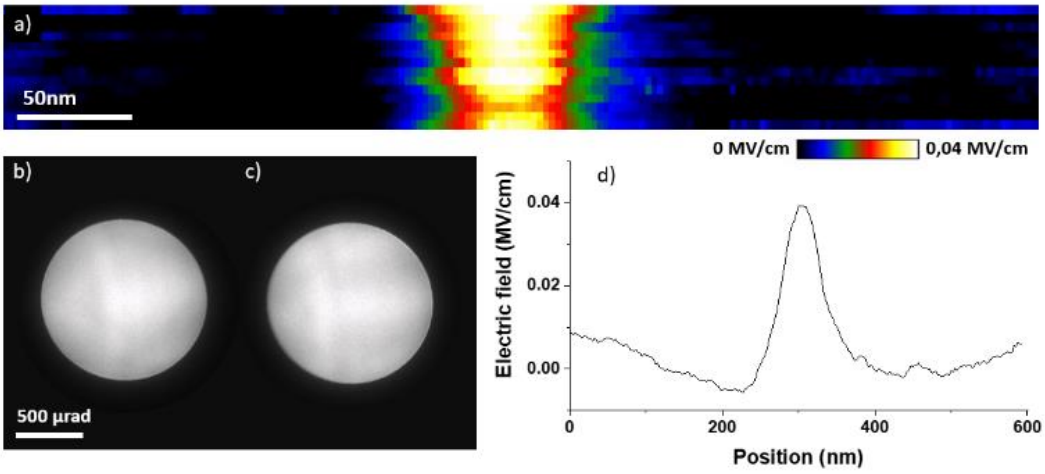

Figure 2-5 : Field mapping of a 200nm thick pn junction in LM-STEM mode with a half convergence angle of 610 µrad and a camera length of 18m. a) Electric field map obtain by a CoM processing. b) Transmitted beam far from the junction. c) Transmitted beam in the depletion region i.e. in presence of an electric field. d) Field profile across the junction extracted from (a).

In this experimental condition it seems that the electric field can be detected but the field values are not as expected. So from this experiment processed by CoM we obtained the signal comparable to a non-quantifyable DPC signal which is much more simple to set up, faster to acquire, does not require and data processing and recquires less storage space.

2.2.2 Diffraction contrast in a real sample when using a convergent beam

The intensity redistribution previously detailed in LM-STEM mode is due to the field varying over a distance comparable to the probe size. Thus, a smaller probe i.e. using a higher convergence angle is needed to achieve a constant field in the probe. Increasing the convergence angle of the beam means that more diffraction contrast will be present. Figure 2-6-(a) to (f) shows transmitted beams that travel through a 200±10 nm thick silicon sample tilted 0.28° from [-110] zone axis. From (a) to (c) the convergence angle is increased from 100 µrad to 800 µrad that covers the convergence angle we used in LM-STEM mode. We can see that until 400 µrad there is little diffraction contrast in the transmitted beam for this specific orientation. This is because with such convergence angle, the beam rays are almost parallel so by tilting the sample a few tens of degrees of axis allow to suppress the dynamical contrast in the beam. At 800 µrad some contrast appears in the beam. Then with the beam depicted in (d), (e) and (f) the contrast in the beam is getting worse as the convergence angle increase. Those three last convergence angles cover the range of angle accessible in Nanobeam STEM mode (NB-STEM mode).

The effects of the dynamical diffraction are shown in Figure 2-6-(g). It is a LACBED pattern simulation in silicon down the [-110] axis with a thickness of 200±10 nm. This pattern helps understand the effect of dynamical diffraction depending on the orientation and the convergence angle [49]. The red circle is equivalent to a beam formed by a 4 mrad convergence angle and a sample tilted 0.3 degrees from zone axis. This LACBED pattern shows the advantage of silicon regarding diffraction, indeed the sample can be tilted in an orientation where the dynamical diffraction has a low effect. This is what the blue circle schematize. It is also a beam formed with a 4mrad convergence angle but this time the tilt chosen lead to very few dynamical diffractions in the transmitted beam.

In a perfect crystal such dynamical contrast would not be a problem. Indeed, as the sample is scanned the orientation stays the same and so should be the contrast in the transmitted beam. But no TEM sample is perfect. For example, there might be lattice bending due to strain relaxation as we reach an edge or an interface or there might be defect such as dislocation. These little imperfections will lead in diffraction contrast variation in the beam.

During the data processing a change in contrast due to lattice defect will lead in a shift and so it could be interpreted as an electric field.

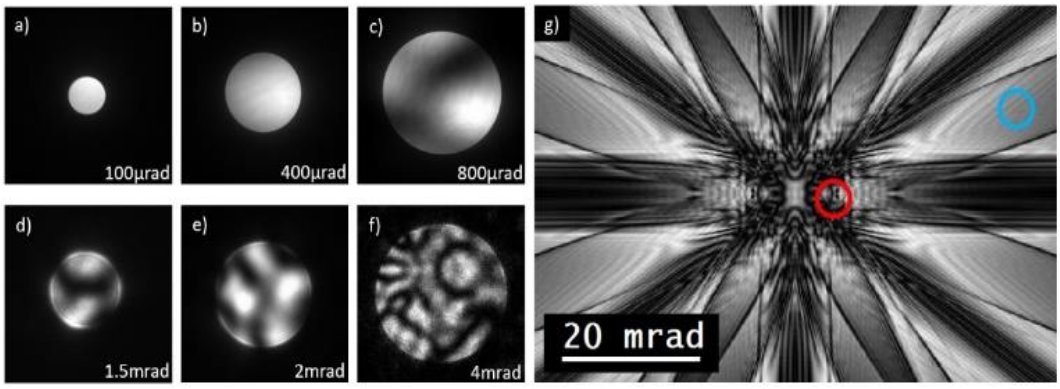

Figure 2-6 : Dynamical diffraction in silicon. From a) to f) image of the transmitted beam recorded on a 200nm thick silicon sample with different convergence angle, the orientation of the sample is 0.3° far from the [-110] zone axis. g) Simulated LACBED pattern of silicon down the [-110] axis for a 200nm thick sample. The red circle represents a 4mrad convergence angle in the orientation where the image a) - f) were recorded. The blue circle represents also a 4mrad convergence angle but this time in an orientation where the dynamical diffraction has a low influence.

Using LM 4D-STEM the electric field in silicon pn junction can be detected. The range of convergence angle used in LM-STEM allows to reach a low diffracting condition with a small sample tilt. The main limitation of LM 4D-STEM is size of the probe. It is limited by the convergence angle and by the difficulties to align the beam properly using the available alignments on the Titan Ultimate. Using LM STEM mode, we could only observe a complex redistribution of intensity due to the field. An additional problem is that in a real specimen the features are in the nm range, so LM STEM would not provide a good enough spatial resolution. Thus, we decided to change the microscope setup and began working in nano beam mode.

2.3 Nanobeam 4D-STEM for field mapping of a silicon pn junction under reverse bias

The nanobeam STEM (NB-STEM) mode uses convergence angle typically from 1 to 5 mrad to provide a smaller probe size and higher spatial resolution. This improvement of the resolution is at the expense of the sensitivity. Let us assume a convergence angle of 3 mrad and we want the beam diameter to be half of the camera size. Using the OneView camera of 6 cm² to record, then the maximum camera length is 5 m. As the beam shift on the detector is proportional to the camera length, the sensitivity has indeed been decreased compare to the one we had in LM-STEM. The previous field values processing by CoM calculation were not quantitative. The redistribution of intensity in the beam is very complex that is why we hope to reach rigid shift in our pn junction configuration in NB-STEM mode. If rigid shift of the transmitted beam can be achieved, then a TM algorithm becomes relevant. The limitation now in NB mode will be more dynamical diffraction appearing in the beam and the reduced camera length i.e. reduced sensitivity in the measurement.

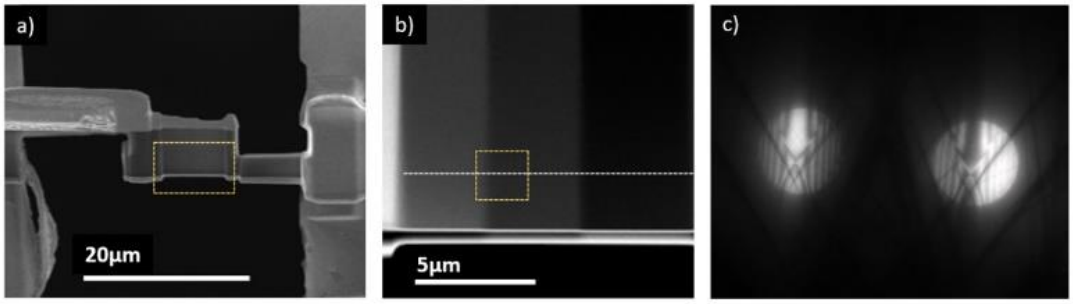

Figure 2-7 : Silicon pn junction sample with electrical contacts prepared by FIB. a) HAADF image of the full FIB lamella solder to the protochip holder. The electrical contacts are visible on top and bottom off the lamella (light grey region), yellow dashed rectangle show the field of view of image b). b) HAADF image of the different thickness. The white dashed line represents the position of the junction. The yellow dashed rectangle represents the area where the following measurement have been done. c) CBED pattern in two beam condition along the (004) axis of silicon. This CBED pattern has been used to determine the thickness of the sample where the DPC and 4D-STEM acquisition were done.

As a test sample we wanted an electric field with the highest vales possible over a large distance. A solution was to apply a reverse bias to the existing pn junction. The sample

prepared by FIB is presented in Figure 2-7. Three areas with different thickness were milled and the crystalline thickness was measured by CBED in a two beam condition [97]. Figure 2-7-(b) shows the three different thickness area and the dotted line represents the position of the junction. The yellow dashed rectangle in Figure 2-7-(b) represent the region of interest on which DPC and-STEM were acquired. Figure 2-7-(c) is a CBED pattern acquired on the region of interest and used to determine the thickness of the sample in this area. From this CBED pattern, the thickness was estimated to 390±10nm. This value is used to calculate quantitative field values. The other thicknesses have also been estimated. The thinnest is 350±10nm and the thickest is 410±10nm. The thicker the sample, the bigger the deflection of the beam is. But thicker sample leads to more dynamical diffraction and more diffuse edges of the beam which leads to more error in the beam shift detection.

2.3.1 Verification of the biasing

As the 4D data acquisition and the processing are time consuming it was necessary to verify that the biasing of the sample worked. DPC is used as a check to see if the applied bias goes through the junction i.e. no short circuit are present in the circuit formed by the sample and the holder. As it was explained in the method chapter, the FIB preparation has to be extremely careful in order to obtain a good electrical contact and avoid short circuits. We performed a LM-DPC field measurement knowing that our results will not be quantitative but we just wanted to see if the signal was changing with the bias. The advantages of doing that instead of a 4D STEM experiment is because in DPC the signal map can be obtain live. Therefore, we have a quick answer is whether or not the biasing condition are good. The current flowing through the junction was limited to 100µA in order to preserve the specimen from heating.

A forward bias, meaning that a positive voltage is applied to the P region relative to de N region, will decrease the difference of potential between the two side of the junction leading to a thinner depletion region and a lower electric field. In the opposite way, if we apply a reverse bias V_B, this voltage will increase the potential. The Fermi level has to stay the same in both side leading in more band bending in the energy diagram. This bigger difference of potential leads to a wider depletion region. When a bias is applied equation 2.10 becomes [94]:

$$W_{dep} = \sqrt{\frac{2\epsilon_s(V_{bi}+V_B)}{q}\left(\frac{1}{N_a}+\frac{1}{N_d}\right)} \tag{2.11}$$

Therefore, the electric field will also increase when a reverse bias is applied. The simulated profiles in Figure 2-2-(b) shows the electric field increase. The LM-DPC acquisition was performed with three different biases. The camera length was set to 12m and the convergence angle was set to 210 µrad for a probe size of several tens of nanometers. Figure 2-8-(a), (b) and (c) show the DPC map for respectively -2 V, 0 V and 1.5 V. So, the 0 V signal is created only by the built-in potential. The -2V bias is a reverse bias as against 1.5 V that is a forward bias. The profile presented in Figure 2-8-(d) have been taken across the junction in the same area with the three different biases. With the convergence angle we set; no rigid shift is expected so the signal is only qualitative. With the reverse bias the DPC signal i.e. the electric field is increase by a factor 2 just as the simulated profile show in Figure 2-2-(b). Regarding the forward bias, as the it is bigger than the built-in potential of our junction ($V_{bi} = 1.09V$), the junction should have disappeared. This means that some of the voltage applied is lost in the total system and not all the voltage is applied across the junction. This DPC experiment shows that a bias can be applied across the junction and an increase in field is measured.

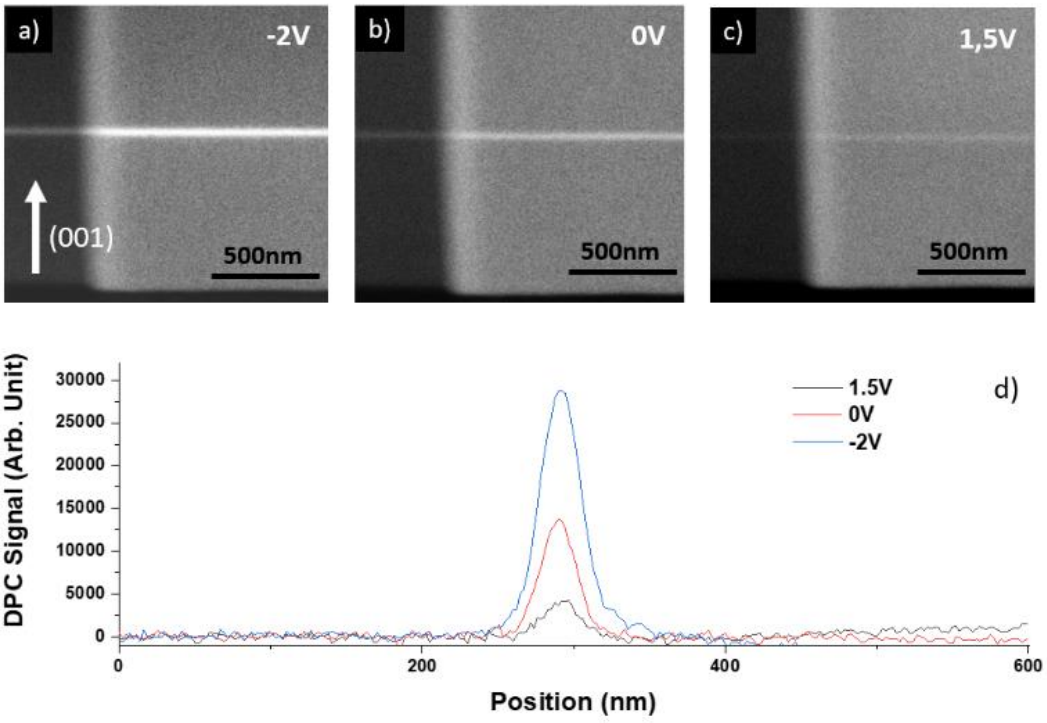

Figure 2-8 : DPC on the silicon pn junction with different biases. a) DPC signal with a reverse bias of 2V. b) DPC signal without bias. c) DPC signal with a forward bias of 1.5V. d) Profiles of the DPC signal taken across the juction for each bias. The results are presented in arbitrary units, the objective is only to show the difference of signal introduce by the bias.

The electrical schematic presented in Figure 2-9 helps understand where the voltage drops. Our first assumption was to neglect the resistance of the substrate and the contact. We know that we have 2V reverse bias and a current of 100 µA going out of our power source. That gives a sample resistance in the range of 10^4 Ω. A rough approximation of the substrate re sistance gives a resistance of $10^5\Omega$. It was calculated for dopant concentration of $10^{15}\ cm^{-3}$, a substrate section of 5µm×400nm and a substrate length of 2µm. So, the junction cannot have a resistance of 10^4 Ω, this resistance is the global resistance of the whole circuit presented in Figure 2-9. This global resistance is smaller than the substrate resistance because in parallel of this resistor there is the equivalent surface resistor. Gallium atoms were implanted at the surface during the FIB preparation, this led to a low surface resistance. So, in the end the junction cannot be considered as the main resistor.

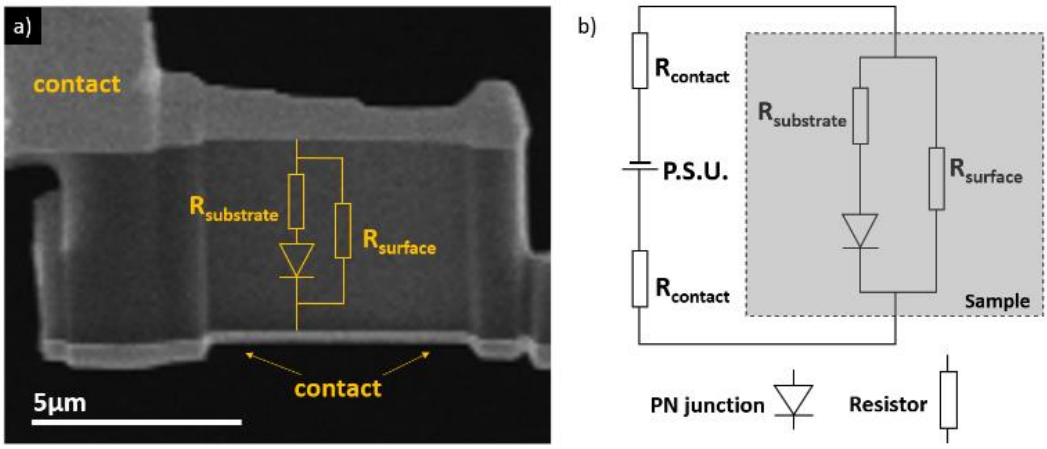

Figure 2-9 : Equivalent electrical circuit of the specimen used for the biasing experiment. a) DF image of the sample with a part of the electrical schematic draw on top. b) Electrical schematic of the whole circuit.

Finally looking back to the DPC signal with 1,5V forward bias we can say that the junction almost disappeared meaning that we are close to apply the 1,09V required to remove the junction. The safest estimation is to say that a third of the voltage drops in circuit and two third in the junction. Meaning that for a reverse bias of 2V the real bias at the junction terminals is about 1.3V. To keep a range of error, we choose to compare the experimental values to both field simulation at 2V and 1V reverse bias.

2.3.2 Field mapping in Nanobeam 4D-STEM

For these experiments, the reverse bias was set at 2.0 V. Using equation 1.26 which makes the link between the deflection angle and the field integrating along the thickness, the deflection was estimated for different camera length. Finally, the camera length was set to 2.05m and the convergence angle set to 1.09mrad. With these values, the transmitted beam fits in the CCD camera and the maximum deflection due to the electric field is estimated to 5.5 pixels when recording 1024x1024 pixel frame. This will be a test to see if the shift will be of 5.5 pixels and if the CoM and TM algorithm can detect the shift.

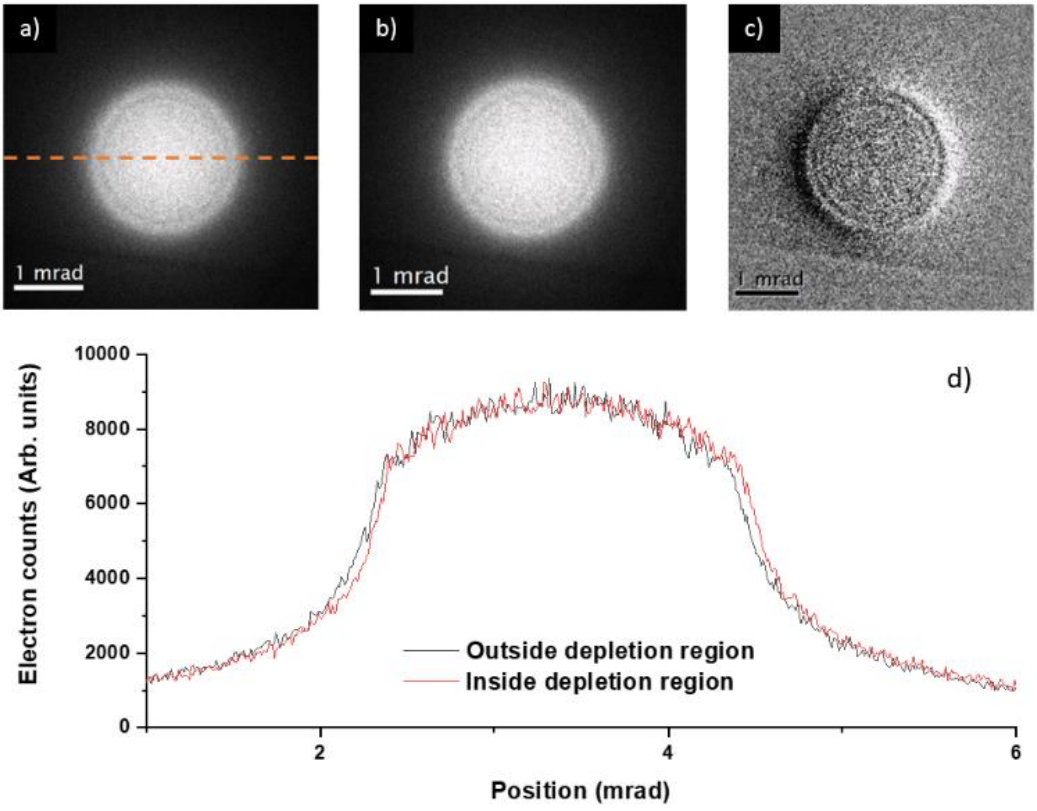

Figure 2-10 : Rigid shift in NB-4D-STEM on a 350 nm thick silicon pn junction sample. The camera length is 2.05 m, the half-convergence angle is 1.09 mrad, the camera resolution is 1024 pix² and the dwell time is 100 ms per diffraction pattern a) and b) shows the transmitted beam recorded far from and inside the depletion region respectively. Meaning that the beam in b) has travel through an area where electric field was present as against the beam in a). c) Subtraction of the beam in (a) to the beam in (b). d) Profile of the electron counts taken across these two beams. The orange dotted line in (a) shows the position where the profiles were taken.

Figure 2-10 summarizes the acquired data. At this orientation, the beam does not have strong dynamical contrast after traveling through the 350 nm thick silicon sample. So, for the 1.09 mrad beam this orientation is a low diffracting orientation. Nevertheless, diffraction effects are present and create a cloud of diffracted electrons around the beam that is why the beam edges are not as sharp as they were in LM-STEM. To achieve such low diffracting orientation a tilt of 1 degree away from zone axis was necessary. This tilt leads to a loss of resolution in projection but as the junction is several tens of nanometer wide, the measurement is still relevant. Later in this manuscript, smaller object will be study and then the loss of resolution will be a matter of importance.

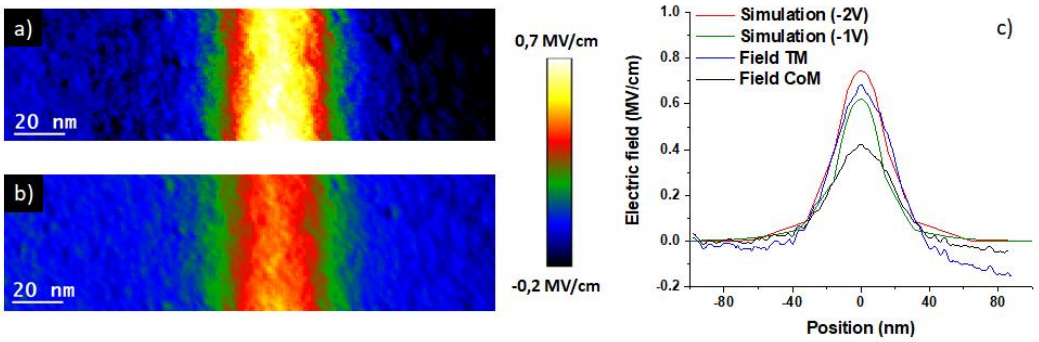

Figure 2-11 : Field mapping of the reverse biased pn junction by 4D-STEM with half-convergence angle of 1.09 mrad. a) Electric field values extracted from the raw data with template matching. b) Electric field values extracted from the raw data with CoM. c) Profiles of the electric field taken across the junction compare to simulation.

The profile depicted in Figure 2-10-(c) shows that the beam undergoes a rigid shift when traveling through depletion region. The shift can be seen by eye on the profile, the red profile is shifted to the right and there is no intensity peak at the edges of the beam. Care was taken, to align as well as possible the de-scan using the pivot points but a small misalignment will always be present in one direction, so the direction of the electric field in the junction was oriented perpendicularly to this direction. This way the shift due to the field is perpendicular to the shift due to de-scan. The camera length of 1m is still a long camera length compare to the typical values chosen for HRSTEM experiments. The problem of using a long camera length is that the microscopes are not really designed for these measurements and it is not easy to align the de-scan. The setting chosen for this experiment leads to a rigid shift of the beam as against the previous experiment done in LM-4D-STEM.

The data sets were processed using two different algorithms. The CoM and the TM algorithms results are depicted in Figure 2-11. The two field maps show that the shift is detected by the two algorithms. By looking at the color scale the electric field extracted by TM is clearly stronger than the one extracted with the CoM algorithm. The profile in Figure 2-11-(c) helps to see the difference and the simulated field profiles are also depicted. The CoM field profile has a maximum of 0,42 MV/cm and the field extracted with template matching has a maximum of 0.68 MV/cm. For both algorithm the results are in the same order of magnitude as expected. The depletion width seems wider than the calculations. This can be explained by the loss in resolution caused by the tilt of the sample. A tilt of 1° on a 350nm thick sample means average of signal over 6nm. The results and the associated SNR are summarized in Table 2-2.

The probe formed by the 1.09mrad half-convergent beam fulfills the requirements for the rigid shift of the beam. This means that the size of the probe is small enough to consider the field constant within it [42]. Regarding the data processing either CoM gives a value of 0.43 ± 0.03 MV/cm and TM give 0.69 ± 0.02 MVcm/cm. These values are close to the expected values. This is hard to assess accurately as the real width of the junction is unknown and not all of the voltage applied to the specimen is across the junction. However, TM seems more precise than CoM in terms of quantitative results in that it falls between the simulations for 1 and 2 V. Therefore, in this condition of acquisition and by processing the data with template matching, the quantitative electric field of the silicon pn junction can be measured.

	TM	**CoM**
Field (MV/cm)	0.69 ± 0.03	0.43 ± 0.02

Table 2-2 : Comparison of electric field extracted by TM and CoM on a NB-4D-STEM data set acquired on a silicon pn junction at 100ms acquisition time. The error was calculated using standard deviation on a 1 µm² area away from the depletion region.

2.3.3 Effect of dynamical diffraction on field mapping by 4D-STEM

The size of the probe is dependent on the convergence angle. In the case of the pn junction, the resolution was good enough with a half-convergence angle of 1.09 mrad. But if the studied system has smaller features the resolution needs to be improved thus the convergence angle must be increased. As the use of a wide convergence angle increases the dynamical

diffraction contrast in the transmitted beam, this contrast will affect the measurement of the beam shift. With silicon, the sample can be tilted to orientation where those diffractions have low impact. TEM is often used to study samples with more complex architectures. Because of the loss of resolution in projection during observation in the TEM, high tilts of the sample will not be possible and even worse in materials such as III-V materials with convergence angle of 1 mrad or more, there is no orientation where the transmitted beam has homogeneous intensity. In this part, the effect of dynamical diffraction contrast will be shown experimentally.

The experimental parameters are the same as previously except for the C2 aperture which was changed from 30 µm to 50 µm. The half-convergence angle in this setup is 3.2 mrad and the sample orientation was changed to a low diffracting orientation. HOLZ lines are still present in the transmitted beam for this value of convergence angle seen in Figure 2-12-(a) (b) and (c), but the shape of the disk is still well defined. A data set was acquired and processed with this condition in order to show the effect of such diffraction influence. Figure 2-12-(a) is a transmitted beam recorded outside depletion region and Figure 2-12-(b) and (c) are transmitted beam recorded inside the depletion region. These three diffraction patterns are taken from positions 1, 2 and 3 which are indicated in Figure 2-12-(f). The profiles depicted in Figure 2-12-(d) show the left edge of the three transmitted beams. From this profile it is clear that the two beams in the junction have been shifted by approximately the same amount. Figure 2-12-(e) shows the same thing; by subtracting the pattern (c) to (b) to show more clearly their difference. In this image, there is almost no contrast due to the edge of the beam meaning again that the beams have been shifted by the same amount. But bright and dark contrasts at the lines position are present, meaning that in the depletion region, from a pattern to the other the HOLZ lines moved. In this case of silicon junction, the movement of the lines is due to the sample bending. The bending leads to distortion of the atomic planes thus diffracting the electron in a different direction compare to perfectly parallel planes. The data was processed using the two different algorithms in order to see how the diffraction contrast influence the beam shift detection. Figure 2-12-(f) and (g) are respectively the field map extracted by TM and the one extracted by CoM. Finally, Figure 2-12-(h) depict profiles of the field taken across the junction from the two field maps. The field maps show relevant results. Firstly, the field map extracted by TM shows unexpected contrast that is independent of the junction. The field in position 2 and 3 should be the same but the color scale indicates a clear difference. As the transmitted beam undergoes the same shift for both positions and only the HOLZ lines move, this shows that the TM is very sensitive to these artefacts. The field map extracted by CoM seems less sensitive to TM on the line movements, but still

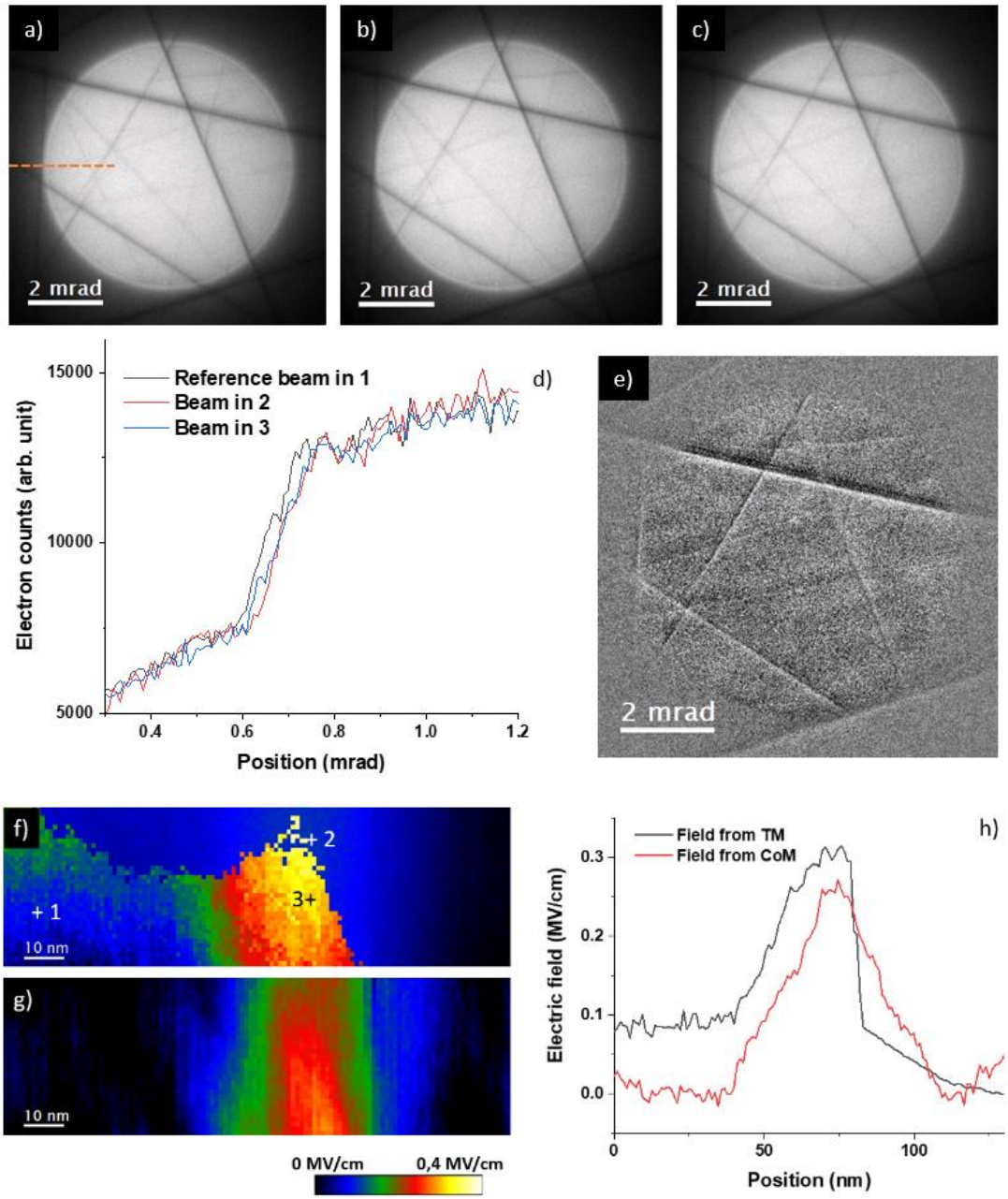

Figure 2-12 : Field mapping of the reverse biased pn junction by NB-4D-STEM in rigid shift condition with dynamical diffraction intentionally present in the transmitted beam. a) Transmitted beam recorded far from the junction (position 1 in map f). b) and c) are transmitted beam recorded inside the depletion region (position 2 and 3 in map f). Meaning that the beam in b) and c) has travel through an area where electric field was present as against the beam in a). d) Profile of the electron counts taken across these three beams. The orange dotted line in (a) shows the position where the profiles were taken. e) Subtraction of beam intensity of b) and c). f) Electric field values extracted from the raw data with TM. g) Electric field values extracted from the raw data with CoM. h) Profiles of the electric field taken across the junction.

for both processing algorithms it is close to 0.3 MV/cm. This value is in the same order of magnitude as the expected value.

2.4 Overcoming the limits imposed by diffraction

It has been shown that the presence of dynamical diffraction can affect the data processing in 4D-STEM. A different strategy can be adopted in order to decrease the dynamical diffraction influence. Either the acquisition parameters need to be different either the processing algorithm has to be improved. We decided to try both. In this part, we will show how energy filtering improves the acquisition, and then we show an improvement of the template matching which uses an artificial template instead of a diffraction pattern presents in the data sets. Finally, we show how orientation average by precession helped us overcome the limits imposed by diffraction during the acquisition.

2.4.1 4D-STEM with energy filtering and improvement of template matching

Energy filtering transmission electron microscopy (EFTEM) is a method that allows selection of the detected electron depending on their energy loss, or removal of the inelastically scattered background from an image. Image contrast and resolution in BF images can be enhanced by using only elastically scattered electrons (zero-loss filtering) [98]–[100]. The objective of using an energy filter for these experiments was to make the beam edges sharper. The experiments were run in a Titan ultimate operating at 200kV acceleration voltage, the half-convergence angle was set to 3.3mrad and camera length was 4m. The sample is the 350 nm thick pn junction with 2V reverse bias. Regarding the energy filtering, the microscope is equipped with a GIF Continuum. The measurements were performed with an energy slit from zero to 10 eV energy loss and without energy filtering. With such energy filtering the electron recorded on the CCD camera are the one that have been elastically scattered. This improves the sharpness of the transmitted beam edges [57]. To test the limits of the 4D-STEM, the orientation was intentionally chosen so diffraction contrasts are present in the 3.3 mrad transmitted beam after travelling the thick silicon sample.

Figure 2-13-(a) and (b) are respectively the transmitted beam recorded with and without filtering. It is clear that the diffuse background of inelastically scattered electrons is removed when filtering. We also try an adapted version of the TM algorithm so that it would follow the movement of the transmitted beam and be less sensitive to the movement of the HOLZ

lines. Here an artificial template is used where a disk of uniform intensity with the same diameter as the transmitted beam. With such template, the algorithm is now only looking for a disk. This TM with disk template will be referred as DTM. Therefore, the measurement should be improved as now we are looking for the movement of a disk that has been sharpened by energy filtering. To see how the filtering improve the data processing the two data sets have been processed with TM and CoM and DTM. The results are presented in Figure 2-13. The six profiles depicted in Figure 2-13-(c) show that whatever the energy filtering and the processing algorithm, the maximum field values found are twice lower than the expectation (between 0.62MV/cm and 0.74MV/cm) but there still in right order of magnitude. Also, the width of the depletion region is consistent with the 70nm we expect. In this orientation the CoM algorithm is sensitive to the line movements and whether or not the beam is filtered, the map in Figure 2-13-(d) and (g) have contrast texture due to diffraction and not to electric field. The noise outside the depletion is the same with and without filtering but the maximum signal detected is greater with filtering, leading to a better SNR (Table 2-3). Then regarding the template matching, Figure 2-13-(e) and (h) are field map from TM algorithm respectively without and with energy filtering. In these two maps the junction is clearly visible and the non-filtered map has noisier background and junction edges. Table 2-3Table 2-3 gives the SNR that also show the influence of energy filtering. The blue/green contrast present in the top right of both TM field maps is here again due to the HOLZ lines movement that is independent of the beam movement. With the DTM processing such lines do not have effect on the field value as it can be seen on the two maps shown in Figure 2-13-(f) and (i) were obtained using the DTM processing. With and without filtering this processing is the best in terms of maximum signal and SNR. Using energy filtering and the DTM allows to increase the SNR by more than a factor three compare to the TM without filtering.

Field (MV/cm)	**TM**	**CoM**	**DTM**
EF	0.58 ± 0.07	0.64 ± 0.09	0.66 ± 0.04
No EF	0.52 ± 0.09	0.44 ± 0.09	0.64 ± 0.04

Table 2-3: Energy filtering influence on the electric field extracted from raw data using CoM, TM and DTM processing.

By removing the diffuse background formed by inelastically scattered electrons, we improved the SNR for every processing algorithm but the difference is small. More importantly, in TM processing the HOLZ lines are still present and the beam movement detection can still be influence by their movement. The lines are due to electrons elastically scattered by specific atomic planes and energy filtering have no influence on Holtz lines. By using an artificial template, the DTM algorithm increase the signal we measure and decrease the noise.

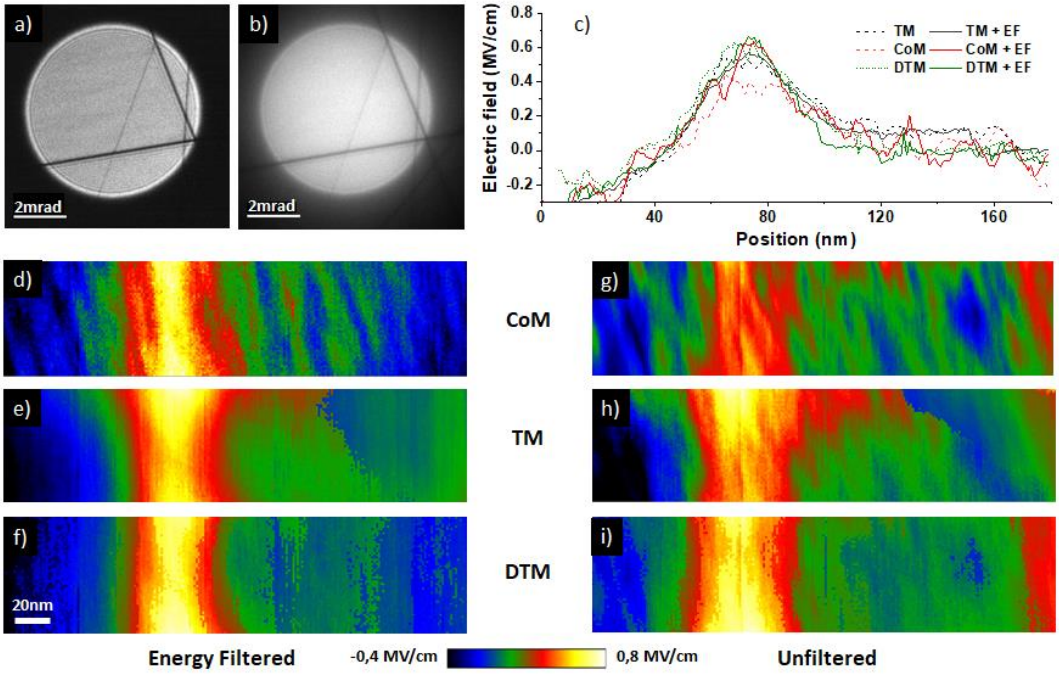

Figure 2-13 : 4D-STEM field mapping with energy filtering. a) and b) are beam respectively from the data set with and without energy filtering. c) is a graph which gather the electric field profiles across the junction for the six different maps d), e) and f) are field map extracted respectively with CoM, TM and DTM from the energy filtered data set. g), h) and i) are field map extracted respectively with CoM, TM and DTM from the unfiltered data set.

2.4.2 Precession to decrease dynamical diffraction

Energy filtering cannot remove the elastically scattered electrons i.e. the HOLZ lines in the transmitted beam. Here, we will use precession in order to average different crystal orientation around the optical axis and thus decrease the Holtz lines contrast. With a homogeneous beam there will be no more need of an artificial template for the TM

processing. Precession is known for the improvement it provides in strain mapping of the measurement of material phases [47]. Such mapping techniques are based on the analysis of diffraction patterns where the distances between the diffracted beams give information about the local lattice spacings. Here only the transmitted beam interests us so precession is used to decrease the dynamical contrast in it [48].

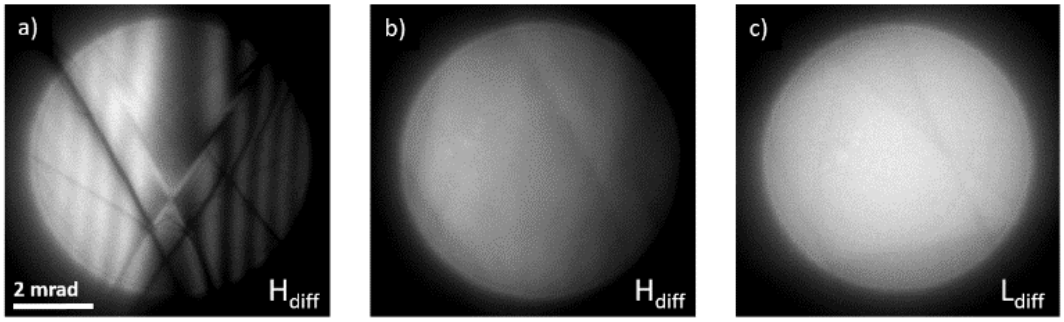

Figure 2-14 : Influence of precession on the transmitted beam reccorded on a CCD camera during NB-4D-STEM acquisition. The junction sample is 390nm thick, the half convergence angle was set to 3.2 mrad. a) Transmitted beam without precession in an orientation where the dynamical diffraction have a high influence. b) Transmitted beam reccorded in the same orientation as a) but this time the electron beam is precessed around the optical axis with a tilt angle of 0.25°. c) Transmitted beam reccorded with precession in an other orientation where the dynamical diffraction have less influence.

The specimen thickness of the pn junction sample studied here was 390 +/- 10 nm. The specimen was also examined under a reverse bias of 2 V in order to increase the signal. Using equation 1.26 which makes the link between the deflection angle and the field integrated along the thickness, the deflection was estimated for different combinations of camera length and convergence angle. The choice was the use of a camera length of 2.05 m and the convergence angle was set to 3.2 mrad. With these parameters, the transmitted beam fits in the CCD camera and the deflection are estimated to 4 pixels when recording 512x512 pixel frame. Three data sets were acquired for this experiment. Figure 2-14 shows a transmitted beam taken from each of the data set. Figure 2-14-(a) and (b) have been taken on the same orientation respectively without and with precession. We will qualify this orientation as a highly diffracting orientation. The precession tilt chosen is 0.1°, the frequency is 5ms-1 and the time of exposure for each acquisition is 100ms. Figure 2-14-(a) and (b) show that the chosen parameters do indeed remove a lot of the dynamical effects from the transmitted

beam. Figure 2-14-(c) shows a transmitted beam acquired with precession with the sample tilted to a low diffracting orientation, and is considered as our reference data set. The choice of the different experimental parameters was done in order to obtain a measurable rigid shift. By comparing Figure 2-15-(a) and (b), it is clear that the beam intensity has not been redistributed. With a convergence angle of 3.2 mrad the probe is again small enough compared to the size of the junction and sees a constant field at each position of the scan. For more clarity, profiles of the beams have been taken and are shown in Figure 2-15-(c). These two profiles show how the transmitted beam is rigidly shifted. The beam image is taken close one to another thereby the de-scan shift can be neglect and the shift is assumed to be only a cause of the electric field in the depletion region. The three data sets have been processed using a CoM and TM algorithms and the results will be discussed here. In Table 2-4 the maximum field values are shown with the error calculated by standard deviation in the region with no electric field. Figure 2-16 summarizes the results obtained after processing. The field values extracted from experimental data are compare to the simulation

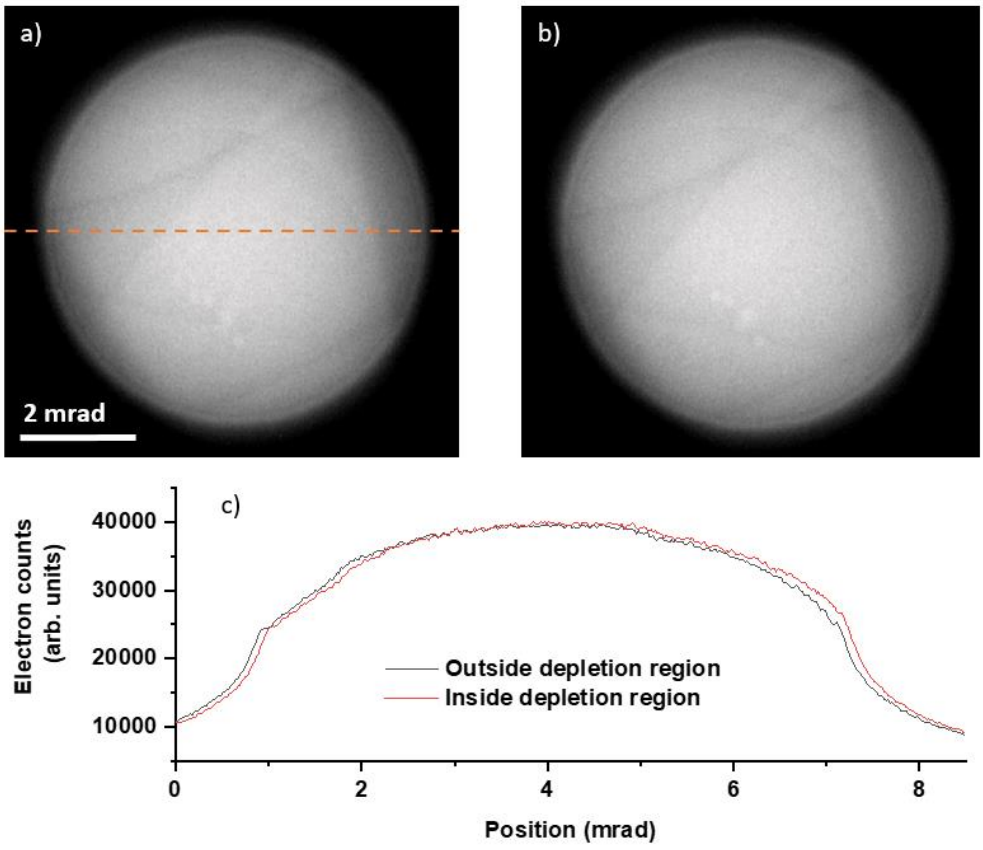

Figure 2-15 : Evidence of rigid shift. a) Image of the transmitted beam Outside of the junction. The red dashed line show where the profile of (c) has been taken. b) Image of the transmitted beam inside the junction. c) Profile of the electron count taken vertically across

previously presented and shown here in Figure 2-16-(g) and (h) respectively with 2V and 1V reverse bias. The simulation suggests an electric field between 0.62 and 0.73 MV/cm and a depletion width of 60±5 nm. Figure 2-16-(a), (b) and (c) have been obtained with the CoM processing. The profiles depicted in Figure 2-16-(i) have been taken across the junction on these three maps and allow to have a better idea of the electric field values obtain on the different data sets. For each data sets processed with CoM, the maximum field value is two times lower than expected but almost constant. Regarding the width of the depletion region, it is also smaller than expected. Still the data set without precession is the noisiest of the three. Then Figure 2-16-(d), (e) and (f) are the electric field map extracted from the three data set with the TM algorithm. Profiles taken across those maps are shown in Figure 2-16-(j). It is clear that the field values obtained with precession are in good agreement with the

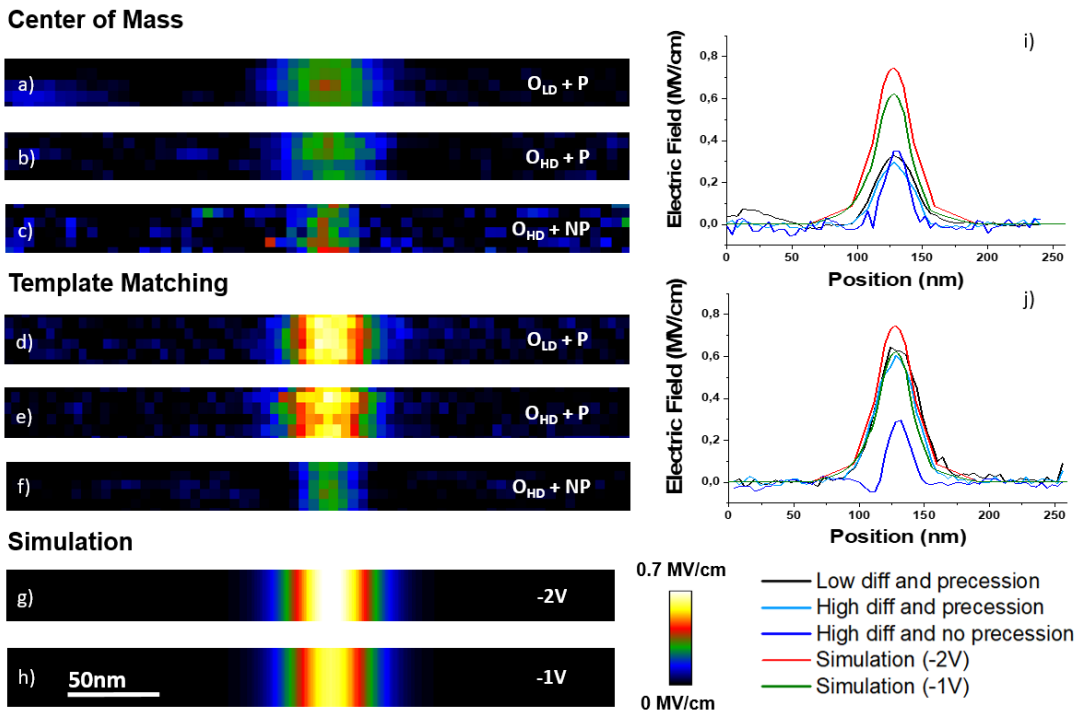

Figure 2-16 : Electric field maps and profiles extracted from 4D-STEM data sets (presented in figure 2.15) using different algotithms. a)–c) are respectively maps from the L_{diff} orientation with precession, H_{diff} orientation with precession and H_{diff} orientation without precession, that have been processed using CoM algorithm. d)–f) show the same data sets that have been calculated using the TM algorithm. g) and h) show simulated map of electrical field with -2 V and -1 V bias. i) Compares simulated field profiles to experimental data processed using CoM. j) Compares simulated field profiles to experimental data processed using TM.

simulation while the data set without precession gives field values far from the expectation. The width of the depletion region is also very close to the width calculated in the simulation. The TM algorithm works well when dynamical diffraction contrasts are limited, either by careful specimen tilting or by the use of precession, as the circumference of the beam can be tracked accurately

Electric field (MV/cm)	**H_{diff} precession**	**H_{diff} no precession**	**L_{diff} precession**
CoM	0.27 ± 0.03	0.34 ± 0.07	0.32 ± 0.02
TM	0.60 ± 0.03	0.29 ± 0.02	0.62 ± 0.04

Table 2-4 : Shows the magnitude of the electric field measured in the silicon p-n junction by CoM and TM algorithms, for both orientations and use or not of precession. The sensitivity has been determined by measuring the standard deviation in the regions that do not contain an electric field.

So, precession improve the field measurement whatever the algorithm used for the processing. The CoM algorithm allows to detect the field in data acquired with precession but the values have been extracted from this experiment are incorrect. The small amounts of dynamical diffraction that are still present in the transmitted been led to inaccuracies in the measurement of the beam shift. The TM algorithm allows quantitative measurement off the field when the dynamical diffraction contrast is not too important. Meaning that the sample is tilted to a low diffraction orientation or meaning that precession is used to decrease diffraction influence.

2.5 Specimen charging

The electric field present in the junction is created by the charges present in the material. The electron beam used to probe the sample will interact with the sample. For holography, the wide plane wave illuminates the sample over a long period and a steady state charging is reached that can be studied. For STEM measurements, the electron beam is scanned over a

rather small area and the beam is blanked between every pixel acquisition. This means that the specimen will dynamically charge. In this section, we show how the beam affect the sample and the measured electric field. The electron dose is the number of electrons that hit the sample by units of time and surface. To increase the electron dose different option are possible. The convergence angle can be increase in order to have a smaller probe with the same current. The C2 aperture can be changed for a bigger one to let more electron flow. We can also change the gun intensity to increase again the electron flow. Maybe the most convenient method is to change the dwell time. This is the option we choose as it allows to change the electron dose without having to re-do alignment in the TEM column. This way we know that the acquisition conditions are exactly the same apart from the dwell time.

The sample studied here is the silicon pn junction in the 350 nm thick area. A reverse bias of 2V was applied. The sample was tilted in an orientation where a 1,09mrad convergent beam has no dynamical contrast. Firstly, DPC was used to assess the changes of signal as a function of the dwell time. The detector used in DPC allows measurement with very short dwell time. Then, for longer dwell time, the 4D-STEM data acquired with the Oneview camera and a state-of-the-art Merlin camera will be processed and compared.

2.5.1 Charging effect in DPC

The study of the electron beam influence on the sample began with DPC. The advantage of DPC is the very short dwell time that can be access with the four-quadrant detector. The speed can be set up to tens of nanosecond. As this is the shorter dwell time accessible for STEM measurement, we hope that the electron dose will not influence the electric field [101].

As we were not interested in quantitative values, for ease, we set the convergence angle to 200 µrad and the camera length to 12 m. The probe current was measured to be from the microscope viewing screen 100pA. Four DPC maps were acquired with different dwell times. The dwell times go from 200ns up to 100µs. The acquisition was performed on the 390 nm thick pn junction with a 2 V reverse bias.

The DPC signal perpendicular to the junction was extracted from the raw data and the results are presented in Figure 2-17. From (a) to (d) the DPC maps are shown. The color scale is in arbitrary units. As the dwell time increase the junction become more and more clear due to

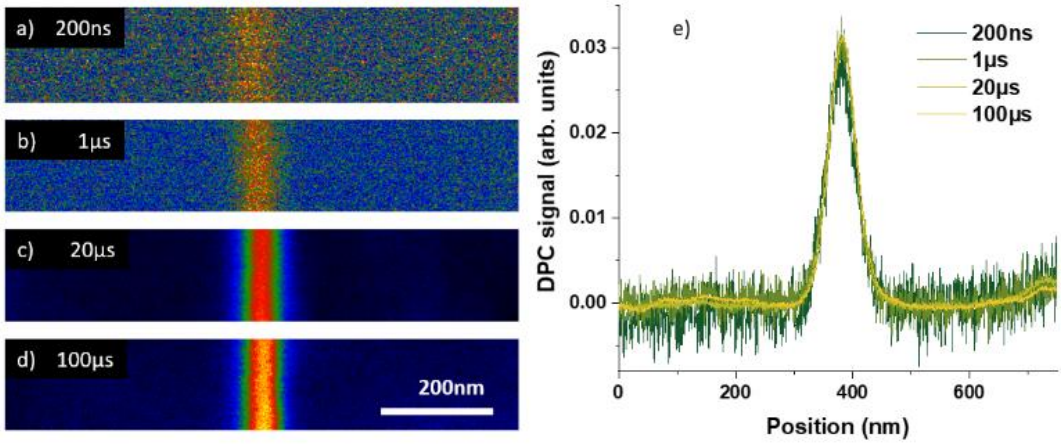

Figure 2-17 : Comparison of DPC signal measured with dwell times from 200ns to 100µs. The measurements were done on the silicon pn junction with 2V reverse bias. a), b), c) and d) are DPC map acquired with different dwell time and presented with the same arbitrary intensity contrast. e) Comparison of profiles average over 50 nm and taken across the junction for the four different dwell times.

the improved signal to noise. To have a better idea of the DPC signal, the profiles shown in Figure 2-17-(e) have been taken across the four maps and average over 500pixels. From these profiles we can say that the maximum signal we measured do not change with the dwell time. So, in this range of dwell time, with a 100 pA current and that probe size of tens of nanometers, the electron beam does not influence the signal measure by DPC. The noise level is high in every map, without the 500 pixels average the junction field would not be visible in the profiles. To have a better idea of the noise, Table 2-5 gather the SNR for the DPC map. The signal was estimated from the average profiles and the noise estimated via standard deviation in a zero-field area.

This DPC experiment allows us to conclude that in the condition of the experiment, the electrons incident on the sample do not influence the measured junction signal [27]. The electron dose received by the sample in this experiment is far smaller than the one received in a NB-4D-STEM acquisition. Indeed, the 200 µrad gives a bigger probe than in NB-STEM and the dwell time is shorter in DPC than in 4D-STEM. For these beam setting, increasing the dwell time from 200 ns up to 100 µs decreases the noise level.

Dwell time	200 ns	1 µs	20 µs	100 µs
Signal (arb. U)	0.03 ± 0.06	0.03 ± 0.04	0.03 ± 0.007	0.03 ± 0.005

Table 2-5 : Comparison of the signal of DPC map for different dwell times.

2.5.2 Charging effect in 4D-STEM

Two cameras were used to test the electron dose influence on the measured electric field in 4D-STEM. The cameras used are a Oneview camera and a Merlin EM. At 512pix² resolution, the Oneview camera can reach 300fps i.e. the acquisition can go as fast as 3ms per point of scan. The Merlin installed in our setup has 256pix² resolution and can record at 1825fps that means 500µs per diffraction pattern. To assess the quality of the data acquired with both cameras, we set the convergence angle to 1.09mrad and the camera length to 2,05m. With these parameters, the beam covers almost the whole Merlin camera. The probe current was set to 100pA. With the One view camera we acquired data with three different dwell times: 500ms, 100ms and 20ms. With the Merlin camera dwell times of 1ms and 10ms were used.

	Merlin		**Oneview**		
Dwell time	**1ms**	**10ms**	**20ms**	**100ms**	**500ms**
Beam intensity	36	71	1708	8695	125665
SNR	15	21	13	26	33

Table 2-6 : Noise level in the diffraction pattern recorded with the Oneview and the Merlin camera using a range of dwell time from 1ms to 500ms

Figure 2-18 shows a diffraction pattern recorded with all the dwell time previously mentioned. From (a) to (c) the patterns are recorded with the Oneview camera. We see that

as the dwell time decrease, the beam becomes less sharp. (d) and (e) were recorded using the Merlin camera with shorter dwell time. To have a better idea of the noise present in this pattern. The Table 2-6 details the noise level in each diffraction pattern. The standard deviation used to calculate the SNR was taken in the blue square in each pattern in Figure 2-18. We can clearly see that the Merlin camera allows to record faster with comparable level of noise. If we compare the SNR at 1ms with the Merlin and at 20ms with the Oneview, the Merlin camera offers a measurement 10 times faster with an equivalent level of noise.

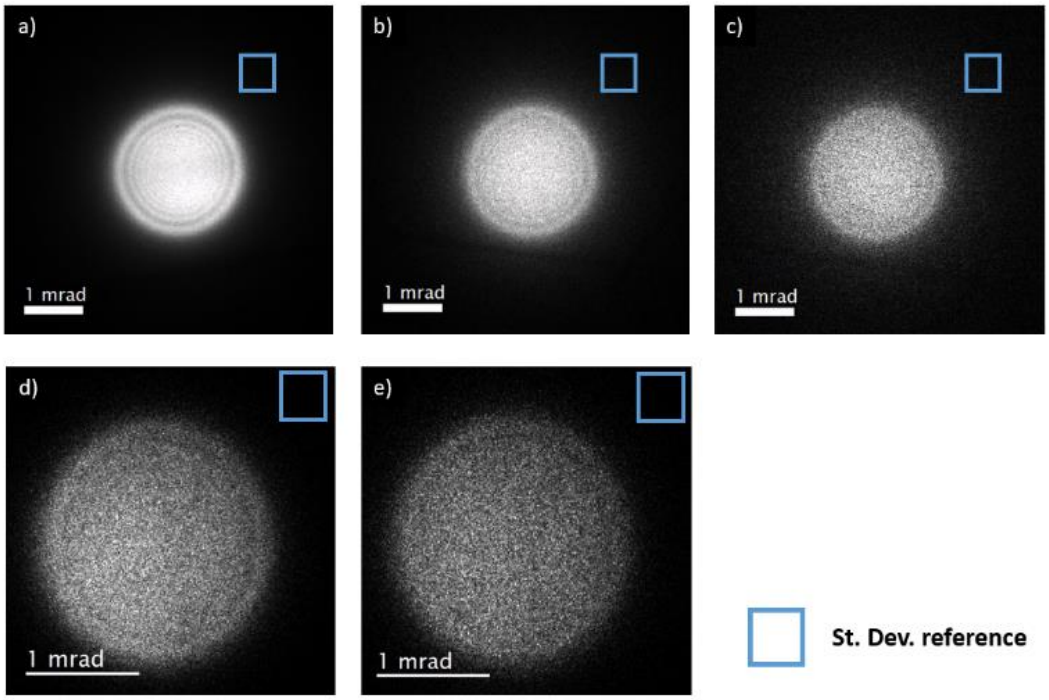

Figure 2-18 : Transmitted beam recorded both with Oneview camera and Merlin camera. a), b) and c) were recorded on the Oneview camera with dwell time of 500ms, 100ms and 20ms respectively. d), e) were recorded on the Merlin camera with dwell time of 10ms and 1ms respectively

Using the Merlin camera allows to record 4D-STEM data with dwell time longer than in DPC but faster that what can be performed with Oneview. Therefore, to test the influence of a higher range of electron dose than in DPC, we performed 4D-STEM on the 390 nm thick pn junction with a 2 V reverse bias using the Merlin camera. The acquisition parameters are a convergence angle of 1.09 mrad and camera length of 2,05 m. Two datasets were acquired with dwell times of 1 ms and 10 ms respectively.

The data were processed using both CoM and TM, the results are presented in Figure 2-19. The field maps are presented from (a) to (d). For more clarity, profiles were taken across the junction and are presented in (e) and (f). The signal detected by TM is slightly higher than

the one detected by CoM, which is coherent with all the previous results. Regarding the electron dose influence, whatever the processing we used, the field that is measured has no significant difference from 1 ms to 10 ms. Only a slight decrease of the noise can be noticed when using the TM processing (see Table 2-7).

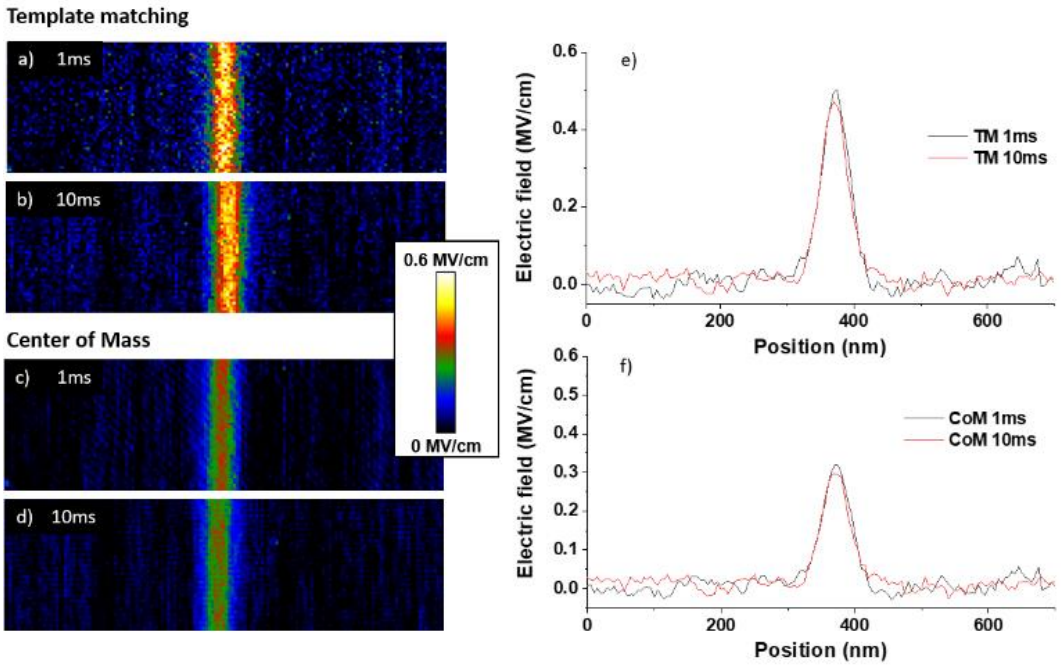

Figure 2-19 : Comparison of 4D-STEM map acquired with dwell time 1ms and 10ms. The measurements were done on the silicon pn junction with 2V reverse bias. a) and b) are field map processed with TM. c) and d) are field map processed with CoM. e) is the comparison of 20pixel wide average profile taken across the TM maps. f) is the comparison of 20pixel wide average profile taken across the CoM maps.

To finish with the study of the electron doses influence on the measured signal, 4D-STEM data set were acquired using the Gatan Oneview camera. With this camera, the influence of the dwell time i.e. the electron dose was experienced in LM-4D-STEM and NB-4D-STEM.

For the LM-4D-STEM experiment, the convergence angle was set to 180 µrad, the camera length to 13.5 m and the beam current to 140 pA. The acquisition was done at recording speed of 20 ms, 100 ms and 500 ms per pixel. The results of these experiments are gathered in Figure 2-20-(a). The fields extracted by CoM from the three LM-4D-STEM data sets have the same maximum value of 0.12 MV/cm. So, the electron dose has no influence on the electric field we measured in this range of dwell time. Only the noise in the field map decreases as the acquisition speed decreases (see Table 2-8).

Merlin	TM		CoM	
Dwell time	**1 ms**	**10ms**	**1 ms**	**10 ms**
Field (MV/cm)	0.50 ± 0.07	0.47 ± 0.04	0.32 ± 0.03	0.30 ± 0.03

Table 2-7 : Comparison of the field values and SNR obtained with TM processing. The data set were acquired with the Merlin and the Oneview camera using a range of dwell time from 1ms to 500ms

For the NB-4D-STEM experiment, the convergence angle was set to 1.1 mrad, the camera length to 3 m and the beam current stays at 140 pA. Again, the acquisition was done at recording speed of 20 ms, 100 ms and 500 ms per pixel. Compare to the LM experiment, the increase of the convergence angle led to a probe six time smaller (equation 1.20). A smaller probe with the same beam current and same dwell times leads to a greater electron dose per units of surface. The results of these experiments are gathered in Figure 2-20-(b). The fields extracted by TM from the three NB-4D-STEM data sets have no significant difference in terms of maximum filed values (see Table 2-8). As for the LM-4D-STEM, only a slight decrease in the noise happened when the acquisition speed decreases.

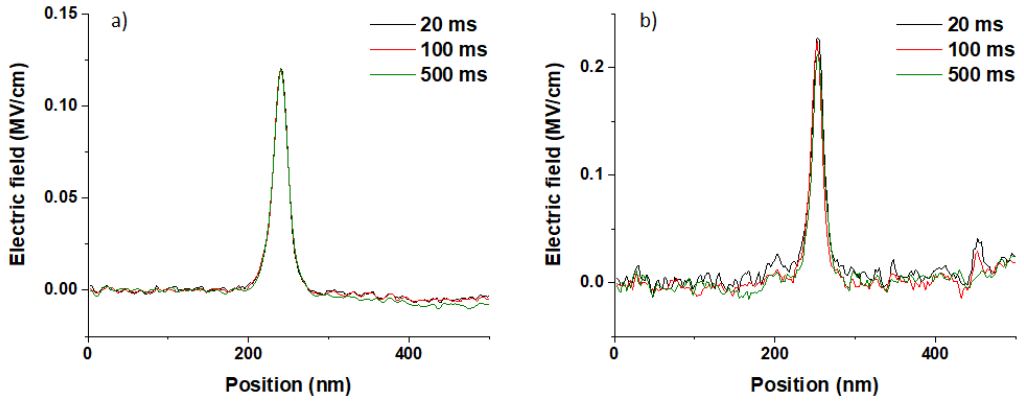

Figure 2-20 : Influence of dwell time in LM-4D-STEM and NB-4D-STEM experiment. The data were acquired with dwell time from 20ms to 500ms. The measurements were done on a silicon pn junction with no bias. Comparison of electric field profiles with different dwell time. a) The data were acquired in LM-4D-STEM and processed using CoM. b) The data were acquired in NB-4D-STEM and processed using TM.

The data acquired using the Merlin camera and the Oneview camera showed that even with a current of 140 pA, a convergence angle of 1.1 mrad and a dwell time up to 500 ms, no significant changes in the measured electric field can be noticed.

These DPC and 4D-STEM experiments allow us to conclude that in the condition of the experiments, the electrons incident on the sample do not influence the electric field we measured on the Silicon pn junction. The parameters used in this section encompass the range of electron doses that the sample received in all the NB-STEM experiments presented in this chapter. Therefore, we believe that none of the results presented in this chapter are influenced by the electron dose.

Oneview	**LM-4D-STEM + CoM**			**NB-4D-STEM + TM**		
Dwell time	**20 ms**	**100 ms**	**500 ms**	**20 ms**	**100 ms**	**500 ms**
Field (MV/cm)	0.12 ± 0.003	0.12 ± 0.001	0.12 ± 0.001	0.23 ± 0.03	0.22 ± 0.03	0.21 ± 0.01

Table 2-8 : Comparison of the field values and SNR obtained with CoM processing. The data set were acquired with the Merlin and the Oneview camera using a range of dwell time from 1ms to 500ms

2.6 Conclusion and discussion

In this chapter, we used a simple pn junction to test various improvements in methodology. The measurements done in LM-STEM mode are proof that the mode cannot be used for quantitative field mapping when using the Titan Ultimate. The best accessible resolution in this mode does not provide a probe small enough to obtained a rigid shift of the transmitted beam. Yet, the sample chosen was a silicon pn junction which is the easiest to study. The depletion region is wide and the sample can be tilted to avoid dynamical diffraction. Nevertheless, LM-4D-STEM can be used to detect the presence of field but not quantitatively. For such measurement DPC or holography are more convenient.

Then it was shown that in NB-STEM mode, field measurement can be achieved and the results seems quantitative. To achieve this a silicon *p–n* junction at a reverse bias of 2 V has been observed by NB-4D-STEM. This measurement was done with different convergence angle in low diffracting orientation in order to show the effect of dynamical diffraction influence the beam shift detection.

Energy filtering was tested in a low diffracting condition but its effectiveness was clearly limited as it has no influence on the diffraction contrast inside the beam. Energy filtering only removes the diffuse background. To demonstrate how precession can reduce the dynamical diffraction, the field was measured with the specimen in a high and low diffracting orientation with a precession angle of 0.1°. Visual inspection of the diffraction patterns shows that a rigid shift occurs when the transmitted beam passes through a region of the specimen containing an electric field. Quantitative measurement of the electric field using a CoM algorithm leads to values that are much less than expected from theory. However, a TM algorithm leads to higher accuracy of the measurements due to the suppression of the influence of dynamical diffraction. Although the specimens examined here have been silicon semiconductor devices, these methods will be particularly useful for the measurement of piezoelectric fields in III–V devices, where dynamical diffraction strongly appears at the interfaces where lattice plane bending can occur.

The last study done in this chapter was regarding the influence of the electron dose on the measured field. Using three different detectors i.e. different ranges of dwell time, we scan the pn junction to see if the signal was influence by the electron dose. In DPC we combined short dwell time (four-quadrant detector) and wide probe (LM mode) leading to very low electron dose. In this condition, the signal was not influenced by the electron beam. In 4D-STEM we used a Oneview camera and a state-of-the-art direct detector (Merlin camera). With these two detectors we showed that in the typical range of dwell time (1 ms - 500 ms) we used for 4D-STEM the signal does not change depending on the dwell time. The results presented in this chapter are not influenced by the electron dose.

3 Influence of interfaces in STEM measurement

The silicon pn junction studied in the previous chapter was extremely simple to analyse. It was homogeneous and the doping introduced a few defects in the lattice that could be neglected. As it was easy to reduce the dynamical diffraction is could almost be considered as a "pure electric field" specimen. However, for real characterization of real samples, the 4D-STEM technique needs to be adapted to more complex samples that contain interfaces.

In our case two interfaces have been studied: SiO_2/Si and Si/SiGe. In the first interface, the SiO_2 is an amorphous oxide and the Si is crystalline. Such change in composition means that it is possible to see if the tails of the electron beam lead to artefacts due to the interface. For the Si/SiGe interface, both sides are crystalline. The strain induced by the epitaxial conditions have an influence on the diffraction pattern. Plus, as the materials are different, the MIP changes from one side to another and this will lead to artefacts.

In this chapter, we will make 4D-STEM measurements on two samples containing an interface in order to show how the results are affected. Firstly, we will study an interface between crystalline Si and SiO_2 layer. This sample will allow us to show the effects of the probe shape influence. Then we will study layers of SiGe grown on a Si substrate. On this sample we begin by using different techniques in order to measure the Germanium concentration quantitatively and compare the results to SIMS. Finally, field measurement and simulation of 4D-STEM are presented in the last part. This sample will help us understand the influence of the mean inner potential at the interface and especially this will emphasize the limits of the NB mode for 4D-STEM field measurement. We tried to overcome the limitation of the NB mode by using a high-resolution mode in 4D-STEM (HR-STEM).

3.1 Study of an SiO2/Si interface

The silicon/silicon-oxide interface is widely used as gate material in complementary metal-oxide semiconductor (CMOS) transistor. The interfaces can also be used to generate strain in n-type devices leading in carrier mobility increase. Nevertheless, here we will study artefacts arising from the amorphous/crystalline interface. In the crystalline structure, the periodicity of the atom's arrangement leads to a diffraction pattern such as that shown in Figure 3-1-(a) shows a diffraction pattern. For an amorphous structure, as no periodicity is present there will not be diffracted spot only a diffuse cloud of electrons randomly deviated. This is shown in Figure 3-1-(b). By changing the contrast of Figure 3-1-(b) it is possible to obtain Figure 3-1-(c) where concentric disks appear. Those disks are due to the distances

between the atoms in the SiO_2 molecules. The Si/SiO_2 interface has been studied by 4D-STEM and compared to simulations to understand how the diffraction pattern can be influence at the vicinity of an interface. Some parameters change from the experimental data to the simulated one. Both have been done at different time for different purpose and more time would have been necessary to change the parameters of one or the other.

3.1.1 Experimental 4D-STEM acquisition

Here the result of a 4D-STEM acquisition is presented. The data set was acquired in NB-STEM mode on a FEI Titan Themis with a convergence angle of 3.2 mrad and a camera length of 2 m. The sample thickness was measured to 70 nm and it is observed down the [110] axis. The diffraction pattern obtained are shown in Figure 3-2. These diffraction patterns are numbered from 1 to 9. The number 1 has been taken in the silicon, then the 2 and 3 have been taken very close to the interface (depicted as the red dotted curve) respectively in the silicon and in the oxide. Then all the other were taken every nanometer as the scan was moving away from the interface. In the BF image the inset is the probe intensity recorded on a CCD camera. After calibration the FWHM of the probe was measured to be 1 nm leading to the choice of a 1 nm step size between the different point of scan.

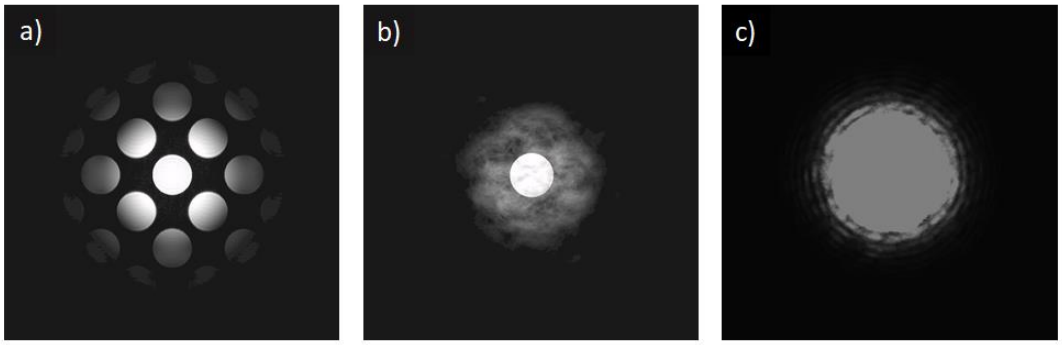

Figure 3-1 : Diffraction pattern comparison between crystalline Si and amorphous SiO_2. Each one has been simulated using µSTEM software with a convergent beam of 5.1mrad half-convergence angle and 20nm thick sample. a) Crystalline Silicon diffraction pattern observed down the (100) axis. b) Silicon oxide diffraction pattern. c) Silicon oxide diffraction pattern where the contrast is saturated at the centre of the pattern such that the SiO_2 disks can be observed.

From this data set, two phenomena can be emphasized. The first one is the behavior of the beams and more especially of the transmitted on at the interface (see Figure 3-2, pattern 2 and 3). The transmitted beam has very bright contrast at its edges. This is because the probe

is not infinitely small and so half of it is going through silicon and the second half is going through the silicon oxide. This complex behavior of the transmitted beam is due to the difference of properties between the two materials and notably the difference of mean inner potential (MIP). This is a case of redistribution of intensity caused by the abrupt change in the MIP. This will be detail later in the SiGe section of this chapter.

A second important observation is the effect of the probe tail. Earlier in this manuscript, the shape of the probe has been described in details. The real shape of the probe is well approximated by using an Airy curve. Such curve has a central peak and small oscillations decreasing exponentially. But only 84% of the intensity is contained in the central peak [42]. The 16% left have an influence and this experiment clearly show that. In Figure 3-2 the patterns 4,5,6 and 7 are in the oxide so there should not be any diffracted beams but we can see the edges of the diffracted beams. For more visibility, a zoom of the pattern 7 is shown with another color range. With those data the effect of the tail probe is noticeable 4 nm away from the interface.

So according to this experiment considering the probe to be only 1nm wide is misleading and the effect of the probe tails cannot be neglected. To be sure of that this effect was not a consequence of a bad microscope alignment, simulations were run to see if such effect were visible.

3.1.2 Diffraction pattern simulated at the vicinity of the interface

The experimental data showed that 4 nm deep in the amorphous layer, the crystalline region still has some influence on the diffraction pattern. In order to assess if it was real or just a problem of microscope alignment, diffraction patterns were simulated on a numerically built Si/SiO_2 structure. The first difference is the orientation through which the interface is observed. In the experiment the electron beam goes down the [110] axis but for simulation we have to observed the structure down the [100] axis. The orientation is different but the interface is parallel to the electron beam direction. As the orientation differs, the diffraction patterns differ and that allow a bigger convergence angle for the simulation without beam overlapping in the pattern. Therefore, a convergence angle of 5.1 mrad was used. A wider convergence angle leads to a smaller probe. That means if the same effect is noticeable with a smaller probe, it will be even more important with a bigger probe. And finally, the sample thickness was set to 20 nm thereby the time required for the simulation was shorter than if the real thickness was set. Although the simulation and experimental parameter are not the same, the choices made the regarding the simulation parameters create a case closer to a

textbook case. This means that if in the simulation the probe tail effect is visible, then it is completely reasonable to see such effect in the experimental data.

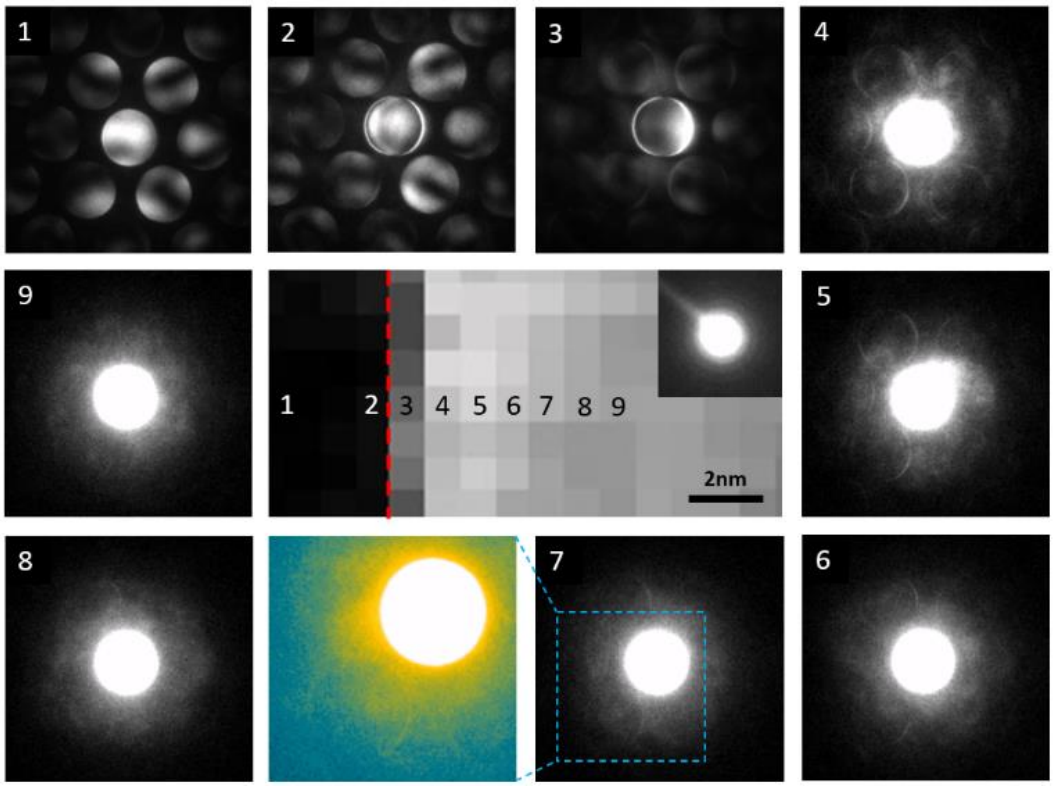

Figure 3-2: Experimental NB-4D-STEM data acquired on a Si/SiO_2 interface down the (110) axis. In the center a BF image of the interface is depicted with the electron probe as an inset and the number correspond to the position the diffraction patterns were recorded.

In Figure 3-3 the results of the simulation are shown. The BF image in the center has the probe as an inset. The measured FWHM of the probe is 1.5Å, which is ten times smaller than the experimental probe. It is because no aberration is included in the simulation parameters. The position of the interface is represented by the red dotted curve and the numbers correspond to the position where the pattern was acquired. Nine diffraction patterns are shown. The number 1 was taken in the crystalline silicon. Then the number 2 and 3 have been taken on each side of the junction and the six last were taken in the oxide with 1nm step between every pattern. A zoom and a change in color scale was done on the pattern number 9 for more clearness.

Here again, the two different effects discussed on the experimental data are present in the simulation. In the pattern 2 and 3, the huge change in the transmitted beam intensity is

noticeable even though the probe is very small. The simulation confirms that this effect is also present in the diffracted beam. The edges are brighter than the rest of the beams. That means that the probe may be small, close to the interface the probe overlaps the two side of the interface that creating this intensity redistribution. The effect is the same but the pattern was taken closer to the interface. Indeed, the sampling was done every 2Å as against the experiment where the sampling was done every nanometer. So, the smaller the probe is the closer to the interface the pattern has to be in order to see the redistribution of intensity.

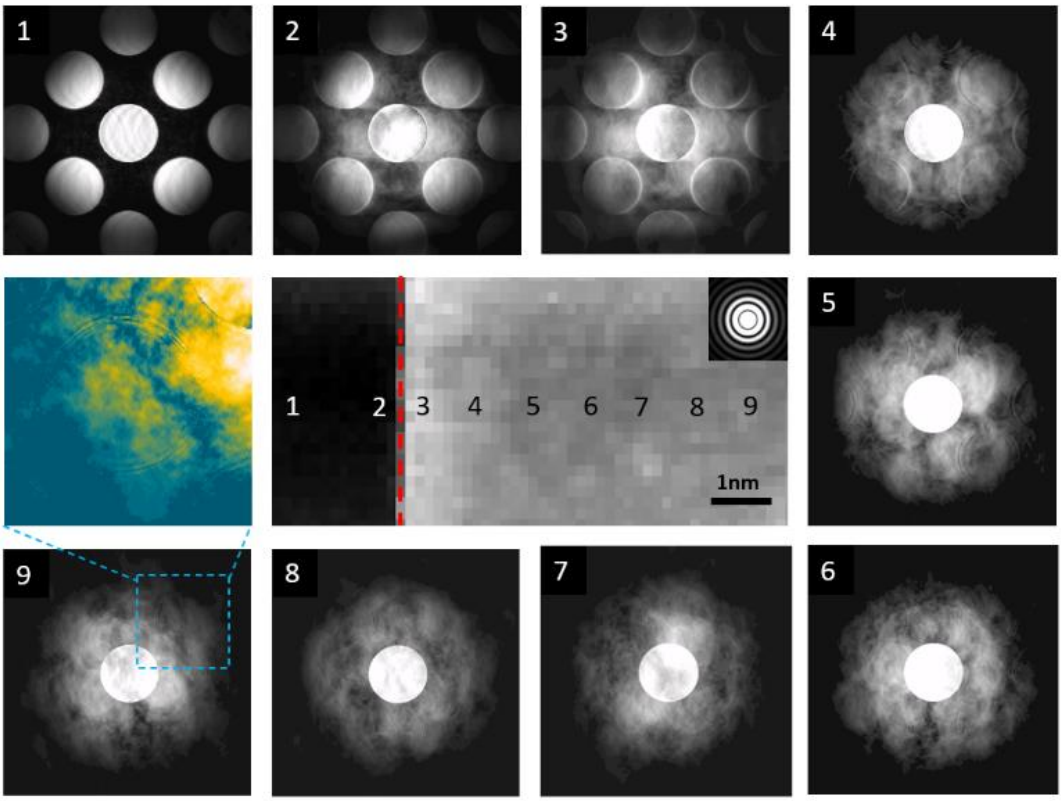

Figure 3-3: Simulated NB-4D-STEM data on a Si/SiO2 interface down the (100) axis. In the center a BF image of the interface is depicted with the electron probe as an inset and the number correspond to the position where the diffraction patterns were recorded.

Then the pattern number 4 to 9 contains the edges of the diffracted beams due to the probe tail still present in the crystalline side. The edges of the diffracted beams can be seen up to 6nm (pattern number 9 and the zoomed in pattern) away from the interface. The effect is small and the contrast had to be change in order to clearly see the edges.

3.1.3 Discussion on the Si/SiO_2 interface

In this section a 4D-STEM results from experiment and a simulation both done on a Si/SiO_2 structure have been shown and explained. The probe size was 1nm with 1nm step for sampling and 1.5Å with 2Å for the sampling respectively for the experiment and the simulation.

In both case the probe has a finite size, so close to the interface, the probe goes through both sides of the interface leading to a complicated redistribution of intensity. With a smaller probe such effect has a shorter range. Furthermore, the edges of diffracted beams are visible 4 and 6 nm away from the crystalline side in the experiment and the simulation respectively. In the case of the simulation, the central Airy disk is 1.5Å and the interface is less than 5Å wide but artefacts are present several nanometers away from the junction. In the imaginary case of an infinitely small probe and a finite sampling such effect will not be present. The probe would go from one side to another without being in both side at the same times. This study shows that in presence of a sharp interface, the probe cannot be reduced to the central Airy disk.

3.2 Ge concentration measurement in SiGe

In this section the sample that is studied is shown in Figure 3-4. This sample is composed of four 10 ± 1nm wide layers of SiGe separate from each other by 30 nm wide silicon barrier. The sample was grown by reduced pressure chemical vapor deposition (RPCVD) on [001] Si substrate. A FIB dual beam operated at 16 kV was used to obtain the 120nm thick parallel-sided TEM lamella. This lamella was extracted from the same wafer as the lamella study by Cooper & al [102] and by A. Béché & al [103]. The sample was designed to have layers with germanium concentration of 10, 20, 30 and 40%. The SIMS profile in Figure 3-4-(d) comes from this last study.

This SiGe sample was chosen for several reason. Firstly, previous study was already done on the same bulk sample so it is well known regarding composition and numerical estimation of strain. The crystal quality of the sample is very high so a tilt of a few degrees around the growth axis allows an orientation where dynamical diffraction can be limited. Figure 3-4-(e) and (f) show respectively, the diffraction pattern obtained in the silicon down the [001] axis and the diffraction pattern obtained after tilting 7° away from this axis. The layers (and the barrier) are quite wide compared to the electron beam, the width of the layer can be seen in

Figure 3-4-(b) and (c). Finally, the main property that motivates this sample choice is the difference of MIP between Si and Ge. Experimental MIP values of Silicon and Germanium can be found in literature [6], [104]–[107]. In this study the reference MIP value of Si and Ge chosen are 12.6 V and 14.7 V respectively which come from the density functional theory (DFT) simulations of P. Kruse and colleagues [108]. However, here we do not compute the measured values of MIP relative to vacuum, but the relative differences between the different layers.

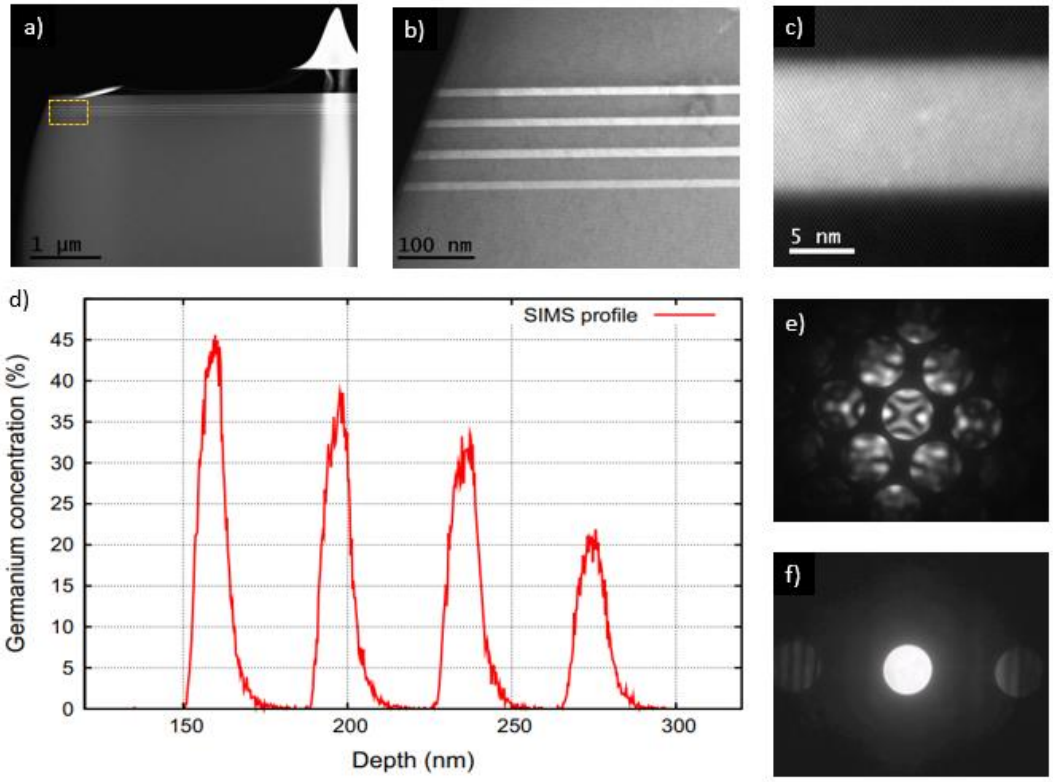

Figure 3-4 : Si/SiGe sample composed of four layers of SiGe grown on a Si substrate. a) STEM HAADF image of the sample the yellow doted square represent the ROI depicted in (b). b) STEM HAADF image of the region of interest with higher magnification. c) HAADF image of the SiGe layer magnified 2.5 million times d) SIMS profile of the Germanium concentration across the layers. e) and d) diffraction pattern record with 3.5mard convergence angle respectively down the (110) axis and in a low diffracting orientation

The SIMS profiles presented in Figure 3-4-(d) gives us Ge concentrations of 20, 31, 38 and 45% in the layers [103]. The SIMS provides quantitative Ge concentration in the growth (or rather depth) direction, but the lateral resolution of this technique of around 100 nm in very modern instruments makes it only suitable for the measurement of 1D samples. Regarding

the width of the layers, the SIMS profiles presents layers with a width close to 15nm instead of the 10nm expected. Also, for each layer, on the right side a "tail" of germanium is present. This is due to the edges of the SIMS crater which leads to a reduction in spatial resolution. The germanium concentration will be measured using HAADF, holography and NB-4D-STEM coupled with precession and compared to the SIMS values which will be our reference.

3.2.1 Quantitative HAADF for Ge concentration and electric field estimation

The SIMS gives the concentration of germanium in the layers from top to bottom 45, 38, 31 and 20%. The SiGe MIP can be calculating using a linear dependence on the germanium concentration [109]. In order to have the highest spatially resolved profile of potential we used quantitative HAADF STEM where the Ge concentration in the different layers has been determined from the Z-contrast intensity. HAADF STEM was performed on the SiGe layers down the [001] zone axis using 20 mrad convergence angle. With these parameters, the atomic columns are visible (see Figure 3-4-c). From these HAADF experimental data, quantitative concentration of germanium can be extracted.

To obtain quantitative HAADF different methods are possible. The first one is the kinematic model. In this model, every electron is only scattered once, so the number of electrons is proportional to the number of atoms along their propagation direction. In this regard, the intensity at each point can be viewed as a linear addition of the contribution from each atom. The equivalent equation is:

$$I_{image} = \sum_{i} I_{atom}(i) \tag{3.1}$$

Where $I_{atom}(i)$ can by express as:

$$I_{atom}(i) = Z^n \exp\left(-\frac{d_i^2}{2c_g^2}\right) \tag{3.2}$$

Where Z is the atomic number of the ith atom, n is power exponent dependant on the collection angle, n is usually between 1,5 and 1,8. c_g is the Gaussian factor and d_i is the distance between the ith atom and the position concerned in the image [110], [111].

The second way to quantify HAADF is to use multi-slices simulation and compare the normalized intensity [112]–[114]. To begin with, the thickness has to be measured. The SiGe sample thickness was determined to be 120±10nm. Knowing the thickness, the simulated intensity must be compared to experimental intensity in order to determine the germanium concentration. As we have access to multi-slices simulation and the thickness measurement is well known, we decided to use this second method to quantify the HAADF. So, the intensity was firstly average in a Voronoi polygon around each atomic column in the HAADF images then the intensities of both experimental and simulated HAADF were normalized using:

$$I_{norm} = \frac{I_{raw} - I_{vac}}{I_{det} - I_{vac}} \tag{3.3}$$

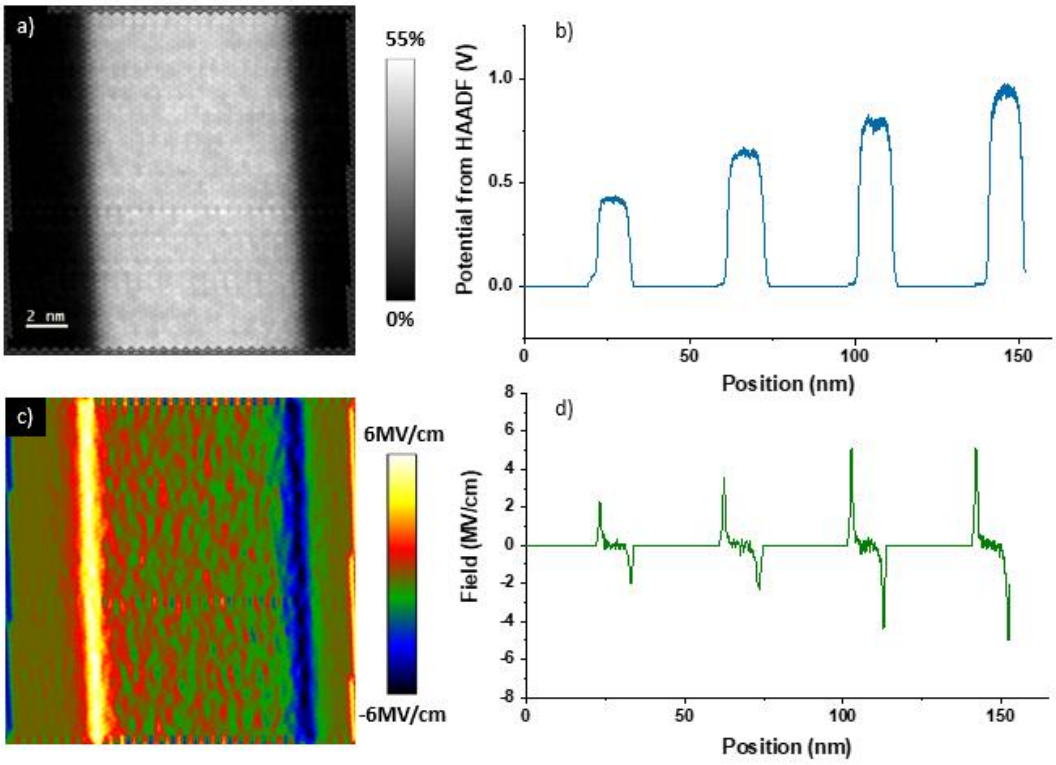

Figure 3-5 : Electric field calculation at Si/SiGe interfaces from quantitative HAADF. a) Quantitative HAADF of the $Si_{55}Ge_{45}$ layer, with intensity proportional to Ge concentration. b) Potential profile across the four layers with a zero-level set to the silicon MIP. c) Field map at the vicinity of the $Si_{55}Ge_{45}$ layers obtained from the quantitative HAADF. d) Electric field derived profile across the four layers derived from the potential in b) with equation 1.1.

Where I_{raw} is the raw image intensity, I_{vac} is the mean vacuum intensity and I_{det} is the mean intensity on the detector. Then HAADF images can be quantified and from HAADF the concentration in the layer were estimated to 21.2%, 30.9%, 36.4% and 45.1%. Figure 3-5-(a) shows the quantitative concentration HAADF image of the layer estimated having 45.1% germanium. The SiGe MIP was calculating using a linear dependence on the germanium concentration. The profile in Figure 3-5-(b) is a profile of the quantitative potential from HAADF across the four layers where the zero level is the silicon MIP. This is the most highly spatially resolved potential profile we can access. The quality of the interface will have a huge influence on the electric field as it depends on the potential derivative i.e. interface sharpness. Figure 3-5-(c) and (d) show respectively the field values of the layer with 45% of germanium and the profile of field across the four layers of SiGe.

The field values obtained here will be our benchmark of field due to the MIP difference of Si and SiGe. The field create by the layer $Si_{0.8}Ge_{0.2}$ is ±2MV/cm and the field created by the layer $Si_{0.55}Ge_{0.45}$ is ±5MV/cm. From the field profile, the width of the interface i.e. the distance where an electric field is present was estimated to 3nm.

3.2.2 Off axis electron holography on SiGe layers

Electron holography allows direct measurement of the electrostatic potential of the sample. From the potential the Germanium concentration and the electric field can be deduced. The holography experiment was performed using the FEI Titan Ultimate at 200kV. As for the previous experiments, a slight tilt of the sample from the [001] axis to avoid dynamical diffraction. To increase the SNR ratio of the acquisition, a series of 16 holograms was taken with 8s of dwell time for each. This way, long cumulative exposure times can be achieved while limiting the effect of drift of the sample as a post-acquisition alignment can be done during the hologram reconstruction. The biprism voltage was set to 250kV leading to a fringe spacing of 1.3nm. Then the combination of a 63kx magnification in Lorentz mode and the use of a 4096pix camera led to 10 pixels per fringes thus reducing information losses.

Then using the reconstruction algorithm presented earlier and a mask radius of 2.6 nm^{-1}, the phase has been reconstructed and it is shown in Figure 3-6-(a). The layers are well resolved in the phase map so the parameters chosen are relevant. Then to convert the phase into an electrostatic potential we need to divide the phase by the interaction constant multiply by the thickness. The interaction constant depends on the acceleration voltage, at 200kV acceleration voltage $C_E = 7.29\,x\,10^{-3} radV^{-1}nm^{-1}$. The electrostatic potential map measured with holography is shown in Figure 3-6-(b). The profiles shown in Figure 3-6-(c)

has been taken across the SiGe layers and is compare to the MIP estimated from quantitative HAADF. The potential found by holography seems very close to the expectation. Indeed, there is an increase of the potential step as we go from the left layer to the right one. The maximum values are in the right order of magnitude. Using the potential in the layers with 20% Ge, a standard deviation in a region with no field, the SNR was estimated to 5 in the potential map. The profile is average over several hundred of pixel thus reducing the noise. So, regarding the potential mapping this holography experiment gives accurate values. Using a linear dependence on the germanium concentration and the average values of MIP in the layers the germanium concentration can be calculated [19]. The concentrations are gathered in Table 3-1.

Electric field is the gradient of the electrostatic potential, so only a derivation is necessary to obtain the field. The potential was derived in both directions to obtained the electric field perpendicular and parallel to the layers. Those two components of the field are respectively shown in Figure 3-7-(a) and (b). For a better reading of the field value, the profile in Figure 3-7-(c) has been taken across the layer in (a).

The first comment that can be made is the fact that the field is zero parallel to the layers. However, perpendicular to the layers there is positive peaks and negative peaks on the sides of the layers which is coherent to the field that a step-in potential creates. The profile shows an increase in the absolute field value as the concentration of Germanium increase. Regarding the values of field there are in the same order of magnitude as the field estimated from HAADF. The width of the field peaks is wider than the peaks obtained from HAADF because the resolution of the holography experiment is not as good as the resolution of HAADF.

As holography is sensitive to the phase change of the electron plane wave, this technique allows accurate measurement of the potential, which can afterward be derived to obtain the electric field. The field values are very sensitive to the spatial resolution of the holography measurement. The layers are 10nm wide so the holography resolution is good enough to obtain potential values in agreement with the estimation based on the highly spatially resolved HAADF STEM measurements.

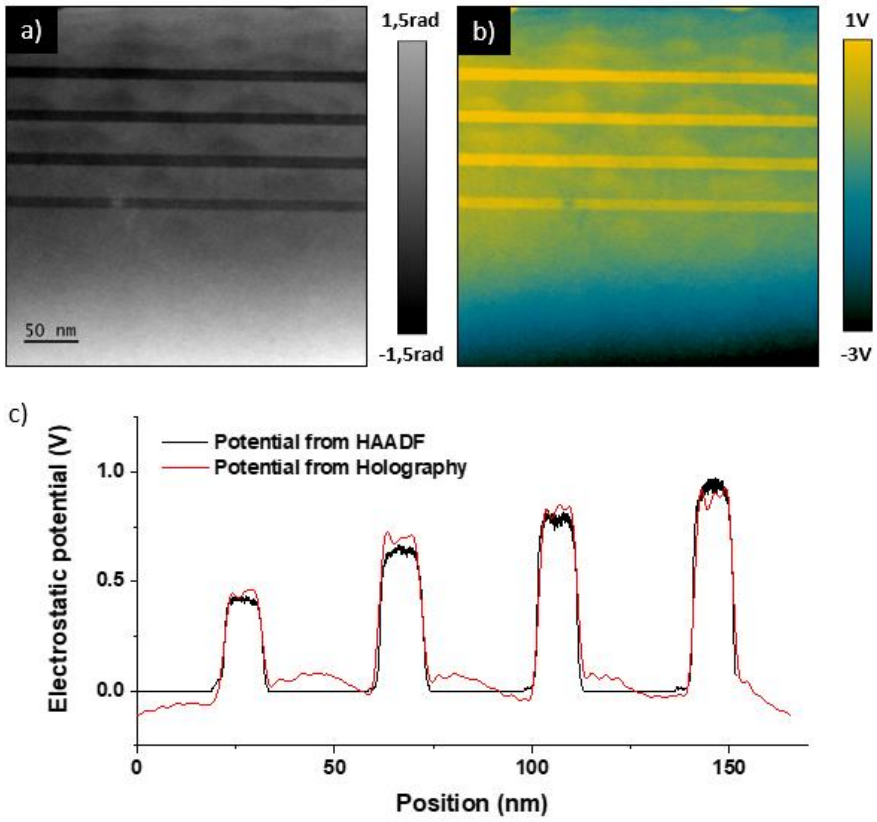

Figure 3-6 : Electrostatic potential measured by holography on the SiGe layers. a) Reconstructed phase of the electron plane wave after traveling through the sample. b) Electrostatic potential calculated from the phase map. c) Profile of the potential taken across the layers and compared to the MIP step estimated with HAADF.

3.2.3 Strain measurement in SiGe with NB-4D-STEM

The change in lattice parameter between the different layers can also be measured by 4D-STEM. At CEA strain maps have been acquired by precession diffraction for more than 10 years which was an early form of 4D-STEM. The SiGe layers were grown by epitaxy on a silicon substrate. Such process leads to lattice match in the in-plane (x) direction (see section 1.4.1). In the growth (y) direction the SiGe lattice is expanded. This tensile expansion depends on the germanium concentration. Here the Ge concentration is deduced from precession electron diffraction (PED) and compared to the values found with other techniques.

For this experiment we choose a camera length of 420 mm coupled with a convergence angle of 3.2 mrad. The measurement is done with the specimen on axis looking down the [110] axis. We used precession in order to illuminate homogeneously transmitted and diffracted beams. For the precession, an angle of 0.25° was chosen. With those parameters the resolution is not deteriorated and homogeneous intensity is present in the 1st and 2nd order diffracted beams.

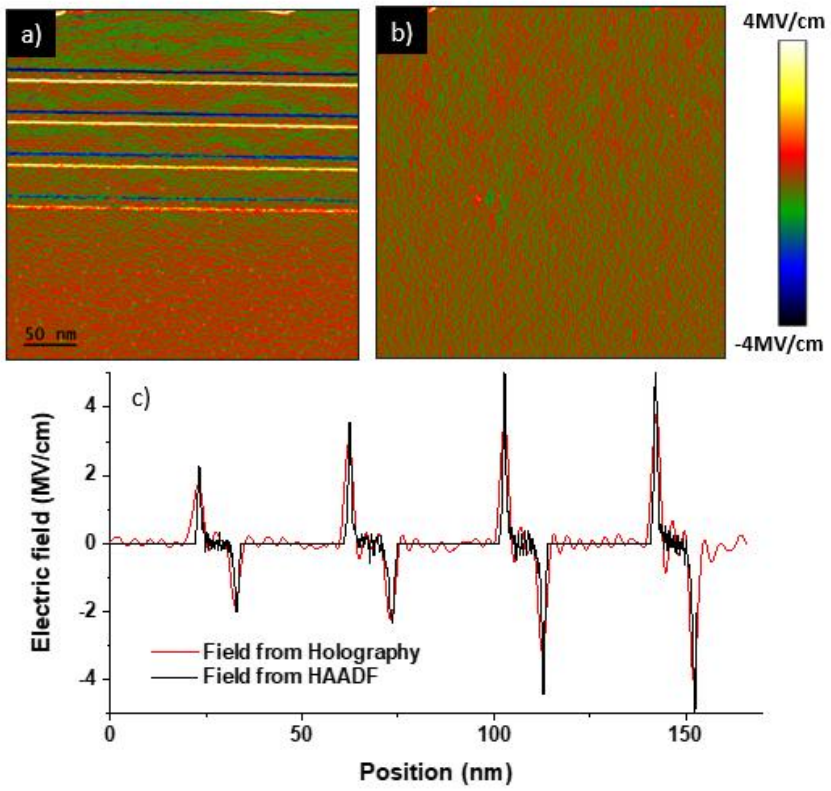

Figure 3-7 : Electric field mapping by electron holography on the SiGe layers. a) Electric field perpendicular to the layers. b) Electric field parallel to the layers. c) Field profile taken across the layer in map a) and compare to our field estimation from HAADF.

The displacement of the diffracted beam from the reference pattern is then calculated giving us a measurement of the deformation in percent relative to the reference. The reference pattern was chosen in the silicon substrate. Figure 3-8-(c) and (d) are diffraction pattern taken respectively in the silicon and in the $Si_{0.55}Ge_{0.45}$ layer. We subtracted the pattern of silicon to the pattern of $Si_{0.55}Ge_{0.45}$, the subtraction of these two diffraction patterns is shown in Figure 3-8-(e). The transmitted beam subtraction appears dark which is normal as the germanium has a bigger atomic number than silicon. Then looking at the subtraction of diffracted beams, all have a white and a dark edge indicating a change in lattice parameters. The strained

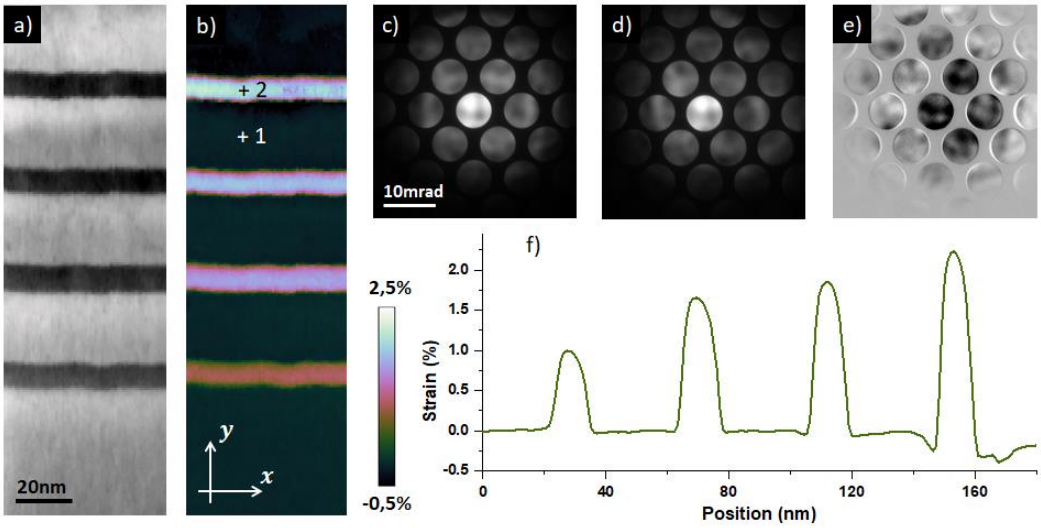

Figure 3-8 : Strain measurement with NB-4D-STEM in the SiGe layers. a) Bright field image reconstructed from the 4D-STEM data set. b) Strain map in percent from zero reference in Silicon. b) Diffraction pattern in the silicon. Taken in position 1in the map in (b). d) Diffraction pattern in the SiGe. Taken in position 2 in the map in (b). e) Subtraction of the pattern (c) to (d). f) Average profile of strain taken across the layer in map (b).

$Si_{0.55}Ge_{0.45}$ lattice parameter is expected to be 2.7% bigger than the Si one. From the beam displacement, the strain map was extracted and is shown in Figure 3-8-(b). For more clarity an average profile was taken across the SiGe layers and is presented in Figure 3-8-(f). The layers in the map are well contrasted compare to the silicon barriers. To attest if these strain values are accurate, the germanium concentration has been calculated from the strain values. Poisson's ratio ν makes the link between relative stretching $\delta L/L$ and relative compressing $\delta l/l$ in the perpendicular direction. The equivalent equation is:

$$\frac{\delta L}{L} = \nu \frac{\delta l}{l} \tag{3.4}$$

Replacing the relative tensile strain and relative compressive strain by the lattice parameters gives:

$$\frac{a_{SiGe\_exp} - a_{SiGe}}{a_{SiGe}} = \nu \ \frac{a_{SiGe} - a_{Si}}{a_{SiGe}} \tag{3.5}$$

Where a_{SiGe_exp} is the SiGe lattice parameter in the growth direction calculated from the strain we measured, the Poisson ratio is assumed to be $\nu = 0.275$ [115]. a_{Si} and a_{SiGe} are respectively the unstrained lattice parameter of Si and SiGe. In this equation a_{SiGe} can be

calculated using a linear dependence of the lattice parameter on the germanium concentration. The experimental lattice parameters of SiGe in the growth direction is:

$$a_{SiGe\_exp} = a_{Si} \times (1 + s) \tag{3.6}$$

Where s is the strain. The relaxed SiGe lattice parameter is:

$$a_{SiGe} = a_{Si} + c_{Ge} \times (a_{Ge} - a_{Si}) \tag{3.7}$$

Now from equation 3.5, 3.6 and 3.7) the germanium concentration c_{Ge} becomes:

$$c_{Ge} = s \times \frac{a_{Si}}{(1 + \nu)(a_{Ge} - a_{Si})} \tag{3.8}$$

The germanium concentrations calculated using equation 3.8 are gathered in Table 3-1. They are in agreement with all the other study. This mean that our strain measurement by PED gives quantitative strain value in the 10nm wide SiGe layers.

Germanium concentration	**Layer 1**	**Layer 2**	**Layer 3**	**Layer 4**
SIMS	20%	31%	38%	45%
HAADF	21.2%,	30.9%	36.4%	45.1%
Holography	21,5%	33.2%	39.2%	42.5%
PED	18.5%	30.6%	34.4%	41.3%

Table 3-1 : Percentage of germanium in the four layers estimated using quantitative HAADF, holography, PED and compared to a SIMS.

3.3 Electric field measurement in SiGe with 4D-STEM

HAADF and electron holography allows us to measure quantitative step of MIP, and from that to estimate the electric field. PED allows the quantitative determination of the germanium concentration from deformation. Now we will show that when it comes to electric field measurement in STEM mode, the Si/SiGe interface creates some artefacts.

3.3.1 Multi-slice simulation of diffraction pattern created near Si/SiGe interface

A Si/SiGe structure was created using the script shown in appendix B. Figure 3-9-(a) shows a small area of the 2D transfer function of the structure summed on 7Å thick specimen. It contains a SiGe layer with 45% of germanium. The contrast is a phase contrast proportional to the potential, the yellow dots are the atomic columns. From the full 2D phase, an average profile was extracted and is presented in Figure 3-9-(b). On this profile there is the mean phase of the silicon and $Si_{0.55}Ge_{0.45}$ summed through 7Å.

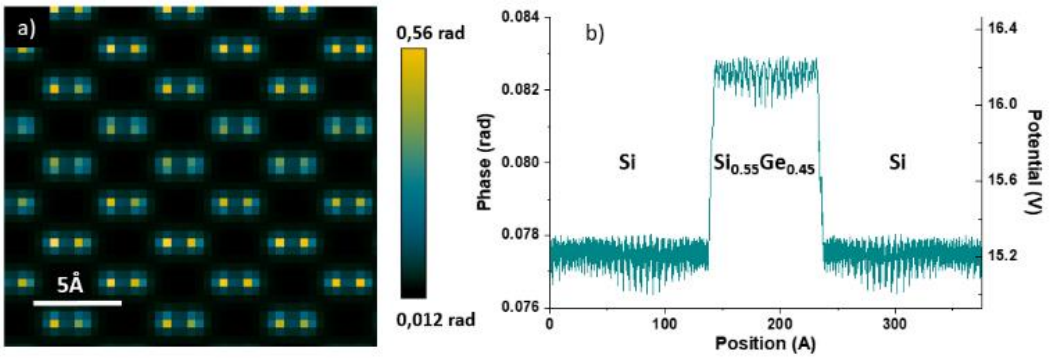

Figure 3-9 : Transmission function of a 7Å thick slice. a) Phase of the transmission function of a 20x25x7 $Å^3$ volume of SiGe. b) Average profile of the transmission function phase across the Si/ $Si_{0.55}Ge_{0.45}$ /Si structure.

It was necessary to check that the simulation transcribe a situation close to reality in terms of step in phase i.e. step in potential. The 4D-STEM experiment presented later in this thesis were acquired at 200kV acceleration voltage, the simulation is done at this same acceleration voltage so the interaction constant is: $\sigma_{200kV} = 7.29 \times 10^{-4}\, rad\, V^{-1}Å^{-1}$. From equation 1.6 and the interaction constant, the mean inner potential of the silicon and the $Si_{0.55}Ge_{0.45}$ layer was calculated. Table 3-2 summarizes the MIP values calculated from the µSTEM phase and compare it to the values found in literature. The column "MIP step" gives the

difference between the silicon MIP and the $Si_{0.55}Ge_{0.45}$ MIP. The values calculated from µSTEM phase are more than a volt higher than what the literature would suggest. But in our case only the difference of potential between Si and $Si_{0.55}Ge_{0.45}$ matters and the value estimated is 1.07 V. This estimation is close to the "expected" value of 0.94 V calculated from the theoretical calculations of the DFT.

So, in the end the simulated SiGe layer has a step of potential slightly bigger than expected but this simulation is our benchmark regarding the effect of an abrupt change in potential on the diffraction pattern. The simulation will have a more abrupt profile than reality so the effect of potential discontinuity will be emphasized. The simulations done on this structure will be compare to our experimental data in order to access the validity of the diffraction pattern behavior as the interface is scanned.

	Si	**Ge**	**$Si_{0.55}Ge_{0.45}$**	**MIP step**
Literature	12.57V	14.67V	13.51V	0.94V
µSTEM	13.82V	/	14.89V	1.07V

Table 3-2 : Mean inner potential of SiGe, comparison of the values found by simulation to the literature [108].

3.3.2 Electric field measurement by NB-4D-STEM

For the electric field measurement near the Si/SiGe interface by 4D-STEM, the first attempt was an off-zone axis NB experiment. Silicon and the germanium have the same crystallographic structure, so by tilting the sample around the growth axis, low diffracting condition are accessible. The camera length was set to 720 mm, the convergence angle to 4.5 mrad. Using the α-tilt of the sample holder, the sample was tilted 8° around the growth direction and less than a degree perpendicular to the growth direction. This way the beam still travels almost parallelly to the interface and no HOLZ lines are present in the beam. The thickness of the sample was measured by CBED to be 120nm. We consider the field estimated by the quantitative HAADF at the interface, 2 MV/cm and 5 MV/cm for the low germanium concentration and the high one thus leading to expected deflections of about 68

µrad and 170 µrad respectively. Recorded on a 1024pix² camera this led into shifts of 1.6pixel and 4pixels.

Figure 3-10 shows how the beam is influenced at the $Si/Si_{0.55}Ge_{0.45}$ interface. Firstly, the beam has no HOLZ lines in it, so the tilt was effective in reducing the effect of dynamical diffraction. Then by visually examining the profiles of experimental beams, we can see that there is no rigid shift. Instead, a redistribution of intensity occurs. This is because the probe formed by the 4.5 mrad convergence angle is not small enough compared to the field

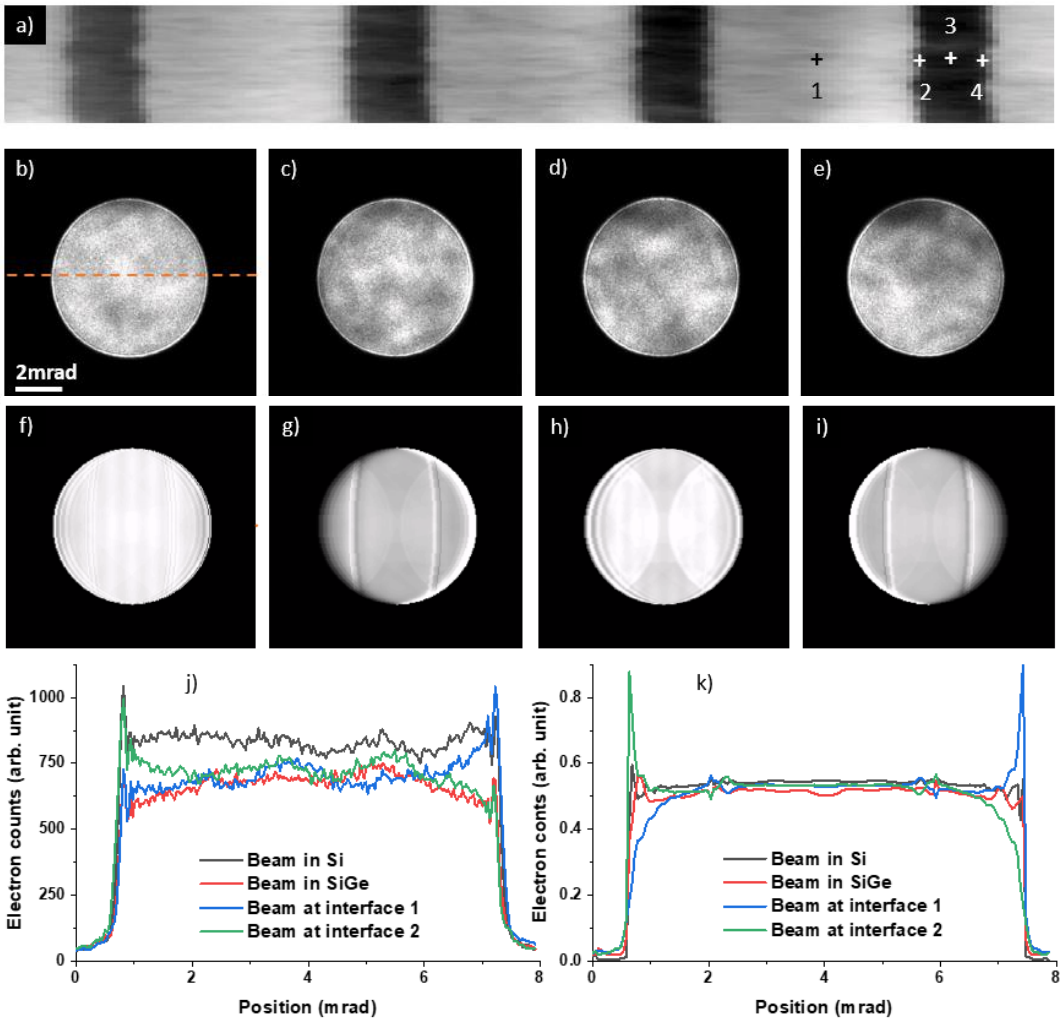

Figure 3-10 : Influence of the $Si/Si_{0.55}Ge_{0.45}$ interface on the electron beam in off-axis NB-4D-STEM. a) BF image reconstructed from the 4D-STEM data set. b),c),d) and e) are experimental electron beam recorded respectively in Si, at the left interface, in SiGe and at the right interface. Same for: f), g), h) and i) but obtained by multislice simulation. j) and k) are profiles taken respectively across the experimental and simulated beams. The orange dashed line in (b) gives the position of the profiles.

variation at the interface [42]. Using equation 1.20 size of the probe encompassing 95% of the intensity is 1Å. In the case of the $Si_{0.55}Ge_{0.45}$, the field estimation from HAADF gives a field variation from zero up to 5MV/cm and back to zero in less than 3nm. In this case the field cannot be consider as constant in the probe. In terms of potential, it means that the probe sees at the same time the Si MIP and the $Si_{0.55}Ge_{0.45}$ MIP. This problem will not happen if we had an infinitely small probe. But we have seen earlier with the Si/SiO_2 interface that the tail of the probe has an influence several nanometers away from the interface. The simulation was run using a convergence angle of 4.5 mrad, a thickness of 120 nm and a tilt of 8° along the layer. First remark regarding the simulation, the contrast in the beam is due to the multislice simulation. The simulated electron beam only goes through a series of thin phase objects thus the electrons stay coherent leading to more interferences. Then regarding the beam deviation, the simulated beams show the same behavior has the experimental one. Figure 3-10-(j) shows a clear redistribution of intensity and no rigid shift. Has we said, the artificial interface in sharper than the real on leading into emphasized effect. Even though there is no rigid shift, the redistribution of intensity can be detected by the CoM algorithm. We also try the TM algorithm to see if a shift could be detected. The results are presented in Figure 3-11. The CoM and TM electric field map are presented next to a virtual dark field image reconstructed from the 4D-STEM data set. Firstly, CoM and TM algorithm gives signal at the edges of the SiGe layers. This means that the field created by the difference of MIP can be detected. The CoM and TM signal have the same trend but the CoM signal is stronger than the TM signal. Both signals have contrast in the silicon barrier between the SiGe layer but no field is expected here. This is due to the contrast present in the beam which influence the detection of the intensity CoM. For this data set we said that no rigid shift of the beam was present but the TM algorithm detected a shift. It means that the cross-correlation is also sensitive to the redistribution of intensity and in this case, the TM algorithm works as a bad CoM algorithm (see section 1.3.5).

To improve the field mapping the same experiment was tried but this time on axis with precession. Performing the experiment on axis permits not to lose spatial resolution in projection. The parameters of acquisition are a convergence angle of 3.2 mrad and a camera length of 420 mm. The diffraction patterns were recorded on a 1024 pix^2 camera. For layer with the highest germanium concentration if a rigid shift happened, the shift of the beam is expected to be 3.8 pixels and 1.5 pixel for the layer with the lowest concentration. To avoid the diffraction contrast in the beam the angle of precession was set to 0.25°. The experimental diffraction patterns are presented in Figure 3-12-(a) to (d). The beam behavior in this precession experiment was also simulated. Simulated diffraction patterns are shown in

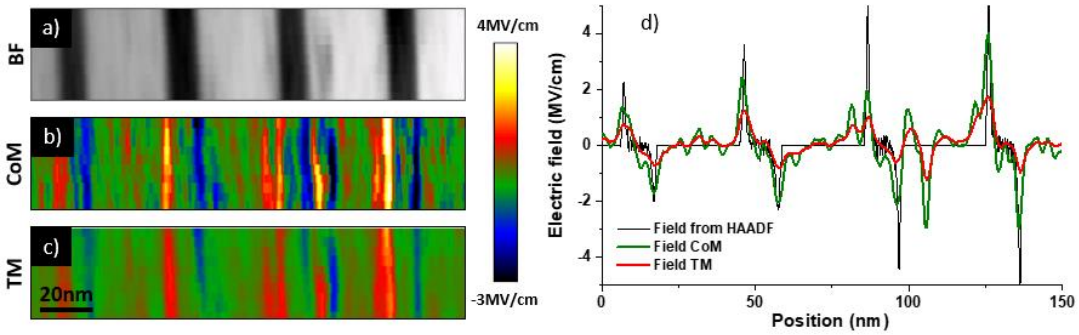

Figure 3-11 : Field mapping by off-axis NB-4D-STEM in SiGe layers. a) BF image reconstructed from 4D-STEM data. b) Electric field extracted from the raw data with the CoM. c) Electric field extracted from the raw data with the TM. d) Profiles of the electric field taken across the four layers of SiGe and compare to the field estimation from HAADF.

Figure 3-12-(e) to (h). From left to right there is the beam in the Si, the beam at the first interface, the beam in the SiGe and the beam at the second interface. Here again in the simulation, the electron beam keeps its coherence along the sample thickness leading to more interference thus more contrast in the beam than in our experimental results where the coherence is lost. Also, in the simulation, the zone axis is perfectly aligned to the optic axis as against in experiment where a perfect alignment cannot be reached. Nevertheless, the recorded transmitted beams are bright with small variation of intensity. The profiles presented in Figure 3-12-(i) and (j) are respectively the profiles of the experimental beams and the simulated ones. In both case the beams behavior is similar. If we take a look at the beam at the interface 1 (blue curve) both simulated and experimental present a peak of intensity on the right and a decrease of intensity on the left side. There is an analogue behavior of the beam at interface 2 but in the opposite direction. So, at the two interface a redistribution of intensity occurs. Here as the beam is not rigidly shifted on the detector, we decided only to process the data with CoM. The results are presented in Figure 3-13, where (a) is a virtual BF image extracted from the transmitted beam intensity. Figure 3-13-(b) is the field map extracted with CoM. For more clarity a profile of field has been taken and is compare to the HAADF field estimation in (c). The noise level is clearly not having important as in the off-axis acquisition. The SNR and field values of both experiments are gathered in Table 3-3. The profile in Figure 3-13-(c) has been average over 25pixels so the noise is reduced. In this profile the field in the Si is almost constant and close to zero, which is what we expect. Then there is a positive peak at every left edge of a SiGe layer and a negative peak at every right edge so the trend is the same as the one estimated from the

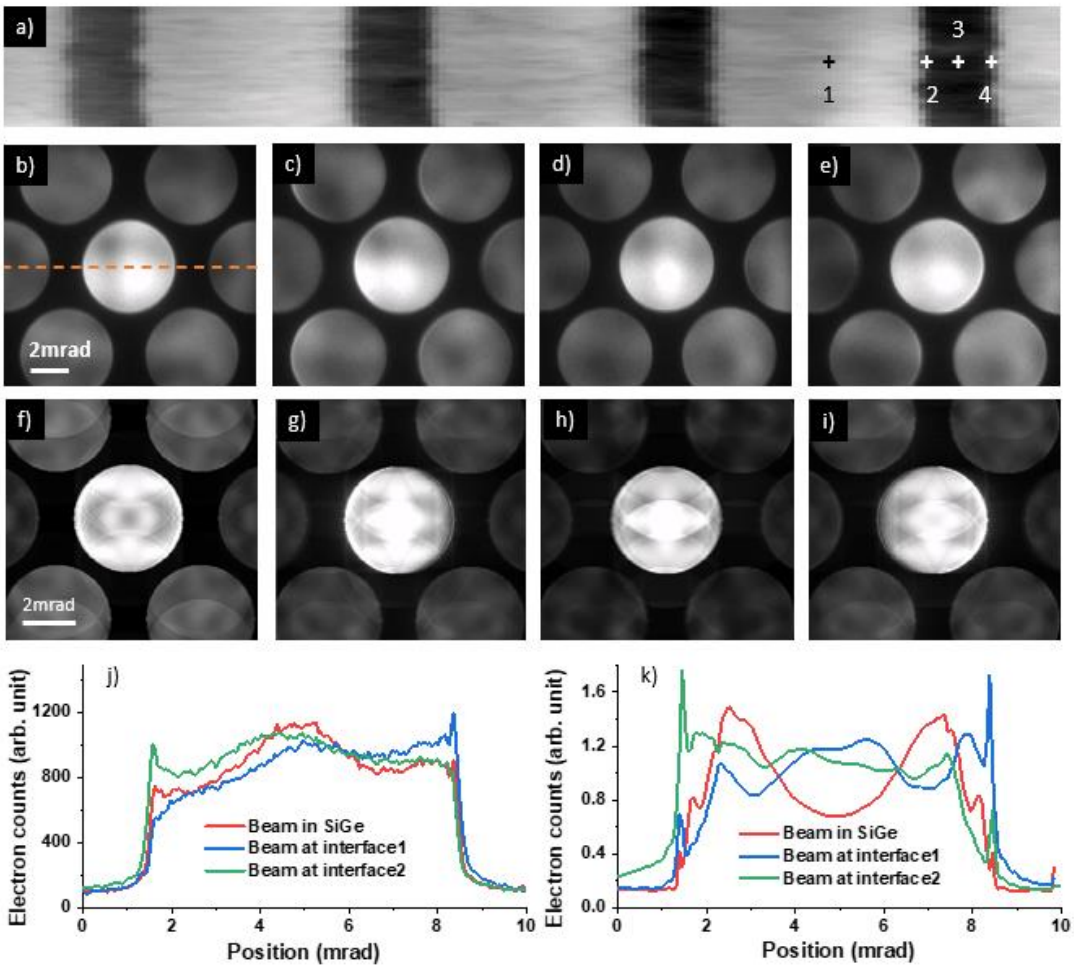

Figure 3-12 : Influence of the Si/$Si_{0.55}Ge_{0.45}$ interface on the electron beam in off axis NB-4D-STEM coupled with precession. a) BF image reconstructed from 4D-STEM data. b),c), d) and e) are experimental electron beam recorded respectively in Si, at the left interface, in SiGe and at the right interface. Same for f), g) h) and i) but obtained by multislices simulation. j) and k) are profiles taken respectively across the experimental and simulated beams. The orange dashed line in (a) gives the position of the profiles.

HAADF. Regarding the maximum field value, they do not increase as we go from low to high germanium concentration in the layer. This means that field we measure might not be quantitative. Then regarding the width of the peaks, in our NB-4D-STEM experiment the peaks are wider than in the HAADF estimation. This can be explained as the probe is a few Angstroms wide in the HAADF and is close to a nanometer wide in the NB-STEM. So, the signal we extracted is the real signal convolve by the probe. Finally, inside the SiGe layer we expect a flat zero field area. But in the profile only the last layer has a clear flat area in the SiGe layer. This effect comes from the probe tail that still sees the interface even so the

majority of the probe intensity is in a zero-field area. We will see later that is lead to difficulties when measuring piezo field in thin layers.

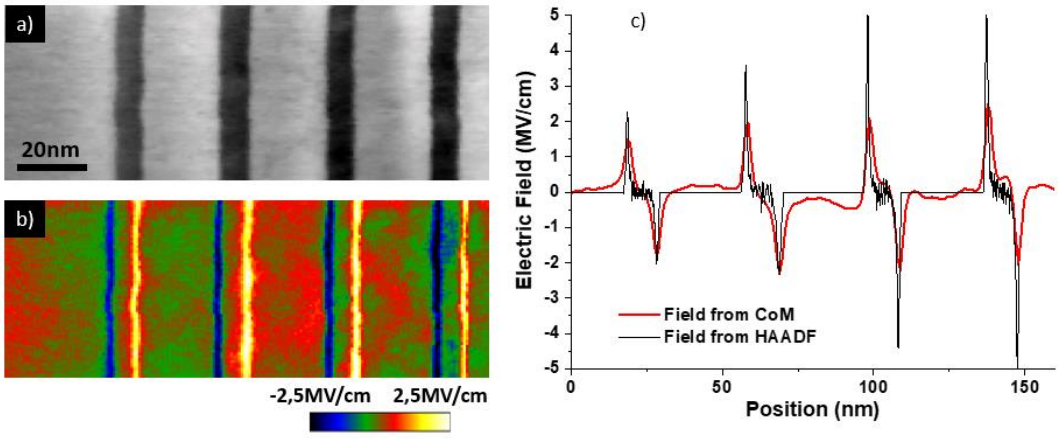

Figure 3-13 : Electric field mapping in on-axis NB-4D-STEM coupled with precession. a) BF image reconstructed from 4D-STEM data set. b) Electric field map extracted from the raw data with the CoM algorithm. c) Profile of the electric field taken across the layers

According to the results we obtained in NB-4D-STEM, the field created by the MIP difference can be detected off axis and on axis when coupling the acquisition with precession. But as the field is variating in a 3nm wide area, the beam undergoes a redistribution of intensity. This redistribution is complex and the results do not seem quantitative. Moreover, a flat zero field area is supposed to be present in the layers but it seems that the interfaces fields have an influence even in the middle of the layers. The probe tail has too much influence in this acquisition condition.

	Off axis CoM	**On axis precession CoM**
Field ($Si_{0.55}Ge_{0.45}$)	4 ± 1.9 MV/cm	2.6 ± 0.2 MV/cm
Field ($Si_{0.80}Ge_{0.20}$)	1 ± 1.9 MV/cm	1.5 ± 0.2 MV/cm

Table 3-3 : Electric field extracted from NB-4D-STEM at Si/SiGe interfaces

3.3.3 Electric field measurement by HR 4D-STEM

We showed that NB-4D-STEM suffers from limited spatial resolution. In order to improve the resolution, experiments were performed in HR-STEM mode. Field measurement in HR-4D-STEM has already been done on a pn junction and here the objective was to reproduce such experiment but this time on an interface [16]. In HR-STEM the resolution accessible is typically tens of Angstrom. We will see that despite this gain in resolution, artefacts lead to uninterpretable data.

A data set was acquired on the two SiGe layers with the largest germanium concentration. The parameters for this HR-4D-STEM experiment are a convergence angle of 25 mrad and a camera length of 110 mm. With such parameters and a 120 nm thick sample, recording on a 1024 pix² camera, the beam shift induced by the 4 MV/cm and 5 MV/cm electric field must be 0,8 pixel and 1 pixel respectively. Using equation 1.20 the probe size is estimated to be 5 Å. The probe is smaller than the 3 nm in which the field varies (see section 3.2.1), therefore we believe that no redistribution of intensity occurs in the transmitted beam. In order to have several points of scan in the 3 nm where the field variated at the interface, the scan step was set to 1 Å.

The results obtain from this HR-4D-STEM experiment are summarized in Figure 3-14. Figure 3-14-(a) show the diffraction pattern recorded in a silicon area. The wide convergence angle that is used creates a complex diffraction pattern. Figure 3-14-(c) show a HR-HAADF image obtain with 25 mrad convergence angle where the atomic columns are visible. From the raw 4D-STEM data set a virtual HAADF was extracted and the shift of the intensity CoM shown in Figure 3-14-(b) and (d) respectively. The CoM shift in (d) has been align to the virtual HAADF which gives the position of the SiGe layers. A periodic behavior of the CoM shift can be noticed. For both layers, the signal has a positive and a negative peak. The peaks intensity is 0,5 ± 0.2 pixel so there are in the right order of magnitude.

Despite this periodic signal some problems remain. The two peaks that are supposed to reflect the influence of the change of MIP are wide and not symmetrical plus the positive peaks seems to be in the middle of the layer and not centered on the interface position. This can be explained by the fact that in this diffraction pattern the transmitted and the diffracted beams overlap. In the sample, electric field is present in the same area as strain. The field has an influence on the whole diffraction pattern and the strain has an influence on the diffracted beams only. We do not know how to separate the two different sources of diffraction pattern movement. The CoM signal presented in Figure 3-14-(d) is influenced by

different sources that cannot be separated and therefore the signal cannot be interpreted as signal due to an electric field.

Another HR-4D-STEM acquisition was done on the two same SiGe layers but this time the HR-4D-STEM was coupled with precession. The convergence angle was reduced to 20 mrad. This reduction of convergence angle allows to access a camera length of 800 mm. The Ceta camera was used with its maximum resolution of 4096 pix². With these setups and the 120 nm thick sample, the expected shift from the 5 MV/cm and 4 MV/cm field are 14 pixels and 11 pixels respectively.

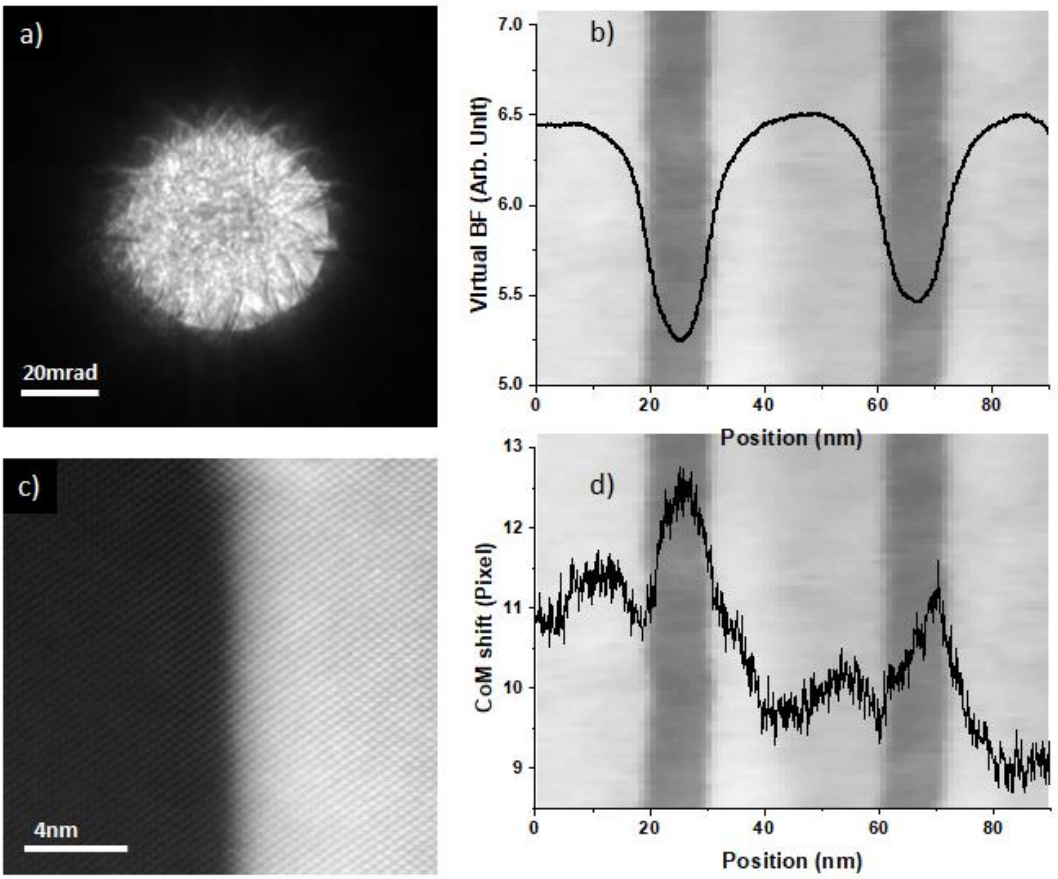

Figure 3-14 : HR-4D-STEM on $Si_{0.55}Ge_{0.45}$ and $Si_{0.62}Ge_{0.38}$ layers. a) Diffraction pattern recorded with 25mrad through a 120nm thick Si area. b) BF image reconstructed from the HR-4D-STEM data set. c) HR-HAADF recorded at the Si/SiGe interface with a 25mrad convergent beam. d) Intensity shift measured using CoM expressed in pixel.

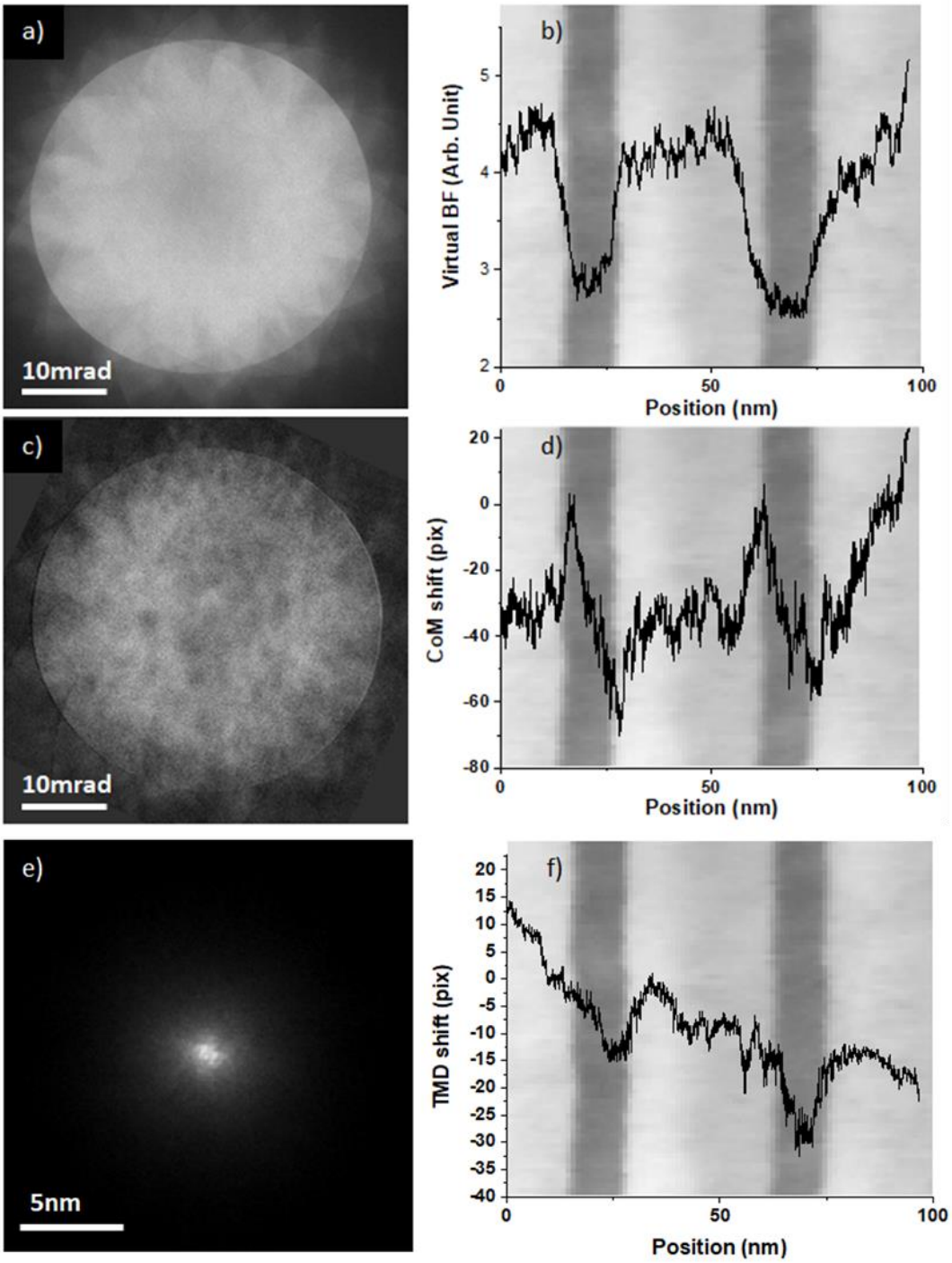

Figure 3-15 : HR-4D-STEM coupled with precession on $Si_{0.55}Ge_{0.45}$ and $Si_{0.62}Ge_{0.38}$ layers. a) Diffraction pattern obtain on a 120nm thick area of silicon with a convergence angle of 20mrad and a precession angle of 0,25°. b) BF extracted from the HR-4D-STEM data set. c) Subtraction of a pattern in the silicon and one at the SiGe/Si interface. d) Intensity shift extracted with CoM. e) Image of the electron probe used for the acquisition. f) Shift of the pattern extracted with DTM.

The intensity average done with precession leads to a transmitted beam brighter than the diffracted ones (see Figure 3-15-a). The beam intensity undergoes an intensity shift represented in Figure 3-15-(c) which is a subtraction of a pattern in the Si and one at the interface. On this subtraction a bright and dark edges are noticeable on the right and on the left respectively. The precession leads to a deterioration of the resolution. An image of the probe is presented in Figure 3-15-(e). As the transmitted beam is brighter the DTM can be used for the data processing. We processed the data with an artificial template in order to not be influence by the intensity around the transmitted beam. From the data set, a virtual HAADF was extracted and is presented in Figure 3-15-(b). The CoM and the DTM shift are align to the HAADF and are respectively presented in Figure 3-15-(d) and (f).

Here again whatever the algorithm that is used, the detected shift is periodic. From the CoM shift, a signal of 30±6 pixels can be measured and for the DTM a signal of 5±1 pixels. But, there is no zero-field area in the layer and the shift peaks are not centered on the interfaces position. A slope seems to be present in the DTM profile, that could be the de-scan but the slope should also be present in the CoM profile. Therefore, the signals detected by CoM and by DTM is influence by different sources that cannot be identified.

The electric field created by the difference of MIP between Si and Si_xGe_{1-x} is challenging to measure. The field is present in a very thin area leading into complex redistribution of intensity difficult to quantify in NB-4D-STEM mode. In this mode, the tail of the probe as an influence even in the middle of the 10 nm wide SiGe layers. Using wide convergence angle in HR-4D-STEM to improve the resolution makes the transmitted and diffracted beams overlap, in this case the different sources of beam intensity displacement cannot be separated even when coupling HR-4D-STEM with precession.

3.4 Conclusion

The interfaces study began with the simple interface of Si/SiO_2. The inhomogeneity present at the interface allows us to have a non-quantitative but visual insight of the range in which the probe tail can influence a measurement. In NB mode, the experimental and simulated dater show the effect of the silicon lattice 4nm and 5nm in the amorphous layer respectively. This means that when processing a diffraction pattern acquired close to an interface, one should keep in mind that the pattern contains information from both side of the interface.

Then a sample composed of 10nm wide SiGe layers embed in Si was studied. From HAADF intensity, holography potential and strain measure by NB-4D-STEM, we measure quantitative Germanium concentration in the SiGe layers. These three techniques works well as they measure quantities that vary at the interface but stay constant in the layers. In addition, the quantitative HAADF allows us to estimate the field we expect as it is the best Germanium profile we can access. The Germanium profile rules the potential profiles, which once derived gives the electric field.

Finally, we used 4D-STEM in NB and HR mode to measure the electric field created by the step of MIP at the interface. In this sample, the field varies from zero to several

MV/cm and back to zero in less than 3nm. This variation of field in a small area led to complex redistribution of intensity in the transmitted beam in NB mode. From such acquisition, the field can be detected using CoM processing. The probe tail has an effect even in the middle of the layers. In order to obtain a quantitative value, we try to decrease the size of the probe. Doing this makes the beam overlap and lead to uninterpretable data. The strain and electric field influence cannot be separated. Our last try was to reach a rigid shift of the transmitted beam in HR mode coupled with precession. In this experiment the transmitted beam is brighter than the rest of the pattern, thus the strain and field influence should be dissociated. Despite the high convergence angle we used the precession decreases the resolution. In the end, the resolution was comparable as in a NB mode acquisition coupled with precession.

When trying to measure field in more complex systems the tail probe will be a real problem. In QW where people want to measure the piezoelectric field, the MIP difference will influence the piezo value because of the tail probe still present outside of the QW.

4 Piezoelectric-field measurement in InGaN quantum wells

The binary alloy gallium nitride (GaN) and the ternary alloy indium-gallium nitride (InGaN) are III-V semiconductors. It means that they comprise elements with three valence electrons and another element having five valence electrons. In this case, the gallium or the indium have three valence electrons and the nitrogen has five. GaN has a high electron mobility and a direct band gap. The GaN wide gap energy of 3.4eV allows visible light emission, making GaN a material of choice of optoelectronics application such as LEDs or lasers [76], [116]. This material is also adapted to high-power and high-frequency devices. Its low sensitivity to ionizing radiation makes GaN a suitable material for solar cells and space application.

The GaN and InGaN quantum well structures studied here have wurtzite structure (hexagonal structure). In this case, in the direction of growth (the $\vec{c}$ axis) the material is polar. Polarity is the separation of the electric charges in the unit cell, leading to an electric dipole moment [117], [118]. To realize InGaN QWs on the GaN substrate, the InGaN layers are grown by epitaxy, thus leading to a tensile strain in the $\vec{c}$ direction. The combination of strain and polarity in the InGaN layers create a piezo-electric field [11]. This piezo-electric field will modify the optical properties of the quantum wells. For example, in GaN band, the wavelength of emission will be red-shifted. This deteriorate the properties compare to what is expected in bulk GaN materials [35], [119]. Measuring precisely this piezo-field is becoming of great interest as it will help to understand properties of the devices as well as being about to quantify efforts to reduce the piezoelectric fields in these materials.

Firstly, in this chapter, the expected piezo-electric field and the MIP influence on the measurement will be discussed. Then we will show to benchmark the study, results that are obtained by holography and DPC. Then multislice simulations done to generate diffraction pattern at the vicinity of the InGaN QW will be explained. After that some limits of 4D-STEM will be emphasized and acquisition at high-speed using a new generation of direct detector will be shown as a way to limit the interaction between the sample and the electron beam. Finally, some way to overcome the limit imposed by dynamical diffraction will be explored.

4.1 Piezo-electric field in GaN/InGaN quantum wells: preliminary work

The sample studied in this chapter is a series of five InGaN quantum wells (QW) embedded in GaN, it comes from a blue emitting micro-LED. The silicon patterned templates used for

the epitaxy leads to QWs that are wider at the edges than central parts of the micro-LEDs. A piezo electric field of several MV/cm is expected in the wells and the wurtzite lattice leads to much more dynamical diffraction than seen for simple cubic Si structures. This sample was chosen for the 4D-STEM measurements as the QWs are much wider (8 nm) than the usual width of InGaN QWs in LEDs (2 nm).

Figure 4-1-(a) shows a HAADF image of the five InGaN layers which are brighter than the rest of the sample as indium has a higher atomic number (Z) than gallium. It can be seen in this image that the width of the wells and the distance between them (the barriers) increase as we get closer to the edge of the sample (0µm zone). So, by doing the acquisition in the 0µm zone, the properties we want to study will be easier to access as the layers are not as thin as usual InGaN QWs. This means that the resolution of our technique will not be as limiting as it could be in typical 2 nm wide InGaN wells used in blue emitting LED. Figure 4-1-(b) and (c) are HAADF and EDX acquired in the 0 µm area. For more clearness, the EDX profiles taken close and far of the edge are presented in Figure 4-1-(d). From these

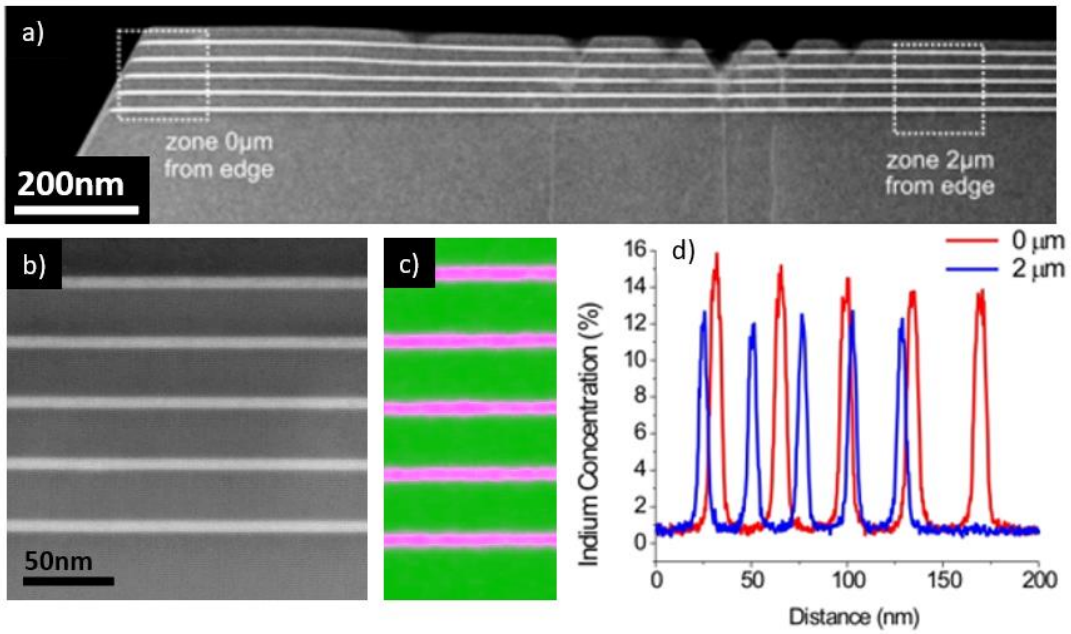

Figure 4-1 : InGaN quantum wells sample. This sample was grown by epitaxy in such condition that the wells and the barriers in between get thicker as we get closer to the left edge. a) HAADF image of the sample taken at magnification 120.10^3. The zone 0µm is the area where our acquisition will be done. b) HAADF image taken on the QW with 320.10^3 magnification. c) EDX map taken on the 0µm area. d) EDX profiles of the indium concentration taken in the 0µm and 2µm area.

profiles the increase in the QW width is more visible. In the area of interest at the edges of the microwires (0 µm), from the HAADF image we measure the QW width to be 7 nm and the barriers are 28 nm wide. In the 2µm zone, the barriers are 20 nm wide and the wells are only 5 nm wide. From the EDX profile we deduced the average Indium concentration to be 13.8±2% [120].

4.1.1 Strain mapping for indium concentration estimation

In order to assess the value of indium concentration we extracted from the EDX, strain measurement was performed using PED. We know that tensile strain will be present as the indium and the gallium have different lattice parameters. The growth done by epitaxy leads to a perfect match of the lattice parameters in the in-plane direction, ($\vec{a}$ axis), so the InGaN will be in compression in this direction and expanded in the $\vec{c}$ axis. Then Poisson's ratio says that the InGaN will be expanded in the $\vec{c}$ direction.

For the strain mapping the convergence angle was set to 3.2 mrad, the camera length to 650 mm and the precession tilt to 0.25°. With these parameters, we can record two orders of diffraction. The beams are not overlapping while looking down the [010] axis of the sample. The diffraction pattern in the GaN and in the InGaN are presented respectively in Figure 4-2-(a) and (b). Figure 4-2-(c) is the subtraction of pattern (b) to (a). That subtraction show that the diffracted beams moved along the $\vec{c}$ axis. The dark and bright contrast at the edges of the beam shows that the beams moved toward the centre as the probe goes into the InGaN i.e. an area where the $\vec{c}$ lattice parameter is bigger. From this 4D-STEM data set, a BF image was extracted. It is presented in Figure 4-2-(d). The InGaN layers are well contrasted with the GaN barriers that attest the quality of the measurements in terms of spatial resolution. The strain map presented in (e) has been extracted from that same data set. The level of noise is low, the SNR was estimated using the maximum strain signal and the standard deviation calculated on a 100nm² square in the GaN barrier. The SNR we calculated is equal to 65. Aside of this acquisition, we performed strain simulation for different indium concentration using the Nextnano software. On the strain profile in Figure 4-2-(f), an increase in the strain is visible from right to left. An increase in strain means an increase in indium concentration. The trend is the same as the one found in EDX. Then if we compare our strain values to the simulated ones, we see that the strain measurement is in agreement with the EDX. The values are also comparable to the one found by Song & al [119]. The QW are close to 14% indium with a slight increase up to a concentration of indium close to 16%.

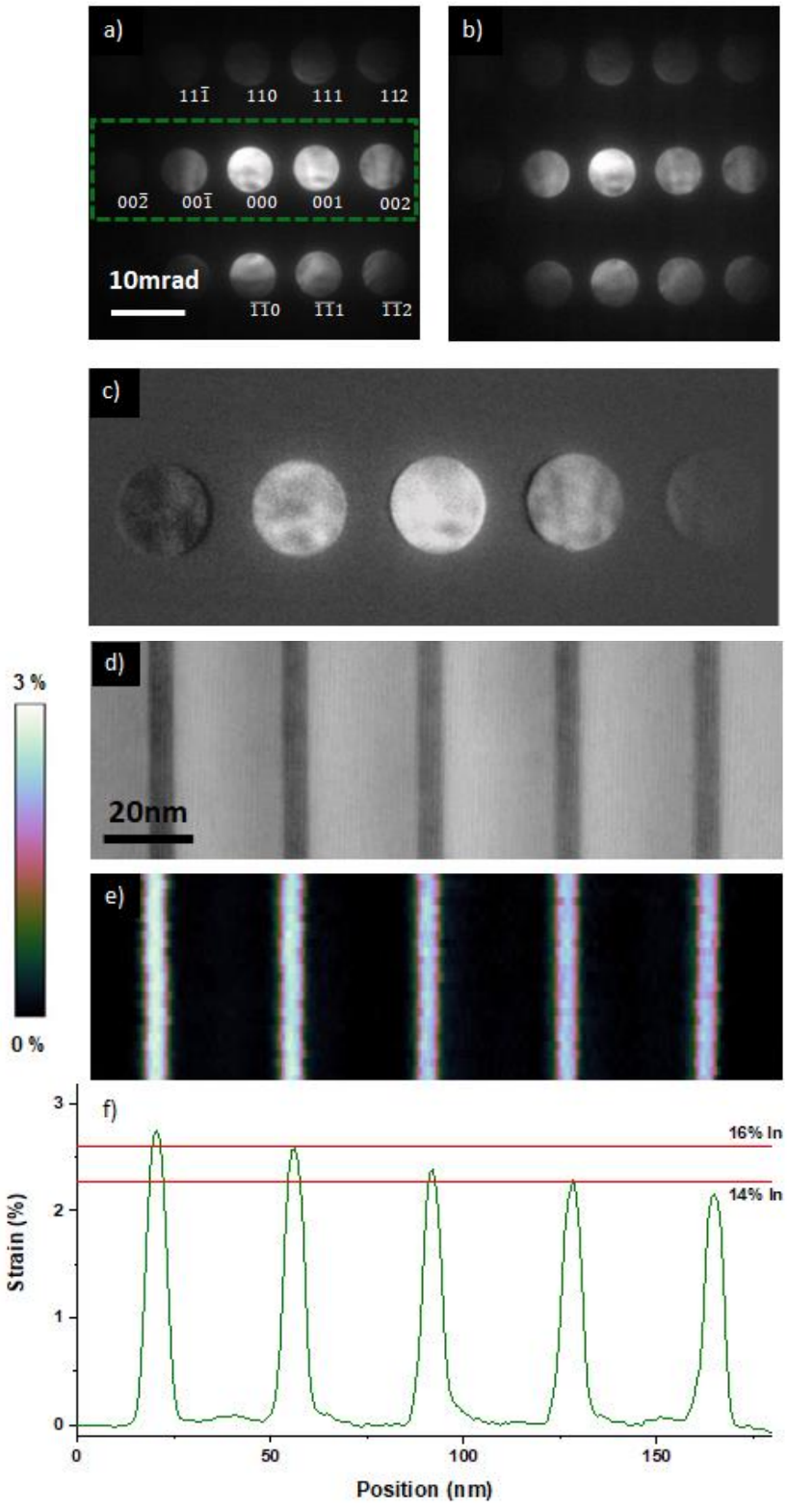

Figure 4-2 : Strain mapping on InGaN quantum wells. a) Diffraction pattern recorded in the GaN substrate. The dotted green rectangle is the area presented in (c). b) Diffraction pattern recorded in the middle of a QW. c) Subtraction of the pattern in the InGaN to the pattern in the GaN. d) BF image of the five InGaN QW. e) Map of the strain component in the $\vec{c}$ direction (perpendicular to the layer). f) Profile of the strain taken across the five layers. The two red lines are the strain values simulated respectively for 14% and 16% indium.

This strain measurement gives us values of indium concentration in agreement with the measured by EDX. The resolution offered by the 3.2 mrad convergent beam is good enough to measure accurately the strain in those 7 nm wide layers. The precession allows to have beam uniformly illuminated leading into a measurement with a very low level of noise. From now on, we will use a concentration of 14 % of indium as reference.

4.1.2 Strain influence on the mean inner potential

As described in chapter 3 the mean inner potential is defined as the average potential over a unit cell. For the large majority of the papers dealing with electric field in InGaN structure the MIP of InN and GaN is considered to be the same [10], [76], [119], [121]. For the few paper that introduce a change in MIP from GaN to InN none of those take into account the strain. As the strain changes the volume of the unit cell, we believe the MIP of a material changes when it undergoes strain. Volume correction of the MIP must done when measuring the MIP in strain material.

From DFT calculation the GaN MIP is 16.9V and the InN one is 18.9V [122]. The MIP of an $In_xGa_{1-x}N$ alloy can be calculating by assuming its linear dependence on the indium concentration. The first $In_xGa_{1-x}N$ MIP calculation was done using DFT values, it is presented as the black plot in Figure 4-3-(b). This first calculation of the alloy MIP is described by the equation:

$$MIP(In_xGa_{1-x}N) = x.MIP_{InN} + (1-x).MIP_{GaN} \quad (4.1)$$

Where MIP_{InN} and MIP_{GaN} are respectively the unstrained MIP of InN and GaN (it is the MIP of a bulk InN or GaN cristal calculating by DFT).

Our InGaN sample is pseudomorphically strained in the alloy layer. Strain results in changes in the lattice parameters i.e. change in the unit cell volume. Figure 4-3-(a) depict this change in volume. The lattice parameter of $In_{0.14}Ga_{0.86}N$ grown on GaN are gathered in Table 4-1. Therefore, the MIP of the layer must be modified by such strain [8]. We assume that the MIP of an $In_xGa_{1-x}N$ layer can be calculated using the equation:

$$MIP(In_xGa_{1-x}N) = x.MIP_{InN}.\frac{V_{InN}}{V_{epitaxy}(x)} + (1-x).MIP_{GaN}.\frac{V_{GaN}}{V_{epitaxy}(x)} \quad (4.2)$$

Where V_{InN} and V_{GaN} are the volume of the unstrained InN and GaN cristal. $V_{epitaxy}(x)$ is the volume of the $In_xGa_{1-x}N$ unit cell strained by the epitaxy, this volume depends on the concentration of Indium. We used the Nextnano software to calculate the strain present in

InGaN layer epitaxied on a GaN substrate for indium concentration from 0% to 50%. From the strain, we calculated the lattice parameters of the strained alloy layers and then the unit cell volumes. With these volumes and equation 4.2 we calculated the MIP with volume correction, it is presented as the red plot in Figure 4-3. We also calculated the influence of the strain when considering the MIP of InN and GaN to be equal, this is presented as the blue plot in Figure 4-3. From this figure we can see that the change in volume has a huge influence on the MIP of an InGaN alloy. In our case for 14% of indium without volume correction the MIP_{InGaN} is 17.17V. With volume correction and the MIP gather in Table 4-1 we calculated the MIP_{InGaN} to be 17.47V. We will consider the MIP closer to reality with the volume correction. So, the difference of potential between GaN (16.9V) and the epitaxied $In_{0.14}Ga_{0.86}N$ (17.47V) is equal to 0.57V. To have more information of how the MIP is influence by strain DFT calculations could be performed using different lattice parameters.

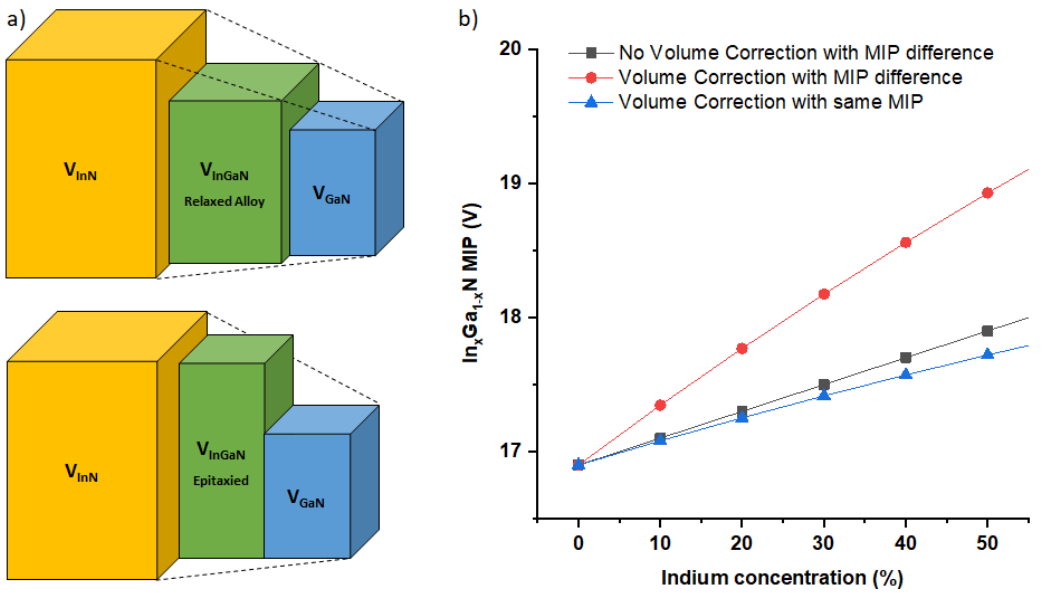

Figure 4-3 : Influence of the strain on the MIP of a InGaN. a) Schematic of the unit cell volume difference between InN, GaN and InGaN alloy either relaxed either epitaxied on GaN. b) Evolution of the InGaN MIP depending on the indium concentration. The black plot is a simple linear interpolation between GaN and InN MIP. The red plot presents a MIP calculating taking into account the change in volume of the unit cell under strained condition. The blue plot shows the influence of the change in volume of the unit cell but this time considering the potential of GaN and InN to be the same and equal to 16.9V.

	InN	**GaN**	**$In_{0.14}Ga_{0.86}N$ epitaxied on GaN**
Lattice constant a = b	3,545Å	3,189Å	3,189Å
Lattice constant c	5,703Å	5,185Å	5.303Å
Unit cell volume	62,07$Å^3$	45,66$Å^3$	47.37$Å^3$
MIP (DFT)	18.9V	16.9V	17.47V

Table 4-1: Basic parameters of InN, GaN and ***$In_{0.14}Ga_{0.86}N$*** *. strained alloy layer with strain influence on the MIP.*

4.1.3 Piezo-electric field and mean inner potential contribution

From the measured width and indium concentration in the layers, the electric field was simulated using Next Nano. The input files where the simulation parameters are shown in appendix C. The indium concentration was set to 14% in the quantum well. The potential profiles obtained with the simulations are presented in Figure 4-4. The software Nextnano assumes that the MIP of the GaN is equal to the InN. In Figure 4-4 we show also the MIP

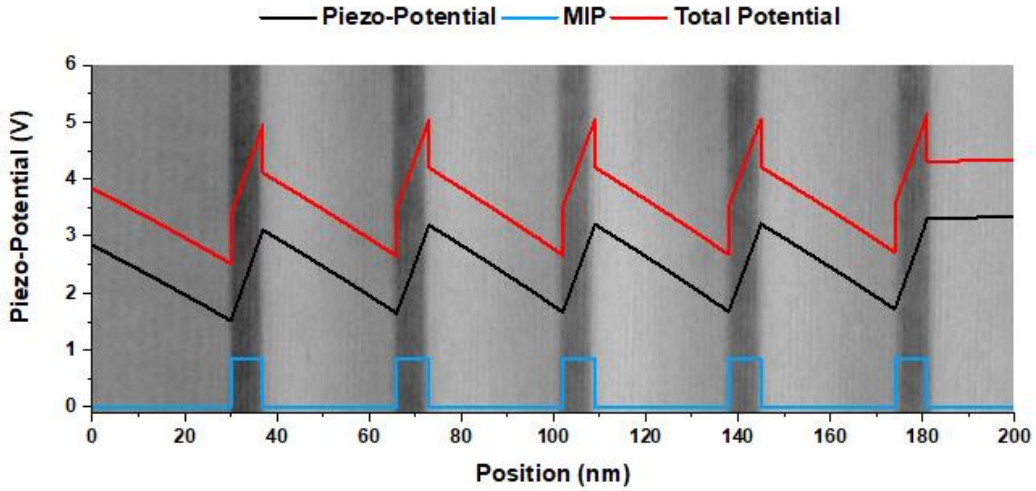

Figure 4-4 : Simulated profiles of potential in $In_{14}Ga_{86}N$ quantum wells. The profiles are presented with a BF image of the sample in the background. The piezo-potential has been simulated using Nextnano. The MIP is estimated using equation 4.2. The total potential is the sum of the two previous one.

difference of GaN and $In_{14}Ga_{86}N$ across the QW. In the previous section of this chapter, the MIP of the $In_{14}Ga_{86}N$ was estimated 0.57V higher than the MIP of GaN. The red plot in Figure 4-4 represents the total potential combining the MIP and the piezo-field. There are three distinct behaviors. First in the 28nm wide GaN barriers, there is a positive slope, which will create a low positive electric field. Then in the 7nm wide QW, the potential has an abrupt negative slope which will lead to an intense negative field. Finally, at both interfaces a discontinuity of potential is present due to the MIP difference. Such discontinuity will create very intense signal in the measurement that can be assimilated to electric field at the interfaces [66]. As for the SiGe shown in chapter 4, there will be a positive and a negative peak of electric field. The expected field is shown in Figure 4-5. The piezo-field in (a)

calculated by derivation of the potential calculated by Nextnano gives about 0.5MV/cm in the barriers and -2.2MV/cm in the QWs. In (b) a schematic of the field we expect is depicted. The sharpness of the interface was not estimated so the intensity of the peaks created by the step of MIP is unknown. However, we know from the SiGe study that such peaks are too thin to be quantitatively measured. In this chapter our objective is to obtain a qualitative field profile where we can discern the MIP contribution from the piezo one.

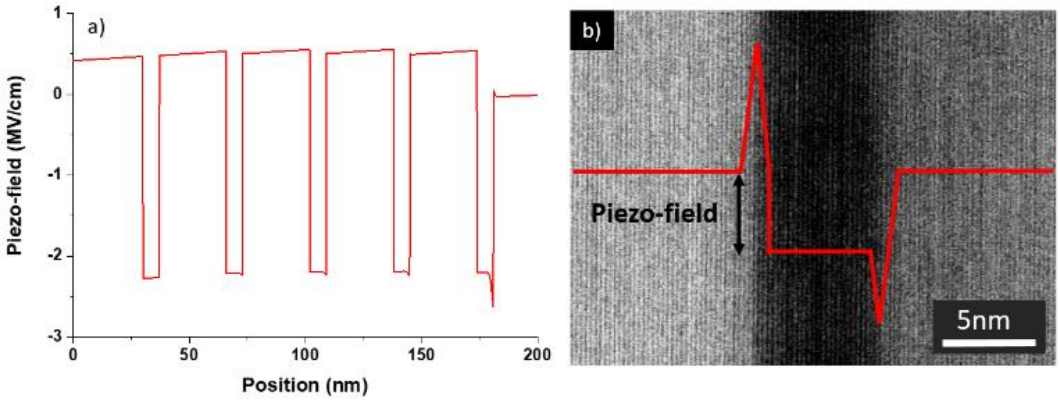

Figure 4-5 : Electric field in $In_{14}Ga_{86}N$ quantum wells. a) Piezo-field simulated using Nextnano. b) Schematic of the expected electric field profile when taking into account the MIP difference between GaN and InGaN.

4.1.4 Field measurement by off axis electron holography

We have seen in the SiGe study that the holography gives a spatial resolution good enough to see the effects from the changes in the MIP at the interfaces. Here the layers are 7nm wide and the material unit cell is no longer simple cubic but hexagonal. The hexagonal crystal system has less symmetry than the cubic one thus the dynamical diffraction has a much more severe impact than for silicon.

The holography data set is composed of 32 holograms each one acquired with 8s acquisition time. The biprism voltage was set to 250V leading to a fringe spacing of 1.58nm. Recording on a Oneview camera with a magnification of 63kx gives a field of view of 460 nm². These settings allow recording each fringe on 14 pixels to preserve contrast. The mask used during the reconstruction algorithm provided a spatial resolution in the reconstructed phase image of 3.0 nm. The operating voltage was 200kV so the interaction constant is $C_E =$

7.29×10^{-3} rad.V^{-1}. Using CBED, the thickness of the sample was measured to be 110±10nm.

Firstly, the reconstructed amplitude image shown in Figure 4-6-(a) reveals dark contrast arising from dynamical diffraction, even though care was taken to minimize this effect. From the reconstructed phase image and using equation 1.6 we can calculate the potential map that is presented in Figure 4-6-(b). For more clarity, an average profile of the potential was taken across the QW. Level of noise in the map was estimated for the potential map. The noise is the standard deviation calculating in a 20nm² box in the map and the signal is the peak-to-peak value measure in the profile. The SNR equal 10. In the potential map we observe oscillations between the QWs which is an effect of the dynamical diffraction observed in the amplitude image.

Regarding these peak-to-peak potential values in the QWs, they are between 0.88V and 1.26V. In our total potential estimation presented in Figure 4-4 the peak-to-peak signal was 1.85V. Therefore, the signal we measure is in the right order of magnitude. The trend of this plot is in agreement with our simulation, abrupt increase of potential alternate with smooth decrease. To obtain quantitative values of the piezoelectric (V_{piezo}) and MIP (V_{MIP}) components of the total potential, we were able to separate these effects. Table 4-2 shows these values for the five different QWs. From the simulations a value of 1.4 V has been obtained for V_{piezo} which is higher than obtained experimentally, which are in the range 0.46-0.53 V. However, the QWs are not perfectly abrupt and as such we would expect to measure values of V_{piezo} that are less than expected. Interestingly the V_{MIP} is also higher than expected.

	1	2	3	4	5
V_{MIP} (V)	0.56	0.70	0.51	0.8	0.62
V_{piezo} (V)	0.53	0.47	0.53	0.47	0.46

Table 4-2 : Quantitative values of V_{piezo} and V_{MIP} obtained from the electron holography results.

We believe that the EDX quantification is correct as well as the measurement of the specimen

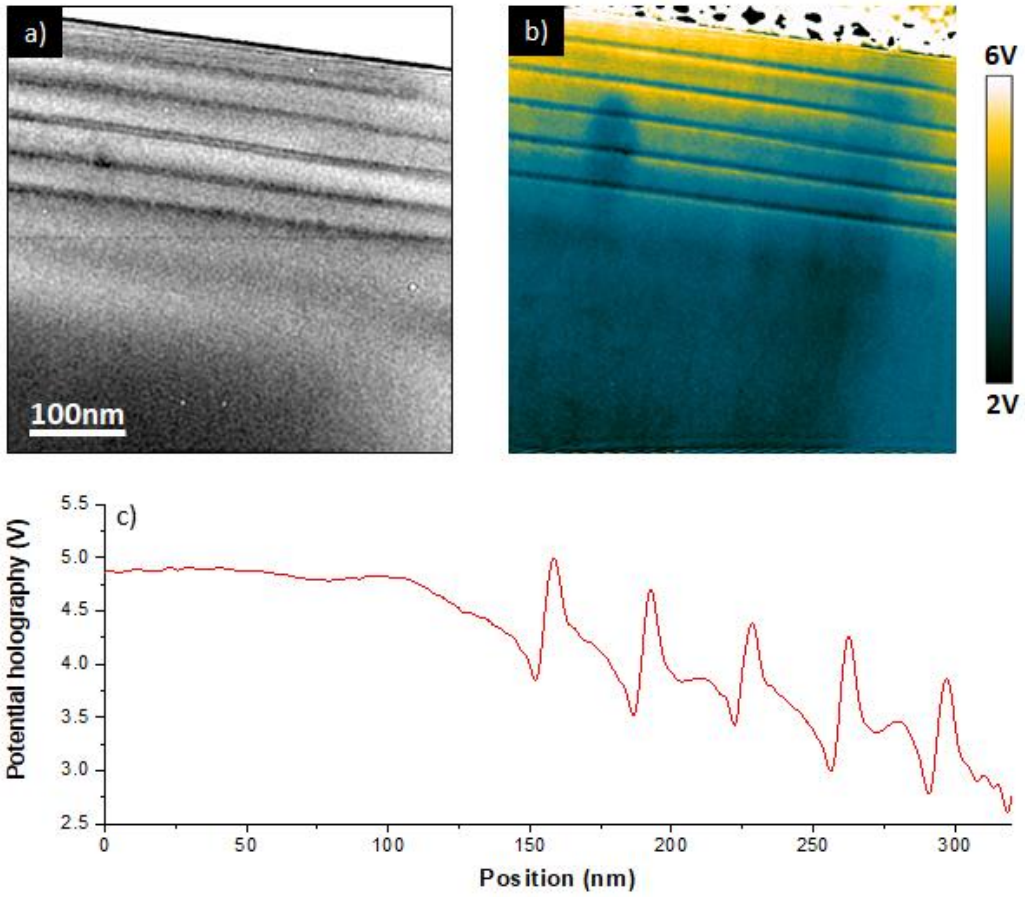

Figure 4-6 : Electrostatic potential of the InGaN QWs measured by off axis holography. a) Amplitude image obtain after reconstruction from the raw hologram series. b) Potential map calculated from the phase map using equation 1.6. c) Profile of the electrostatic potential taken across the QW.

thickness by CBED. Therefore, at this time, we can propose that these high values of the step in V_{MIP} arise from disorder in the QWs which would have the effect of locally changing the MIP.

To calculate the electric field, the potential was derived in the [110] and [001] direction. The results are presented in Figure 4-7. The QWs appears clearly on Figure 4-7-(a) but no significant signal is noticeable in (b). So, the potential was not variating parallel to the wells. The profile of electric field in (c) gives us the field value from the map. The level of noise was calculated in the field map, with standard deviation on a 400nm² area and the signal was taken as the average field values in the wells. The SNR is equal to 10. From the peak indicated B in Figure 4-7-(c), the electric field values are comprised between -2 and -3 MV/cm, which is in the order of magnitude of the piezo field that is expected. Regarding the trend, there is negative field in the InGaN layers and in the barriers, there is a small positive field, almost constant. However, the MIP field contribution cannot be distinguished from the piezo one. Another difference with the simulation, is the presence of positive peaks of field

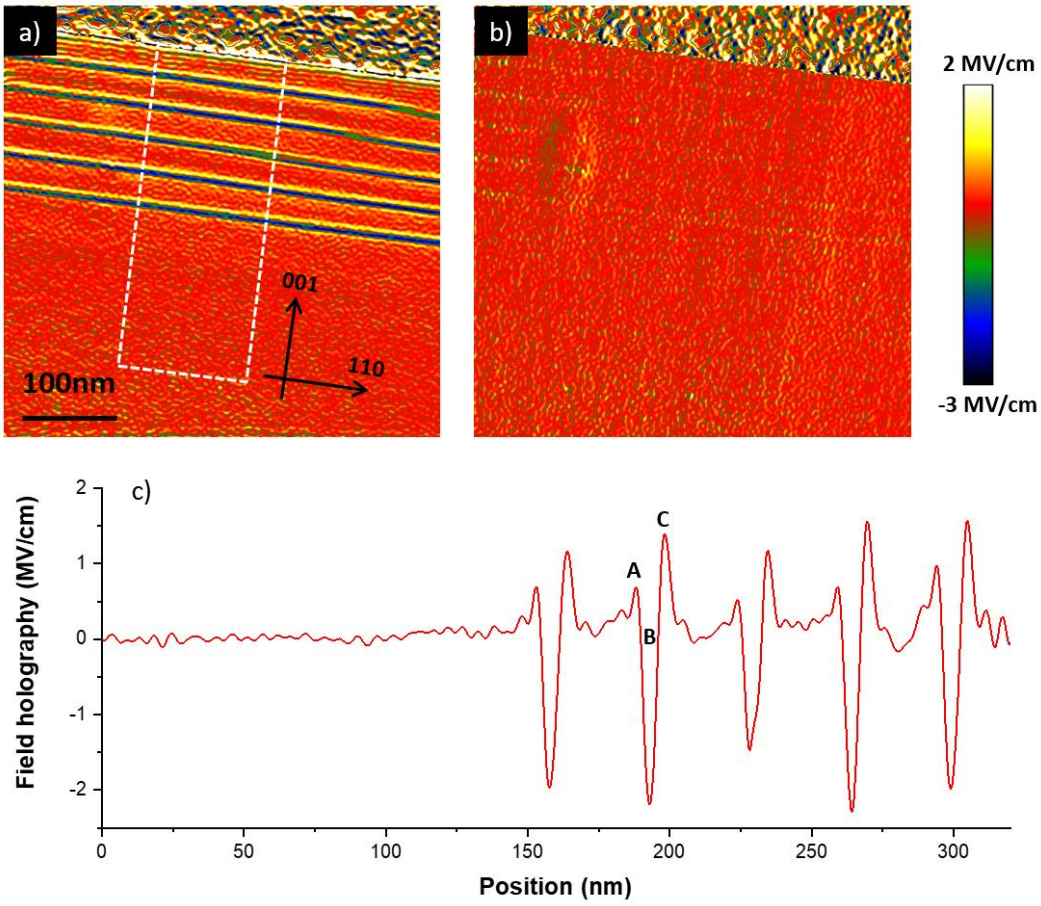

Figure 4-7 : Electric field in $In_{14}Ga_{86}N$ QWs measured by off axis holography. a) and b) Are the components of the field respectively perpendicular and parallel to the layers. c) Profile of the electric field taken across the QW in map (a).

on both side of the InGaN layer indicated as A and C. Such effect does not come from the MIP difference. Boureau & al have shown that by manually removing the MIP influence in

the potential profile, the piezo field can be recovered [36]. Their approach leads to accurate piezo field measurement.

Finally, this holography experiment does not allow to reach resolution good enough to be able to differentiate the contribution of the MIP and the contribution of the piezo potential which is linked to the piezo field by equation 1.1. This experiment will be our benchmark in terms of field values and accessible resolution for field mapping in IIIV materials.

4.1.5 Limits imposed by dynamical diffraction highlighted by DPC

With electron holography, despite the quality of the measured potential, in terms of electric field, the accessible resolution does not allow to separate the contribution of the MIP from the piezoelectric potential. Therefore STEM-based field measurements were explored to try to improve the spatial resolution. In electron holography, the dynamical diffraction is an issue but the plane wave used in holography is an asset as a slight tilt away from zone axis permit to suppress the dynamical diffraction. As previously discussed, in STEM we use a convergent probe, so field measurements with DPC STEM will be more influenced by the dynamical diffraction and that is what we will show in this part.

DPC was done in different orientations to show the limit imposed by diffraction in STEM field measurement. To begin with, the convergence angle was set to 3.2mrad and the camera length to 1.15m. With the 110nm thick sample and an expected field of 2.2MV/cm in the wells, the deflection was calculated using equation 1.26 to be 70µrad. The expected shift of the transmitted on the detector is about 80 µm. As a comparison, the inner radius of the detector is 1.5 cm. A DPC map presented in Figure 4-8-(c) was acquired on [1-10] zone axis. Then the sample was tilted 5° around the [001] axis and less than 1° around the [110] axis in order not to lose resolution in projection. The maps are presented in Figure 4-8-(b). Using equation 1.15 the loss in resolution for 1° on a 110nm thick sample is calculated to be 1.9nm. Then the sample was tilted 5° away from zone axis but in the other direction. The convergence angle was set to 1.09 mrad and the camera length set to 2.3 m. With these parameters the expected shift is 160 µm. Again, it is a small fraction of 3 cm radius of the detector. A DPC map was acquired in this orientation and is presented in Figure 4-8-(a). For more clarity average profiles were taken across the wells and are presented in (d). The map (a) taken on axis has been influenced by the dynamical diffraction and the QWs are not clearly observed. The signal we detect is dominated by the dynamical diffraction and even with an averaged profile the wells are not visible. A second map acquired off zone axis present a periodicity but the shape of the field profiles is far from our expectation. As the

measurement is sensitive to the dynamical diffraction it is more likely that the periodicity comes from diffraction periodicity due to strain or lattice changes. Finally, by changing the orientation and reducing the convergence angle we manage to obtained a DPC map where the wells are visible. The profile taken across this map shows a trend close to the one expected. There is a peak on the right side of each well, which can be explained by the MIP step then the signal drops down in the wells. Here again the contribution the piezo effect and the MIP cannot be separate.

As the QWs studied are 7 nm wide, measuring the field on axis could prevent loss of resolution by projection. However, this DPC experiment shows that diffraction dominates the behavior of the transmitted beam intensity when trying to measure field on axis. The results also show that by tilting the sample along the wells, low diffracting condition can be found and STEM measurement can be performed. But to reach such low diffracting condition the convergence angle was decreased. Low convergence angle plus sample tilt leads to lose in resolution and in this case, the MIP influence cannot be separated from the piezo one.

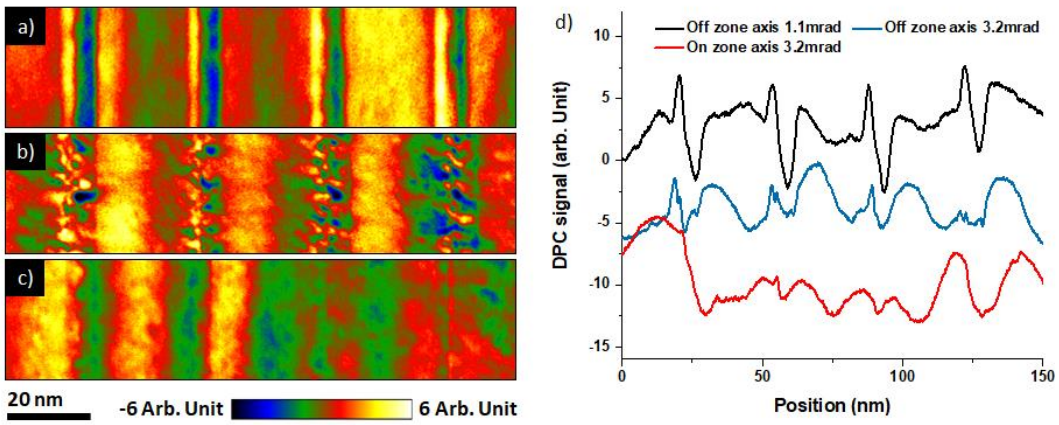

Figure 4-8 : Influence of the sample orientation on the DPC signal measured across the QWs. a) DPC map taken 5° away from zone axis with a convergence angle of 1.09mrad. b) DPC map taken 5° away from zone axis with a convergence angle of 3.2mrad. c) DPC map looking down the [1-10] zone axis with a convergence angle of 3.2mrad. d) Profiles of DPC signals taken across the three DPC maps.

4.2 Multi-slices simulation of diffraction pattern

In order to know if the diffraction pattern experimentally obtained correspond to the theory prediction, diffraction patterns were simulated using µSTEM. The way the simulation is run and the parameters used are detail in section 1.6. In the previous section it was shown that the electric field measured in InGaN has several origins which are the MIP and the piezo effect coming from the combination of polarity and strain. To understand better how each source of field influence the diffraction pattern, the simulation started taking only the MIP into account then only a piezo-field. To finish both were added together in order to have a simulation as close to reality as possible to understand better how to process the data. These three simulations will be detailed in this section.

4.2.1 Simulation with only mean inner potential influence

The first results presented are from a simulation of the GaN/InGaN structure where the potential only depends on the atomic potential and its distribution. Before running the simulation, the transmission function given by µSTEM from the tailored structure created using the script in appendix C. This transmission function is proportional to the potential (see equation 1.6). Figure 4-9-(a) shows a profile taken across the 2D transmission function. The transmission function presented here is the change in phase that the electron wave undergoes when traveling the 5.5Å thick slice. The step-in phase in the middle of the profile correspond to the InGaN layer. From this change in phase, using equation 1.6 the equivalent potential can be calculated. The results are gathered in Table 4-3, the potential step between the GaN and the $In_{0.14}Ga_{0.86}N$ is 0.4V in µSTEM. There are a range of different steps of potential using the different methods. The one obtained by simulation will be considered to be correct within the order of magnitude and the key point is the effect of the step in potential on the diffraction pattern.

The simulated beams presented in (c), (d) and (e) are respectively from the GaN area and at interfaces 1 and 2. For more clarity, horizontal profiles of the intensity in the three beams are presented in Figure 4-9-(b). From the beams and the profiles, it can be noticed that at both interfaces, no rigid shift occurs but the intensity inside the beam is redistributed. The behavior here is the same as the one shown earlier with the SiGe layer in chapter 4. The step in phase i.e. step in potential leads to complex redistribution of intensity at the vicinity of the $GaN/In_{0.14}Ga_{0.86}N$ interface.

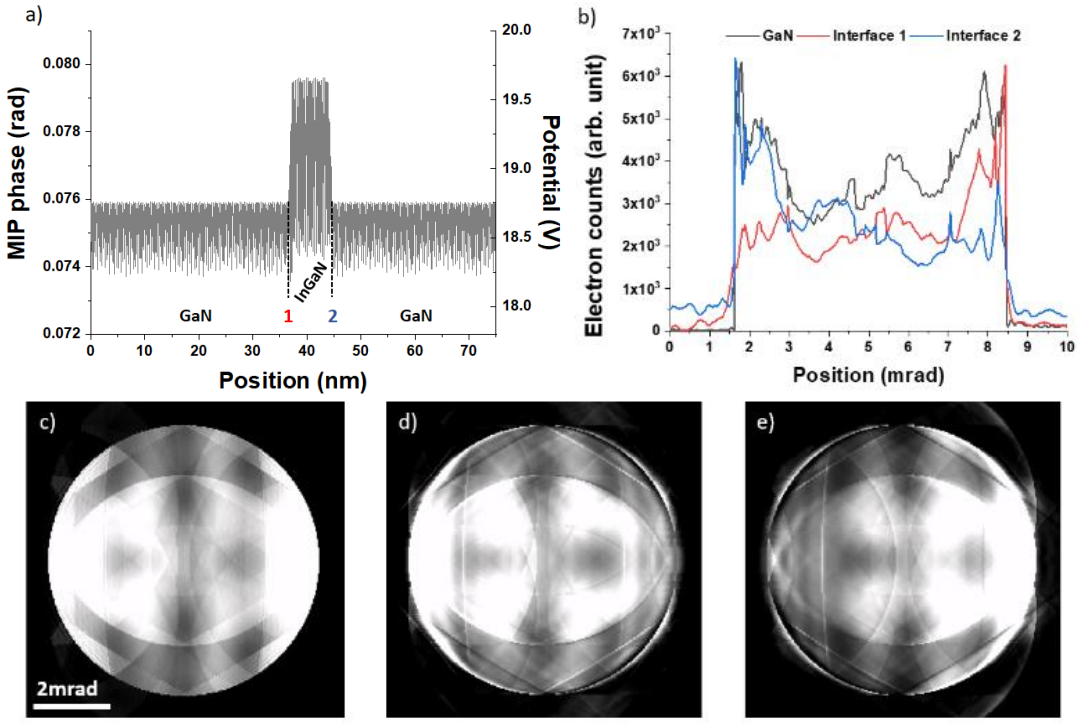

Figure 4-9 : Transmitted beam simulation at the vicinity of an $In_{0.14}Ga_{0.86}N$ QW with precession. a) Average profile of the transmission function. The low level is the GaN and the high level is the $In_{0.14}Ga_{0.86}N$. b) Profiles taken across the beams presented in (c), (d) and (e) which are respectively a transmitted beam simulated in the GaN, at interface 1 and at interface 2.

	GaN	**$In_{0.14}Ga_{0.86}N$**	**MIP step**
MIP_{IAA} + Strain	19.51V	19.70V	0.19V
MIP_{DFT} + Strain	16.9V	17.47V	0.57V
µSTEM	18.7V	19.1V	0.4V

Table 4-3: Comparison of the potential calculated from literature and µSTEM. MIP_{IAA} and MIP_{DFT} are calculated from isolated atoms approximation and density functional theory. µSTEM mean inner potential is calculated from the transmission function. All three InGaN mean inner potential were calculated using equation 1.6.

4.2.2 Simulation with only the piezo field influence

In addition to the change of MIP in the InGaN QWs, a piezo field is expected. This piezo field is present in the 7nm wide layer. To see the effect of only a piezo field on the transmitted beam, simulation was run on a GaN matrix on which a piezo field was added. To do so, an artificial change in phase was inputted to µSTEM. The GaN bulk structure used for this simulation is 3.2 x 805 x 5.5Å^3.

For the first simulation of this section, what is qualified as a wide piezo field was created. For an accelerating voltage of 200 kV and a convergence angle of 3.2 mrad, using equation 1.20, the probe size is calculated to be 3 nm. In this simulation the piezo field i.e. the phase ramp is present over 40 nm. Thus, the probe is more than ten times smaller than the area where the phase varies. To add a piezo field to the simulation an additional transmission function was created. The script use to create such transmission function is presented in appendix C. The field expected in the wells is -2.2 MV/cm, this electric field over 400 Å represent a change in potential of 8.8 V. Using equation 1.6, in a 5.5Å thick structure this represents a phase difference of 8×10^{-3}rad. The transmission function of this 5.5Å thick structure is presented in Figure 4-10-(a). With the total simulation thickness of 110nm and a field of 2.2 MV/cm a shift of 2.4 pix is expected using equation 1.26 and 1.28. When comparing a beam in the zero-field area with a beam in presence of the electric field, a rigid shift is noticed. Figure 4-10-(b) is a comparison of the two beams, a horizontal rigid shift of 2 pixels is present. Having a 40nm wide area of constant electric field allows to reach a rigid shift condition with a convergence angle of 3.2mrad and an aberration free probe.

The second simulation that was run is closer to the case of the studied InGaN QWs. In this second simulation the transmission function includes a 70 Å wide area with a piezo field of -2.2 MV/cm representing the well and a 308 Å wide area with a field of 0.5 MV/cm. The GaN barrier between to wells is supposed to be 280 Å but to suppress the discontinuity at the border of the structure this width was chosen so the phase goes back to the initial level. The second transmission function is presented in Figure 4-10-(c). In this condition the probe is only two times smaller than the area with electric field. The simulated beams in the area with field present a redistribution of intensity. Figure 4-10-(d) compare a beam simulated with no field and one in the 70Å wide QW where the redistribution of intensity is noticeable.

This simulation shows that even without the influence of the MIP and without any aberration of the probe, the rigid shift condition cannot be reach in the 7nm wide QW with a convergence angle of 3.2mrad.

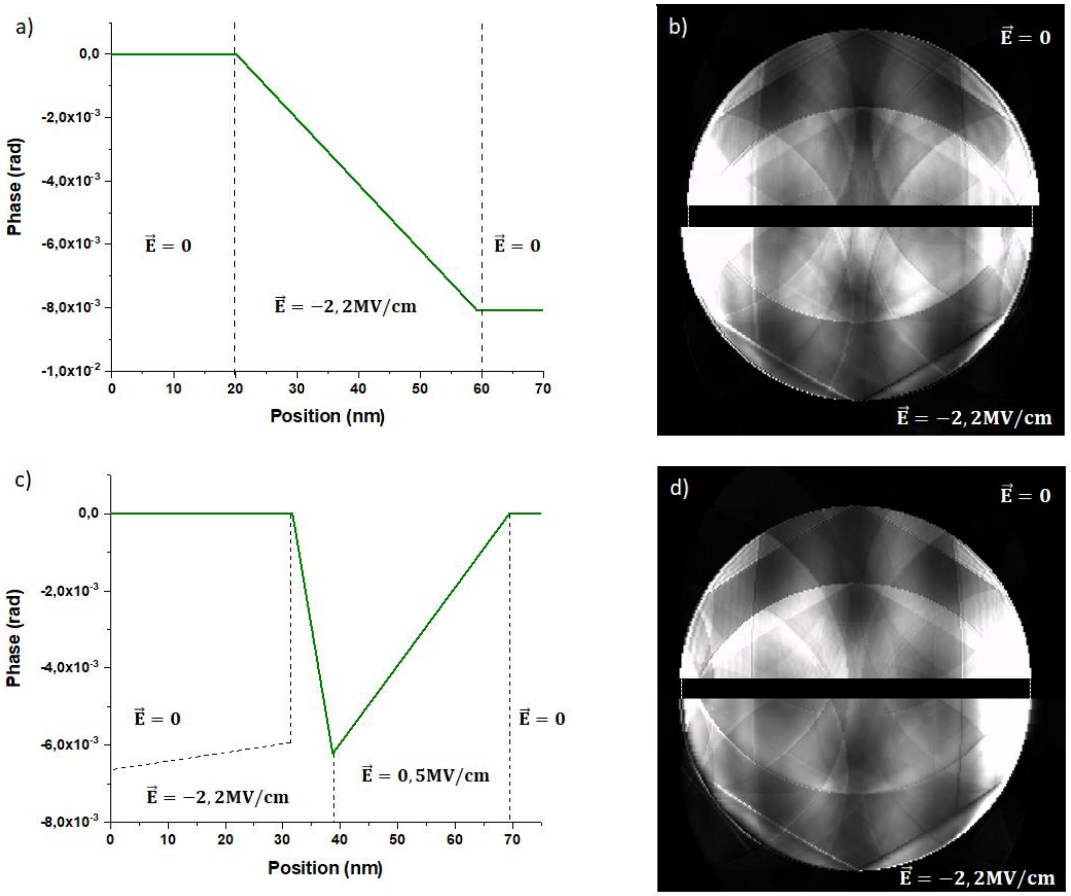

Figure 4-10 : Simulation of the influence of a pure piezo-field on the transmitted beam. a) Transmission function of a 5.1 Å thick slice, in the "wide piezo" case; the piezo field is constant over 40 nm. b) Comparison of the beam in the region with no field and in presence of the piezo field showing a rigid shift. c) Transmission function of a 5.1 Å thick slice, in the "thin piezo" case; the piezo field is constant over 7 nm. d) Comparison of the beam in the region with no field and in presence of the piezo field showing only a redistribution of intensity.

4.2.3 Simulation with mean inner potential and piezo-field combined

To obtained a simulation closer to experiment, both the MIP and piezo field contribution are now included. The structure is the same as the one presented in section 4.2.1. For this last simulation, an artificial transmission function was input into µSTEM so the piezo field is accounted for. This transmission function represented as the back plot in Figure 4-11 is equivalent as the one presented in Figure 4-12-(c). The plotted data in black has a constant potential area which is the zero-field reference, then the 70 Å wide area with a field of -2.2 MV/cm and the barrier area with a positive field of 0.5 MV/cm. The total transmission

function is presented as the red profile in Figure 4-11. The plotted data in blue is the transmission function of the atomic structure, it takes into account the MIP.

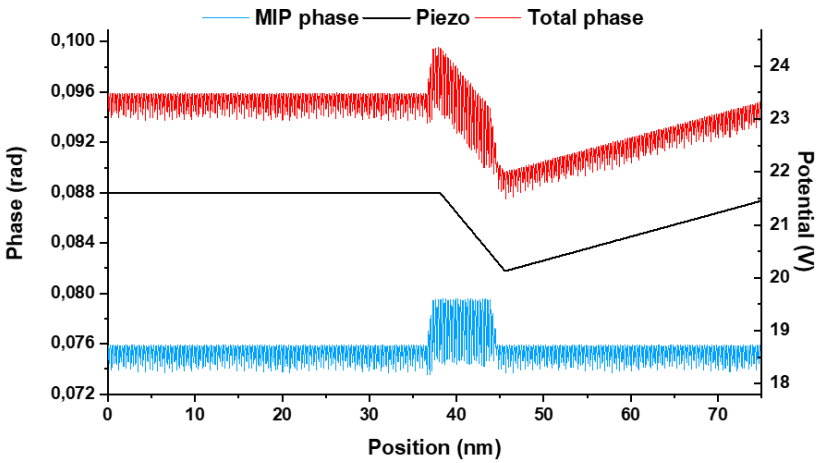

Figure 4-11 : Transmission function in µSTEM with piezo-field and MIP. Profile of the projected transmission function taken across the slice. The scale on the left is the projected phase across the slice and on the right, it is the equivalent potential calculated using equation 1.6. For more clarity the black and red plot are displaced. In blue, the profile of the mean inner potential calculated by µSTEM. In black, the piezo potential added to the simulation. This piezo potential was estimated using Nextnano (see Figure 4-4 and Figure 4-10–c). In red, the sum of both.

The previous simulation already showed that the 7nm wide layer is too thin to allow a rigid shift of the beam due to the piezo field in NB-STEM mode. This more complete simulation tends to show how the redistribution of intensity in the well differs from the one at the interface. The beam presented in Figure 4-12-(a), (b) and (c) have been simulated in the GaN, in the InGaN layer and at the right interface on the transmission function. The profiles in (d),(e) and (f) have been taken across the beams. The beam in GaN has a quasi-symmetric distribution of intensity. Then once the probe is incident on the InGaN, the intensity is redistributed with an intense peak of intensity that appears on the right side of the beam. Then the beam taken at the right interface presents also a peak of intensity at its right edge plus there is a thin low peak at the left edge. This peak on the left is the signature of a potential discontinuity i.e. an infinite electric field.

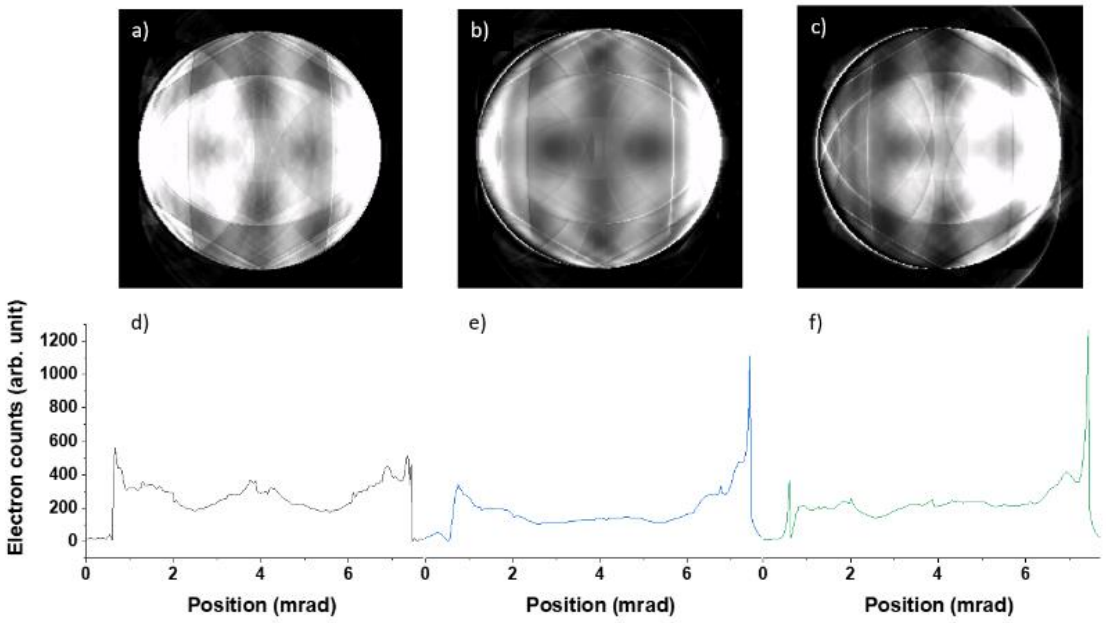

Figure 4-12 : Simulation of the influence of piezo field and MIP on the transmitted beam. a) Transmitted beam simulated in the GaN. b) Transmitted beam simulated in the InGaN layer. c) Transmitted beam simulated at the interface of InGaN and GaN. d) Profile taken across the beam in (a). e) Profile taken across the beam in (b). f) Profile of the beam in (c).

This simulation shows that no rigid shift is expected in the $In_{0.14}Ga_{0.86}N$ with a convergence angle of 3.2 mrad. The redistribution of intensity occurs in the simulation even with an aberration free probe. From this simulation, we no more expect to experimentally obtained a rigid shift in the layers with a convergence angle of 3.2 mrad. Nevertheless, the redistribution of intensity in Figure 4-12-(e) is different than the one in (f). Therefore, using a CoM processing should allow to detect a difference of shift in the well compare to the shift at the interfaces.

4.3 Piezo field measurement by 4D-STEM

As the thickness of the InGaN sample is 110 nm and the piezo field is -2.2 MV/cm, using equation 1.26 the deflection angle is calculated to be 70 µrad. This deflection angle is comparable with that induced by the pn junction in chapter 3. Here the electric field is more intense (-2.2 MV/cm versus 0.7 MV/cm) is present in a much narrower area than the depletion region of the junction (7nm versus 80nm).

4.3.1 Field measurement in NB-4D-STEM mode

For the first experiment, the beam convergence was set to 1.1 mrad, the camera length to 3 m and the Oneview camera record with a binning 4 (1024pix²). In this condition, using equation 1.26 and 1.28 with a pixel size of 15 µm, the deflection of the beam should appear on the detector as a shift of 7 pix. The current of the probe was 100pA and the dwell time was 0.25s, with this combination of parameters, the beam is bright. The results of this experiment are presented in Figure 4-13. The transmitted beam presented in (a) does not have strong dynamical effects in it. The sample was tilted 7° away from zone axis. The tilt is done around the [001] axis but a slight tilt (less than a degree) around the [010] axis was necessary to found such low diffracting orientation. From the profiles presented in (b) it can be assessed that no rigid shift has occurred. Also, a slight redistribution of intensity can be noticed in the profiles taken at the interfaces (Figure 4-13-b). Regarding the beam in the InGaN no shift nor redistribution of intensity can be noticed. Therefore, the data were processed using only the CoM. The field map obtained is shown in Figure 4-13-d. The field we measure is periodic across the QW. For more clarity, an average profile of the field is presented in (e). The profile shows positive peaks at the left edge of the QW, that peaks have values in the range of 0.5±0.1 and 1.1±0.1 MV/cm. Then there are negatives peaks at the right edge of the wells. The negative peaks have values in the range of -1±0.1 MV/cm and -0.7±0.1MV/cm. The error of measurement is estimated by calculating the standard deviation in a zero-field area. In this profile, the contribution of the piezo field is not visible. Between the positive and negative peaks, a constant negative field is expected in the wells. The resolution of this experiment does not allow to measure the piezo field contribution. However the reproducibility of the measurements is good.

To increase the spatial resolution of the experiment, the convergence angle was increased to 3.3 mrad by changing the C2 aperture from 10 µm to 30 µm. The spatial resolution of our experiment is increased in theory by a factor of 3. Using equation 1.20 that takes into account the Airy rings to provide 95% of the total beam intensity, the probe diameter is now estimated to $d_{0.95} = 2.97\ nm$. The results from this new data set are presented in Figure 4-14. The transmitted beam in the GaN substrate is presented in (a). A HOLZ line is present in the beam. To find this orientation the sample was tilted 5° around the [001] direction and a tilt of 1° around the [010] direction was necessary to found this orientation where the dynamical

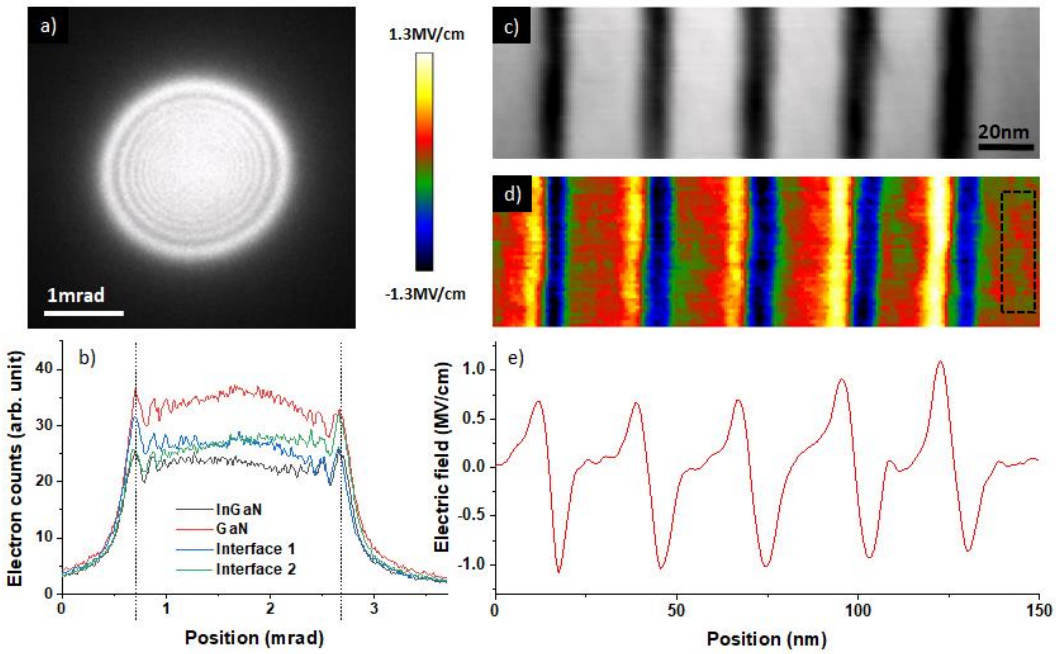

Figure 4-13: Field mapping of InGaN QW NB-4D-STEM with convergence angle of 1.09 mrad. a) Transmitted beam in the GaN barrier. b) Comparison of the profiles of the beam in the GaN, in the InGaN and at both interfaces of a QW. c) Brigth field image reconstruced from the 4D-STEM data set. d) Field map of the five QW. The shift of the transmitted beam was obatined using CoM. The dashed rectangle is the area used for the standard deviation. e) Profile of the electric field taken across the five QW.

diffraction is not a limit. Again equation 1.15 gives a loss in resolution of 1.9 nm for 1° tilt and a 110 nm thick sample. The other parameters are the same as previously so the expected shift on the camera is 7 pixels. Looking at the profiles in Figure 4-14-(b) it can be seen that there is no rigid shift of the beam when the beam is in the QW, so CoM was used once more. The field map calculated is presented in (d) below the BF image extracted from the same data set. The profile in (e) was taken across the QWs. From this profile we can see the quantitative value of field. As in the previous experiment, at the edges of the wells, a positive peak (1 MV/cm) and a negative one (-1 MV/cm) are measured. Thus, despite having improved the spatial resolution, the contribution of the piezo field cannot be separated from the MIP one in experiment.

With these two NB-4D-STEM experiments, periodic field profiles were obtained but the piezo field influence seems to be covered by the MIP influence. With the convergence angle of 1.1mrad the spatial resolution was worse than with 3.3mrad. But with 3.3mrad the diffraction has a stronger influence so the sample must be tilted further away from zone axis.

The tilt around the [110] direction that is required to avoid diffraction effect leads to a loss in resolution by projection. In the end, neither of these two experiments allows to measure

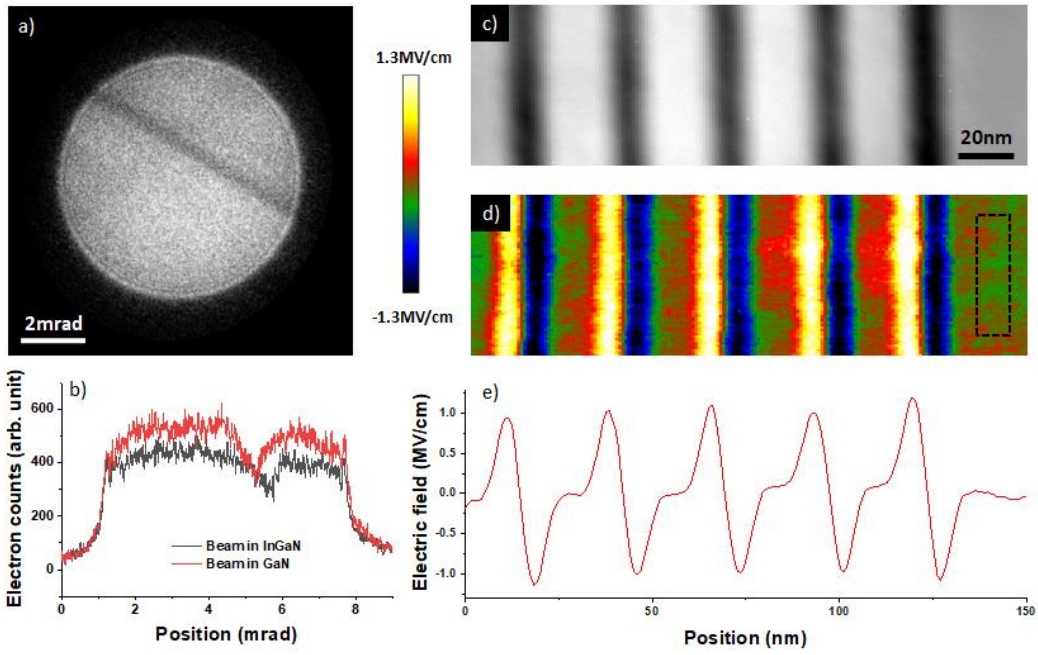

Figure 4-14 : Field mapping of InGaN QW NB-4D-STEM with convergence angle of 3.3 mrad. a) Transmitted beam in the GaN barrier. b) Comparison of the profiles of the beam in the GaN, in the InGaN. c) Brigth field image reconstruced from the 4D data set. d) Field map of the five QW. The shift of the transmitted beam was obatined using CoM. The dashed rectangle is the area where the standard deviation was calculated. e) Profile of the electric field taken across the five QW.

the piezo electric field inside the quantum wells.

4.3.2 Field measurement in HR-4D-STEM mode

In order to increase the resolution, the TEM was operated in standard HR-STEM mode. The convergence angle was set to 17mrad and the sample was viewed down the [010] zone axis. The camera length was set to 580mm and the diffraction pattern is record on $512pix^2$. With these parameters, the expected shift on the detector is less than a pixel. Nevertheless, we acquired a data set in these conditions as CoM processing gives shift with sub-pixel precision.

The results are presented in Figure 4-15. In (a) and (b) the beam in GaN and InGaN are shown. It can be seen that with an HR convergence angle when looking the sample on axis,

the quantity of diffraction contrast present in the transmitted beam is very important [49]. The edge of the transmitted beam cannot be clearly defined. The data were processed using only CoM. The CoM shift is shown in (d) bellow the BF image extracted from the same data set. Figure 4-15-(e) shows the profile of the CoM shift expressed in pixels taken across the three InGaN layers. The BF image shows three InGaN layers well contrasted with the GaN barriers so the resolution of the experiment is good enough to see 7nm wide layer. Regarding the CoM shift, the signal is periodic across the three layers. However, the evolution of the shift is not as the one expected from the field. The maximums of shift are at the right of the layers and the minimums are at the left. This shift is clearly dominated by other properties than electric field. The contrast in a transmitted beam can be influence by the strain, the thickness variation, the lattice bending, and whatever defects that are present in the lattice. In the case off InGaN QWs many parameters change as the probe goes from GaN to InGaN. Especially, strain appears because of the difference of lattice parameter between InN and GaN. Also, some artefact might come from the sample damaged by the intense focused beam.

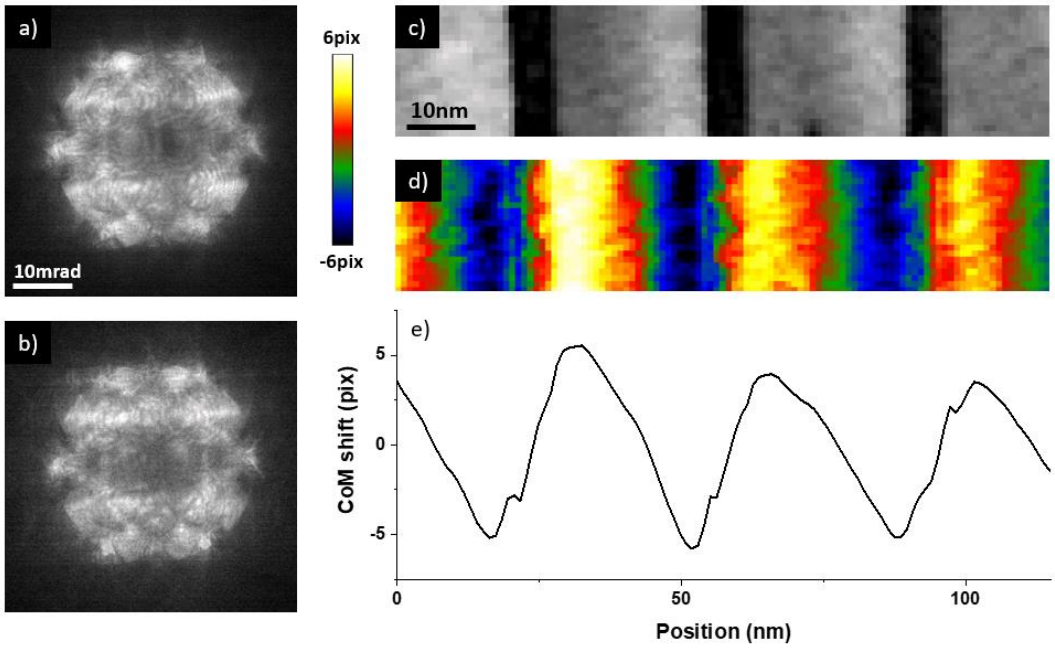

Figure 4-15 : Field mapping of InGaN QW with HR-4D-STEM. a) Diffraction pattern in the GaN substrate. b) Diffraction pattern in an InGaN layer. c) BF image reconstruct from the 4D data set. d) Field map obtained using CoM processing. e) Field profile taken across the 3 layers showing the periodicty of the measurement

Sample damage will be detail in section 4.4.

This HR-STEM technique was resported to have been successful in a GaAs pn junction [16]. Here, the beam goes from a pure GaN to an alloy with 14% of indium. The change of

materials makes this experiment more challenging. Some properties such as strain and MIP are completely different from GaN to InGaN and will have an influence on the diffraction pattern comparable to the piezo field [66]. The parameters use here allows in theory to reach very good resolution but the quantity of information contained in the transmitted beam is such that the different contribution cannot be separated. If this data was to be interpreted, very sophisticated simulation and processing algorithm would be required to take into account the effects of all the overlapping beams.

4.3.3 Artefacts from lamella relaxation

In Chapter 2, the influence of thickness variation as an artefact of 4D-STEM experiment was discussed. The InGaN sample contains strained layers. It is known that the TEM lamella edges have a tendency to relax. This relaxation is due to the fact that the lamella has been extracted from a bulk sample. Once the TEM lamella is extracted, at the edges, the strained layer relaxes [123], [124]. The schematic presented in Figure 4-16 depict the lamella relaxation. Equation 1.38 gives the link between the gradient of thickness and the deflection angle due to it. From the piezo field in the InGaN layer with a thickness of 110nm a deflection of 70µrad is expected. Beam deflection can also be caused by a thickness gradient. In our InGaN sample at 200kV acceleration voltage, to obtain a deflection angle of 70µrad, using equation (1.39) from Wu et al [77], the gradient of thickness has to be equal to 1.41. This is equivalent to an angle of 54°. Assuming that the lattice relaxation appends at both top and bottom surfaces, this is equivalent to the angle $\delta = 27°$ in Figure 4-16. The following

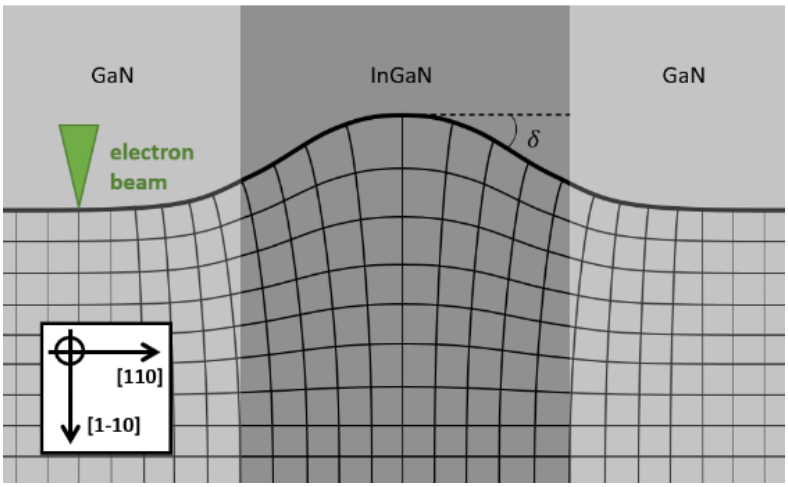

Figure 4-16: Schematic of the lattice relaxation at the edge of a TEM lamella. The lattice relaxation has been emphasized.

experiment was run to see if the lattice relaxation can create sufficient angle to induce deflection of the beam comparable to the one due to the electric field.

To have a proof of the relaxation of the InGaN lamella, CBED pattern were acquired in HR-STEM away from zone axis. The sample was tilted along the QW of 5° and 2° perpendicular to the layer. In this orientation with the 17 mrad convergence angle, the transmitted beam is full of HOLZ line. The sample was probed every 6nm, from the middle of one QW to the middle of the next one. The results of this CBED acquisition are gathered in Figure 4-17. The different CBED patterns were taken at the different position represented by the red circle in (a). From (b) to (g) the beam scans every 6nm from the left QW to the next one. The red

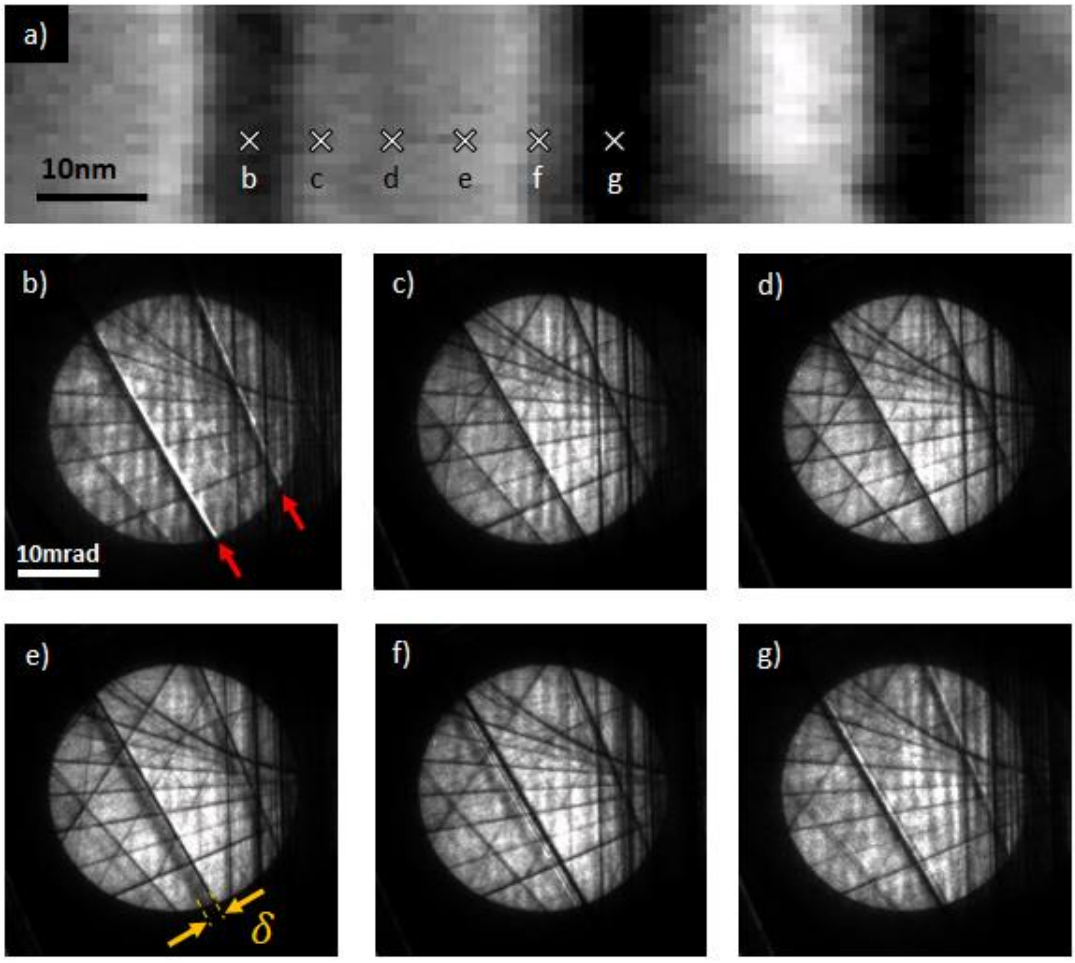

Figure 4-17 : Evidence of lamella relaxation in off axis CBED pattern. a) BF image of the sample, reconstruct from the 4D-STEM data set. The position where the CBED pattern were recorded are represented by the crosses. From b) to g) it is CBED pattern taken from left to right in the BF image. The red arrows in b) point the lines that are influence by the lamella relaxation.

arrows in (b) show the lines we focus on. The HOLZ lines are split which is a typical signature of lattice bending. The distance between the HOLZ lines provides information about the angle between the atomic planes. Therefore, by measuring the maximum distance (in radians) between the lines, the maximum angle δ between the planes can be calculated. From this data set the maximum distance between the lines is equal to 2 mrad therefor $\delta_{max} = 0.11°$. This angle is several orders of magnitude lower than the angle that is required to obtain a deflection comparable to the electric field one.

From this experiment we conclude that the lamella relaxation creates a gradient of thickness. This gradient of thickness is hundred times lower than what is required to create a deflection of tens of micro-radians. So, in the 4D-STEM measurement done on the InGaN layers, the deflection due to thickness variation can be neglected.

4.4 Improvement brought by new generation of fast cameras

It is known that the InGaN can be damaged by the electron beam. Figure 4-18 gives an insight of how the InGaN sample can be damaged by the beam [49]. Two 4D-STEM data sets were acquired, one with 250ms dwell time and the second with 50ms. Respective transmitted

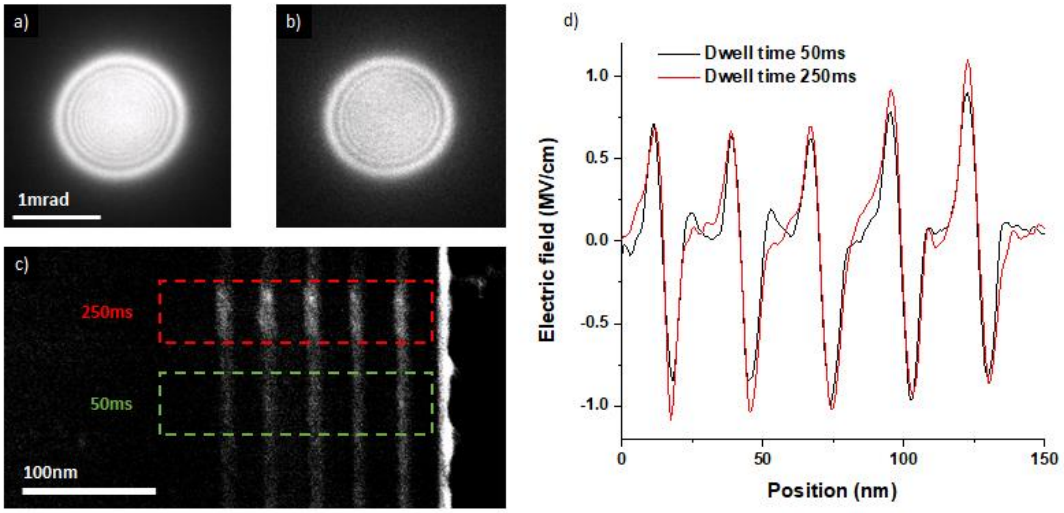

Figure 4-18 : Evidence of beam damage on the InGaN sample. a) 3.2mrad transmitted beam. Recorded with a current of 100pA and 250ms dwell time. b) Same as (a) but the dwell time is 50ms. c) Dark field image of the sample after the acquisition of the two 4D-STEM datasets. The contrast was increased so the damages induce by the beam are visible. d) Electric field profile extracted by CoM from the two datasets.

beams of the experiment are presented in (a) and (b). The orientation of the sample is the same as the one in section 4.3.1 (Figure 4-13). Both beams are homogenous and no HOLZ line are present. The electric field was calculated for the two data set and are presented in Figure 4-18-(d). In this range of dwell time there is no significant changes in the field profiles but looking at the DF image in (c), it is visible that the layers have stronger contrast in the 250ms area. It is due to the formation of In-rich cluster cause by the irradiation. Here we can see that the threshold electron beam dose before damage is observed uses a 100pA beam current and 50 ms dwell time. To reduce sample damage, a new generation of fast camera with high efficiencies offers a solution. As shown in section 2.5 the Merlin camera installed in the Titan Ultimate TEM we used allows measurement 20 times faster than the Oneview camera with the same level of noise. Therefore this method of recording 4D-STEM data sets should simultaneously reduce damage and improve signal to noise.

In this section, 4D-STEM measurements are done at high speed on the InGaN sample using fast Merlin camera. NB-STEM and HR-STEM mode are experienced to see if a low electron dose changes the measured signal.

4.4.1 NB-4D-STEM at high speed

To assess the effects of beam damage on the results, the same experiment as shown in Figure 4-13 was done but this time with shorter dwell times of 1 ms and 10 ms. The two measurements were done on adjacent regions of the sample. The results are presented in Figure 4-19. The convergence angle was set to 1 mrad and the camera length to 2.4 m. The camera is 14 mm² and record 256 pix² frame. With these parameters the transmitted beam covers almost all the camera width as it can be seen in Figure 4-19-(a) and (b). The orientation of the sample is away from zone axis. The sample was tilted several degrees around the [001] axis and less than a degree around the [110] axis. The two beams presented in (a) and (b) have mostly a difference of intensity due to the different dwell times and both present low frequency contrast from diffraction. The expected shift on the detector was calculated using equation 1.26 and 1.28 to be 7 pixels. The data sets were processed using CoM calculation and the field map are presented in (d) and (e) bellow the BF image extracted from the dataset acquired at 10 ms. For more clarity an average profile was taken across the InGaN layer and is shown in (f). The profiles show that the dwell time from 1 to 10s does not changes the trend of the detected field. The field from the dataset acquired at 10ms dwell time seems to be more influence by the interfaces. In the GaN barriers the difference between the two profiles is not significant. Regarding the piezo-electric field the CoM processing does not detect a constant field in the layer. As for the experiment presented in section 4.3,

only the influence of the interfaces is detected. The combination of sample tilt and 1mrad convergence angle gives a resolution that does not allow to separate the piezo effect from the interface influence.

4.4.2 HR-4D-STEM at high speed

Measurements using Merlin camera were also done with high convergence angle. The convergence angle was set to 17mrad, it is a typical value used for HR-STEM. The sample was also tilted a few degrees of axis but with this convergence angle Holtz lines are present in the beam as it can be seen in Figure 4-20-(a) and (b). With this convergence angle it was necessary to set a short camera length, which was set to 115mm. With this camera length and the 256pix² of the Merlin camera the expected shift on the detector is 0.25pix. This shift is smaller than a pixel. Despite the theoretical sub-pixel precision of CoM processing (see chapter 1, section 1.3.5), a 0.25 pixel shift will be difficult to detect especially with all the diffraction contrast present in this orientation. The field map extracted by CoM is presented

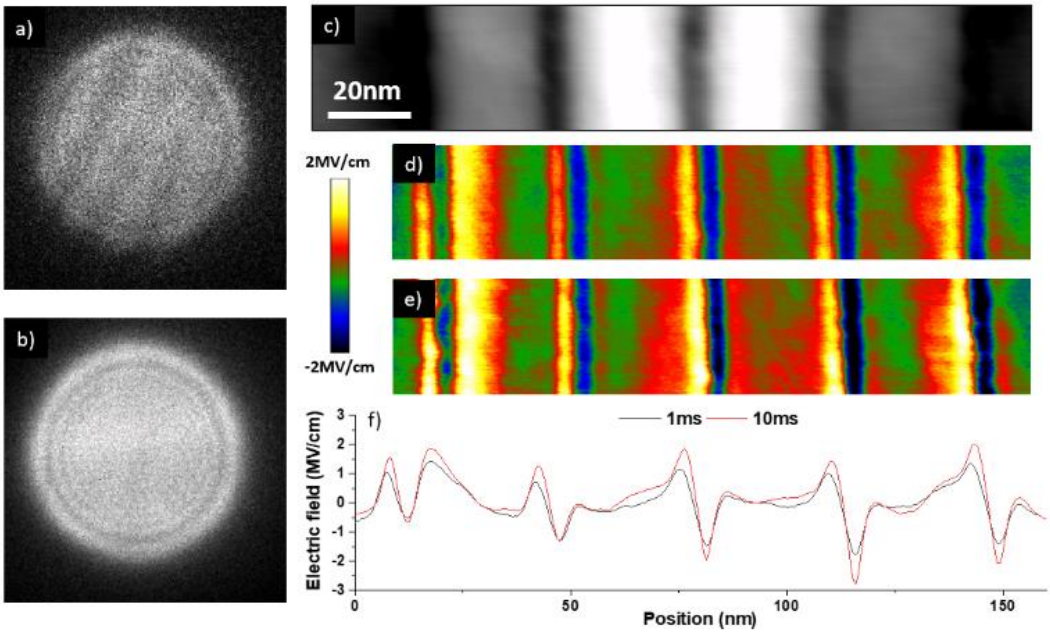

Figure 4-19 : Off axis NB-4D-STEM on InGaN QW using a fast Merlin camera. The acquisitions were performed with a current of 100pA, the convergence angle is 1 mrad and the camera length is 2.4 m. a) Transmitted beam recorded with 1ms dwell time. b) Transmitted beam recorded with 10 ms dwell time. c) BF image extracted from the 10 ms dataset. d) and e) are field map extracted by CoM respectively from the 1ms dataset and the 10 ms dataset. f) Comparison of field profile taken across the layers in the maps d) and e).

in (d). A profile taken across the map is presented in (e). The field calculated from this dataset present strong variation in the GaN barriers where no field is expected. The diffraction contrast in the transmitted beam caused this variation. Regarding the QW the signal is strongly influenced by the GaN/InGaN interface. The signal detected at the interface is in the range of 10 MV/cm. This signal is not due to the MIP but when comparing Figure 4-20-(a) and (b) it seems more reasonable to say that it comes from the change in contrast in the beam due to strain and lattice bending. The resolution gain from 1 mrad to 17 mrad goes with strong diffraction effect leading to artefacts that makes the field profile less periodic than in NB-STEM mode (section 4.3).

The last experiment presented in Figure 4-21, uses the same experimental parameters as the previous experiment and acquired on zone axis. This way there is no loss in resolution by projection, comparing the BF image in Figure 4-20-(c) and the one in Figure 4-21-(c) gives us an insight of how the resolution is improved by tilting the sample on axis. Two 4D-STEM

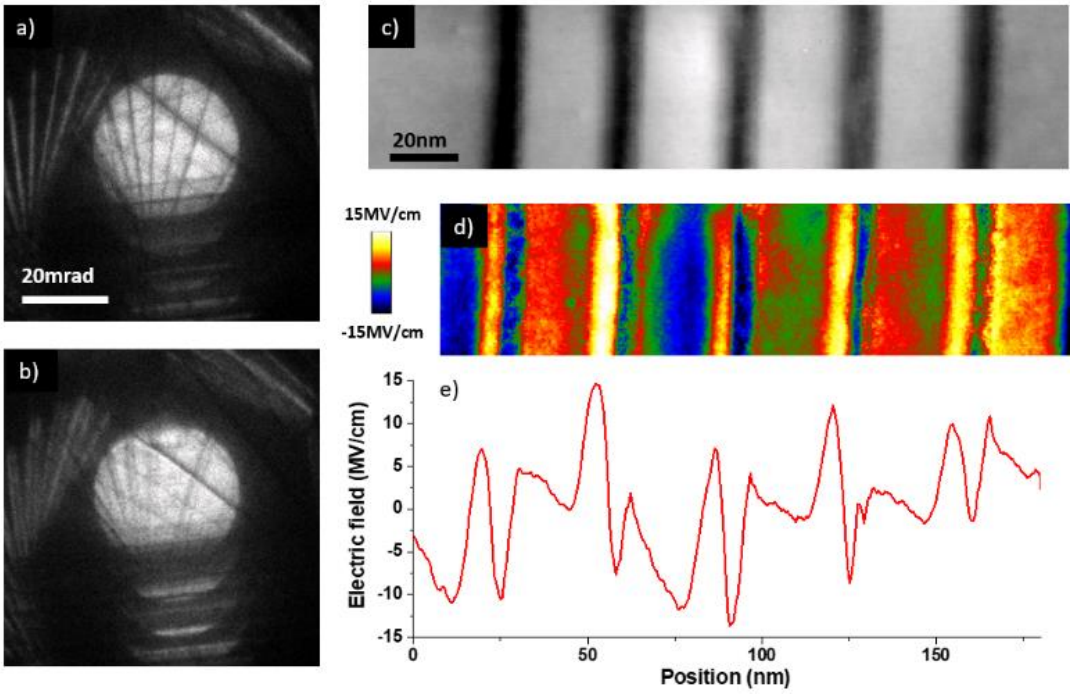

Figure 4-20 : Off axis HR-4D-STEM on InGaN QW using a fast Merlin camera. The acquisition was performed with a current of 100 pA, a convergence angle of 17 mrad and a camera length of 115 mm. a) Transmitted beam recorded with 10 ms dwell time in the GaN. b) Transmitted beam recorded with 10 ms dwell time close to the Gan/InGaN interface. c) BFimage extracted from the dataset. d) Electric field map extracted by CoM e) Electric field profile taken across the layers in the maps d).

datasets were acquired respectively at 1 ms and 10 ms dwell time. Respective diffraction pattern of both datasets are presented in Figure 4-21-(a) and (b). The field was extracted from both dataset using CoM and the field map are presented in (d) and (e). The two maps look similar. The profile in (f) has been taken across the InGaN layers and also shows that the field extracted from both dataset is similar but has nothing in common with the expected electric field. As for the HR experiment presented in the section 4.3.2, the intensity CoM movement depends on many things: electric field, strain, lattice bending and change in composition. The signal we measure is extremely complex to interpret and to separate the effect of the electric field from the other components.

As for the experiment presented in section 4.3.2 the parameters here allow to reach an HR resolution but the complexity of the beam intensity makes the CoM shift uninterpretable. Again, very sophisticated simulation and processing algorithm would be required to interpret the data.

The experiment done with the fast Merlin camera allows us to make electric field measurement on InGaN quantum wells with reduced damages on the sample. The results obtain in this section are similar to the on obtained with the Gatan Oneview. Even at high

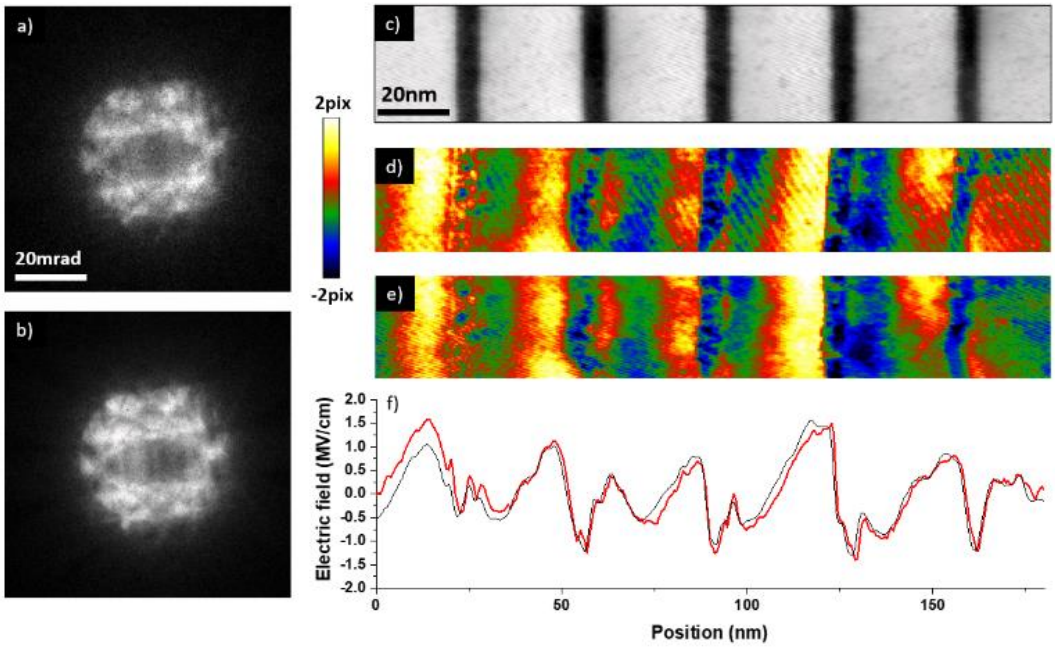

Figure 4-21 : On axis HR-4D-STEM on InGaN QW using a fast Merlin camera. The acquisition was performed with a current of 100 pA, a convergence angle of 17 mrad and a camera length of 115 mm. a) Transmitted beam recorded with 1 ms dwell time. b) Transmitted beam recorded with 10 ms dwell time. c) BFimage extracted from the 10 ms dataset. d) and e) are field map extracted by CoM respectively from the 1 ms dataset and

speed, no compromise made between resolution and diffraction effect allows to separate piezo field from the rest.

4.5 Overcoming diffraction artefacts and inelastic scattering

In the previous sections none of the experiments allowed us to separate the piezoelectric field from the artefacts from the mean inner potential differences. The acquisitions done off-axis lacked spatial resolution. In the experiments performed closer to the zone axis, despite the gain in resolution the results were dominated by diffraction artefacts and inelastic scattering. In order to overcome the inelastic scattering and the diffraction artefacts improvements in data acquisition and processing have been investigated and the results are detailed in this section.

4.5.1 Effect of energy filtering

Electrons inelastically scattered form a halo of electrons around the electron beam. The CoM processing could be influenced by this halo. Experiments were performed using an energy filter such that only elastically scattered electrons were detected.

As for the pn junction in section 2.4.1, energy filtering was coupled with 4D-STEM for acquisition on the InGaN sample. The convergence angle was set to 3.3 mrad the camera length with the GIF was 5.5 m and the Oneview camera record 1024 pix² frame. With these parameters, the deflection of 70 µrad due to the piezo field in the 110 nm thick sample should results in a shift of 9 pixels on the detector. The energy slit was set so the electron energy loss is between zero and 10 eV were detected. The dwell time for each diffraction pattern was 0.1 s. The sample was tilted to a low diffracting orientation. Two acquisitions were run: one with a low current of 10 pA and one with a typical current of 100pA. Beams of both data sets are presented respectively in Figure 4-22 a) and b). From the two data set BF image and field map have been extracted. The BF image extracted from the 100pA dataset is presented in (c). The field map respectively acquired with 10pA and 100pA are presented in Figure 4-22-(d) and (e). A field profile is presented in (f).

The two series acquired with energy filtering does not present much difference. The peak-to-peak signal is close from one another. We estimated the average peak to peak signal to be 1.3 MV/cm and 1.1 MV/cm respectively for the series acquired with 10 pA and the one at 100 pA. The SNR of each map was estimated on the zero-field area (left side of Figure 4-22-

d and e). The results are gathered in Table 4-4. The SNR of these two series show that the bright beam created with higher current lead to less noise. The difference present in the profile (f) are assumed to be due to the limited reproducibility of the techniques and to the fact that the data where not acquired exactly on the same area.

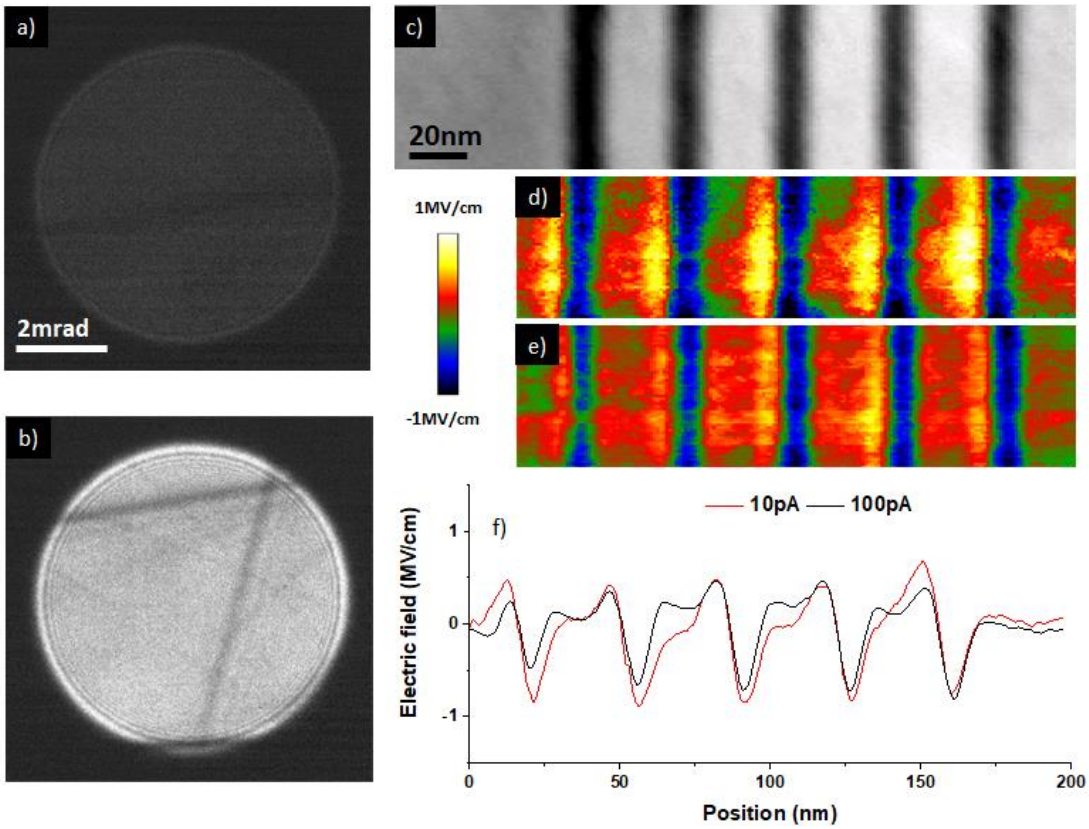

Figure 4-22 : Energy filtered NB-4D-STEM on InGaN quantum wells. The energy loss of electron is from zero to 10eV. a) 3.3 mrad transmitted beam with 10 pA current. Same for b) with 100 pA current. c) BF image reconstructed from the 100 pA dataset. d) Electric field map extracted with CoM from the 10 pA dataset. Same for e) but from the 100 pA dataset. f) Comparison of electric field profile taken across the InGaN layers in both field map.

The energy filtered data are also compared to the data presented in Figure 4-14. The convergence angle of these three series is the same. The SNR calculated for the series without energy filtering is higher than the two obtained with energy filtering. This is not what was expected, when the same experiment was done one the silicon pn junction the energy filtering improved the SNR. As against for the silicon junction, here the unfiltered series was acquired without the GIF. Adding the GIF leads to an increase of the camera length and introduce some image distortion. A longer camera length leads to less electron counts per pixel in the

recorded beam. This can explain the increase in the noise. However, the energy filtering does not allow to separate the MIP contribution from the piezo-field one.

From figure	**5.14**	**5.22**	**5.22**
Energy filtering	No	Yes	Yes
Beam current	100pA	10pA	100pA
Camera length	3m	5.5m	5.5m
SNR	24	9	13

Table 4-4: SNR calculated for both energy filtered series and compared to the series presented in figure-5-14. The parameters that differ from one series to another are remind.

4.5.2 Coupling 4D-STEM with precession

We have seen that using a lower convergence angle such as 1 mrad leads to the formation of a beam that does not have adequate spatial resolution. However, by increasing the convergence angle for better spatial resolution, dynamical diffraction effects dominate. Plus tilting the specimen leads to another loss of spatial resolution. As a solution to these problems, we use precession to combine a higher convergence angle with observation down the [010] zone axis to overcome the loss in resolution.

For these precession experiments, a FEI Themis operated at 200 kV was used. The first data set was acquired with a convergence angle of 3.2 mrad and a camera length of 650mm. The 6 cm² Ceta camera recording with a 1024 pix² frame allows to have two order of diffraction and the beams are not overlapping. The expected deflection of 70 µrad should results in 1.5 pixels shift on the detector. In order to decrease the dynamical diffraction influence, precession was used with a beam tilt 0.25°. In a 110 nm thick sample, a precession angle of 0.25° leads to a reduction in spatial resolution of 0.5 nm which is less than 10% of the width of the QWs.

To assess the quality of the dataset regarding the spatial resolution, the strain was extracted as it was done in Figure 4-2. This strain measurement is detailed in Figure 4-23. Comparing the strain map with and without precession in (d) and (e) shows already how the precession improves the results. For more details, the profiles in (f) compare the strain measured with and without precession. The precession improves the accuracy of the detection of the beam

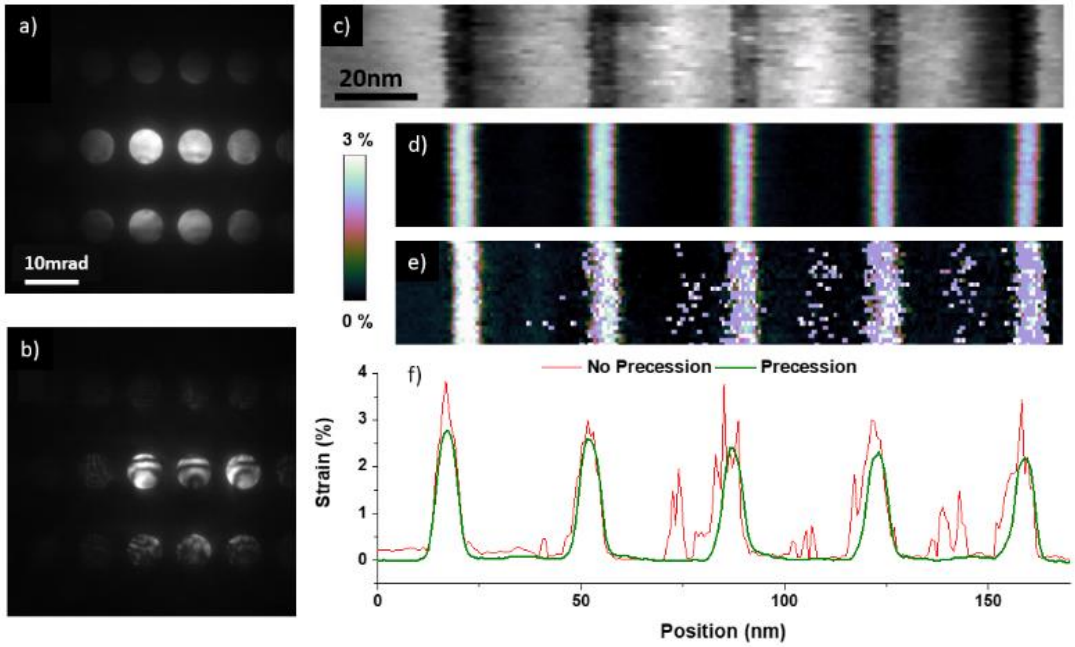

Figure 4-23 : Precession electron diffraction to improve strain measurement in NB-STEM. a) GaN diffraction pattern recorded down the [1-10] axis. The beam was precessed around the optical axis with a tilt of 0.25°. b) GaN diffraction pattern recorded down the same axis but without precession. c) BF image reconstruct from the dataset with precession. d) and e) Are respectively strain map extracted from the dataset with and without precession. f) Comparison of strain profiles taken across the InGaN layers.

position and so the strain evaluation. The values of strain are in agreement with the theoretical values of strain calculated for 14% and 16% of indium which gave respectively 2.27% and 2.60% strain (see Figure 4-2). So, a NB-4D-STEM acquisition on axis with a 3.2mrad convergent beam coupled with precession allows to measure quantitatively the strain in 7nm wide QWs. More importantly, we demonstrate that the data set has an appropriate spatial resolution to measure the strain in the QWs.

Regarding the electric field extraction, the CoM processing was run on both datasets with and without precession. And the results are presented in Figure 4-24. A mask was applied so the CoM is calculated in an area slightly larger than the transmitted beam as presented in Figure 4-24-(a) and (b). The field map extracted from the two datasets are shown in (d) and (e). The field map obtained with precession seems better than the one without precession but still QWs are not easily seen. The comparison of the average field profile in (f) gives a better idea of the improvement that precession offers. Even with an average profile, without precession the measurement of the field in the QWs has not been successful and it is difficult

to even determine their presence. On the other hand, the field profile with precession is now periodic. For each QW, a positive peak and a negative one are present at the interfaces. So, the MIP change is detected. In all the barriers the signal has the same shape. Regarding the

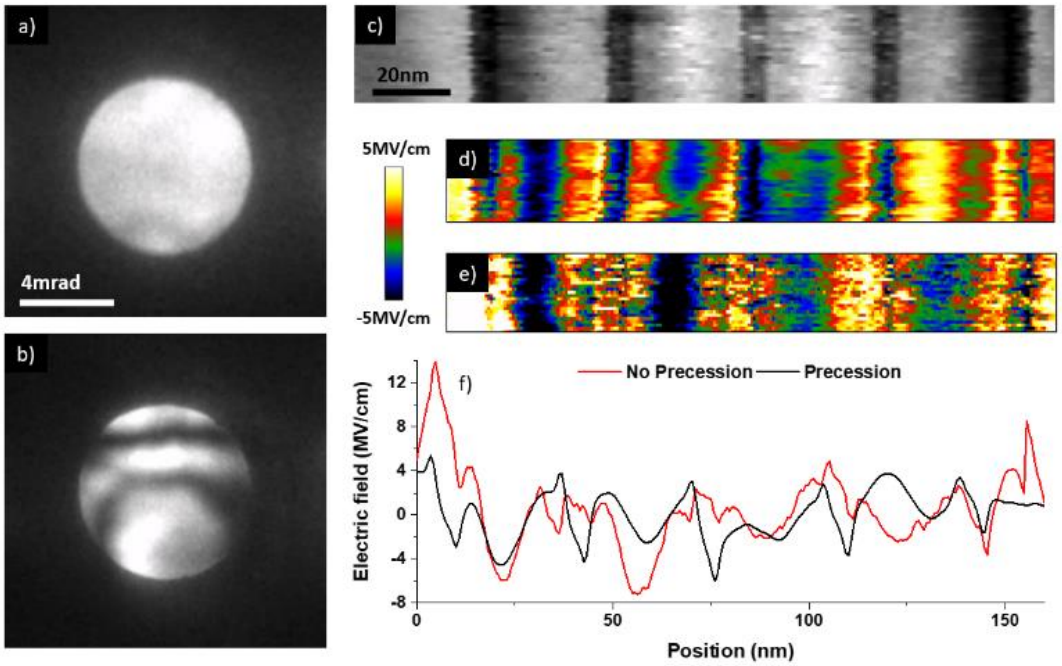

Figure 4-24: NB-4D-STEM coupled with precession for electric field measurement on InGaN QWs. The acquisition parameters are optimized for strain mapping. a) 3.2 mrad transmitted beam recorded with precession. b) 3.2 mrad transmitted beam recorded without precession. c) BF image reconstruct from the dataset with precession. d) Field map extracted with CoM from the dataset with precession. Same for e) but without precession. f) Comparison of field profile taken across the InGaN layers in both field map.

piezo field contribution, it cannot be separated from the MIP change. In the middle of the QWs only a slight change in the slope of the field is noticeable. The dataset is optimized for strain mapping and not field mapping. The expected shift of 1.5 pixel is too small to be correctly detected by the CoM processing.

Camera length	**650mm**	**2.5m**
Beam intensity	5000 ± 120	560 ± 40

Table 4-5 : Beam intensity depending on the camera length

The shift of the beam on the detector is proportional to the camera length (see equation 1.28). In order to increase the sensitivity, the parameters were kept as for the previous experiment but the camera length was increase from 650 mm to 2.5 m. With this value of camera length only the transmitted beam is present on the detector (see Figure 4-25-a). The expected shift due to the piezo-field is now 6 pixels. The field map in Figure 4-25-(d) and the profile in (e) shows that increasing the camera length degrades the detection of the piezo-field. In the middle of the InGaN layers, there is at best a change in the slope of the field. The signal is higher at the edges of the map than in the middle. The profile in (f) shows less periodicity due to the presence of the QWs than the profile obtained with a shorter camera length. Increasing the camera length means that the same 3.2 mrad beam will be record on more pixels. From a camera length of 650mm to one of 2.5m the number of electrons per pixel is divided by almost 15. That can be seen on the profiles in Figure 4-25-(b) which shows the difference of intensity depending on the camera length. The SNR of the diffraction patterns were also calculated for both camera length. Table 4-5 summarized values of SNR. The signal i.e. the beam intensity is a mean value of electron counts in the beam and the noise is

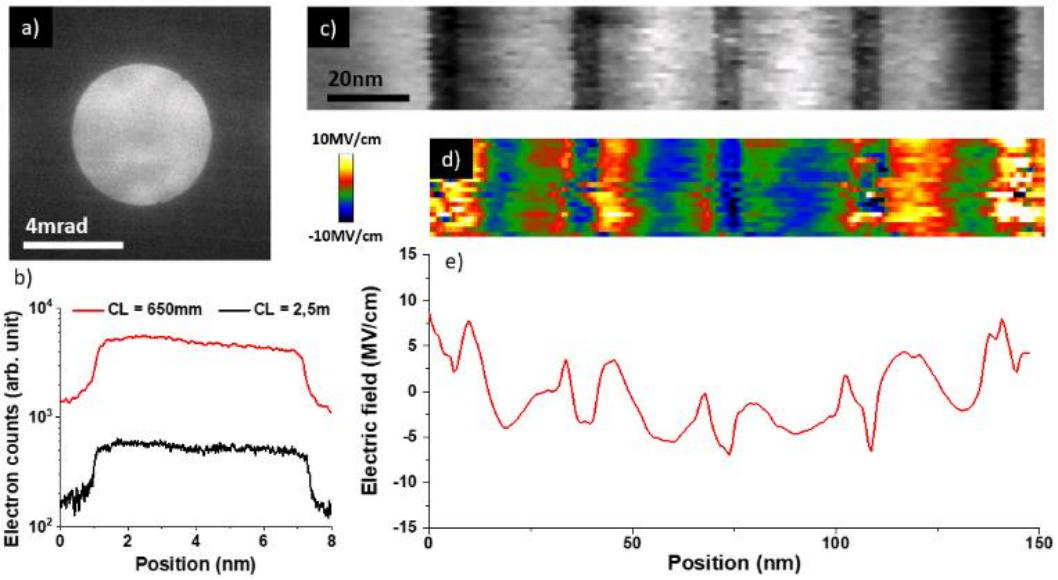

Figure 4-25: Influence of the camera length on NB-4D-STEM coupled with precession in InGaN QWs. Here compared to Figure 4-24, the camera length has been increased so only the transmitted beam appears on the detector. a) 3.2mrad transmitted beam recorded with precession. b) Comparison of the electron count in the transmitted beam with camera length of 650mm and 2.5m. c) BF image reconstruct from the dataset with precession. d) Field map extracted with CoM e) Field profile taken across the InGaN layers in the field map.

estimated with a standard deviation outside of the transmitted beam. In the end the gain of sensitivity induce by the increase of the camera length (equation 1.28) is less important than the increase of the noise of the diffraction pattern. To overcome that limit, an increase of the beam current or the dwell time could lead to better SNR at long camera length. But it was already shown in section 4.4 that increasing the electron doses can damage the sample which would be the advantage of using a fast camera such as the Merlin.

4.5.3 Using template matching to detect the redistribution of intensity

Processing the data with CoM did not allow to separation of the MIP contribution from the piezo-field. In chapter 3 we have seen that the TM detects the beam intensity shift even when only a redistribution of intensity occurs. The field extracted by such processing is no longer quantitative but the measured electric field will still be presented in MV/cm.

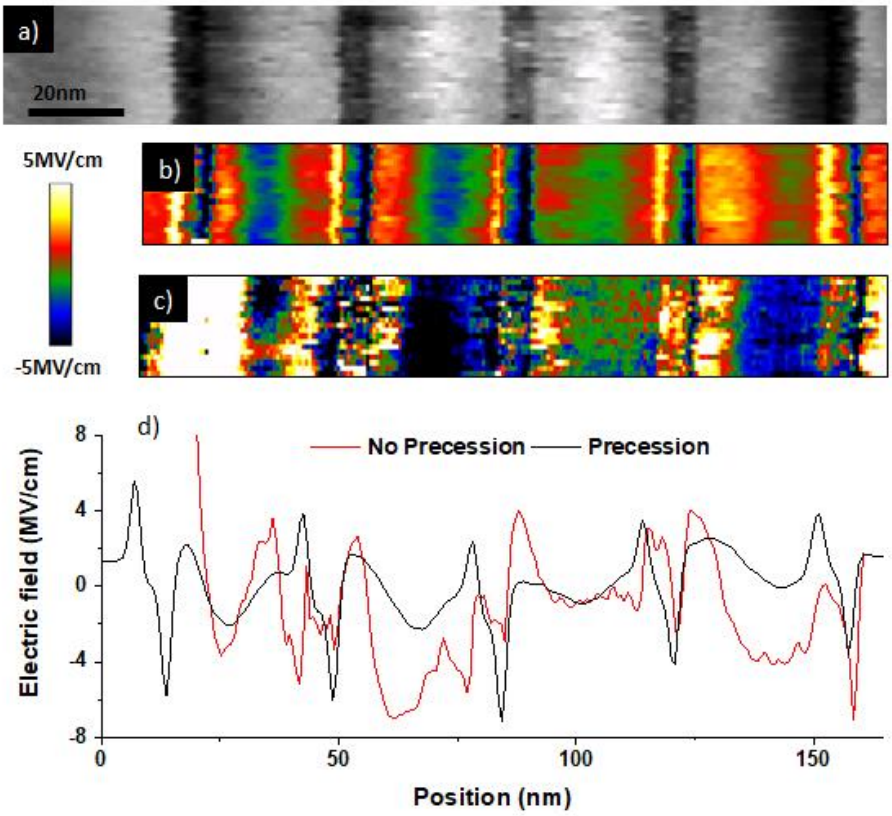

Figure 4-26: TM processing on NB-4D-STEM data set acquired on InGaN QW with and without precession. The acquisition parameters are optimized for strain mapping. a) BF image reconstruct from the dataset with precession. b) Field map extracted with TM from the dataset with precession. Same for c) but without precession. d) Comparison of field profile taken across the InGaN layers in both field map.

The data acquired with the 650mm camera length on the InGaN sample were processed using TM. A mask was applied to the pattern so only the transmitted beam is present in the template (see pattern in Figure 4-24-a and b). The results with TM are presented in Figure 4-26. Comparing the map with and without precession, respectively in (b) and (c) shows that precession improves the precision of the shift detection by TM (as it was the case for CoM). The profile with precession in Figure 4-26-(d) presents signal more periodic due to detection of the QWs than the one extracted by CoM presented in Figure 4-24-(f). The precision of the TM is better than the one of CoM. The standard deviation calculated in a zero-field area is higher for the CoM map (0.59 MV/cm) than for the TM (0.31 MV/cm). The TM stabilized the shift detection compare to CoM. In the middle of the QWs the influences of both interfaces are separated by an almost constant field. Even if the values are not quantitative, it seems that the influence of the piezo field was separated from the ones of the interfaces.

4.5.4 Template matching of whole diffraction pattern

The electric field deviates all the electrons that pass through the sample, so the whole diffraction pattern should be shifted by the field. Instead of applying a mask and detect only the shift of the transmitted beam, we try to detect the shift of the whole diffraction pattern presented in Figure 4-27. From the expansion of the lattice for the InGaN layer in the $\vec{c}$ direction, the diffracted beams g_{001} on the right of the transmitted beam slightly move to the left and in the opposite direction for the diffracted beam $-g_{001}$. The transmitted beam should not be affected by the strain The pattern stays symmetric.

Figure 4-27 shows the results obtained using the TM processing on the whole diffraction pattern. The two datasets, with and without precession were processed and are respectively presented in (c) and (d). With precession the signal is less noisy. The QWs are contrasted with the barriers. The average profiles in (e) gives a better vision of the signal detected by TM. Without precession the QWs are not always visible, there is no periodicity. On the other the signal with precession the QWs are clearly visible. In the barriers the signal varies less than when the TM was applied to the transmitted beam. On each side of the InGaN layer a peak is present, so the MIP influence seems to be detected. But more importantly, a constant field value is detectable in the wells. The field value in the wells is close to the -2.2 MV/cm expected from the simulation and the results seemed very encouraging.

The signal in the barrier has less variation here than when detecting the central beam movement. The TM on the whole pattern will be sensitive to the position of all the beam. In the barriers were there is no field variation but only small changes in the contrast of the beam,

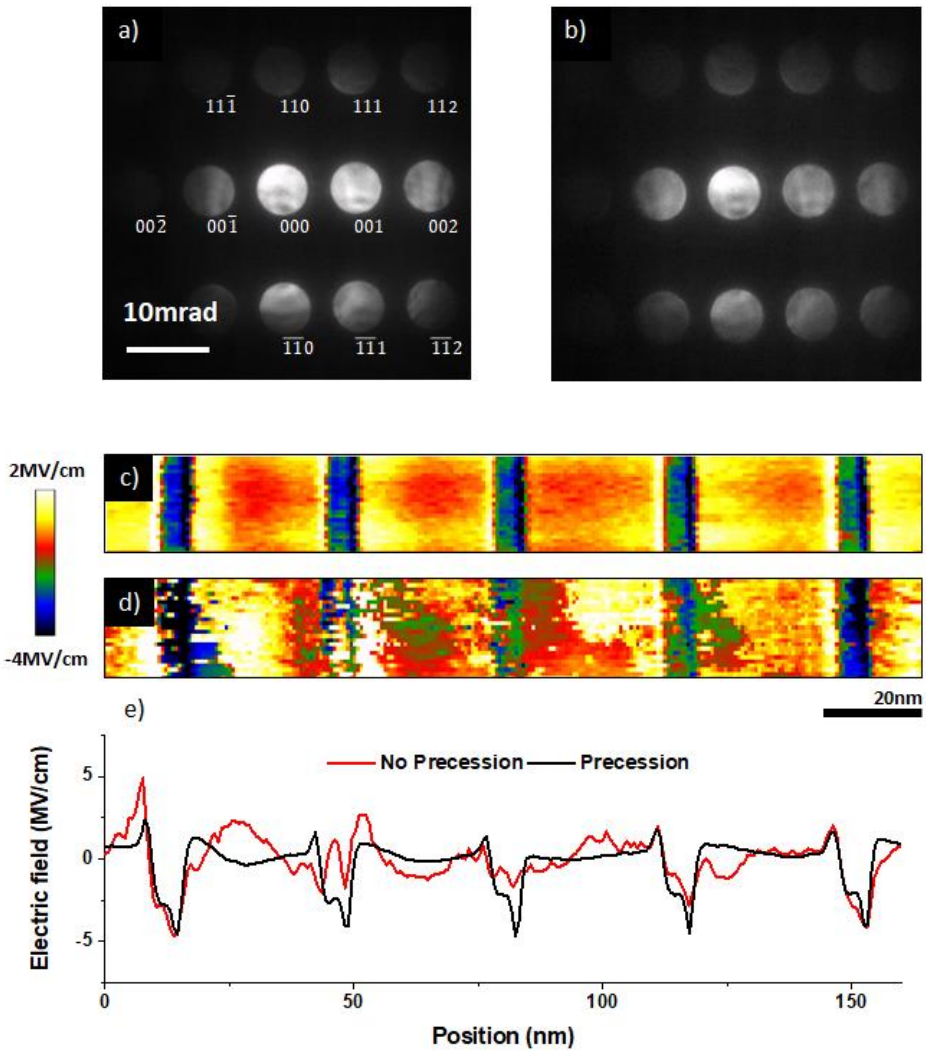

Figure 4-27 : NB-4D-STEM data processing by TM using diffraction pattern containing multiple diffracted beams. a) GaN diffraction pattern recorded down the [1-10] axis. The beam was precessed around the optical axis with a tilt of 0.25°. b) GaN same as (a) but without precession. c) Field map extracted with TM from the dataset with precession. Same for d) but without precession. e) Comparison of field profile taken across the InGaN layers in both field map.

using the whole pattern as a template allows to stabilize the TM. Regarding the signal detected in the InGaN layer, it was already said that strain has an influence on the pattern. With the experimental data we cannot know from what phenomenon, strain or field, the signal is coming. In order to show what is the influence of strain on the field detection with the whole diffraction pattern, simulations were performed.

For the simulation presented in Figure 4-12 an atomic structure of the sample was created (using script in Appendix A). In this structure, strain is present in the $\vec{c}$ direction. In the InGaN layer a tensile stress is present, the atomic planes strained tensily by 2.27% compared to the GaN bulk. This first structure was used and in addition an artificial structure was created in which the InGaN atomic planesare strained by 3.35% compared to the GaN but with the same indium concentration. In other words, only strain was increased in this artificial structure compare to the first one meaning that the same information was present in the diffracted beams except they were in different positions in reciprocal space. For both structure a 4D-STEM data set was simulated across the well. By comparing the pattern of the two structures, the strain effect on signal detected by TM will be visible. Once the diffraction patterns were simulated, the TM processing was applied to the simulated data. The results are presented in Figure 4-28. In Figure 4-28-(a) are compared the signal from TM on the transmitted beam and from TM on the whole diffraction pattern. Same in Figure 4-28-(b) but on the simulated data and on the structure containing an artificial higher strain. The processing using the whole diffraction pattern leads to a higher piezo-field value for experimental and simulated data, the trend is the same. In the simulated data, with a convergence angle of 3.4 mrad, a field of 2.2 MV/cm in a 110 nm thick structure and 2048 pix² diffraction pattern, the expected shift is 3.96 pixels (represented as the dashed line in Figure 4-28-b). The processing using the whole diffraction pattern gives a value of piezo-field close to this expected shift. The shift obtained on the structure containing the artificial strain is higher than expected so is seems that the strain influences the signal. It was just a coincidence that that processing with whole diffraction pattern gave a shift value close to the expected one. An explanation to the strain influence is the fact that the GaN (also true for the InGaN) is a polar material. It means that for such material, in the $\vec{c}$ the alternance of gallium and nitrogen atoms is not symmetric. This leads to a non-symmetric intensity in the diffraction pattern in the $\vec{c}$ direction. This means that the weight of the beams on the right and the ones on the left of the transmitted beam will not be the same when the cross-correlation of the pattern is calculated.

In this section we have shown that the detection of the redistribution of intensity by TM is possible. Such processing leads to results with trends closer to expectation than the one obtained by CoM. There is less noise with TM than with CoM because the cross-correlation is less sensitive to the contrast in the beam than the CoM calculation. The TM gives the expected trend but the values are not quantitative. Finally, the use of the whole diffraction pattern in the TM processing was tried. With this processing, at first it seemed that the measurements of the piezoelectric field in the QWs was improved. However, simulations

showed that the movement of the beam due to strain influences the value of the piezo-field. Therefore, this way of processing provides incoherent results in non-symmetric materials.

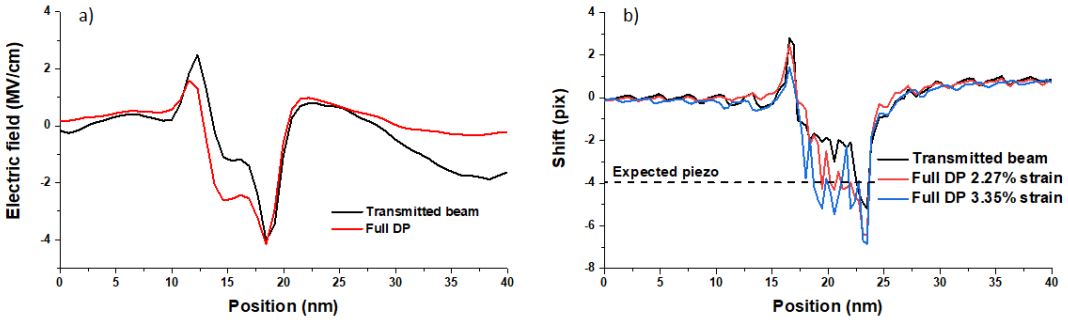

Figure 4-28 : Comparison of the electric field obtained by TM on the transmitted beam and TM on the whole diffraction pattern. The effects of strain are investigate in the simulated data using a structure containing an artificial strain of 3.36% in the layer. a) Experimental data processed by TM. b) Simulated data processed by TM.

4.5.5 Improved of field maps through advanced data processing

The simulations shown previously in Figure 4-5 suggests that the electric field should be constant in the QWs. This is reasonable if there are only charges at the top and bottom interface of each QW. In the NB-STEM coupled with precession measurements previously shown, the signal detected by CoM present strong variation of signal in the barriers (see figure Figure 4-24). This variation was assumed to be artefacts coming from the residual dynamical diffraction contrast still present in the transmitted beam despite the use of precession. This section shows the results obtained by fitting the background and removing it from the data. The data processed here are from the experiments shown in Figure 4-23 and Figure 4-24.

The results of the background fitting and subtraction on the non-processed data are presented in Figure 4-30. In Figure 4-30-(a) there is the virtual BF image reconstructed from the dataset. The orange rectangles show the area that are not taken into account in the data fitting as the signal of interest is present here. In Figure 4-30-(b) the field map with no post processing is shown. Figure 4-30-(c) shows the fitted background and in (d) there is the field map obtained after this background subtraction. Figure 4-29-(e) shows the profile of the field detected by CoM and the fitted background. In the QWs (indicated by the orange rectangles in a) the background is estimated using a Python interpolation function. Figure 4-29-(f) shows the field obtained after subtraction. After the background subtraction the QWs are visible in the field map as positive values of field which is incorrect. In the case of a non-

precessed dataset acquired on axis, the dynamical diffraction has a very strong influence on the intensity so the results found after background subtraction are incoherent. This processing shows that the shift of intensity detected by the CoM algorithm in the QWs is due to something else than electric field and the background subtraction cannot improves the results.

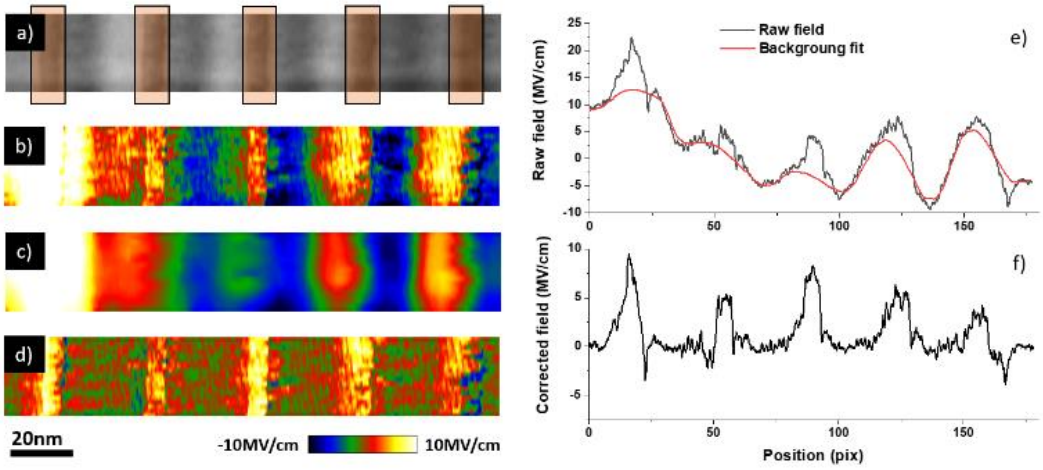

Figure 4-29 : Dynamical diffraction removal by background fitting on a NB-4D-STEM data acquired without precession. a) BF image of the sample reconstruct from the data set. The data in the orange rectangles are not taking into account during the background fitting. b) Field map extracted by CoM from a data set acquired without precession. c) Map of the fitted background. d) Field map obtained after subtraction of the background. e) Profiles of the raw electric field and the background fitting. f) Field profile after the background subtraction.

The same background removal was performed on the data set acquired in NB-4DSTEM mode coupled with precession. The results are presented in Figure 4-30. The data are presented in the same way as in Figure 4-29. In Figure 4-30-(d) and (f), the field obtained after subtraction is periodic and has a trend close to the simulations in Figure 4-5-(b). The influence of both interfaces is present and a visible change of slope in the middle of the layer indicates that the resolution is good enough to separate the MIP influence form the piezo one. Still there is no constant field that can be noticed in the QWs so it is difficult to extract quantitative values of the piezo-field. The data obtained by 4D-STEM coupled with precession are slightly influence by the dynamical diffraction but some small change in the beam contrast still subsist (see Figure 4-24-a). The field signal present in the wells has a stronger influence than the diffraction contrasts and the background subtraction works in this case. Values of between 1.5 and 5.1 MV/cm-1 have been measured as the piezoelectric fields

compared to a value of 2.2 MV/cm expected from simulations. Therefore at this time, although it is successful even to visualize the piezoelectric field, quantification still remains a challenge.

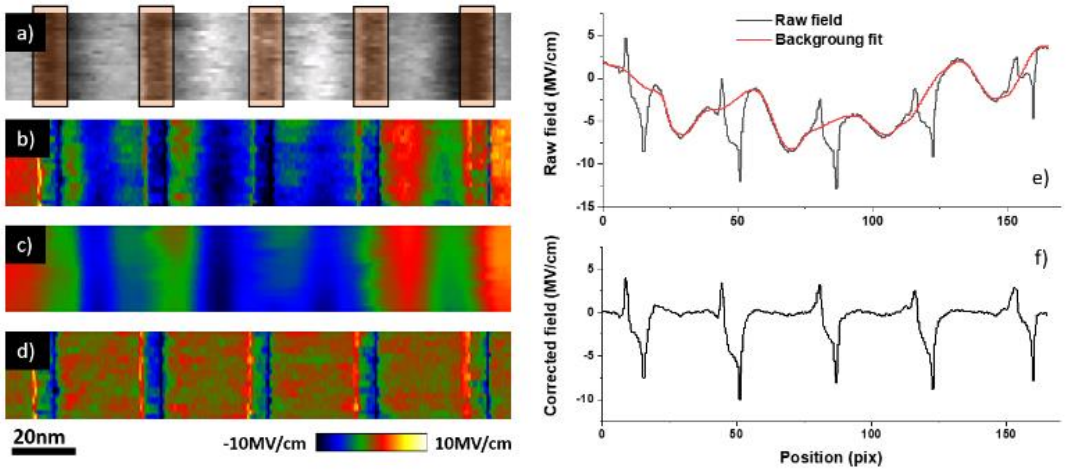

Figure 4-30 : Dynamical diffraction removing by background fitting on NB-4D-STEM data acquired with precession. a) BF image of the sample reconstruct from the data set. The data in the orange rectangles are not taking into account during the background fitting. b) Field map extracted by CoM from a data set acquired with precession. c) Map of the fitted background. d) Field map obtained after subtraction of the background. e) Profiles of the raw electric field and the background fitting. f) Field profile after the background subtraction.

The data treatment presented in this section allows to reach a field profile diffraction-free in the barriers and with slight diffraction effect in the wells. In the end the influence of the piezo-field and the MIP can be differentiate when using 4D-STEM coupled with precession and using background subtraction treatment.

4.6 Conclusion

Holography gave the benchmark of field measurement in the 7 nm wide InGaN QWs with a resolution of 3nm in the potential map. These measurements are routine and previous quantitative work on the measurement of piezoelectricity in 2 nm wide QWs have been reported. However, after differentiating the potential to provide a quantification of the electric field, the QWs were visible but the influence of the MIP and piezo-field cannot be separated from each other.

Next, we showed that when using a convergent beam for DPC, there are strong dynamical diffraction artefacts when performing STEM field measurements. The 4D-STEM measurement in NB and HR mode showed that despite trying many different experimental parameters, no compromise between resolution, sensitivity and reducing dynamical diffraction artefacts allowed the piezo-electric field to be measured quantitatively in the 7 nm wide InGaN QWs. Either the resolution does not allow the separation of the MIP from the piezoelectric field, or the detected signal is dominated by diffraction artefacts. Nevertheless, from these experiments it was shown that artefacts from the lamella relaxation could be neglected.

The presence of sample damage was highlighted and fast measurement using new generation of camera were demonstrated. These fast acquisitions did not allow us to measure the piezo field quantitatively through reduced beam damage. Such fast acquisition gave equivalent results as the previous one but more quickly with reduced electron dose.

The diffraction artefacts and the inelastic scattering were overcome in the last section. The energy filtering allowed to remove the inelastically scattered background which decreased the noise but the inelastic scattering does not have a major influence in the 4D-STEM measurement through the 100 nm thick GaN specimen. These experiments did not allow to quantitative measurement of the piezoelectric field. The combination of 4D-STEM with precession overcame the diffraction artefacts while acquiring data on axis. The loss in projection with precession is much smaller than that seen when tilting the sample. Still the influences of the MIP and the piezo one are mixed.

Finally, with an improved data treatment, the last diffraction artefacts present in the results were removed. From these last results the field profile is very close to what was expected from theory and simulation. But still large variations in the values of the piezoelectric field measurement suggest that there are still problems. However, for the first time, these improvements allowed the components of the piezoelectric field be separated from the MIP.

Conclusion

The different studies done during this Phd allowed us to determine what are the best parameters for 4D-STEM field mapping. These studies also permitted us to highlight how 4D-STEM can overcome the limits encountered when performing both DPC and holography and also the new limits that 4D-STEM reaches.

The thorough study of the silicon pn junction began by showing that from holography, quantitative electric field values of 0.62 ± 0.07 MV/cm can be obtained on a -2 V biased junction. It was also showed how DPC (without complex calibration) could be used to detect live, the variation of field during reverse biasing. The LM-4D-STEM was shown to be non-quantitative on the pn junction. Indeed, the low resolution accessible in this mode does not allow to reach the condition for a rigid shift of the beam. LM-4D-STEM allows field measurement comparable to what can be observed with DPC. The best parameters for field mapping on a pn junction were found to be in NB-4D-STEM mode. The main limits in this mode are the intensity contrast present in the beam due to dynamical diffraction and therefore the sample must be tilted in away from a zone axis thus leading into loss in resolution in projection. To overcome these limits energy filtering was performed, it permits to reduce the noise of the field map but did not improve the accuracy.

The best solution that we found was to couple NB-4D-STEM with precession. With precession field map were obtained in highly diffracting orientation with a level of noise lower than in holography (0.60 ± 0.03 MV/cm). Regarding the data processing it was showed that CoM model used during this work leads to results always much less than expected [125]. The TM processing was found to be more accurate, when processing data where a rigid shift is present. This silicon junction study showed that 4D-STEM could improve upon the limits of DPC (resolution, calibration, missing data) and coupled with precession 4D-STEM overcomes some limits of holography (vacuum reference, influence of dynamical diffraction, noise in the field map).

Then the study of interfaces by 4D-STEM highlighted some artefacts encountered in 4D-STEM. The experiments and simulation performed on the Si/SiO_2 interface allowed us to have a visual insight of how far the probe tail can influence the measurements. It was found that in our NB-4D-STEM experiment, the probe tail had an influence on the diffraction pattern 4 nm away from the interface.

Considering the work on the SiGe, 4D-STEM was successfully used to measure the strain and deduce the quantitative germanium concentration. The concentration we measured was in agreement with values found by SIMS, HAADF and holography.

Regarding the electric field measurement, holography allowed to have quantitative electrostatic potential in the SiGe layers. From this potential, values of electric field can be derived. Then the NB-4D-STEM mode was applied to the SiGe layers for the measurement of the electric field. The interface region where an intense electric field is caused from the differences in MIP in the materials led to a redistribution of intensity, so the results could only be processed by CoM. From the work on Si, we already demonstrated that quantitativity by CoM in thick specimens is incorrect. The results also showed that the spatial resolution of the experiment is deteriorate by the influence of the probe tail. This leads to artefacts in the measurements, the abrupt change of potential at the SiGe interface has an influence almost all through the 10 nm wide layers. HR-4D-STEM was then performed as an attempt to improve the resolution of the measurements but the complexity of the diffraction pattern recorded with all of the diffracted beams in this mode leads to uninterpretable data. Therefore, in general when studying interfaces, the tail of the probe must be considered. Even neglecting the effect of dynamical diffraction, if it is needed to electrically characterize a SiGe sample, or similar, a quantitative measurement of the potential by holography seems more adequate.

From the nitride QWs study it was showed that holography requires more advanced processing in order to obtain piezo electric field values. Then we showed that NB-4D-STEM encounters artefacts due to the abrupt change of MIP present between GaN and InGaN. It also suffers a loss of resolution due to the necessary tilt of the sample for avoiding the dynamical diffraction.

Again, HR-4D-STEM was shown to be uninterpretable on these nitride QWs. The new generation of fast camera was found to be useful in this case of beam sensitive materials. The small exposure time allows to prevent from beam damage on the sample. Finally, NB-4D-STEM coupled with precession and processed by advanced algorithm allows to measure field profile where piezo electric field can be decorrelated from the MIP influence. The measurement of quantitative electric field in 7 nm wide nitride QWs highlights the limits of 4D-STEM. For electron holography, an image corrector was used as well as advanced reconstruction techniques to resolve 2 nm wide InGaN QWs in GaN. For the holography the use of a plane wave also allowed the elimination of dynamical diffraction while keeping the region of interest aligned with the beam such that no information was lost in projection.

Therefore, although the experimental procedure is complicated and the use of advanced processing is necessary for both techniques, for electron holography the experiment has been successfully demonstrated.

To conclude, 4D-STEM is clearly an improvement of the simple DPC method. The data recorded in 4D-STEM allows to understand better the behavior of the transmitted beam. Quantitative field values can be obtained with 4D-STEM which was not possible in DPC as the spatial distribution of the transmitted electrons is not recorded. The 4D-STEM data provides information that could in principle be processed to extract quantities such as: thickness, strain, composition, BF image, magnetic field, electric field, plus even with simultaneous EDX acquisition. Therefore 4D-STEM is potentially a versatile tool for nm-scale resolved semiconductor characterization.

Compared to holography in regard of electrostatic characterization 4D-STEM does overcome some limits that holography faces (limited field of view and being able to take a reference from anywhere) but the artefacts created by interfaces makes the electric field measurement more problematic than electrostatic potential measurement. 4D-STEM and holography must both be improved to follow the reduction in size of the semiconductor components. The huge amount of information recorded by 4D-STEM is a strength of that technique, but the size of the recorded data makes it a problem. Even if progress have been made in the storage capacity, the amount of data keeps increasing. This amount of data acquired makes 4D-STEM more time consuming than a holography processing. Often the electron holography data can be treated during experiments, live on the TEM microscope. For 4D-STEM, the data can be trapped on the microscope for many days as even the transfer to a powerful computing resource can be problematic. However, advances in data processing such as LiberTEM [126] can be used to rapidly process data, and slowly the internal infrastructure at CEA is allowing fast data transfer.

Outlook

The results obtained during this work give an insight of the improvements and limits of 4D-STEM compared to holography and DPC. Future studies must be performed onto 4D-STEM and its derivate methods to overcome the limits. Here are ways research could follow to improve the 4D-STEM field measurement.

Most of this work was performed on a scintillator-based Gatan Oneview camera as at the beginning of this project we did not see that acquiring 10 frames a second would be a problem. For strain mapping as performed at CEA LETI, this speed of acquisition has been largely sufficient [127]. However, the latest generation of fast CMOS cameras are also more efficient which means that lower beam currents can be used with shorter acquisition times to limit specimen damage [70]. As such better algorithms and systematic studies would be required to understand the maximum speed and minimum beam dose that could be used for accurate measurements of the fields by 4D-STEM.

What was previously done by DPC is now possible by 4D-STEM assuming that the system can store and process the new amount of data generated by 4D-STEM. The data management is maybe the biggest challenge with these new techniques. Improvement could be done in the field of live processing which do not require data storage. Also, some researches are beginning in the field of big data and artificial intelligence to process the large amount of data [127].

During this thesis, we became aware that holography provides an advantage in that a plane wave is used that allows the dynamical diffraction to be more easily removed. The use of a convergent beam by 4D-STEM means that dynamical diffraction is often present even when the specimen is carefully tilted. This can be limited in simple cubic lattice samples such as pure Si, but in device with interfaces, or hexagonal lattices, this is much more difficult to remove. Additionally, holography is more mature and the acquisition process is quick to perform and routine. The improvements obtained with the coupling of precession with 4D-STEM are promising. Indeed in 2023 a paper in Nature Nanotechnology took our method of using precession to do simple studies of the electron gas in IIIV semiconductor interfaces by DPC [66]. More work is required in improving the use of precession for both 4D-STEM and holography, to try to understand the optimum conditions and the effects of precession on accurate data treatment.

The spatial resolution reached in a state-of-the-art microscope is not good enough to measure electric field in today's nano-electronics devices by 4D-STEM, this is partly due to the complex shape of the electron beam. The second problem that 4D-STEM reaches is the compromise between the resolution in real space and the one in reciprocal space. If the experiments reach a better resolution, it means that the convergence angle has been increase and so the beam is bigger on the detector and more diffuse which makes its position more difficult to determine. More research must be done in the field of 4D-STEM to see if it can overpass the limits of resolution, maybe in HR-4D-STEM mode coupled with precession in

a dedicated microscope. Thus regarding the probe size, ptychography which is a derivate technique from 4D-STEM could also make improvements as it allows the aberrations of the microscope and probe to be removed during processing [128]. This technique uses a defocused probe, overlapping diffracted beams that interfere, and oversampled scanning positions, plus a complex iterative data reconstruction which should in theory allows to extract the phase image at the exit of the specimen [129], [130]. However, thick samples are typically used for measurements of the potential in semiconductor devices and in general, this samples are used for ptychographic reconstructions.

In summary, during this Phd subject I have seen an explosion in the interest in 4D-STEM for the measurement of fields in semiconductor samples. At the beginning of this Phd we quickly saw that both the acquisition of the 4D-STEM data, plus the processing was much more complex than originally thought. As such we decided to compare the 4D-STEM to off-axis electron holography so that we could better understand the problems involved in the two techniques. Today, it seems that the use of a plane wave in electron holography greatly simplifies the measurement of electrical potentials (and magnetic potentials) in semiconductor devices. However, the great interest in 4D-STEM appears to be aiding the progress which was demonstrated recently in Nature Nanotechnology using precession to eliminate the effects of dynamical diffraction. Therefore, at this time I recommend that off-axis electron holography should be used as it is mature as a versatile tool for mapping the electrical properties of samples. However, the story for 4D-STEM is not finished and future developments will surely make this a more robust technique.

Appendix

A. Script to convert xyz file into µSTEM input file

```
import matplotlib.pyplot as plt
import numpy as np
import tkinter as tk

class Atom () :
   "Definition of a class to gather atom properties"
   def __init__(self):
      self.name = "no_name"
      self.number = 0
      self.Z = '-1'
      self.DW = '-1 '
      self.lattice = []

   def get_param(self):
      "get atomic number and Debye-Weller factor from the user"
      def save_param():
         self.Z = e1.get()
         self.DW = e2.get()
         print("Z =",self.Z)
         print("DW =",self.DW)
         master.destroy()
      master = tk.Tk()
      tk.Label(master, text= self.name).grid(row=0)
      tk.Label(master, text="atomic number : ").grid(row=1)
      tk.Label(master, text="Debye Weller factor :").grid(row=2)
      e1 = tk.Entry(master)
      e2 = tk.Entry(master)
      e1.grid(row=1, column=1)
      e2.grid(row=2, column=1)
      tk.Button(master, text='Save', command = save_param).grid(row=3, column=1,
sticky=tk.W, pady=4)
      tk.mainloop()

   def thickness_max(self, thick_max):
         thinner_lattice = []
         in_num = 0
         for i, coord in enumerate (self.lattice):
            if coord[2] < thick_max :
               thinner_lattice.append(coord)
               in_num += 1
            else :
```

```
            None
        self.lattice = thinner_lattice
        self.number = in_num
        print(f"There is {self.number} {self.name} atoms in the first {thick_max} nanometers")

def get_at_pos(line):
    l= line.split(' ')
    l = l[:-1] + l[-1].split('\n')
    #print(l)
    while '' in l :
        l.remove('')
    entity = l[0]
    l= l[1:]
    at_pos = [np.float(e) for e in l ]
    #µstem_at_pos = [at_pos[0], at_pos[2], at_pos[1]]
    µstem_at_pos = [at_pos[1], at_pos[2], at_pos[0]]
    return(entity, µstem_at_pos)

def get_dim(file_xyz):
    for n, line in enumerate (file_xyz) :
        if n == 0 :
            nb_at = line.split(' ')[-1]
            nb_at = float(nb_at.split('\n')[0])
            #print(nb_at)
            #print(type(nb_at))
        if n == 1 :
            l= line.split(' ')[1:]
            g = l[-1].split('\n')
            dimension = [np.float(e) for e in l[:-1] + g[:-1]]
            return(nb_at, dimension)

def extract_lattice(input_name):
    file = open(input_name, "r")
    #(nb_atom, dim_superlattice) = get_dim(file)
    entities = []
    for m, line in enumerate (file) :
        #if m ==10 :
        #    break
        if m < 2 :
            None
        if m == 2 :
            entities.append(Atom())
            (atom_name, at_pos) = get_at_pos(line)
            entities[-1].lattice.append(at_pos)
            entities[-1].name = atom_name
            entities[-1].number += 1
```

```
        if m > 2 :
            (atom_name, at_pos) = get_at_pos(line)
            if entities[-1].name != atom_name :
                entities.append(Atom())
            entities[-1].name = atom_name
            entities[-1].lattice.append(at_pos)
            entities[-1].number += 1
        #print('line n° ',m)
    file.close()
    return(entities)

def delete_coordiante_offset (entities):
    xmin = 1000
    ymin = 1000
    zmin = 1000
    xmax = -1
    ymax = -1
    zmax = -1
    for atom in entities :
        for a in atom.lattice :
            if a[0] < xmin :
                xmin = a[0]
            elif a[1] < ymin:
                ymin = a[1]
            elif a[2] < zmin:
                zmin = a[2]
            elif a[0] > xmax :
                xmax = a[0]
            elif a[1] > ymax:
                ymax = a[1]
            elif a[2] > zmax:
                zmax = a[2]
            else :
                None
    min_coordinate = [xmin, ymin, zmin]
    max_coordinate = [xmax, ymax, zmax]
    dim = [xmax-xmin, ymax-ymin, zmax-zmin]
    for atom in entities :
        offsetless_lattice = []
        for b in atom.lattice :
            x = (b[0] - min_coordinate[0])
            y = (b[1] - min_coordinate[1])
            z = (b[2] - min_coordinate[2])
            offsetless_lattice.append([x,y,z])
        atom.lattice = offsetless_lattice
    return(None)
```

```
def normalize_lattice (entities):
    xmin = 1000
    ymin = 1000
    zmin = 1000
    xmax = -1
    ymax = -1
    zmax = -1
    for atom in entities :
        for a in atom.lattice :
            if a[0] < xmin :
                xmin = a[0]
            elif a[1] < ymin:
                ymin = a[1]
            elif a[2] < zmin:
                zmin = a[2]
            elif a[0] > xmax :
                xmax = a[0]
            elif a[1] > ymax:
                ymax = a[1]
            elif a[2] > zmax:
                zmax = a[2]
            else :
                None
    dim = [xmax-xmin, ymax-ymin, zmax-zmin]
    for atom in entities :
        offsetless_lattice = []
        for b in atom.lattice :
            x = b[0] /dim[0]
            y = b[1] /dim[1]
            z = b[2] /dim[2]
            offsetless_lattice.append([x,y,z])
        atom.lattice = offsetless_lattice
    return(dim)

def visualize(entities):
    for at in entities :
        tab = np.array(at.lattice)
        fig = plt.figure()
        fig, ax1 = plt.subplots(1, figsize =(5,5))
        ax1.plot(tab[: , 0], tab[: ,2], 'o')
        fig.show()
        fig, ax2 = plt.subplots(1, figsize =(5,5))
        ax2.plot(tab[: , 1], tab[: ,2], 'o')
        fig.show()
        fig, ax3 = plt.subplots(1, figsize =(5,5))
        ax3.plot(tab[: , 1], tab[: ,0], 'o')
        fig.show()
```

```
        print("shape tab ", np.shape(tab))


def writte_µSTEM_input(output_name, dim_superlattice, entities):
    converted_file = open(output_name +".xtl", "w")
    converted_file.write(output_name + '\n')
    for i in range(3):
        converted_file.write(str(dim_superlattice[i]) + ' ')
    for i in range(3):
        converted_file.write('90.0' + ' ')
    converted_file.write('\n')
    converted_file.write(str(len(entities)) + '\n')
    for atom in entities:
        print("atom number", atom.number)
        converted_file.write(atom.name + '\n')
        converted_file.write(' '+ str(atom.number) +' '+ atom.Z +' '+'1.0' +' '+ atom.DW + '\n')
        for j in range(atom.number):
            for k in range(3):
                converted_file.write(' ' + str(round(atom.lattice[j][k],5)))
            converted_file.write('\n')
    converted_file.close()
    print("DONE")

def main () :
    input_name  = 'Si_SiO2_system-102.xyz.txt'
    output_name = 'Si_SiO2_interface_bricolée_µSTEM'
    thickness = 2
    (Entities) = extract_lattice(input_name)
    print( f'The raw lattice contains {len(Entities[0].lattice)} atoms of {Entities[0].name}' )
    print( f'The raw lattice contains {len(Entities[1].lattice)} atoms of {Entities[1].name}' )
    #visualize(Entities)
    delete_coordiante_offset(Entities)
    for at in Entities :
        at.thickness_max(thickness)
    (dim_superlattice) = normalize_lattice (Entities)
    visualize(Entities)
    #for at in Entities :
    #    at.get_param()
    Entities[0].Z = '14'
    Entities[0].DW = '0.006686'
    Entities[1].Z = '8'
    Entities[1].DW = '0.00927'  #les parametres sont entré ici plutôt qu'avec la fonction
get_param
    print("dim ",dim_superlattice)
    writte_µSTEM_input(output_name, dim_superlattice, Entities)

  main()
```

B. Script to generate a superlattice of Si with a 10nm wide SiGe layer

```
# ## 0. Libraries
import numpy as np
import matplotlib.pyplot as plt
import math as m
from mpl_toolkits import mplot3d
get_ipython().run_line_magic('matplotlib', 'inline')
from random import *
import os
from datetime import date


# ## 1. Parameters
# creation of supercell of GaN/InGaN bilayers with the following direction of the cell
# x_box  // [1,1,0]_GaN
# y_box //  c_GaN
# z_box //  [-1, 1, 0]_GaN (corresponds certainly to the  a* direction)  will be the beam direction
# this supercell will be used the input cell file in the muSTEM software
# 2 basis are used in this script :
#    a crystallographic basis (named Bc  for crystal basis) defined by the (a, b, c) vectors,
#     the basis of the box : x_box/norm(x_box), y_box/norm(y_box), z_box/norm(z_box) which is hereafter simply named (x, y, z) or Bb (for box basis)

name = 'SiGe_layer'
cell_type = 'diamond'
Si_norm_a = 5.43 #Angstrom
Ge_norm_a = 5.66 #Angstrom
theta = np.pi/4
Vec_a = np.array([1,0,0])
Vec_b = np.array([0,1,0])   # coordinate in the base (a,b,c)
Vec_c = np.array([0,0,1])
nb_at = 3 # Silicium, Germanium, Silicium in the SiGe layer
Ge_concentration1 = 0.20
Ge_concentration2 = 0.31
Ge_concentration3 = 0.38
Ge_concentration4 = 0.45
Concentration = Ge_concentration4
Z_Si = 14
Z_Ge = 32       # atomic number
DW_Si =  0.006685932   # Debaye-Waller factor
DW_Ge =  0.007485102
SiGe_norm_a = (Concentration * Ge_norm_a + (1-Concentration)*Si_norm_a)
strain = 0.0243 #calculated with Poisson ration of SiGe~0.275
end_name = f"_Si{1-Concentration}Ge{Concentration}"
```

```
fullname = name + end_name
print (end_name,"lattice parram",SiGe_norm_a, "\n","Strain = ",strain, "\n","Ge concentration = ",Concentration, "\n",fullname)
# to go from base (a,b,c) to (x,y,z)
cartesian = np.array([[Si_norm_a*m.cos(theta), 0, Si_norm_a*m.sin(theta)],
                      [Si_norm_a*m.cos(theta), 0, -Si_norm_a*m.sin(theta)],
                      [0, Si_norm_a, 0 ]])

# ## 2.Dimensions

X = 8       # in Angstrom
Y = 400
T = 8       # x and y dimensions and thickness  (our sample is 185nm thick)
Layer_width = 100   #width of the QW in Angstrom
i_1D    = int(X/(2*Si_norm_a*np.cos(theta)))-1
i_2D    = int(T/(2*Si_norm_a*np.cos(theta)))-1
i_3D    = int(Y/Si_norm_a)-1
i_Layer = int (Layer_width/Si_norm_a)
print(i_1D, i_2D, i_3D, i_Layer)

# Unit cell

Unit_Si = np.array([[ 0,   0,   0],
                    [1/4,  1/4, 1/4],
                    [1/2,  1/2,  0],
                    [3/4,  3/4, 1/4],
                    [1/4, -1/4, 3/4],
                    [1/2,   0, 1/2],
                    [3/4,  1/4, 3/4],
                    [ 1,  1/2, 1/2],
                    [1/2, -1/2,  0],
                    [3/4, -1/4, 1/4],
                    [ 1,   0,  0],
                    [5/4,  1/4, 1/4],
                    [3/4, -3/4, 3/4],
                    [ 1, -1/2, 1/2],
                    [5/4, -1/4, 3/4],
                    [3/2,   0, 1/2],
                    [ 1,  -1,  0],
                    [5/4, -3/4, 1/4],
                    [3/2, -1/2,  0],
                    [7/4, -1/4, 1/4]])          # 20 Silicon atoms the super unit cell
Shift = np.array([1/8, 1/8, 1/8])
for e in Unit_Si:
    e += Shift
# need to determined later the shift so limit cond is okay
#Super Lattice will be generally in 3 steps
```

```
# step 1 : the unit "GaN" cell is repeated along the x_box direction (in this particular case a+b direction)
# step 2 : the cells generated in step 1 are repeated along the z_box direction (in fact b-a direction )
# step 3 : the cells generated in step 1 and 2 are repeated along the y_box direction (in fact c_GaN direction)
#         this step 3 will create the different layers


''' realisation of step 1D'''
Super_Si_1D = np.array(Unit_Si)      # initialisation of the first step important that Super_Ga_1D is a new array different
# from the Unit_Ga object
for j in range(i_1D):
   for k in range(len(Unit_Si)):
      Unit_Si [k]  += Vec_a + Vec_b  # creation of the first "line of cells"
   Super_Si_1D = np.concatenate((Super_Si_1D, Unit_Si))


''' realisation of step 2D'''
Super_Si_2D = np.array(Super_Si_1D)
for j in range (i_2D):
   for k in range (len(Super_Si_1D)):
## creation of the first "plane of cells"
         Super_Si_1D[k] += Vec_a -Vec_b
   Super_Si_2D = np.concatenate((Super_Si_2D, Super_Si_1D))


''' realisation of step 3D'''
# here the different layer will be created (GaN layer then the InGaN QW and finally a second GaN layer)
Super_Si_3D = np.array(Super_Si_2D)
for j in range (int((i_3D-i_Layer)/2)):
## creation of the 3D supercell
   for k in range (len(Super_Si_2D)):
      Super_Si_2D[k] += Vec_c
   Super_Si_3D = np.concatenate((Super_Si_3D, Super_Si_2D))
for j in range (i_Layer):
   for k in range (len(Super_Si_2D)):
      Super_Si_2D[k] += Vec_c * (1 + strain)
   Super_SiGe_Si_3D = np.array(Super_Si_2D) if j==0 else np.concatenate((Super_SiGe_Si_3D, Super_Si_2D))
   Super_SiGe_Ge_3D = np.array(Super_Si_2D) if j==0 else np.concatenate((Super_SiGe_Ge_3D, Super_Si_2D))
for j in range (i_3D - (int((i_3D-i_Layer)/2) + i_Layer)):
   for k in range (len(Super_Si_2D)):
      Super_Si_2D[k] += Vec_c
```

```
    Super_Si_3D = np.concatenate((Super_Si_3D, Super_Si_2D))
Super_Si       = np.matmul(Super_Si_3D,       cartesian)
Super_SiGe_Si = np.matmul(Super_SiGe_Si_3D, cartesian)
Super_SiGe_Ge = np.matmul(Super_SiGe_Ge_3D, cartesian)
Shift          = np.matmul(Shift,             cartesian)

# Normalization (position equal to a fraction of the supercell size)
## Get the maximun in each column and add the distance before the next atom in order to not have an atom in 0 and 1 position.
## This way there is no border problem, MuStem can apply its border conditiosn in x_box and y_box directions.
## In the y_box direction (1-0.8772)*norm_c represent the distance between the last nitrogen atom and the next Gallium atom
Dim_X = max(np.max(Super_Si[:,0]),np.max(Super_SiGe_Si[:,0]),np.max(Super_SiGe_Ge [:,0])) + Shift[0]
Dim_Y = max(np.max(Super_Si[:,1]),np.max(Super_SiGe_Si[:,1]),np.max(Super_SiGe_Ge [:,1])) + Shift[1]
Dim_T = max(np.max(Super_Si[:,2]),np.max(Super_SiGe_Si[:,2]),np.max(Super_SiGe_Ge [:,2]))
print(Dim_X, Dim_Y, Dim_T)
Norm = [1/Dim_X,1/Dim_Y,1/Dim_T]
Super_Si      *= Norm
Super_SiGe_Si *= Norm
Super_SiGe_Ge *= Norm
print(np.shape(Super_Si))
print(np.shape(Super_SiGe_Si))
print(np.shape(Super_SiGe_Ge))
print(Dim_X, Dim_Y, Dim_T)


# ## 4. Export input file for MuSTEM
fullname += f"_{int(Dim_X)}x{int(Dim_Y)}x{int(Dim_T)}"
file = open(fullname+'.xtl', 'w')
file.write(fullname + '\n')
file.write(' ' + str(round(Dim_X,7)) +'  '+ str(round(Dim_Y,7)) +'  '+ str(round(Dim_T,7)) + ' 90.0000  '+ '90.0000  '+'90.0000 \n')
file.write (str(nb_at)+ '\n')
## Silicon
file.write('Si \n')
file.write(' ' +str(len(Super_Si))+' '+str(Z_Si)+' '+ '1.0 ' + str(round(DW_Si,7))+'\n')
for i in range (len(Super_Si)):
    file.write(str(round(Super_Si[i,0],7))+' ')
    file.write(str(round(Super_Si[i,1],7))+' ')
    file.write(str(round(Super_Si[i,2],7))+'\n')
## Silicon in SiGe
```

```
file.write('\n Si \n')
file.write(' ' +str(len(Super_SiGe_Si))+' '+str(Z_Si)+' '+ str(1-Concentration) +' '+ str(round(DW_Si,7))+'\n')
for j in range (len(Super_SiGe_Si)):
   file.write(str(round(Super_SiGe_Si[j,0],7))+' ')
   file.write(str(round(Super_SiGe_Si[j,1],7))+' ')
   file.write(str(round(Super_SiGe_Si[j,2],7))+'\n')
## Germanium in SiGe
file.write('\n Ge \n')
file.write(' ' +str(len(Super_SiGe_Ge))+' '+str(Z_Ge)+' '+ str(Concentration) +' ' + str(round(DW_Ge,7))+'\n')
for k in range (len(Super_SiGe_Ge)):
   file.write(str(round(Super_SiGe_Si[k,0],7))+' ')
   file.write(str(round(Super_SiGe_Si[k,1],7))+' ')
   file.write(str(round(Super_SiGe_Si[k,2],7))+'\n')

file.close()
```

C. Script to generate a superlattice of GaN with an GaN/InGaN QW

```
# ## 0. Libraries
import numpy as np
import matplotlib.pyplot as plt
import math as m
from mpl_toolkits import mplot3d
get_ipython().run_line_magic('matplotlib', 'inline')
from random import *
import os
from datetime import date

# ## 1. Parameters
# creation of supercell of GaN/InGaN bilayers with the following direction of the cell
# x_box  // [1,1,0]_GaN
# y_box //  c_GaN
# z_box //  [-1, 1, 0]_GaN (corresponds certainly to the  a* direction)  will be the beam direction
# this supercell will be used the input cell file in the muSTEM software
# 2 basis are used in this script :
#    a crystallographic basis (named Bc  for crystal basis) defined by the (a, b, c) vectors,
#     the basis of the box : x_box/norm(x_box), y_box/norm(y_box), z_box/norm(z_box) which is hereafter simply named (x, y, z) or Bb (for box basis)
name = 'GaN_InGaN_1QW'
Strain_bool = 'no' # 'yes' or 'no' or 'huge'
cell_type = 'hexagonal'
gamma  = m.radians(120)
gam2   = gamma/2
norm_a = 3.189 #Angstrom
norm_b = norm_a #Norm of the primitive cell vector
norm_c = 5.185
norm2_110 = norm_a * m.cos(m.radians(30))
print(norm2_110, norm_a * np.sqrt(3)/2)
Vec_a = np.array([1,0,0])
Vec_b = np.array([0,1,0])   # coordinate in the base (a,b,c)
Vec_c = np.array([0,0,1])
nb_at = 3 # Indium, Gallium, Nitrogen
In_concentration = 0.14
Z_Ga = 31
Z_N  = 7       # atomic number
Z_In = 49
DW_Ga =  0.2455   # Debaye-Waller factor
DW_In = 0.3853
DW_GaN_N = 0.2842
DW_InGaN_N = 0.3591
if Strain_bool == 'yes':
    strain = 0.0227
    fullname = name + '_strained'
```

```
elif Strain_bool == 'huge':
   strain = 0.8
   fullname = name + '_hugestrained'
else :
   strain = 0
   fullname = name + '_unstrained'
print (strain, fullname)
cartesian = np.array([[norm_a*m.cos(gam2),     0,     -norm_a*m.sin(gam2)],     # to go from base (a,b,c) to (x,y,z)
                      [norm_b*m.cos(gam2),     0,     norm_b*m.sin(gam2)],
                      [0,                norm_c,     0                ]])


# ## 2.Dimensions
X = 4          # in Angstrom
Y = 800
T = 12          # x and y dimensions and thickness  (our sample is 185nm thick)
WQ_width = 70    #width of the QW in Angstrom
i_1D = int(X/norm_a)-1
i_2D = 2*int(int((T/norm2_110))/2)-1
i_3D = int(Y/norm_c)
i_QW = int (WQ_width/norm_c)
print(i_1D, i_2D, i_3D, i_QW)


# ## 3. Unit cell and Superlattice creation

# Unit cell
Unit_Ga = np.array([[0,0,0],      [-1/3,1/3,0.5]   ])       # 2 Gallium atoms in the unit cell
Unit_N  = np.array([[0,0,0.3772], [-1/3,1/3,0.8772]])       # 2 Nitrogen atoms in the unit cell
#Shift = np.array([[1/6, 1/3, 0.5*(1-0.8772)], [1/6, 1/3, 0.5*(1-0.8772)]])
Shift = np.array([[1/4, 1/4, 0.5*(1-0.8772)], [1/4, 1/4, 0.5*(1-0.8772)]])
Unit_Ga += Shift
Unit_N  += Shift
#Super Lattice will be generally in 3 steps
# step 1 : the unit "GaN" cell is repeated along the x_box direction (in this particular case a+b direction)
# step 2 : the cells generated in step 1 are repeated along the z_box direction (in fact b-a direction )
# step 3 : the cells generated in step 1 and 2 are repeated along the y_box direction (in fact c_GaN direction)
#         this step 3 will create the different layers

# realisation of step 1
Super_Ga_1D = np.array(Unit_Ga)     # initialisation of the first step important that Super_Ga_1D is a new array different from the Unit_Ga object
Super_N_1D  = np.array(Unit_N)
```

```
for i in range(i_1D):
   Unit_Ga [0]  += Vec_a + Vec_b
# creation of the first "line of cells"
   Unit_Ga [1]  += Vec_a + Vec_b
   Unit_N [0]   += Vec_a + Vec_b
   Unit_N [1]   += Vec_a + Vec_b
   Super_Ga_1D = np.concatenate((Super_Ga_1D, Unit_Ga))
   Super_N_1D  = np.concatenate((Super_N_1D, Unit_N))

# realisation of step 2
Super_Ga_2D =  np.array(Super_Ga_1D)
Super_N_2D  =  np.array(Super_N_1D)
for j in range (i_2D):
   for k in range (len(Super_Ga_1D)):
## creation of the first "plane of cells"
      if j/2==int(j/2):
         Super_Ga_1D[k] += Vec_b
         Super_N_1D[k]  += Vec_b
      else:
         Super_Ga_1D[k] -= Vec_a
         Super_N_1D[k]  -= Vec_a
   Super_Ga_2D = np.concatenate((Super_Ga_2D, Super_Ga_1D))
   Super_N_2D  = np.concatenate((Super_N_2D,  Super_N_1D))

# realisation of step 3 : here the different layer will be created (GaN layer then the InGaN
QW and finally a second GaN layer)
Super_Ga_3D =  np.array(Super_Ga_2D)
Super_GaN_N_3D  =  np.array(Super_N_2D)
Super_InGa_3D = []
for j in range (int((i_3D-i_QW)/2)):                    ## creation of the 3D
supercell
   for k in range (len(Super_Ga_2D)):
      Super_Ga_2D[k] += Vec_c
      Super_N_2D[k]  += Vec_c
   Super_Ga_3D = np.concatenate((Super_Ga_3D, Super_Ga_2D))
   Super_GaN_N_3D  = np.concatenate((Super_GaN_N_3D,  Super_N_2D))
Super_InGaN_N_3D = []
for j in range (i_QW):
   for k in range (len(Super_Ga_2D)):
      Super_Ga_2D[k] += Vec_c * (1-strain)
      Super_N_2D[k]  += Vec_c * (1-strain)
   Super_InGa_3D       =       np.array(Super_Ga_2D)     if     j==0     else
np.concatenate((Super_InGa_3D, Super_Ga_2D))
   Super_InGaN_N_3D    =       np.array(Super_N_2D)      if     j==0     else
np.concatenate((Super_InGaN_N_3D, Super_N_2D))
for j in range (i_3D - (int((i_3D-i_QW)/2) + i_QW)):
   for k in range (len(Super_Ga_2D)):
```

```
        Super_Ga_2D[k] += Vec_c
        Super_N_2D[k]  += Vec_c
    Super_Ga_3D    = np.concatenate((Super_Ga_3D, Super_Ga_2D))
    Super_GaN_N_3D = np.concatenate((Super_GaN_N_3D,  Super_N_2D))


Super_Ga       = np.matmul(Super_Ga_3D,        cartesian)
Super_GaN_N    = np.matmul(Super_GaN_N_3D,     cartesian)
Super_InGa     = np.matmul(Super_InGa_3D[2:,:], cartesian)
Super_InGaN_N  = np.matmul(Super_InGaN_N_3D,   cartesian)
Shift          = np.matmul(Shift[0],           cartesian)
# Normalization (position equal to a fraction of the supercell size)
## Get the maximun in each column and add the distance before the next atom in order to not have an atom in 0 and 1 position.
## This way there is no border problem, MuStem can apply its border conditiosn in x_box and y_box directions.
## In the y_box direction (1-0.8772)*norm_c represent the distance between the last nitrogen atom and the next Gallium atom
Dim_X  =  max(np.max(Super_Ga[:,0]),np.max(Super_GaN_N[:,0]),np.max(Super_InGa[:,0]),np.max(Super_InGaN_N [:,0])) + Shift[0]
Dim_Y  =  max(np.max(Super_Ga[:,1]),np.max(Super_GaN_N[:,1]),np.max(Super_InGa[:,1]),np.max(Super_InGaN_N [:,1])) + Shift[1]
Dim_T  =  max(np.max(Super_Ga[:,2]),np.max(Super_GaN_N[:,2]),np.max(Super_InGa[:,2]),np.max(Super_InGaN_N [:,2])) #+ Shift[2]
Norm = [1/Dim_X,1/Dim_Y,1/Dim_T]
Super_Ga      *= Norm
Super_InGa    *= Norm
Super_GaN_N   *= Norm
Super_InGaN_N *= Norm
print(Shift)


# ## 4. Export input file for MuSTEM
fullname += f"_{int(Dim_X)}x{int(Dim_Y)}x{int(Dim_T)}"
file = open(fullname+'.xtl', 'w')
file.write(fullname + '\n')
file.write(' ' + str(round(Dim_X,7)) +'  '+ str(round(Dim_Y,7)) +'  '+ str(round(Dim_T,7))
+ ' 90.0000  '+ '90.0000  '+'90.0000 \n')
file.write (str(nb_at +2)+ '\n')
## Gallium
file.write('Ga \n')
file.write(' ' +str(len(Super_Ga))+' '+str(Z_Ga)+' '+ '1.0 ' + str(DW_Ga)+'\n')
for i in range (len(Super_Ga)):
    file.write(str(round(Super_Ga[i,0],7))+' ')
    file.write(str(round(Super_Ga[i,1],7))+' ')
    file.write(str(round(Super_Ga[i,2],7))+'\n')
## Gallium in the InGaN side
```

```
file.write('\n Ga \n')
file.write(' ' +str(len(Super_InGa))+' '+str(Z_Ga)+' '+ str(1-In_concentration) +' ' + str(round(DW_Ga,7))+'\n')
for k in range (len(Super_InGa)):
   file.write(str(round(Super_InGa[k,0],7))+' ')
   file.write(str(round(Super_InGa[k,1],7))+' ')
   file.write(str(round(Super_InGa[k,2],7))+'\n')
## Nitrogen in GaN
file.write('\n N \n')
file.write(' ' +str(len(Super_GaN_N))+' '+str(Z_N)+' '+ '1.0 ' + str(DW_GaN_N)+'\n')
for j in range (len(Super_GaN_N)):
   file.write(str(round(Super_GaN_N[j,0],7))+' ')
   file.write(str(round(Super_GaN_N[j,1],7))+' ')
   file.write(str(round(Super_GaN_N[j,2],7))+'\n')
## Nitrogen in InGaN
file.write('\n N \n')
file.write(' ' +str(len(Super_InGaN_N))+' '+str(Z_N)+' '+ '1.0 ' + str(DW_InGaN_N)+'\n')
for j in range (len(Super_InGaN_N)):
   file.write(str(round(Super_InGaN_N[j,0],7))+' ')
   file.write(str(round(Super_InGaN_N[j,1],7))+' ')
   file.write(str(round(Super_InGaN_N[j,2],7))+'\n')
## Indium in the InGaN side
file.write('\n In \n')
file.write(' ' +str(len(Super_InGa))+' '+str(Z_In)+' '+ str(In_concentration)+' ' + str(round(DW_In,7))+'\n')
for l in range (len(Super_InGa)):
   file.write(str(round(Super_InGa[l,0],7))+' ')
   file.write(str(round(Super_InGa[l,1],7))+' ')
   file.write(str(round(Super_InGa[l,2],7))+'\n')
file.close()
```

References

[1] Semiconductor Industry Association, “International Technology Roadmap for Semiconductors (ITRS),” 2015. https://www.semiconductors.org/resources/2015-international-technology-roadmap-for-semiconductors-itrs/

[2] W. D. Rau, P. Schwander, F. H. Baumann, W. Höppner, and A. Ourmazd, “Two-Dimensional Mapping of the Electrostatic Potential in Transistors by Electron Holography,” *Phys. Rev. Lett.*, vol. 82, no. 12, pp. 2614–2617, Mar. 1999, doi: 10.1103/PhysRevLett.82.2614.

[3] P. A. Doyle and P. S. Turner, “Relativistic Hartree–Fock X-ray and electron scattering factors,” *Acta Crystallogr. Sect. A*, vol. 24, no. 3, pp. 390–397, May 1968, doi: 10.1107/S0567739468000756.

[4] D. Rez, P. Rez, and I. Grant, “Dirac–Fock calculations of X-ray scattering factors and contributions to the mean inner potential for electron scattering,” *Acta Crystallogr. A*, vol. 50, no. 4, pp. 481–497, Jul. 1994, doi: 10.1107/S0108767393013200.

[5] G. Radi, “Complex lattice potentials in electron diffraction calculated for a number of crystals,” *Acta Crystallogr. Sect. A*, vol. 26, no. 1, pp. 41–56, Jan. 1970, doi: 10.1107/S0567739470000050.

[6] M. Y. Kim, J. M. Zuo, and J. C. H. Spence, “Ab-initio LDA Calculations of the Mean Coulomb PotentialV0 in Slabs of Crystalline Si, Ge and MgO,” *Phys. Status Solidi A*, vol. 166, no. 1, Art. no. 1, Mar. 1998, doi: 10.1002/(SICI)1521-396X(199803)166:1<445::AID-PSSA445>3.0.CO;2-N.

[7] M. Schowalter, J. T. Titantah, D. Lamoen, and P. Kruse, “*Ab initio* computation of the mean inner Coulomb potential of amorphous carbon structures,” *Appl. Phys. Lett.*, vol. 86, no. 11, p. 112102, Mar. 2005, doi: 10.1063/1.1885171.

[8] C. L. Zheng, K. Scheerschmidt, H. Kirmse, I. Häusler, and W. Neumann, “Imaging of three-dimensional (Si,Ge) nanostructures by off-axis electron holography,” *Ultramicroscopy*, vol. 124, pp. 108–116, Jan. 2013, doi: 10.1016/j.ultramic.2012.09.004.

[9] J. Curie and P. Curie, “Développement par compression de l’électricité polaire dans les cristaux hémièdres à faces inclinées,” *Bull. Société Minéralogique Fr.*, vol. 3, no. 4, pp. 90–93, 1880, doi: 10.3406/bulmi.1880.1564.

[10] M. Lohr *et al.*, “Quantitative measurements of internal electric fields with differential phase contrast microscopy on InGaN/GaN quantum well structures: Measurements of internal electric fields,” *Phys. Status Solidi B*, vol. 253, no. 1, Art. no. 1, Jan. 2016, doi: 10.1002/pssb.201552288.

[11] D. Carvalho *et al.*, “Direct Measurement of Polarization-Induced Fields in GaN/AlN by Nano-Beam Electron Diffraction,” *Sci. Rep.*, vol. 6, no. 1, Art. no. 1, Sep. 2016, doi: 10.1038/srep28459.

[12] E. Völkl, L. F. Allard, and D. C. Joy, *Introduction to Electron Holography*. Boston, MA: Springer US, 1999. doi: 10.1007/978-1-4615-4817-1.

[13] J. Li, M. R. McCartney, R. E. Dunin-Borkowski, and D. J. Smith, “Determination of mean inner potential of germanium using off-axis electron holography,” *Acta Crystallogr. A*, vol. 55, no. 4, Art. no. 4, Jul. 1999, doi: 10.1107/S010876739801719X.

[14] D. B. Williams and C. B. Carter, *Transmission Electron Microscopy*. Boston, MA: Springer US, 2009. doi: 10.1007/978-0-387-76501-3.

[15] J. Murray Gibson, “Breakdown of the weak-phase object approximation in amorphous objects and measurement of high-resolution electron optical parameters,” *Ultramicroscopy*, vol. 56, no. 1–3, Art. no. 1–3, Nov. 1994, doi: 10.1016/0304-3991(94)90143-0.

[16] A. Beyer *et al.*, “Quantitative Characterization of Nanometer-Scale Electric Fields via Momentum-Resolved STEM,” *Nano Lett.*, vol. 21, no. 5, Art. no. 5, Mar. 2021, doi: 10.1021/acs.nanolett.0c04544.

[17] P. A. Midgley, “An introduction to off-axis electron holography,” *Micron*, vol. 32, no. 2, pp. 167–184, Feb. 2001, doi: 10.1016/S0968-4328(99)00105-5.

[18] M. R. McCartney and D. J. Smith, “Electron Holography: Phase Imaging with Nanometer Resolution,” *Annu. Rev. Mater. Res.*, vol. 37, no. 1, Art. no. 1, 2007, doi: 10.1146/annurev.matsci.37.052506.084219.

[19] H. Lichte *et al.*, “Electron Holography: Applications to Materials Questions,” *Annu. Rev. Mater. Res.*, vol. 37, no. 1, Art. no. 1, Aug. 2007, doi: 10.1146/annurev.matsci.37.052506.084232.

[20] B. Haas, J.-L. Rouvière, V. Boureau, R. Berthier, and D. Cooper, “Direct comparison of off-axis holography and differential phase contrast for the mapping of electric fields in semiconductors by transmission electron microscopy.,” *Ultramicroscopy*, vol. 198, pp. 58–72, Mar. 2019, doi: 10.1016/j.ultramic.2018.12.003.

[21] D. Cooper, “Off-axis electron holography for the measurement of active dopants in silicon semiconductor devices,” *J. Phys. Appl. Phys.*, vol. 49, no. 47, Art. no. 47, Nov. 2016, doi: 10.1088/0022-3727/49/47/474001.

[22] A. Harscher and H. Lichte, “Experimental study of amplitude and phase detection limits in electron holography,” *Ultramicroscopy*, vol. 64, no. 1–4, pp. 57–66, Aug. 1996, doi: 10.1016/0304-3991(96)00019-8.

[23] H. Lichte, “Performance limits of electron holography,” *Ultramicroscopy*, vol. 108, no. 3, Art. no. 3, Feb. 2008, doi: 10.1016/j.ultramic.2007.06.006.

[24] E. Voelkl and D. Tang, “Approaching routine phase resolution for off-axis type holography,” *Ultramicroscopy*, vol. 110, no. 5, pp. 447–459, Apr. 2010, doi: 10.1016/j.ultramic.2009.11.017.

[25] R. A. McLeod, M. Bergen, and M. Malac, “Phase measurement error in summation of electron holography series,” *Ultramicroscopy*, vol. 141, pp. 38–50, Jun. 2014, doi: 10.1016/j.ultramic.2014.03.001.

[26] V. Boureau, R. McLeod, B. Mayall, and D. Cooper, “Off-axis electron holography combining summation of hologram series with double-exposure phase-shifting:

Theory and application," *Ultramicroscopy*, vol. 193, pp. 52–63, Oct. 2018, doi: 10.1016/j.ultramic.2018.06.004.

[27] D. Cooper, C. Ailliot, R. Truche, J.-P. Barnes, J.-M. Hartmann, and F. Bertin, "Experimental off-axis electron holography of focused ion beam-prepared Si p-n junctions with different dopant concentrations," *J. Appl. Phys.*, vol. 104, no. 6, p. 064513, Sep. 2008, doi: 10.1063/1.2982415.

[28] D. Cooper *et al.*, "Dopant profiling of focused ion beam milled semiconductors using off-axis electron holography; reducing artifacts, extending detection limits and reducing the effects of gallium implantation," *Ultramicroscopy*, vol. 110, no. 5, pp. 383–389, Apr. 2010, doi: 10.1016/j.ultramic.2010.02.001.

[29] D. Cooper, R. Truche, and J.-L. Rouviere, "Reduction of electrical damage in specimens prepared using focused ion beam milling for dopant profiling using off-axis electron holography," *Ultramicroscopy*, vol. 108, no. 5, pp. 488–493, Apr. 2008, doi: 10.1016/j.ultramic.2007.08.006.

[30] N. I. Kato, Y. Kohno, and H. Saka, "Side-wall damage in a transmission electron microscopy specimen of crystalline Si prepared by focused ion beam etching," *J. Vac. Sci. Technol. Vac. Surf. Films*, vol. 17, no. 4, pp. 1201–1204, Jul. 1999, doi: 10.1116/1.581795.

[31] D. Cooper *et al.*, "Improvement in electron holographic phase images of focused-ion-beam-milled GaAs and Si p-n junctions by *in situ* annealing," *Appl. Phys. Lett.*, vol. 88, no. 6, p. 063510, Feb. 2006, doi: 10.1063/1.2172068.

[32] D. Cooper, P. Rivallin, J.-M. Hartmann, A. Chabli, and R. E. Dunin-Borkowski, "Extending the detection limit of dopants for focused ion beam prepared semiconductor specimens examined by off-axis electron holography," *J. Appl. Phys.*, vol. 106, no. 6, p. 064506, Sep. 2009, doi: 10.1063/1.3195088.

[33] P. K. Somodi, A. C. Twitchett-Harrison, P. A. Midgley, B. E. Kardynał, C. H. W. Barnes, and R. E. Dunin-Borkowski, "Finite element simulations of electrostatic dopant potentials in thin semiconductor specimens for electron holography," *Ultramicroscopy*, vol. 134, pp. 160–166, Nov. 2013, doi: 10.1016/j.ultramic.2013.06.023.

[34] N. Shibata *et al.*, "Imaging of built-in electric field at a p-n junction by scanning transmission electron microscopy," *Sci. Rep.*, vol. 5, no. 1, Art. no. 1, Sep. 2015, doi: 10.1038/srep10040.

[35] Q. Wei, Z. Wu, K. Sun, F. A. Ponce, J. Hertkorn, and F. Scholz, "Evidence of Two-Dimensional Hole Gas in p-Type AlGaN/AlN/GaN Heterostructures," *Appl. Phys. Express*, vol. 2, no. 12, p. 121001, Nov. 2009, doi: 10.1143/APEX.2.121001.

[36] V. Boureau and D. Cooper, "Highly spatially resolved mapping of the piezoelectric potentials in InGaN quantum well structures by off-axis electron holography," *J. Appl. Phys.*, vol. 128, no. 15, p. 155704, Oct. 2020, doi: 10.1063/5.0020717.

[37] K. T. Moore, E. A. Stach, J. M. Howe, D. C. Elbert, and D. R. Veblen, "A tilting procedure to enhance compositional contrast and reduce residual diffraction contrast in energy-filtered TEM imaging of planar interfaces," *Micron*, vol. 33, no. 1, Art. no. 1, Jan. 2002, doi: 10.1016/S0968-4328(00)00072-X.

[38] D. B. Williams and C. B. Carter, *Transmission Electron Microscopy*. Boston, MA: Springer US, 2009. doi: 10.1007/978-0-387-76501-3.

[39] K. Müller-Caspary *et al.*, "Measurement of atomic electric fields and charge densities from average momentum transfers using scanning transmission electron microscopy," *Ultramicroscopy*, vol. 178, pp. 62–80, Jul. 2017, doi: 10.1016/j.ultramic.2016.05.004.

[40] T. S. McKechnie, *General Theory of Light Propagation and Imaging Through the Atmosphere*, vol. 196. in Springer Series in Optical Sciences, vol. 196. Cham: Springer International Publishing, 2016. doi: 10.1007/978-3-319-18209-4.

[41] J. K. Weiss, R. W. Carpenter, and A. A. Higgs, "A study of small electron probe formation in a field emission gun TEM/STEM," *Ultramicroscopy*, vol. 36, no. 4, Art. no. 4, Sep. 1991, doi: 10.1016/0304-3991(91)90124-O.

[42] L. Clark *et al.*, "Probing the limits of the rigid-intensity-shift model in differential-phase-contrast scanning transmission electron microscopy," *Phys. Rev. A*, vol. 97, no. 4, Apr. 2018, doi: 10.1103/PhysRevA.97.043843.

[43] C. Mahr, K. Müller-Caspary, T. Grieb, F. F. Krause, M. Schowalter, and A. Rosenauer, "Accurate measurement of strain at interfaces in 4D-STEM: A comparison of various methods," *Ultramicroscopy*, vol. 221, p. 113196, Feb. 2021, doi: 10.1016/j.ultramic.2020.113196.

[44] J. A. Hachtel, J. C. Idrobo, and M. Chi, "Sub-Ångstrom electric field measurements on a universal detector in a scanning transmission electron microscope," *Adv. Struct. Chem. Imaging*, vol. 4, no. 1, p. 10, Dec. 2018, doi: 10.1186/s40679-018-0059-4.

[45] S. Fang *et al.*, "Atomic electrostatic maps of 1D channels in 2D semiconductors using 4D scanning transmission electron microscopy," *Nat. Commun.*, vol. 10, no. 1, p. 1127, Mar. 2019, doi: 10.1038/s41467-019-08904-9.

[46] K. Müller *et al.*, "Atomic electric fields revealed by a quantum mechanical approach to electron picodiffraction," *Nat. Commun.*, vol. 5, no. 1, Art. no. 1, Dec. 2014, doi: 10.1038/ncomms6653.

[47] J.-L. Rouviere, A. Béché, Y. Martin, T. Denneulin, and D. Cooper, "Improved strain precision with high spatial resolution using nanobeam precession electron diffraction," *Appl. Phys. Lett.*, vol. 103, no. 24, Art. no. 24, Dec. 2013, doi: 10.1063/1.4829154.

[48] L. Bruas, V. Boureau, A. P. Conlan, S. Martinie, J.-L. Rouviere, and D. Cooper, "Improved measurement of electric fields by nanobeam precession electron diffraction," *J. Appl. Phys.*, vol. 127, no. 20, Art. no. 20, May 2020, doi: 10.1063/5.0006969.

[49] B. Haas, J.-L. Rouvière, V. Boureau, R. Berthier, and D. Cooper, "Direct comparison of off-axis holography and differential phase contrast for the mapping of electric fields in semiconductors by transmission electron microscopy.," *Ultramicroscopy*, vol. 198, pp. 58–72, Mar. 2019, doi: 10.1016/j.ultramic.2018.12.003.

[50] D. J. Taplin, N. Shibata, M. Weyland, and S. D. Findlay, "Low magnification differential phase contrast imaging of electric fields in crystals with fine electron probes," *Ultramicroscopy*, vol. 169, pp. 69–79, Oct. 2016, doi: 10.1016/j.ultramic.2016.07.010.

[51] L. Reimer, *Transmission electron microscopy: physics of image formation and microanalysis*, vol. 36. Springer, 2013.

[52] J. Zweck, J. N. Chapman, S. McVitie, and H. Hoffmann, “Reconstruction of induction distributions in thin films from DPC images,” *J. Magn. Magn. Mater.*, vol. 104–107, pp. 315–316, Feb. 1992, doi: 10.1016/0304-8853(92)90813-4.

[53] H. Rose, “Phase contrast in scanning transmission electron microscopy,” *Optik*, vol. 39, pp. 416–436, 1974.

[54] N. H. Dekkers and H. De Lang, “Differential phase contrast in a STEM,” *Optik*, vol. 41, pp. 452–456, 1974.

[55] H. Rose, “Nonstandard imaging methods in electron microscopy,” *Ultramicroscopy*, vol. 2, pp. 251–267, Jan. 1976, doi: 10.1016/S0304-3991(76)91538-2.

[56] M. Krajnak, D. McGrouther, D. Maneuski, V. O. Shea, and S. McVitie, “Pixelated detectors and improved efficiency for magnetic imaging in STEM differential phase contrast,” *Ultramicroscopy*, vol. 165, pp. 42–50, Jun. 2016, doi: 10.1016/j.ultramic.2016.03.006.

[57] S. Toyama *et al.*, “Quantitative electric field mapping of a p–n junction by DPC STEM,” *Ultramicroscopy*, vol. 216, p. 113033, Sep. 2020, doi: 10.1016/j.ultramic.2020.113033.

[58] J. Zweck, F. Schwarzhuber, J. Wild, and V. Galioit, “On detector linearity and precision of beam shift detection for quantitative differential phase contrast applications,” *Ultramicroscopy*, vol. 168, pp. 53–64, Sep. 2016, doi: 10.1016/j.ultramic.2016.05.007.

[59] G. Lee *et al.*, “Influence of combinatory effects of STEM setups on the sensitivity of differential phase contrast imaging,” *Micron*, vol. 127, p. 102755, Dec. 2019, doi: 10.1016/j.micron.2019.102755.

[60] S. Majert and H. Kohl, “High-resolution STEM imaging with a quadrant detector—Conditions for differential phase contrast microscopy in the weak phase object approximation,” *Ultramicroscopy*, vol. 148, pp. 81–86, Jan. 2015, doi: 10.1016/j.ultramic.2014.09.009.

[61] F. Schwarzhuber, P. Melzl, and J. Zweck, “On the achievable field sensitivity of a segmented annular detector for differential phase contrast measurements,” *Ultramicroscopy*, vol. 177, pp. 97–105, Jun. 2017, doi: 10.1016/j.ultramic.2017.02.005.

[62] M. Wu and E. Spiecker, “Correlative micro-diffraction and differential phase contrast study of mean inner potential and subtle beam-specimen interaction,” *Ultramicroscopy*, vol. 176, pp. 233–245, May 2017, doi: 10.1016/j.ultramic.2017.03.029.

[63] H. G. Brown *et al.*, “Measuring nanometre-scale electric fields in scanning transmission electron microscopy using segmented detectors,” *Ultramicroscopy*, vol. 182, pp. 169–178, Nov. 2017, doi: 10.1016/j.ultramic.2017.07.002.

[64] K. Müller-Caspary *et al.*, “Comparison of first moment STEM with conventional differential phase contrast and the dependence on electron dose,” *Ultramicroscopy*, vol. 203, pp. 95–104, Aug. 2019, doi: 10.1016/j.ultramic.2018.12.018.

[65] B. D. Levin, C. Zhang, B. Bammes, P. M. Voyles, and R. B. Bilhorn, “4D-STEM with a direct electron detector,” *Microscopy and analysis*, vol. 34, 2020.

[66] S. Toyama *et al.*, “Real-space observation of a two-dimensional electron gas at semiconductor heterointerfaces,” *Nat. Nanotechnol.*, Mar. 2023, doi: 10.1038/s41565-023-01349-8.

[67] H. Yang *et al.*, “4D STEM: High efficiency phase contrast imaging using a fast pixelated detector,” *J. Phys. Conf. Ser.*, vol. 644, p. 012032, Oct. 2015, doi: 10.1088/1742-6596/644/1/012032.

[68] H. Yang, T. J. Pennycook, and P. D. Nellist, “Efficient phase contrast imaging in STEM using a pixelated detector. Part II: Optimisation of imaging conditions,” *Ultramicroscopy*, vol. 151, pp. 232–239, Apr. 2015, doi: 10.1016/j.ultramic.2014.10.013.

[69] T. J. Pennycook, A. R. Lupini, H. Yang, M. F. Murfitt, L. Jones, and P. D. Nellist, “Efficient phase contrast imaging in STEM using a pixelated detector. Part 1: Experimental demonstration at atomic resolution,” *Ultramicroscopy*, vol. 151, pp. 160–167, Apr. 2015, doi: 10.1016/j.ultramic.2014.09.013.

[70] B. C. da Silva *et al.*, “The influence of illumination conditions in the measurement of built-in electric field at p–n junctions by 4D-STEM,” *Appl. Phys. Lett.*, vol. 121, no. 12, p. 123503, Sep. 2022, doi: 10.1063/5.0104861.

[71] M. J. Zachman, Z. Yang, Y. Du, and M. Chi, “Robust Atomic-Resolution Imaging of Lithium in Battery Materials by Center-of-Mass Scanning Transmission Electron Microscopy,” *ACS Nano*, vol. 16, no. 1, pp. 1358–1367, Jan. 2022, doi: 10.1021/acsnano.1c09374.

[72] V. Boureau, L. Bruas, M. Bryan, J.-L. Rouvière, and D. Cooper, “Quantitative Measurement of Electric Fields in Microelectronics Devices by In-Situ Pixelated STEM,” *Microsc. Microanal.*, vol. 28, no. S1, pp. 480–482, Aug. 2022, doi: 10.1017/S1431927622002586.

[73] D. J. Taplin, N. Shibata, M. Weyland, and S. D. Findlay, “Low magnification differential phase contrast imaging of electric fields in crystals with fine electron probes,” *Ultramicroscopy*, vol. 169, pp. 69–79, Oct. 2016, doi: 10.1016/j.ultramic.2016.07.010.

[74] M. C. Cao *et al.*, “Theory and practice of electron diffraction from single atoms and extended objects using an EMPAD,” *Microscopy*, vol. 67, no. suppl_1, pp. i150–i161, Mar. 2018, doi: 10.1093/jmicro/dfx123.

[75] S. E. Zeltmann *et al.*, “Patterned probes for high precision 4D-STEM bragg measurements,” *Ultramicroscopy*, vol. 209, p. 112890, Feb. 2020, doi: 10.1016/j.ultramic.2019.112890.

[76] M. Lohr *et al.*, “Differential phase contrast 2.0—Opening new ‘fields’ for an established technique,” *Ultramicroscopy*, vol. 117, pp. 7–14, Jun. 2012, doi: 10.1016/j.ultramic.2012.03.020.

[77] M. Wu and E. Spiecker, “Correlative micro-diffraction and differential phase contrast study of mean inner potential and subtle beam-specimen interaction,” *Ultramicroscopy*, vol. 176, pp. 233–245, May 2017, doi: 10.1016/j.ultramic.2017.03.029.

[78] L. Wang *et al.*, “Dynamics of the charging-induced imaging instability in transmission electron microscopy,” *Nanoscale Adv.*, vol. 3, no. 11, pp. 3035–3040, 2021, doi: 10.1039/D1NA00140J.

[79] R. S. Pantelic, J. C. Meyer, U. Kaiser, and H. Stahlberg, “The application of graphene as a sample support in transmission electron microscopy,” *Solid State Commun.*, vol. 152, no. 15, pp. 1375–1382, Aug. 2012, doi: 10.1016/j.ssc.2012.04.038.

[80] S. Majert and H. Kohl, “High-resolution STEM imaging with a quadrant detector—Conditions for differential phase contrast microscopy in the weak phase object approximation,” *Ultramicroscopy*, vol. 148, pp. 81–86, Jan. 2015, doi: 10.1016/j.ultramic.2014.09.009.

[81] F. Hüe, M. Hÿtch, H. Bender, F. Houdellier, and A. Claverie, “Direct Mapping of Strain in a Strained Silicon Transistor by High-Resolution Electron Microscopy,” *Phys. Rev. Lett.*, vol. 100, no. 15, Art. no. 15, Apr. 2008, doi: 10.1103/PhysRevLett.100.156602.

[82] M. L. Lee, E. A. Fitzgerald, M. T. Bulsara, M. T. Currie, and A. Lochtefeld, “Strained Si, SiGe, and Ge channels for high-mobility metal-oxide-semiconductor field-effect transistors,” *J. Appl. Phys.*, vol. 97, no. 1, Art. no. 1, Jan. 2005, doi: 10.1063/1.1819976.

[83] D. Cooper, A. Béché, J. M. Hartmann, V. Carron, and J.-L. Rouvière, “Strain mapping for the semiconductor industry by dark-field electron holography and nanobeam electron diffraction with nm resolution,” *Semicond. Sci. Technol.*, vol. 25, no. 9, Art. no. 9, Sep. 2010, doi: 10.1088/0268-1242/25/9/095012.

[84] T. Takeuchi *et al.*, “Determination of piezoelectric fields in strained GaInN quantum wells using the quantum-confined Stark effect,” *Appl. Phys. Lett.*, vol. 73, no. 12, Art. no. 12, Sep. 1998, doi: 10.1063/1.122247.

[85] V. S. Ban *et al.*, *Heteroepitaxial Semiconductors for Electronic Devices*. New York, NY: Springer, 2013.

[86] C. Mahr *et al.*, “Influence of distortions of recorded diffraction patterns on strain analysis by nano-beam electron diffraction,” *Ultramicroscopy*, vol. 196, pp. 74–82, Jan. 2019, doi: 10.1016/j.ultramic.2018.09.010.

[87] J. S. Barnard, D. N. Johnstone, and P. A. Midgley, “High-resolution scanning precession electron diffraction: Alignment and spatial resolution,” *Ultramicroscopy*, vol. 174, pp. 79–88, Mar. 2017, doi: 10.1016/j.ultramic.2016.12.018.

[88] R. Vincent and P. A. Midgley, “Double conical beam-rocking system for measurement of integrated electron diffraction intensities,” *Ultramicroscopy*, vol. 53, no. 3, Art. no. 3, Mar. 1994, doi: 10.1016/0304-3991(94)90039-6.

[89] L. A. Giannuzzi and F. A. Stevie, “A review of focused ion beam milling techniques for TEM specimen preparation,” *Micron*, vol. 30, no. 3, pp. 197–204, Jun. 1999, doi: 10.1016/S0968-4328(99)00005-0.

[90] L. J. Allen, A. J. D′Alfonso, and S. D. Findlay, “Modelling the inelastic scattering of fast electrons,” *Ultramicroscopy*, vol. 151, pp. 11–22, Apr. 2015, doi: 10.1016/j.ultramic.2014.10.011.

[91] M. Schowalter, A. Rosenauer, J. T. Titantah, and D. Lamoen, “Temperature-dependent Debye–Waller factors for semiconductors with the wurtzite-type structure,” *Acta Crystallogr. A*, vol. 65, no. 3, Art. no. 3, May 2009, doi: 10.1107/S0108767309004966.

[92] M. Schowalter, A. Rosenauer, J. T. Titantah, and D. Lamoen, “Computation and parametrization of the temperature dependence of Debye–Waller factors for group IV, III–V and II–VI semiconductors,” *Acta Crystallogr. A*, vol. 65, no. 1, pp. 5–17, Jan. 2009, doi: 10.1107/S0108767308031437.

[93] P. Ganster, G. Tréglia, and A. Saúl, “Atomistic modeling of strain and diffusion at the Si / SiO 2 interface,” *Phys. Rev. B*, vol. 81, no. 4, Art. no. 4, Jan. 2010, doi: 10.1103/PhysRevB.81.045315.

[94] J. H. Leck, *Theory of semiconductor junction devices: a textbook for electrical and electronic engineers*. Elsevier, 2013.

[95] P. C. Zalm, “Ultra shallow doping profiling with SIMS,” *Rep. Prog. Phys.*, vol. 58, no. 10, pp. 1321–1374, Oct. 1995, doi: 10.1088/0034-4885/58/10/004.

[96] D. S. McPhail, “Applications of Secondary Ion Mass Spectrometry (SIMS) in Materials Science,” *J. Mater. Sci.*, vol. 41, no. 3, Art. no. 3, Feb. 2006, doi: 10.1007/s10853-006-6568-x.

[97] D. Delille, R. Pantel, and E. Van Cappellen, “Crystal thickness and extinction distance determination using energy filtered CBED pattern intensity measurement and dynamical diffraction theory fitting,” *Ultramicroscopy*, vol. 87, no. 1–2, Art. no. 1–2, Mar. 2001, doi: 10.1016/S0304-3991(00)00067-X.

[98] J. Trinick and J. Berriman, “Zero-loss electron microscopy with the Zeiss EM902,” *Ultramicroscopy*, vol. 21, no. 4, pp. 393–397, Jan. 1987, doi: 10.1016/0304-3991(87)90039-8.

[99] B. Schaffer, G. Kothleitner, and W. Grogger, “EFTEM spectrum imaging at high-energy resolution,” *Ultramicroscopy*, vol. 106, no. 11–12, pp. 1129–1138, Oct. 2006, doi: 10.1016/j.ultramic.2006.04.028.

[100] P. Xu, R. F. Loane, and J. Silcox, “Energy-filtered convergent-beam electron diffraction in STEM,” *Ultramicroscopy*, vol. 38, no. 2, pp. 127–133, Nov. 1991, doi: 10.1016/0304-3991(91)90113-K.

[101] D. Cooper, A. C. Twitchett-Harrison, P. A. Midgley, and R. E. Dunin-Borkowski, “The influence of electron irradiation on electron holography of focused ion beam milled

GaAs p-n junctions," *J. Appl. Phys.*, vol. 101, no. 9, Art. no. 9, May 2007, doi: 10.1063/1.2730557.

[102] M. P. Vigouroux *et al.*, "Strain mapping at the nanoscale using precession electron diffraction in transmission electron microscope with off axis camera," *Appl. Phys. Lett.*, vol. 105, no. 19, p. 191906, Nov. 2014, doi: 10.1063/1.4901435.

[103] A. Béché, J. L. Rouvière, J. P. Barnes, and D. Cooper, "Strain measurement at the nanoscale: Comparison between convergent beam electron diffraction, nano-beam electron diffraction, high resolution imaging and dark field electron holography," *Ultramicroscopy*, vol. 131, pp. 10–23, Aug. 2013, doi: 10.1016/j.ultramic.2013.03.014.

[104] M. A. Gribelyuk, V. Ontalus, F. H. Baumann, Z. Zhu, and J. R. Holt, "Electron holography of devices with epitaxial layers," *J. Appl. Phys.*, vol. 116, no. 17, Art. no. 17, Nov. 2014, doi: 10.1063/1.4898859.

[105] J. Li, M. R. McCartney, R. E. Dunin-Borkowski, and D. J. Smith, "Holography Measurement of Mean Inner Potential of Germanium," *Microsc. Microanal.*, vol. 4, no. S2, Art. no. S2, Jul. 1998, doi: 10.1017/S1431927600023187.

[106] M. Gajdardziska-Josifovska, M. R. McCartney, W. J. de Ruijter, D. J. Smith, J. K. Weiss, and J. M. Zuo, "Accurate measurements of mean inner potential of crystal wedges using digital electron holograms," *Ultramicroscopy*, vol. 50, no. 3, Art. no. 3, Aug. 1993, doi: 10.1016/0304-3991(93)90197-6.

[107] R. S. Pennington, C. B. Boothroyd, and R. E. Dunin-Borkowski, "Surface effects on mean inner potentials studied using density functional theory," *Ultramicroscopy*, vol. 159, pp. 34–45, Dec. 2015, doi: 10.1016/j.ultramic.2015.07.011.

[108] P. Kruse, M. Schowalter, D. Lamoen, A. Rosenauer, and D. Gerthsen, "Determination of the mean inner potential in III–V semiconductors, Si and Ge by density functional theory and electron holography," *Ultramicroscopy*, vol. 106, no. 2, Art. no. 2, Jan. 2006, doi: 10.1016/j.ultramic.2005.06.057.

[109] P. Formanek and M. Kittler, "Potential and Limitations of Electron Holography in Silicon Research," *Solid State Phenom.*, vol. 108–109, pp. 603–608, Dec. 2005, doi: 10.4028/www.scientific.net/SSP.108-109.603.

[110] P. Hartel, H. Rose, and C. Dinges, "Conditions and reasons for incoherent imaging in STEM," *Ultramicroscopy*, vol. 63, no. 2, pp. 93–114, Jun. 1996, doi: 10.1016/0304-3991(96)00020-4.

[111] Z. W. Wang, Z. Y. Li, S. J. Park, A. Abdela, D. Tang, and R. E. Palmer, "Quantitative Z-contrast imaging in the scanning transmission electron microscope with size-selected clusters," *Phys. Rev. B*, vol. 84, no. 7, p. 073408, Aug. 2011, doi: 10.1103/PhysRevB.84.073408.

[112] T. Grieb *et al.*, "Determination of the chemical composition of GaNAs using STEM HAADF imaging and STEM strain state analysis," *Ultramicroscopy*, vol. 117, pp. 15–23, Jun. 2012, doi: 10.1016/j.ultramic.2012.03.014.

[113] H. Kauko *et al.*, "Compositional characterization of GaAs/GaAsSb nanowires by quantitative HAADF-STEM," *Micron*, vol. 44, pp. 254–260, Jan. 2013, doi: 10.1016/j.micron.2012.07.002.

[114] R. Andreas and S. Marco, *STEMSIM-a new software tool for simulation of STEM HAADF Z-contrast imaging*, vol. 120. in Proceedings in Physics, vol. 120. Springer, 2008.

[115] J. J. Wortman and R. A. Evans, "Young's Modulus, Shear Modulus, and Poisson's Ratio in Silicon and Germanium," *J. Appl. Phys.*, vol. 36, no. 1, pp. 153–156, Jan. 1965, doi: 10.1063/1.1713863.

[116] S. Nakamura, T. Mukai, and M. Senoh, "Candela-class high-brightness InGaN/AlGaN double-heterostructure blue-light-emitting diodes," *Appl. Phys. Lett.*, vol. 64, no. 13, pp. 1687–1689, Mar. 1994, doi: 10.1063/1.111832.

[117] F. Bernardini and V. Fiorentini, "Macroscopic polarization and band offsets at nitride heterojunctions," *Phys. Rev. B*, vol. 57, no. 16, pp. R9427–R9430, Apr. 1998, doi: 10.1103/PhysRevB.57.R9427.

[118] F. Bernardini, V. Fiorentini, and D. Vanderbilt, "Spontaneous polarization and piezoelectric constants of III-V nitrides," *Phys. Rev. B*, vol. 56, no. 16, Art. no. 16, Oct. 1997, doi: 10.1103/PhysRevB.56.R10024.

[119] K. Song *et al.*, "Correlative High-Resolution Mapping of Strain and Charge Density in a Strained Piezoelectric Multilayer," *Adv. Mater. Interfaces*, vol. 2, no. 1, Art. no. 1, 2015, doi: 10.1002/admi.201400281.

[120] B. Damilano *et al.*, "Blue to yellow emission from (Ga,In)/GaN quantum wells grown on pixelated silicon substrate," *Sci. Rep.*, vol. 10, no. 1, Art. no. 1, Dec. 2020, doi: 10.1038/s41598-020-76031-3.

[121] W. Lü, C. R. Li, and Z. Zhang, "Study of band structure InxGa1−xN⁄GaN multiple quantum wells by high-resolution electron microscopy and electron holography," *Appl. Phys. Lett.*, vol. 86, no. 4, p. 041902, Jan. 2005, doi: 10.1063/1.1856138.

[122] M. Schowalter, A. Rosenauer, D. Lamoen, P. Kruse, and D. Gerthsen, "*Ab initio* computation of the mean inner Coulomb potential of wurtzite-type semiconductors and gold," *Appl. Phys. Lett.*, vol. 88, no. 23, p. 232108, Jun. 2006, doi: 10.1063/1.2210453.

[123] F. Houdellier, D. Jacob, M. J. Casanove, and C. Roucau, "Effect of sample bending on diffracted intensities observed in CBED patterns of plan view strained samples," *Ultramicroscopy*, vol. 108, no. 4, Art. no. 4, Mar. 2008, doi: 10.1016/j.ultramic.2007.04.003.

[124] L. Clément, R. Pantel, L. F. Tz. Kwakman, and J. L. Rouvière, "Strain measurements by convergent-beam electron diffraction: The importance of stress relaxation in lamella preparations," *Appl. Phys. Lett.*, vol. 85, no. 4, Art. no. 4, Jul. 2004, doi: 10.1063/1.1774275.

[125] L. Wu, M.-G. Han, and Y. Zhu, "Toward accurate measurement of electromagnetic field by retrieving and refining the center position of non-uniform diffraction disks in Lorentz 4D-STEM," *Ultramicroscopy*, vol. 250, p. 113745, Aug. 2023, doi: 10.1016/j.ultramic.2023.113745.

[126] A. Clausen *et al.*, “LiberTEM: Software platform for scalable multidimensional data processing in transmission electron microscopy,” *J. Open Source Softw.*, vol. 5, no. 50, p. 2006, Jun. 2020, doi: 10.21105/joss.02006.

[127] D. Cooper, T. Denneulin, N. Bernier, A. Béché, and J.-L. Rouvière, “Strain mapping of semiconductor specimens with nm-scale resolution in a transmission electron microscope,” *Micron*, vol. 80, pp. 145–165, Jan. 2016, doi: 10.1016/j.micron.2015.09.001.

[128] Y. Jiang *et al.*, “Electron ptychography of 2D materials to deep sub-ångström resolution,” *Nature*, vol. 559, no. 7714, pp. 343–349, Jul. 2018, doi: 10.1038/s41586-018-0298-5.

[129] C. Ophus, “Four-Dimensional Scanning Transmission Electron Microscopy (4D-STEM): From Scanning Nanodiffraction to Ptychography and Beyond,” *Microsc. Microanal.*, vol. 25, no. 3, Art. no. 3, Jun. 2019, doi: 10.1017/S1431927619000497.

[130] T. J. Pennycook, G. T. Martinez, C. M. O’Leary, H. Yang, and P. D. Nellist, “Efficient Phase Contrast Imaging via Electron Ptychography, a Tutorial,” *Microsc. Microanal.*, vol. 25, no. S2, pp. 2684–2685, Aug. 2019, doi: 10.1017/S1431927619014156.